Study of Hadron Production in The Context of Quark-Hadron Phase Transition

A Thesis submitted to the

University of Allahabad

for the degree of

Doctor of Philosophy
in Science

by

Uma Shankar Gupta

under the supervision of

Dr. Vivek Kumar Tiwari

Department of Physics

University of Allahabad

Allahabad – 211002, India

Year 2011

Certificate

This is to certify that the Ph.D. thesis titled **Study of Hadron Production in The Context of Quark-Hadron Phase Transition** submitted by Uma Shankar Gupta (Enrollment no. 05AU/680) for the award of the degree of Doctor of Philosophy is a record of bona fide research work done under the supervision of Dr. Vivek Kumar Tiwari. It is further certified that the thesis represents original and independent work by the candidate and collaboration was necessitated by the nature and scope of the problems dealt with.

Dr. Vivek Kumar Tiwari
Thesis Supervisor
Dept. of Physics
University of Allahabad

Prof. M. C. Sharma
Head, Dept. of Physics
University of Allahabad

Prof. S. D. Dixit
Dean, Science Faculty
University of Allahabad

Declaration

This thesis titled **Study of Hadron Production in The Context of Quark-Hadron Phase Transition** is a presentation of my original research work. Whenever contributions of others are involved, every effort is made to indicate this clearly, with due reference to the literature and acknowledgement of collaborative research and discussions. The work is original and has not been submitted earlier as a whole or in part for a degree or diploma at this or any other Institution or University. This work was done under guidance of Dr. Vivek Kumar Tiwari, Dept. of Physics, University of Allahabad.

Uma Shankar Gupta

Ph.D. Candidate

Acknowledgments

I would like to express immense gratitude towards my Ph.D supervisor Dr. Vivek Kumar Tiwari for his guidance, support and encouragement at every step of my research work without which this thesis would not have been possible.

I am very grateful to Prof. Ajit M. Srivastava for his collaboration and numerous physics discussions. It is a pleasure to acknowledge his support and encouragement during all these years of my thesis work.

I would like to express my sincere gratitude towards Shikha madam for her motherly care and blessings.

I am thankful to Prof. Sanatan Digal, Dr. Rajarshi Ray, Dr. Vishwanath Layak, Dr. Tamal Mukherjee and Dr. Ananta Prasad Mishra for very fruitful academic discussions and helping me at different stages during the completion of my Ph.D. work. I am very thankful to Ranjita for being collaborator and a great friend of mine. I am equally thankful to Saumia PS and Partha Bagachi also.

I am giving my special thanks to Amit Pathak, Anurag Tripathi, Rajarshi Tiwri, Trilochan Bagarthi and M. C. Kumar for helping me to learn different codes and software packages.

I express my sincere thanks to Prof. M. C. Sharma, Prof. Indira Mehrotra and Prof. Pradeep Kumar for support and encouragement. I am thankful to all my mates, youngers and seniors here in this department for the kind help, value and companion that I always have been receiving from them. I would like to gratefully acknowledge the support of the office of my department that they provided me throughout my thesis work.

I gratefully acknowledge the financial support of the Department of Atomic Energy-Board of Research in Nuclear Sciences (DAE-BRNS), India, under the research grant No. 2003/37/15/BRNS and grant No. 2008/37/13/BRNS. I also acknowledge the computational support of the computing facility which has been developed by the Nuclear

Particle Physics group of the Physics Department, Allahabad University under the Center of Advanced Studies(CAS) funding of UGC India.

Finally, I will not say thanks to my mother, brothers, Garima, Neelima, Jagriti, Vyom parashar, Abhishek Atreya, Raghvendra Yadav rather I'll prefer to be in debt throughout my life.

Contents

List of Tables

List of Figures

Chapter 1

Introduction

1.1 Particles and their interactions

The dynamics of nature is governed by four fundamentals interactions namely strong interaction (1), electromagnetic interaction (10^{-2}), weak interaction (10^{-13}) and gravitational interaction (10^{-38}). Here in parentheses, we have indicated the relative strength of these interactions normalized with respect to the strength of strong interaction. All the material particles carrying electric charge interact via electromagnetic force which is responsible for most of the happenings in our day to day life. This interaction is mediated by electrically neutral photons which are the massless gauge bosons resulting due to the invariance of electromagnetic interaction under local $U(1)$ gauge symmetry. The most fundamental material particles of nature called quarks and leptons, come in three different families of six flavors. The dynamics of flavor change gives rise to weak interaction which gets mediated by three heavy gauge bosons $W^{\pm}$ and Z^0. The idea of unifying different forces at an extremely high energy and a very small distance scale became a reality due to the discovery of the principle of gauge invariance for non-abelian Yang-Mills theories. The weak and electromagnetic interactions got unified in a single framework of electroweak theory with $SU_L(2) \times U_Y(1)$ gauge group and Higgs mechanism of spontaneous symmetry breaking for giving mass to the massive gauge bosons [1–3]. Now the Standard Model of particle physics has a firm grounding in sound theoretical principles with largely verifiable experimental predictions. Leaving the gravitational interaction aside, the Standard Model gives a unified description of strong interaction with the electroweak interaction in the framework of $SU_C(3) \times SU_L(2) \times U_Y(1)$ gauge invariant grand unified quantum field theory. Strong interaction is special in the sense that it can be cleanly detached from the rest of the Standard Model and studied separately as an individual theory. The proper theory of strong interaction is known as Quantum Chromodynamics (QCD) with the gauge group of $SU_C(3)$ for colour(C) charges. In nature, the formation of nuclei and interaction of nucleons (neutrons and protons) is governed by the strong force. Residual strong interaction among the nucleons, leads to the formation of nuclei and the QCD dynamics of the most fundamental particles called quarks and gluons, leads to the formation of composites known as nucleons. The particle content of the standard model has been shown in Fig.1.1.

The hadronic vacuum of the low energy QCD, is populated by light mesons (pions, etas and kaons starting with $m_\pi = 140$MeV) and heavy baryons (protons, neutrons, deltas, sigmas, lambdas, cascades and omegas starting with $m_N = 1$GeV). According to the similarity of their masses and other properties (like charge, isospin, strangeness, etc.), baryons and mesons were grouped into definite geometrical patterns known as the eightfold way which was invented by Gell-Mann and Ne'eman in 1961. Fig.1.2. shows the ordering for the meson and baryon octet. Later in 1964, Gell-Mann proposed that different geometrical patterns, emerging from the similarity in the properties of hadrons (baryons and mesons), can be explained as multiplets which result due to the different kinds of combinations of the three flavors of quarks (antiquarks) occurring in the fundamental representation of global $SU_f(3)$ flavor symmetry. The existence of Δ^{++} with three up quarks and parallel spins was mysterious because it was violating the Pauli exclusion principle. Y. Nambu and O. W. Greenberg working independently, resolved this mystery

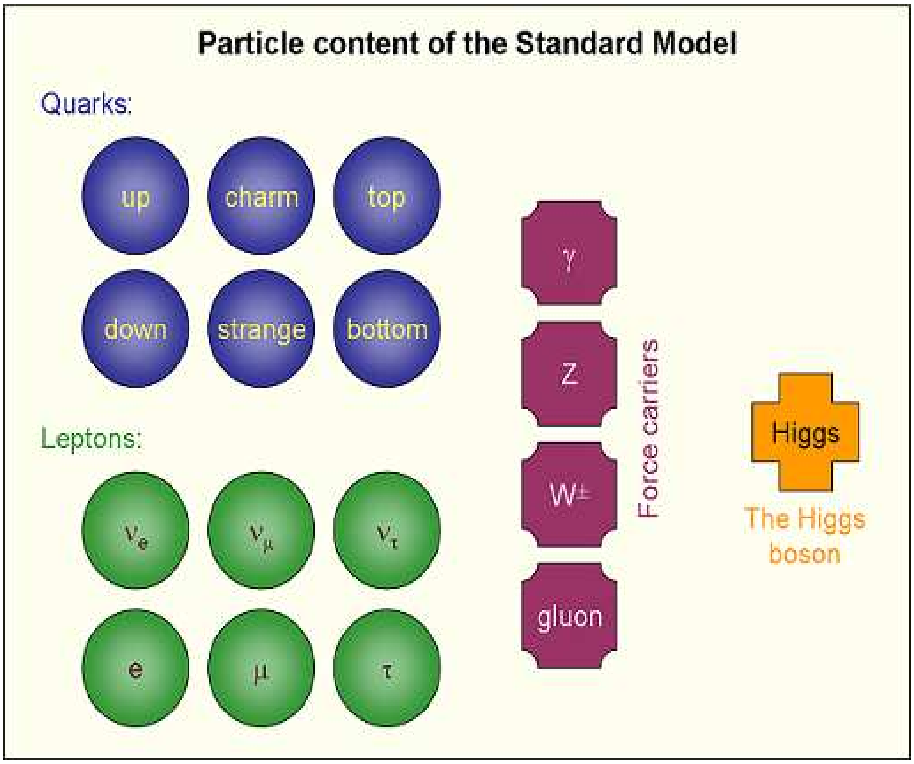

Figure 1.1: Particle content of the standard model

in 1970s by postulating an additional $SU(3)_C$ local gauge degree of freedom responsible for strong interaction dynamics. Later, this was renamed as colour charge.

Quarks and gluons are the basic units that carry the colour charge of strong interaction symbolically known as colour charge C. Quarks come in three colours namely red, blue and green and they continuously change their colour by the exchange of gluons which are eight massless vector gauge bosons mediating the strong interaction. We can not observe isolated quarks and gluons in experiments. Three quarks of different colours form colour singlet baryons while mesons are colourless combination of a quark and an antiquark. Thus the colour charge of strong interaction remains confined within the radius ($\sim$ 1 fm) of observed hadrons. This peculiar property of QCD is known as colour *confinement* [4, 5].

We do not have a proper understanding of colour confinement because it is a non-

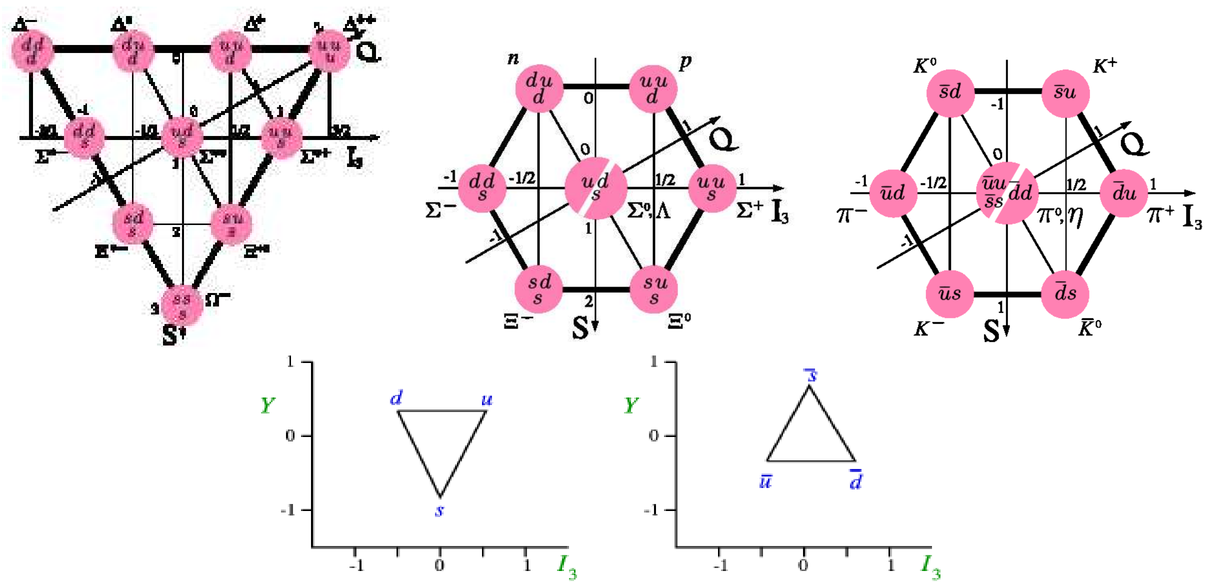

Figure 1.2: Baryon decuplet, baryon and meson octet, and quark antiquark triplet.

perturbative feature of QCD. In the low energy regime of QCD, when momentum transfer is very small ($q^2 << (100\text{ MeV})^2$) or the distance of resolution is large, the running QCD coupling constant becomes large ($\alpha_s \gg 1$) and the field theoretic perturbative expansion in the powers of coupling constant fails. As a consequence, the force between quarks and gluons becomes confining and shows a strong linear increase with the distance. The phenomenon of confinement is also witnessed in the results of numerical simulations of QCD on a discrete space-time lattice (lattice QCD) but still, we do not have a mathematical proof for it.

Since unlike photons, gluons themselves are charge carriers of strong force, their interaction with each other makes QCD a highly nonlinear theory with strikingly different behaviour at low and high energy scales. In the regime of very high energy and large momentum transfer ($q^2 >> (100\text{ MeV})^2$) at very small distance resolutions, QCD becomes an *asymptotically free* theory [4,5] and the running coupling constant becomes quite small ($\alpha_s \ll 1$). The interaction among the quarks and gluons becomes weak at small distances and the perturbative expansion works very well. The predictions of perturbative QCD

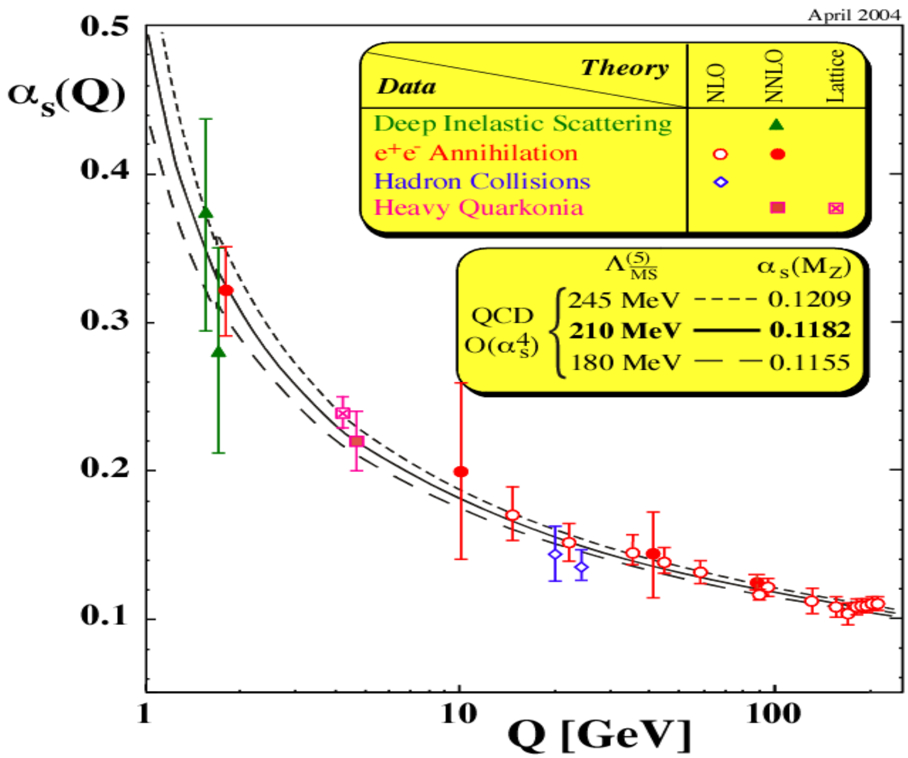

Figure 1.3: Theoretical values of running QCD coupling obtained from the perturbation theory compared with experimental values. Figure taken from [6].

have been widely confirmed in Deep Inelastic Scattering (DIS) experiments. In 1973, D. Gross, D. Politzer and F. Wilczek discovered the phenomenon of asymptotic freedom and they were awarded noble prize for this discovery in 2004. The variation of running coupling constant α_s with respect to the momentum transfer Q has been shown in Fig.1.3. In the regime of large momenta where the perturbation theory is well behaved, we observe a good agreement of the theory with the experiments. However, the running coupling constant moves towards the Landau pole in perturbation theory for small momenta and the perturbation theory predicts its own breakdown at this scale.

QCD is essentially well understood in the low as well as high energy limits. But, the connection between these two extremes, is not known even today and the QCD in the nonperturbative regime is still an open sector of the standard model.

1.2 Quark hadron phase transition: a motivation

Traditional particle physics essentially dealt only with the intrinsic structure of near ground state hadrons while traditional nuclear physics could throw light only onto the ground state of the extended QCD nuclear matter. What happens to the normal hadronic matter (collection of hadrons/nuclei) when it is heated or compressed to very high temperatures or densities? Hagedorn in his seminal work exploring the "statistical bootstrap model" [7] of hadronic/resonant/fireball matter arrived at the limits of hadronic matter stability and calculated the limiting energy density of about $1\text{GeV}/\text{fm}^3$ corresponding to the Hagedorn limiting temperature in the vicinity of $T \sim 160 - 170$ MeV [8] beyond which hadronic matter becomes unstable. Studies of extended strongly interacting matter *started looking beyond the limits* of hadronic matter stability when it was realized that partons i.e. quarks and gluons are the elementary carriers of the colour charge of strong interaction. Owing to the property of asymptotic freedom, QCD now implies a partonic matter phase beyond these limits in which the individual hadrons get dissolved into their constituents and produce a collective form of matter known as the quark gluon plasma (QGP). Thus one has to consider a phase transition occurring from hadronic phase to the QGP phase along the quark hadron phase boundary. Analogous to the insulator conductor transition in the atomic matter, the deconfinement transition generates a colour conducting medium of quarks and gluons where the colour charge of strong interaction gets liberated over large distances (~ 20 fm).

Comprehensive understanding of QCD confinement-deconfinement transition is of a fundamental importance also for understanding the primordial cosmological expansion of the early universe that passed through the QCD colour confining phase transition to hadrons at about five microseconds after the Big Bang. When the temperature was very high (at about $T \sim 150 - 200$ MeV $\sim 10^{12}$ K), the Big Bang matter evolved towards hadronization featuring a quark over antiquark density excess of 10^{-9} only resulting in a very small density (small chemical potential) of baryonic matter. Research in the

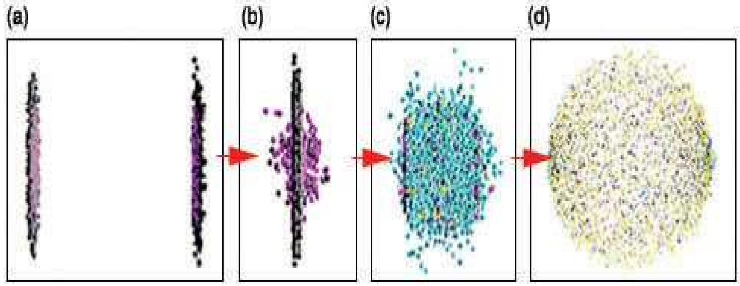

Figure 1.4: Schematic diagram showing the QGP formation in heavy ion collision experiments.

area of astrophysics gives another interesting impetus for studying quark hadron phase transition which is expected to take place in the very late stages of an evolving star (supernovae, hypernovae) when it is not able to sufficiently resist its gravitational collapse. It is expected that such stars may crush down to such high densities that nucleons do not remain in their hadronic state. Thus one may get a cold but highly dense blob of quark matter in the neutron star interiors or in the matter formed by the neutron star mergers.

Convergence of questions arising from astrophysics, cosmology (neutron star interior, supernovae dynamics, cosmological evolution in the early universe) and fundamental nuclear/hadronic physics (extended nuclear matter and its collective properties, excited hadronic matter and its limits of existence) led to the birth of research field known as Relativistic Heavy Ion Collision Physics in the late 1960's [8]. The behaviour of strongly interacting matter under extreme conditions of temperatures and densities can be studied experimentally using collisions between heavy nuclear projectiles at relativistic energies. In such collisions an initial dynamics of compression and heating converts the incident, cold nuclear ground state matter into a fireball of hadronic or partonic matter, thus populating the QCD matter phase diagram with the deconfined state of QGP which exists over a wide domain of temperature and density [9–13]. The energy available at Super Proton Synchrotron (SPS at CERN) or at collider facilities; Relativistic Heavy Ion Collider (RHIC at BNL), Large Hadron Collider (LHC at CERN), suffices to reach plasma

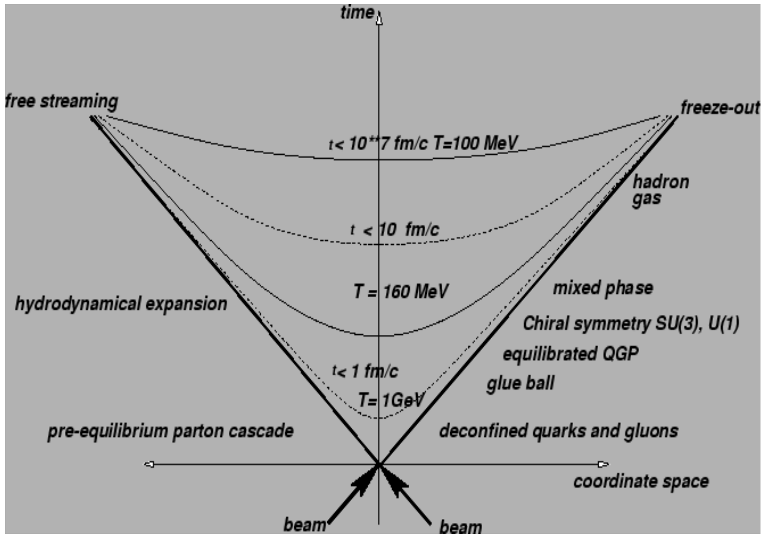

Figure 1.5: Stages of QGP evolution in heavy ion collision experiments.

temperature up to 1 GeV, i.e. far beyond the quark hadron phase transition critical temperature, of about 170 MeV. Fig.1.4 shows a schematic diagram for the formation of QGP in a head on (zero impact parameter) ultra-relativistic collision of two heavy nuclei of pancake shape which happen to pass through each other. The QGP produced is known as the baryon less (nearly zero chemical potential) plasma in this case. Recently, it was shown that the new state of matter produced at RHIC is far away from the hot QGP which is asymptotically free. This RHICE nuclear matter has indicated a strongly coupled regime of QGP which is called strongly coupled quark gluon plasma (sQGP) [14–17]. Recent developments in QGP physics can be found in reviews, e.g., see ref. [9, 18–23].

The QGP produced in these experiments is a transient state which exists for a very short period of time. It gets converted quickly into hadrons after a brief evolution passing through the stages of hydrodynamic expansion, thermalization, chemical and thermal freeze out. Information regarding different stages of the QGP evolution is obtained through the analysis of the particles captured by the detectors. This makes the interpretation of experimental results extremely difficult. The proper understanding of these results, require a detailed study of the thermodynamics of the system. Different statistical tools of analysis are used to study the system. Fig.1.5 shows the different stages of formation and evolution of QGP.

1.3 QCD phase transition and order parameters

The study of the different aspects of quark hadron phase transition is a tough and challenging task because it requires the understanding of inputs and ideas from research in diverse fields like statistical mechanics, condensed matter physics, nuclear physics, cosmology, astrophysics, finite temperature version of Yang-Mills quantum field theories, symmetry breaking phase transitions leading to the formation of topological objects and structures, etc.

Common example of the phase transitions are change of substance from solid to liquid (melting) or from liquid to gas (boiling or evaporation). Their inverse processes i.e. freezing and condensations respectively, also represent such transitions. Ferromagnetic materials exhibit a long range ordering phenomenon at the atomic level which causes the unpaired electron spins to line up parallel with each other in a region called domain. Each domain has a net magnetic moment but the bulk material will usually be demagnetized because of the random orientation of different domains with respect to each other. Even an extremely small external magnetic field, causes magnetic domains to line up with each other and material shows up net magnetism. This long range order vanishes above the Curie temperature ($\simeq$ 1000 K for iron) and there is a phase transition of the system to the disordered phase of paramagnetic state. Another example is that of superconductivity where resistance of some metals like mercury and lead, becomes zero below a certain critical temperature. Then there is the phenomenon of superfluidity, liquid helium behaves like a normal fluid unless cooled below some critical temperature when it becomes superfluid where the viscous drag becomes zero. Yet another such fascinating system is liquid crystal, above certain temperature it behaves like isotropic liquid and below that it also shows partly crystal like properties.

For equilibrium phase transitions, the phases of system are well defined and one can draw a phase diagram in the plane of intrinsic parameters of the system like temperature, pressure, density (chemical potential) etc. In the language of statistical mechanics, the system should be in its lowest free energy state (ground state). In equilibrium situations, free energy is analytic almost over the whole phase diagram and the regions where it becomes non analytic are called phase boundaries which demarcate different phases. Phase transitions result, when the system is driven from one phase to another across the phase boundary by the change of parameters like temperature, chemical potential etc.

The physics of phase transitions is often associated with the spontaneous breakdown of certain continuous symmetries. Spontaneous symmetry breaking occurs in a situation where the interaction governing physics of the system remains invariant under certain symmetry transformation while the system settles down spontaneously in one of the various possible equivalent ground states allowed by that transformation. Symmetry breaking phase transition can always be characterized by an *order parameter* (OP) which is nonzero in one phase and becomes zero in the other. The long range order of atomic magnets in the ferromagnetic phase is given by magnetization vector which is an example of order parameter (OP). The rotational symmetry of magnetization vector which is zero in paramagnetic state, gets spontaneously broken when nonzero value of the magnetization in a domain, chooses certain orientation in the ferromagnetic phase of the substance below the Curie temperature. The set of values of OP field which minimize the free energy of the system in a particular phase, constitute the *order parameter space*. The OP field is usually called the Higgs field, and the OP space is called the *vacuum manifold*. When we change the parameters like temperature, chemical potential etc., the OP field may either jump discontinuously or change continuously when the system goes through the phase transition. Discontinuous jump of the OP field signals a first order phase transition while continuous change in the OP field gives rise to second order or continuous phase

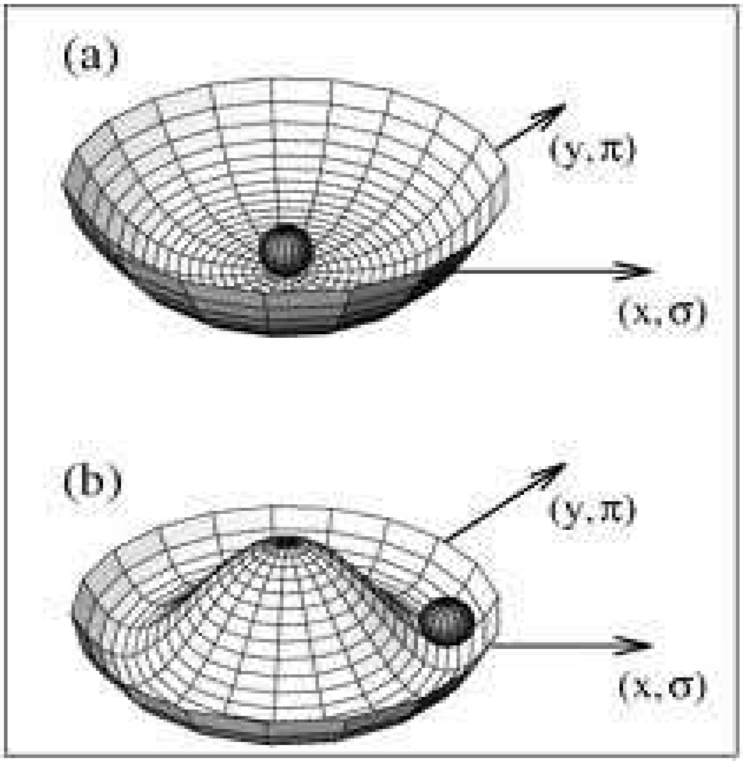

Figure 1.6: Spontaneous symmetry breaking: cartoon of the effective potential constructed in the plane of $x \to \sigma$, $y \to \vec{\pi}$ fields.

transition.

We need suitable order parameters for constructing the theory of quark hadron phase transition. Hence we look for the continuous and discrete global symmetries of the QCD. In the zero quark mass limit, QCD can be studied by a characteristic known as chiral symmetry. In the infinite quark mass limit, the discrete global Z(3) symmetry of QCD at finite temperature allows us to study the phenomenon of colour confining - deconfining phase transition. In the extremely high density limit, QCD phase transition can be studied as colour super-conductivity. The understanding of colour confinement and $U_A(1)$ axial symmetry breaking is also being attempted in terms of instantons of $SU(3)$ gauge theory [24].

1.4 Chiral symmetry breaking/restoring phase transition

Here we will discuss the chiral symmetry in brief. It is well known that the basic QCD Lagrangian has the global $SU_{R+L}(N_f) \times SU_{R-L}(N_f)$ symmetry for N_f flavors of massless quarks. The axial (A=R-L) part of this symmetry known as the chiral symmetry, is spontaneously broken by the formation of a chiral condensate in the low energy hadronic vacuum of QCD and one gets $(N_f^2 - 1)$ massless Goldstone bosons according to the Goldstone's theorem. Chiral condensate which works as the order parameter field of the chiral symmetry breaking phase transition at low temperatures is nothing but the Bose condensate of the underlying quark degrees of freedom much like the Cooper pairs in superconductors and liquid He^3 and electrons in superfluids [25]. The order of the chiral symmetry restoring phase transition at high temperature depends on the number of quark flavors and their masses. The $SU_L(2) \times SU_R(2)$ group describing chiral symmetry for two massless flavors in QCD, is isomorphic to the $O(4)$ group of the rotational symmetry for magnetization vector in ferromagnet [26]. In both cases continuous symmetry is spontaneously broken and we get spin waves in ferromagnets and massless pions in the two flavour QCD as massless Goldstone modes. Fig.1.6 shows the cartoon of effective potential constructed in plane of $x \rightarrow \sigma$, $y \rightarrow \vec{\pi}$ fields. The effective potential which is symmetric in $(\sigma, \vec{\pi})$ fields in Fig.1.6(a), represents chiral symmetry restored phase. Effective potential in Fig.1.6(b), shows the spontaneous break down of the chiral symmetry where pions are zero energy massless excitations in the valley and for three independent directions of pions, the valley represents a three sphere (S^3). Since the ferromagnetic transition is of second order, the two massless flavours chiral transition at high temperature and zero baryon chemical potential, turns second order in the presence of $U_A(1)$ anomaly by the powerful universality arguments. For three massless quarks, $N_f = 3$, the chiral transition is always first order [26, 27]. Just as an external magnetic field breaks the rotational symmetry of the ferromagnet, small quark masses in real life explicitly break the chiral symmetry of the QCD Lagrangian. However, the observed lightness of pions in nature suggests that we have an approximate chiral symmetry for QCD with two flavors of light u and d quarks. Small finite quark masses make the chiral transition a rapid/smooth crossover in some ranges of baryon chemical potential and temperature.

1.5 Confinement-Deconfinement (C-D) phase transition

QCD is a non abelian gauge theory where quarks coming in three colours, constitute the fundamental representation of $SU_C(3)$ colour group while gluons form the adjoint representation and hence come in eight types. The low energy structure of the QCD vacuum is confining where colour charge of the strong interaction is confined inside the hadrons. At extremely high temperature and densities corresponding to energy density of 1GeV/fm^3, the phase transition from hadronic matter to QGP is termed as the confinement-deconfinement (C-D) transition. The gluon dynamics is responsible for the colour confinement due to its self interaction. If the masses of the quarks are considered infinite, finite temperature QCD in the absence of dynamical quarks, behaves as a pure $SU_C(3)$ hot gauge theory which shows the invariance under the global $Z_C(3)$ center symmetric transformations of the colour gauge group. The Center symmetry which is a symmetry of hadronic vacuum, gets spontaneously broken in the high temperature regime of QGP.

The thermal expectation value of the Wilson line (Polyakov loop) $\langle l(x) \rangle$ is related to the free energy of a static colour charge. It vanishes in the low temperature confining phase. If one interprets $\langle l(x) \rangle \sim exp^{-F_Q/T}$ where F_Q is the free energy of an infinitely heavy quark [12,28], then $\langle l(x) \rangle = 0$ implies that the free energy is infinite corresponding to the confinement of colour charges. Non zero value of $\langle l(x) \rangle$ in the high temperature phase implies that the free energy is finite. This means that colour degrees of freedom have got liberated signaling transition to the deconfining phase. Therefore the Polyakov loop expectation value $\langle l(x) \rangle$ can serve as the order parameter of C-D phase transition [29].

For N_c colours $SU(N_c)$ pure gauge Yang-Mills theory, the action has a global $Z(N_c)$ symmetry. This symmetry is also broken spontaneously by the non zero expectation value of the Polyakov loop in the high temperature phase. The pure gluonic theory for $N_c = 2$ and 3, have been studied in lattice gauge simulations with the finite-size scaling analysis [30, 31]. It has been shown that there is a second-order phase transition for $N_c = 2$ and a first order phase transition for $N_c = 3$. For $N_c = 2$ the critical exponent has been found to agree with the same universality class as that of $Z(2)$ Ising spin model. Further, the effective potential for the Polyakov loop constructed in the Landau - Ginzburg approach, has a cubic invariant for $N_c = 3$ hence one naturally gets first order phase transition [31–33]. Recent studies of the pure gluonic theory with $N_c = 4, 6, 8, 10$ indicate that the transition is of first order for $N_c \geq 3$ and becomes stronger as N_c increases [34,35]. This behaviour is similar to that of the 3D N_c-state Potts model [36]. Effective theory analysis which accounts for the effect of dynamical quarks in the results of pure gauge $N_c = 3$ lattice simulations, concludes that the real life C-D transition in QCD is a rapid crossover [37]. Even though the center symmetry in the real life QCD is always broken with the inclusion of dynamical quarks in the pure gauge QCD system, one can regard the Polyakov loop as an approximate order parameter because it is a good indicator of a rapid crossover in the C-D transition [9, 37, 38].

The first principle lattice QCD Monte Carlo simulations [39–54] give us important information and insights regarding various aspects of the quark hadron phase transition, like the restoration of chiral symmetry in QCD, order of the C-D phase transition, richness of the QCD phase structure and mapping of the phase diagram. Unfortunately progress in lattice QCD calculations has got severely hampered due to the QCD action becoming complex on account of the fermion sign problem [39] when baryon density/chemical potential is non zero. Though several methods have been developed to circumvent the sign problem at small baryon chemical potentials, a general solution to the sign problem for all chemical potentials is yet to be devised. Further since lattice calculations are technically involved and various issues are not conclusively settled within the lattice community, one resorts to the calculations within the ambit of phenomenological models where the effective potential is constructed in terms of effective degrees of freedom. These models serve to complement the lattice simulations and give much needed insight about the regions of phase diagram inaccessible to lattice simulations.

1.6 Thesis overview

In recent years, effective potential models, having the pattern of chiral symmetry breaking as that of QCD like the linear sigma models (LSM) [55–62] the quark-meson (QM) models(see e.g. [61, 63–72] and Nambu-Jona-Lasinio (NJL) type models [63, 73–78] have led to the investigation of the properties and structure of chiral symmetry restoring phase transition at sufficiently high temperature and density. Later these models were extended to incorporate the features of C-D transition where chiral condensate and Polyakov loop got simultaneously coupled to the quark degrees of freedom. Thus Polyakov loop augmented PNJL models [79–95], Polyakov loop augmented linear sigma models (PLSM) and Polyakov loop augmented quark meson models (PQM) [96–104] have facilitated the investigation of the full QCD thermodynamics and phase structure at zero as well as finite quark chemical potential and it has been shown that bulk thermodynamics of the effective models agrees well with the lattice QCD data.

In chapter 2, we have discussed the QCD Lagrangian, the formulation of statistical QCD at finite temperature and density in a medium, center symmetry for finite temperature QCD and its spontaneous as well as explicit break down, C-D transition and Polyakov loop order parameter, chiral symmetry of QCD Lagrangian and its spontaneous as well as explicit break down, Landau-Ginzburg analysis of chiral transition in effective theory framework, QCD phase structure and phase diagram. Finally, we have given a brief description of the experimental indications for the QCD phase transition.

In this thesis, the presentation of about two third of the total volume of research work, is centered around effective model building where the features of spontaneous breakdown of both the chiral symmetry as well as the center Z(3) symmetry of QCD has been incorporated in one single model. We have combined, the chiral condensate and the Polyakov loop simultaneously to the quark degrees of freedom in the $SU_L(2) \times SU_R(2)$ and $SU_L(3) \times SU_R(3)$ linear sigma models. We thus constructed Polyakov quark meson models for two flavours and three flavours of quark. These models have incorporated the symmetries and symmetry breaking scenarios of QCD in a realistic way. These are QCD like theories which can give a realistic description of quark hadron phase transition. We have investigated in detail the phase structure, phase diagram and the interplay of chiral symmetry restoration and C-D phase transition.

In chapter 3 we have improved the effective potential of Polyakov loop extended Quark Meson Model (PQM) for the two quark flavour by considering the contribution of fermionic vacuum loop and explored the phase structure and thermodynamics of the resulting PQMVT model (Polyakov Quark Meson Model with Vacuum Term) in detail at non zero as well as zero chemical potentials. The QCD phase diagram together with the location of critical end point (CEP) has been obtained in μ, and T plane in both the models PQMVT and PQM. The PQMVT model analysis has been compared with the calculations in PQM model in order to bring out the effect of fermionic vacuum term on the thermodynamics of the physical observables [105].

In chapter 4 we have investigated the influence of Polyakov loop on meson mass and mixing angle calculations in scalar and pseudoscalar sector, in the framework of generalized 2+1 flavor quark meson linear sigma model enlarged with the inclusion of the Polyakov loop [101]. Since we are lacking in the experimental information on the behaviour of mass and mixing angle observables in the medium, a comparative study of these quantities in different models and circumstances becomes all the more desirable. We have derived the modification of meson masses due to the $\bar{q}q$ contribution in the presence of Polyakov loop. We have studied how the inclusion of Polyakov loop, qualitatively and quantitatively affects the convergence of the masses of chiral partners, when the parity doubling takes place as the temperature is increased through T_c and the partial restoration of chiral symmetry is achieved. We will also be studying the effect of Polyakov loop on the interplay of $SU_A(3)$ chiral symmetry and $U_A(1)$ symmetry restoration.

Very recently, an interesting line of investigation has been opened up in our current research work where the non trivial topology of spontaneously broken Z(3) symmetric vacuum of pure gauge QCD, has been exploited to study the dynamics of C-D phase transition in the context of relativistic heavy ion collision experiments [106–108]. It is well known from the condensed matter systems that the spontaneous breaking of the continuous or discrete symmetry, leads to the formation of topological defects. These are solitonic solutions of the classical field equations for the system. Non trivial topology of the vacuum manifold (OP space) brings topological defects into the existence. Topological arguments being universal in nature, do not depend on the details of the phase transition dynamics but only on the symmetry of the system. Common example of the topological defects are domain walls, cosmic strings and monopoles that could have formed during the cosmological phase transitions at different stages in the evolution of universe. In the case of C-D transition in pure gauge QCD, spontaneous break down of the Z(3) symmetry in the high temperature phase of QGP, gives rise to three different Z(3) vacua which are degenerate. The interpolation of the Polyakov loop order parameter field $\langle l(x) \rangle$ between three different degenerate Z(3) vacua leads to the formation of domain walls (Z(3) interfaces). The line like intersection of three different Z(3) interfaces lead to the formation of topological string called QGP string where the order parameter $l(x)$ becomes zero. Thus the core of such string is in confining phase [107]. Detailed field theoretic numerical simulations for the complex scalar field (Polyakov loop) have been carried out in ref. [107] to study the dynamics C-D phase transition which starts during the pre-equilibrium stage in relativistic heavy-ion collision experiments. A simple model of quasi-equilibrium system was assumed for this stage with an effective temperature which first rises (with rapid particle production) to a maximum temperature $T_0 > T_c$, and then decreases due to continued plasma expansion. The formation of Z(3) walls and associated strings in the initial transition from confining (hadronic) phase to denconfining phase, has been investigated via the so called Kibble mechanism [109]. The essential physics of the Kibble mechanism is contained in a sort of domain structure arising after any phase transition which represents random variation of the order parameter at distances beyond the typical correlation length. Using the results of lattice gauge theory, Pisarski's phenomenological construction of effective potential for Polyakov loop [37,110–112] shows a weak first order phase transition. This potential has been used to implement the domain structure where the weak first order C-D transition proceeds via bubble nucleation, leading to the well defined domain structure. The field configurations corresponding to the bubble profile got numerically generated using the Coleman technique [113]. QGP bubbles having different Z(3) vacua inside them, are randomly nucleated on the lattice in the false vacuum background of the hadronic phase and evolved through the equation of motion. In the course of their time evolution, expanding QGP bubbles of different Z(3) vacua come close and then coalesce with each other. The coalescence of QGP bubbles, leads to the formation of Z(3) walls and strings. The evolution of Z(3) walls and string networks can be numerically seen and studied in these simulations. Possible experimental signatures resulting from the presence of Z(3) wall networks and associated strings in relativistic heavy ion collision experiments, have been discussed in ref. [107].

In the chapter 5 of the thesis, we have reported our novel work of numerical simulation of first order quark hadron phase transition via bubble nucleation (which may be appropriate, for example, at finite baryon chemical potential) in the context of relativistic heavy ion collision experiments. We have investigated, the effects of explicit breaking of Z(3) symmetry due to the presence of dynamical quarks on the formation and evolution of Z(3) walls and associated QGP strings within the Polyakov loop model. We calculated the bubble profiles using Coleman's technique of bounce solution, for the true vacuum as well as for the metastable Z(3) vacua, and estimated the associated nucleation probabilities. These different bubbles are randomly nucleated on the lattice in the false vacuum background of the hadronic phase and then evolved by the equation of motion calculated from the Polyakov loop effective potential. The resulting formation and dynamics of Z(3) walls and QGP strings, has been studied. Further, we analyzed various implications of the existence of these Z(3) interfaces and the QGP strings, especially in view of the effects of the explicit breaking of the Z(3) symmetry on the formation and dynamical evolution of these objects. Finally, we discussed possible experimental signatures of Z(3) walls and strings with explicit symmetry breaking [114]. **Chapter 6** summarizes conclusions and appendix given in **chapter 7** contains formulae for the first and second derivatives of the grand potential with respect to temperature and chemical potential.

Chapter 2

Symmetries of QCD and its phase structure

Quantum Chromodynamics (QCD) which is commonly accepted as the correct description of strong interaction, is a non abelian gauge theory. In the extremely high energy domain, the non abelian nature of the gauge theory makes the strong interaction very weak and the theory becomes perturbative. This property known as asymptotic freedom has got strong verification in deep inelastic electron-proton and proton-proton collision experiments. The constant that couples the most basic units of QCD (quarks and gluons), becomes large in low energy domain. The theory turns non-perturbative and confining. The observed degrees of freedom in nature for low energy domain are hadrons which are composite structures of quarks and gluons where they always remain confined. We do not have a proper understanding of strong interaction physics in the intermediate energy domain which connects the non perturbative hadronic vacuum to the vacuum of perturbative QCD.

In order to understand the transition from ordinary hadronic matter to the plasma of quarks and gluons at very high temperature and baryon densities, we need to know the collective behaviour of statistical QCD in the bulk of hot and dense medium. The quark hadron phase transition may be the result of a non analytic change in the bulk properties of QCD in certain temperature and density (chemical potential) regimes. We need to construct proper order parameters for QCD that distinguish two phases (QGP and hadronic) by their non analytic behaviour at the phase boundary. Order parameters are often associated with the spontaneous breakdown of some internal symmetry that distinguishes two thermodynamic phases at the microscopic level of the interaction dynamics. Hence one needs to study the symmetry structure (local as well as global) of strong interaction dynamics in order to construct order parameter for the QCD phase transition. QCD is a highly complex theory which reveals rich phase structure in different energy regimes. In certain approximations, the symmetry structure of QCD Lagrangian allows for the construction of at least three order parameters for quark deconfinement, chiral symmetry restoration and colour superconducting phase transitions in different temperature/density regimes.

The current chapter gives a brief description of statistical QCD in a medium , the symmetry structure of the QCD Lagrangian, the phase structure of QCD and finally the experimental indications for QCD phase transition. First we shall introduce the QCD Lagrangian with the most striking property of gauge invariance under a $SU_c(3)$ local gauge transformation in section 2.1. Next we will give a brief description of the finite temperature formulation of statistical QCD in section 2.2. The center symmetry Z(3) of $SU_c(3)$ gauge group is very useful for the construction of order parameter for confinement-deconfinement phase transition. We will present its discussion in the next section 2.3. For massless quarks, QCD Lagrangian exhibits the property of chiral symmetry. In real life, QCD shows an approximate chiral symmetry for light flavours of quarks. The experimentally observed hadronic spectrum at low energy gives a strong evidence for the spontaneous breakdown of chiral symmetry. The next section 2.4 describes chiral symmetry, its explicit as well as spontaneous breakdown. We will also be giving a brief description of the Landau-Ginzburg analysis of the chiral transition based on universality arguments in the framework of linear sigma model. Next we will describe the phase structure of QCD and the construction of phase diagram in the temperature and chemical potential plane in section 2.5. We will give a brief description of experimental indications for QCD transition in the end.

2.1 QCD Lagrangian

The QCD Lagrangian is given by the following expression

$$\mathcal{L}_{QCD} = \bar{\Psi}\left(i\gamma^{\mu}D_{\mu} - M\right)\Psi - \frac{1}{4}F^{a}_{\mu\nu}F^{\mu\nu}_{a} \tag{2.1}$$

The quark field spinor $\Psi(x)$ is a $4N_cN_f$ component column matrix. N_c is the number of colours, N_f is the number of flavours and 4 corresponds to the Dirac components of the spinor field. M is quark mass matrix, γ^{μ} are the Dirac matrices and the covariant derivative D_{μ} is defined by

$$D_{\mu} = \partial_{\mu} - ig_sA_{\mu} \tag{2.2}$$

where $A_{\mu} = A^{a}_{\mu}T^{a}$, $T^{a} = \lambda_a/2$, are the $(N_c^2 - 1)$ generators of $SU(N_c)$ symmetry, λ_a are the Gell-Mann matrices. The gluon degrees of freedom A_{μ} are coupled to the fermionic field by the strong coupling constant g_s. QCD Lagrangian is invariant under the following local gauge symmetry transformations for the quark and gluon fields

$$\Psi(x) \rightarrow \Psi^{'}(x) = U(x)\Psi(x) \quad A_{\mu}(x) \rightarrow A^{'}_{\mu}(x) = U(x)\left(A_{\mu}(x) + \frac{i}{g_s}\partial_{\mu}\right)U^{\dagger}(x) \tag{2.3}$$

where $U(x) = e^{-iT^{a}\alpha^{a}(x)} \in SU(N_c)$ and $\alpha^{a}(x)$ are space time dependent $(N_c^2 - 1)$ independent parameters of the $SU(N_c)$ group. The gluon field strength tensor $F_{\mu\nu}$ is given as

$$F^{a}_{\mu\nu} = \partial_{\mu}A^{a}_{\nu} - \partial_{\nu}A^{a}_{\mu} + g_sf^{abc}A^{b}_{\mu}A^{c}_{\nu} \tag{2.4}$$

where f^{abc} are the structure constants for SU(3). The transformation law for the field strength is written as

$$F^{a}_{\mu\nu}T^{a} \rightarrow U(x)F^{a}_{\mu\nu}T^{a}U^{\dagger}(x) \tag{2.5}$$

Notice that the $F^a_{\mu\nu}$ is not a gauge invariant quantity since there are eight field strengths (for $N_c = 3$ colours), each associated with an independent direction corresponding to eight generators for $SU_c(3)$ symmetry transformation. However, the gauge invariant combination $-\frac{1}{2}\mathrm{Tr}_c[\left(F^a_{\mu\nu}\right)^2] = -\frac{1}{4}F^a_{\mu\nu}F^{\mu\nu}_a$ gives the kinetic energy term for the vector gluonic fields A_μ.

In contrast to photons in Quantum Electrodynamics (QED), gluons themselves are the carries of colour charge and hence they interact with each other. Consequently the QCD Lagrangian contains cubic and quartic terms in A_μ arising from the term $\frac{1}{4}F_{\mu\nu}F^{\mu\nu}$. This makes QCD, a very nontrivial interacting field theory with strikingly different properties in the high and low energy domains.

2.2 Statistical QCD In Medium

In order to know the properties of statistical QCD in the hot and dense medium, one needs to evaluate the density matrix (ρ) at finite temperatures T and chemical potentials μ

$$\rho = e^{-\beta(\mathcal{H}-\mu\mathcal{N})} \tag{2.6}$$

where β is the inverse temperature, $\mathcal{H}$ is the Hamiltonian of the system and $\mathcal{N}$ is the particle number operator. The thermal expectation value of an operator $\mathcal{A}$ can be obtained as

$$\langle\mathcal{A}\rangle_\beta = \frac{1}{\mathcal{Z}}\mathrm{Tr}[\mathcal{A}\ \rho] \tag{2.7}$$

The normalization factor ($\mathcal{Z}$) called grand canonical partition function is defined as

$$\mathcal{Z} = \mathrm{Tr}\left[\rho\right] = \mathrm{Tr}\left[e^{-\beta(\mathcal{H}-\mu\mathcal{N})}\right] \tag{2.8}$$

In the standard approach, the statistical density operator ρ is regarded as the time evolution operator in imaginary time $\tau = it$ over the interval $[0,\beta]$. For the case of scalar field, the partition function can be expressed in terms of the following Euclidean path integral

$$\mathcal{Z}(T,V) = \oint \mathcal{D}\phi \exp\Big[- \int_0^\beta \mathrm{d}\tau \int_{\mathrm{V}} \mathrm{d}^3\mathrm{x} \mathcal{L}^{\mathrm{E}}\left[\phi(\mathbf{x},\tau)\right]\Big] \tag{2.9}$$

where $\mathcal{L}^E$ is the Euclidean Lagrangian for the scalar field and the field ϕ satisfies the periodic boundary conditions for bosons, $\phi(x,0) = \phi(x,\beta)$. Fermionic fields have to obey antiperiodic boundary conditions $\Psi(x,0) = -\Psi(x,\beta)$ due to their spinor nature. Finite temperature field theory, thus becomes equivalent to a Euclidean field theory in a four dimensional space time with the time component compactified on a ring with circumference $\beta = \frac{1}{T}$. The thermal expectation value of the operator $\mathcal{A}[\phi]$ in contact with a heat bath can be written as

$$\langle \mathcal{A} \rangle_\beta = \frac{1}{\mathcal{Z}} \oint \mathcal{D}\phi \, \mathcal{A}[\phi] \exp\Big[- \int_0^\beta \mathrm{d}\tau \int_{\mathrm{V}} \mathrm{d}^3\mathrm{x} \, \mathcal{L}^{\mathrm{E}}\left[\phi(\mathbf{x},\tau)\right]\Big] \tag{2.10}$$

Since the Eq.(2.9) is similar to the generating functional $\mathcal{Z}[J]$ for vanishing external source J at zero temperature, both perturbative Feynman diagram calculations and lattice gauge theory techniques can be easily adopted to evaluate $\langle \mathcal{A} \rangle_\beta$.

In order to obtain the expression for QCD partition function, the trace of density matrix is evaluated by summing over all possible quantum states which satisfy the Gauss' law for the colour fields. The expression for QCD partition function $\mathcal{Z}_{QCD}(T,V,\mu)$ follows as [115]

$$\mathcal{Z}_{QCD}(T,V,\mu) = \int \mathcal{D}\overline{\Psi}\, \mathcal{D}\Psi \, \mathcal{D}A_\mu \exp\Big[- \int_0^\beta \mathrm{d}\tau \int_{\mathrm{V}} \mathrm{d}^3\mathrm{x} \left(\mathcal{L}^{\mathrm{E}}_{\mathrm{QCD}} - \mu\mathcal{N}\right)\Big] \tag{2.11}$$

where $\mathcal{L}^E_{QCD}$ is the Euclidean version of the QCD Lagrangian, μ is the quark chemical potential and $\mathcal{N} = \Psi^\dagger\Psi$.

Different calculational frameworks arise due to the various choices possible for time path in Eq.(2.11). We are using the so called imaginary time formalism in our work which results due to the simple choice of direct path. The major advantage of this formalism comes from the Fourier language of the finite temperature Feynman rules which are very similar to those of vacuum theory, except that the propagators now have imaginary and discrete energies. The loop integrals are replaced by

$$\int \frac{d^4p}{(2\pi)^4} \rightarrow iT \sum_{n=-\infty}^{+\infty} \int \frac{d^3p}{(2\pi)^3} \tag{2.12}$$

where the summations runs over discrete set of Matsubara frequencies ω_n. The delta functions conserving energy momentum become

$$(2\pi)^4 \, \delta^4(p) \rightarrow \frac{(2\pi)^3}{iT} \, \delta_{n,0} \, \delta^3(\mathbf{p}) \tag{2.13}$$

The Matsubara frequencies appear due to the following replacement of p_0

$$p_0 \longrightarrow \omega_n = \begin{cases} \frac{2\pi i}{\beta} n & \text{for bosons} \\ \frac{\pi i}{\beta}(2n+1) & \text{for fermions} \end{cases}$$

The center $Z(N_c)$ of the gauge group $SU(N_c)$ can be separated as a global symmetry in the finite temperature treatment due to the requirement of periodic boundary conditions for gauge bosons. The center symmetry $Z(3)$ for QCD turns out to be very useful in understanding confinement.

2.3 Z(3) Symmetry And Confinement

The center symmetry can be studied by considering a system without quarks i. e. pure gauge Yang-Mills theory. The partition function for this can be written as

$$Z_g(\beta) = \int DA_\mu \mathrm{e}^{-\mathrm{S_g[A]}} \tag{2.14}$$

where A_μ is the gauge field and the action for pure gauge theory

$$S_g[A] = -\frac{1}{2} \int_0^\beta d\tau \int d^3x \, \mathrm{Tr} \, [F^a_{\mu\nu} F^{\mu\nu}_a] \tag{2.15}$$

In Eq.(2.14) the gluonic fields are obeying periodic boundary conditions in the Euclidean time direction

$$A_\mu(\mathbf{x}, \tau + \beta) = A_\mu(\mathbf{x}, \tau) \tag{2.16}$$

The principle of gauge invariance demands the invariance of action $S_g[A]$ under the transformation

$$A_\mu(\mathbf{x},\tau) \to A'_\mu(\mathbf{x},\tau) = U(\mathbf{x},\tau)\left(A_\mu(\mathbf{x},\tau) + \frac{i}{g_s}\partial_\mu\right)U^\dagger(\mathbf{x},\tau) \tag{2.17}$$

where $U(\mathbf{x},\tau) \in SU(N_c)$.

The boundary condition (2.16) is to be satisfied by the transformed gauge fields also.

We have two types of gauge transformations

$$U(\mathbf{x},\tau+\beta) = U(\mathbf{x},\tau); \quad \text{and} \quad \mathrm{U}(\mathbf{x},\tau+\beta) = \mathrm{gU}(\mathbf{x},\tau) \tag{2.18}$$

where $g \in SU(N_c)$ and it is space-time independent with $g^\dagger g = 1$. The periodic transformations of the first type do not impose any restrictions but if the twisted gauge transformations of the second type are examined closely, we find

$$\begin{aligned}
A'_\mu(\mathbf{x},\tau) &= A'_\mu(\mathbf{x},\tau+\beta) \\
&= U(\mathbf{x},\tau+\beta)\left[A_\mu(\mathbf{x},\tau+\beta) + \frac{i}{g_s}\partial_\mu\right]U^\dagger(\mathbf{x},\tau+\beta) \\
&= g\,U(\mathbf{x},\tau)\left[A_\mu(\mathbf{x},\tau) + \frac{i}{g_s}\partial_\mu\right]\left[U^\dagger(\mathbf{x},\tau)\,g^\dagger\right] \\
&= g\,A'_\mu(\mathbf{x},\tau)\,g^\dagger
\end{aligned} \tag{2.19}$$

Hence we conclude that the periodic boundary conditions are satisfied by the transformed vector potential only if $g\,A'_\mu(\mathbf{x},\tau) = A'_\mu(\mathbf{x},\tau)\,g$. Since only the center of the group $SU(N_c)$ commutes with all the $SU(N_c)$ gauge transformations, g needs to be a center element i. e. $g \in Z(N_c)$. Such an element commuting with all the elements of group, will be proportional to the identity matrix and can be written as

$$g = zI \quad \text{with} \quad \mathrm{z} = \exp\left(\frac{2\pi \mathrm{im}}{\mathrm{N_c}}\right) \in \mathrm{Z(N_c)}; \qquad \mathrm{m} \in 0, 1, \cdots \;\; \mathrm{N_c} - 1 \tag{2.20}$$

where I is the identity matrix of dimension N_c. Thus we have identified another symmetry known as center symmetry under which the pure gauge theory gluonic action for the QCD remains invariant [116, 117].

2.3.1 Order parameter for C-D transition: Polyakov loop

For the pure gauge $SU(N_c)$ Yang-Mills theory, the center symmetry $Z(N_c)$ leads to an interesting nontrivial consequence for the Polyakov loop operator which is a Wilson-Wegner loop in the temporal direction. At zero temperature, the measure of quark confinement is given by the Wilson-Wegner loop

$$W = \mathrm{Tr}\,\mathcal{P}\exp\left[\mathrm{i}\,\mathrm{g_s}\oint \mathrm{dx}^\mu\,\mathrm{A}_\mu\right] \tag{2.21}$$

here $\mathcal{P}$ denotes the path ordering and A_μ is the vector potential that describes the gluon fields. The action of a Wilson-Wegner loop is proportional to its area for confining theories while for non confining theories it is proportional to its perimeter [118]. Polyakov loop operator is defined as

$$L(\mathbf{x}) = \mathcal{P}\exp\left[\mathrm{i}\,\mathrm{g_s}\int_0^\beta \mathrm{d}\tau\,\mathrm{A}_0(\mathbf{x},\tau)\right] \tag{2.22}$$

where $A_0(\mathbf{x},\tau)$ is the time component of the gauge field A_μ in the Euclidean space, τ is the Euclidean time [29]. After Wick rotating to imaginary time, R^4 is replaced by the space time cylinder $S^1 \times R^3$ with circumference β.

Here, we define normalized colour traces of Polyakov loop operator as

$$l(\mathbf{x}) = \frac{1}{N_c}\mathrm{Tr}_c\,L(\mathbf{x}), \qquad l^\dagger(\mathbf{x}) = \frac{1}{N_c}\mathrm{Tr}_c\,L^\dagger(\mathbf{x}) \tag{2.23}$$

The Polyakov loop operator connects a colour source at Euclidean time $\tau = 0$ with a colour sink at $\tau = \beta$. Since we have periodicity in Euclidean time, source and sink are at the equivalent positions. If we calculate the grand canonical thermal average ($\langle l(\mathbf{x})\rangle_\beta$) of the Polyakov loop, the path integral is equivalent to the thermodynamic trace over all states in which there is one static quark at fixed position ($\mathbf{x}$) in the space

$$\langle l(\mathbf{x})\rangle_\beta = \frac{1}{Z_g(\beta)}\oint DA_\mu\,l(\mathbf{x})\,\mathrm{e}^{-\mathrm{S_g[A]}} \tag{2.24}$$

The denominator of this expression is equivalent to the canonical partition function of a thermodynamic system with exactly one quark at position ($\mathbf{x}$) averaged over all colours.

$$Z_{q(\mathbf{x})}(\beta) = \oint DA_\mu\,l(\mathbf{x})\,\mathrm{e}^{-\mathrm{S_g[A]}} \tag{2.25}$$

Thus

$$\langle l(\mathbf{x})\rangle_\beta = \frac{Z_{q(\mathbf{x})}(\beta)}{Z_g(\beta)} = e^{-\beta\, F_q} \tag{2.26}$$

$$\Phi = \langle l(\mathbf{x})\rangle_\beta = e^{-\beta\, F_q} \quad \text{and} \quad \bar{\Phi} = \langle l^\dagger(\mathbf{x})\rangle_\beta = e^{-\beta\, F_{\bar{q}}} \tag{2.27}$$

where F_q ($F_{\bar{q}}$) is an excess of free energy for an infinitely heavy static quark (anti-quark) in a hot gluonic medium. Similarly the excess free energy $F_{q\bar{q}}(|\mathbf{x}-\mathbf{y}|)$ for an anti-quark at $\mathbf{x}$ and a quark at $\mathbf{y}$ is given by

$$\langle l^\dagger(\mathbf{x})\, l(\mathbf{y})\rangle_\beta = e^{-\beta\, F_{q\bar{q}}(|\mathbf{x}-\mathbf{y}|)} \tag{2.28}$$

We notice that $\Phi = \bar{\Phi} = 0$ implies an infinite free energy for a single static quark source [32, 117, 119, 120]. It means all open colour sources are infinitely suppressed, i. e. colour is confined. The potential between a quark and an anti-quark increases linearly at long distances, $F_{q\bar{q}}(r \to \infty) \to \sigma r$ with $r = (|\mathbf{x}-\mathbf{y}|)$ which leads to $\Phi \to 0$ and $\langle l^\dagger(r \to \infty)\, l(0)\rangle \to 0$. σ is the string tension that binds a quark with an anti-quark. On the other hand, in the deconfined phase, the free energy of a single quark (anti-quark) becomes finite ($F_q(F_{\bar{q}}) < \infty$) giving rise nonzero values to Φ and $\bar{\Phi}$ [23, 121–123]. In the string picture, the process of deconfinement is viewed as the melting of the string. Thus we conclude from above discussion that Φ and $\bar{\Phi}$ are useful order parameters for distinguishing a confining from a deconfining phase in gauge theories without fermions.

The action of pure gauge theory is symmetric under the twisted gauge transformations but the thermal expectation value of normalized Polyakov loop operator transforms as

$$\Phi \to \Phi^{'} = z\Phi \tag{2.29}$$

Thus the low energy confining vacuum state for which $\Phi = 0$, is symmetric under the center $Z(N_c)$ transformations while the center symmetry is spontaneously broken for nonzero value of Φ. We conclude that the order parameter Φ is associated with the spontaneous break down of $Z(N_c)$ center symmetry for the pure gauge theory.

The situation changes in the presence of dynamical quarks. If we consider a Yang-Mills theory with dynamical quark fields in the fundamental representation of $SU(N_c)$, the fermionic quark fields have to obey antiperiodic boundary conditions in the Euclidean time direction

$$\Psi(\mathbf{x}, \tau + \beta) = -\Psi(\mathbf{x}, \tau) \tag{2.30}$$

When we apply a gauge transformation $U(\mathbf{x}, \tau)$, the fermions transform as $\Psi(\mathbf{x}, \tau) \rightarrow \Psi^{'}(\mathbf{x}, \tau) = U(\mathbf{x}, \tau)\, \Psi(\mathbf{x}, \tau)$;

$$\begin{aligned} \Psi(\mathbf{x}, \tau + \beta) \rightarrow \Psi^{'}(\mathbf{x}, \tau + \beta) &= U(\mathbf{x}, \tau + \beta)\Psi(\mathbf{x}, \tau + \beta) \\ &= -z\, I\, U(\mathbf{x}, \tau)\, \Psi(\mathbf{x}, \tau) \\ &= -z\, U(\mathbf{x}, \tau)\, \Psi(\mathbf{x}, \tau) \end{aligned} \tag{2.31}$$

We are forced by this equation to restrict the twisted gauge transformation to $z = 1$, if we want to fulfill the boundary condition (2.30). Thus the center symmetry is no longer respected in the presence of quarks and we say that the center symmetry has been explicitly broken.

Even if the center symmetry is explicitly broken in the high temperature phase, the temperature variation of Polyakov loop expectation value shows fast and rapid change near crossover transition and the Polyakov loop susceptibility shows a peak in lattice simulations [39]. Hence we consider the Polyakov loop as an approximate order parameter which is an indicator of the confinement-deconfinement transition.

2.4 The Chiral Symmetry

In the limit of zero quark mass for different flavours of quark, QCD Lagrangian shows a very interesting property known as the chiral symmetry. In the real world, quarks come in six flavours, three of them known as up (u), down (d) and strange (s) are light while the other three charm (c), bottom (b) and top (t) are heavy. Here quark flavours are labeled as light and heavy in reference to typical hadronic mass scale of about 1 GeV. Each quark flavour behaves in the same way under the influence of strong interaction. They differ only in their masses and mass dependent properties. Quark masses are basically running parameters in the QCD and the theory can be formulated for any quark mass. If one considers light quarks as massless in QCD, this approximation is quite close to the physical situation for two flavours of u ($m_u = 4 - 6$ MeV) and d ($m_d = 8 - 10$ MeV) quarks. The mass of strange quark ($m_s = 140 - 200$ MeV) is also sufficiently small when it is compared to 1 GeV scale of hadronic masses. Thus chiral symmetry can be considered as an approximate symmetry even for three flavours of quarks in QCD. In the massless world which is known as the chiral limit, QCD Lagrangian can be written in terms of completely decoupled left handed and right handed quark fields

$$\mathcal{L}^0_{QCD} = \overline{\Psi}_L i\gamma^\mu D_\mu \Psi_L + \overline{\Psi}_R i\gamma^\mu D_\mu \Psi_R - \frac{1}{4} F_{\mu\nu} F^{\mu\nu} \tag{2.32}$$

where

$$\Psi_L = P_L \Psi \qquad \Psi_R = P_R \Psi \qquad \bar{\Psi}_L = \bar{\Psi} P_R \qquad \bar{\Psi}_R = \bar{\Psi} P_L \tag{2.33}$$

where P_L and P_R are left handed and right handed projection operators respectively and are defined as

$$P_L = \frac{1}{2}(1 - \gamma_5) = P_L^\dagger \qquad P_R = \frac{1}{2}(1 + \gamma_5) = P_R^\dagger \tag{2.34}$$

The projection operators have the following properties

$$\begin{aligned} &P_L + P_R = 1 \qquad &P_L^2 = P_L \qquad &P_R^2 = P_R \\ &P_L P_R = P_R P_L = 0 \qquad &\gamma_\mu P_L = P_R \gamma_\mu \qquad &\gamma_\mu P_R = P_L \gamma_\mu \end{aligned} \tag{2.35}$$

Here Ψ_L and Ψ_R are 3 component column matrices representing the 3 left handed and 3 right handed light quarks respectively. We can easily see that the Lagrangian given in Eq.(2.32) is invariant under the unitary transformation $U_L(3)$ and $U_R(3)$ acting on Ψ_L and Ψ_R respectively.

$$\begin{aligned} \Psi_L \rightarrow \Psi_L^{'} = U_L \Psi_L \,; \qquad U_L = e^{-i(\sum_{a=1}^{8} \alpha_L^a T^a + \alpha_L \mathrm{I})} \\ \Psi_R \rightarrow \Psi_R^{'} = U_R \Psi_R \,; \qquad U_R = e^{-i(\sum_{a=1}^{8} \alpha_R^a T^a + \alpha_R \mathrm{I})} \end{aligned} \tag{2.36}$$

where α_L^a and α_R^a are parameters for the left and right handed transformations. The $T^a = \lambda^a/2$, λ^a are $(a = 1, 2, \dots\ 8)$ Gell Mann matrices in flavour space. α_L and α_R represent a global phase change for all the flavours of left handed and right handed fields. Noether's theorem says that there are total $2 \times (8 + 1) = 18$ conserved currents and conserved charges. The left handed and right handed currents for $SU_L(N_f) \times SU_R(N_f)$ transformations can be written as

$$j_{R,\,L}^{\mu,a}(x) = \overline{\Psi}_{R,\,L}(x)\,\gamma^{\mu}\,\frac{\lambda^a}{2}\Psi_{R,\,L}(x) \tag{2.37}$$

We know that $U(N_f)$ can be written as the product of $SU(N_f)$ and a complex phase $U(1)$. The complete symmetry group of Lagrangian can be decomposed into an equivalent set of vector $(V = R + L)$ and axial vector $(A = R - L)$ transformations

$$U_L(3) \times U_R(3) \;\; \cong \;\; SU_V(3) \times SU_A(3) \times U_V(1) \times U_A(1) \tag{2.38}$$

and the corresponding vector and axial vector currents are

$$\begin{aligned} V^{\mu,a} = j_R^{\mu,a}(x) + j_L^{\mu,a}(x) = \overline{\Psi}\gamma^{\mu}\frac{\lambda^a}{2}\Psi; \quad A^{\mu,a} = j_R^{\mu,a}(x) - j_L^{\mu,a}(x) = \overline{\Psi}\gamma^{\mu}\gamma^5\frac{\lambda^a}{2}\Psi \\ V^{\mu} = j_R^{\mu}(x) + j_L^{\mu}(x) = \overline{\Psi}\gamma^{\mu}\mathrm{I}\Psi; \qquad \mathrm{A}^{\mu} = \mathrm{j}_{\mathrm{R}}^{\mu}(\mathrm{x}) - \mathrm{j}_{\mathrm{L}}^{\mu}(\mathrm{x}) = \overline{\Psi}\gamma^{\mu}\gamma^5\mathrm{I}\Psi \end{aligned} \tag{2.39}$$

The flavour singlet vector current V^{μ} resulting due to $U_V(1)$ symmetry, gives the conservation of net baryonic charge. The flavour singlet axial vector current A^{μ} does not remain conserved, due to the anomalous breaking of $U_A(1)$ symmetry by quantum effects.

$$\partial_{\mu} A^{\mu} = \frac{N_c\, g_s^2}{32\,\pi^2}\,\epsilon_{\mu\nu\rho\sigma}\,F_a^{\mu\nu}F_a^{\rho\sigma}, \qquad\qquad \epsilon_{0123} = 1 \tag{2.40}$$

It has been shown that the $U_A(1)$ symmetry is broken to $Z_A(3)$ symmetry by instanton effects [124, 125]. However, instantons get screened at sufficiently high temperature and hence $U_A(1)$ symmetry can be restored in this regime. The mass splitting of η and $\eta^{'}$ mesons together with the singlet octet mixing angles, are connected to the $U_A(1)$ anomaly. In chapter four (4), we will be exploring the pattern of $U_A(1)$ restoration and its interplay with the chiral symmetry ($SU_A(3)$) restoration trend at high temperatures.

The mass term $\mathcal{L}^M_{QCD} = -\overline{\Psi}M\Psi$ with the mass matrix $\mathbf{M} = \mathrm{diag}\,(\mathrm{m_u},\, \mathrm{m_d},\, \mathrm{m_s})$, mixes left and right handed quarks in the QCD Lagrangian as given below

$$\overline{\Psi}^i M_{ij}\Psi^j = \overline{\Psi}^i_R M_{ij}\Psi^j_L + \overline{\Psi}^i_L M_{ij}\Psi^j_R \tag{2.41}$$

where $i, j = 1, 2\cdots N_f$. If one takes, $m_u = m_d = m_s = m$, the vector current representing flavour symmetry $SU_V(3)$ remains conserved while a nonzero value of m leads to the explicit breaking of $SU_A(3)$ chiral symmetry and axial current diverges. Divergences of axial vector and vector currents are given below

$$\begin{aligned}
\partial_\mu A^{\mu,\,a} &= i\,\overline{\Psi}\,\{T^a, M\}\,\gamma_5\,\Psi \\
\partial_\mu V^{\mu,\,a} &= -\,i\,\overline{\Psi}\,[M, T^a]\,\Psi \\
\partial_\mu V^{\mu,\,a} &= 0 \qquad \text{if} \quad \mathrm{m_u} = \mathrm{m_d} = \mathrm{m_s} = \mathrm{m}
\end{aligned} \tag{2.42}$$

In the observed mass spectrum of hadrons, pions are the lightest particle with masses of $m_\pi = 140$ MeV which are much lighter than the other hadrons $m_H \geq 1$ GeV. This mass gap and the fact that hadrons do not appear in the parity doublet, strongly suggest that the chiral symmetry is broken spontaneously at low energies [9,126–128]. The spontaneous breaking of chiral symmetry means that the low energy hadronic vacuum of QCD does not possess the chiral symmetry while the QCD Lagrangian does. Vector symmetry is intact in the low energy vacuum while the axial vector symmetry is not, it means vector charges annihilate the QCD vacuum while the axial vector charges do not.

$$Q^a_V\,|0\,\rangle = 0, \qquad Q^a_A\,|0\,\rangle \neq 0 \tag{2.43}$$

Further, since $Q_A^a\,|0\,\rangle \neq 0$, states $|\phi^a\rangle$ must exist such that,

$$|\phi^a\rangle = Q_A^a\,|0\,\rangle \tag{2.44}$$

These states are energetically degenerate with the vacuum since $[H, Q_A^a] = 0$.

Because Q_A^a's are axial charge, the states $|\phi^a\rangle$ represent eight pseudoscalar mesons which are massless. We remind that index 'a' counts the number of broken symmetry generators. These massless excitations are the so called Goldstone bosons ($(N_f^2 - 1)$ in number) which result due to the spontaneous breaking of chiral symmetry $SU_L(N_f) \times SU_R(N_f) \rightarrow SU_V(N_f)$. For $N_f = 2$ three pions are Goldstone bosons. Since chiral symmetry is explicitly broken by a small amount due to the presence of very small u and d current quark masses in the QCD Lagrangian, the pions observed in nature are not completely massless. Hence they are termed as pseudo-Goldstone bosons. For $N_f = 3$ flavours, the pseudo-Goldstone bosons are represented by the pseudoscalar meson octet, comprising pions, kaons and the eta meson. Since chiral symmetry is more strongly broken by the larger strange quark mass, the pseudoscalar mesons carrying strangeness are heavier than the pions [9, 55].

In spin models with ferromagnetic interactions having zero external magnetic field in the background, the rotational symmetry of the system is spontaneously broken due to the appearance of nonzero magnetization $M \neq 0$ in the low temperature phase of ferromagnetism. Analogously, in the low temperature QCD vacuum, the spontaneous breaking of chiral symmetry results due to the appearance of nonzero vacuum expectation value $\langle \overline{\Psi}^i \Psi^j \rangle_{\text{vac.}} \neq 0$ for the chiral condensate. We introduce another effective representation for the so called chiral condensate and its complex conjugate, via

$$\Phi^{ij} \sim \langle \overline{\Psi}^i_L \Psi^j_R \rangle \quad , \qquad \Phi^{ij\dagger} \sim \langle \overline{\Psi}^i_R \Psi^j_L \rangle \tag{2.45}$$

A nonvanishing expectation value $\langle \overline{\Psi}^i \Psi^j \rangle \neq 0$ is then equivalent to $\Phi^{ij} + \Phi^{ij\dagger} \neq 0$. Φ^{ij} is $N_f \times N_f$ matrix in flavour space and under flavour chiral rotation $U_L(N_f) \times U_R(N_f)$, it transforms as $\Phi \rightarrow \Phi' = U_L \Phi U_R^\dagger$. The components of the matrix field Φ represent, the effective mesonic degrees of freedom in the pseudo scalar and scalar sectors. Nonzero value of the chiral condensate breaks the chiral symmetry similar to the effect of mass term in the QCD Lagrangian. Since nothing distinguishes one quark flavour from another in the chiral limit ($\mathbf{M}_{ij} = 0$), the vacuum expectation value $\Phi^{ij}_{\text{vac.}} = \phi_0 \delta^{ij}$ (other possible spontaneous chiral symmetry breaking scenarios are discussed in detail in ref [55, 129]. This chiral condensate breaks the chiral $U_L(N_f) \times U_R(N_f)$ symmetry spontaneously to $U_V(N_f)$.

The rotational symmetry in spin models, gets restored above some critical temperature and the magnetization vanishes in the high temperature paramagnetic phase of the system. For this ferromagnetic to paramagnetic phase transition, magnetization serves as the order parameter. Similarly in the high temperature phase of QCD, one expects that Φ^{ij} will become zero above some critical temperature. The symmetry of the ground state will then be restored to the original chiral symmetry, i. e., $SU_L(N_f) \times SU_R(N_f)$, if the $U_A(1)$ anomaly is still present, or $SU_L(N_f) \times SU_R(N_f) \times U_A(1)$, if instantons are sufficiently screened at the transition temperature such that the $U_A(1)$ symmetry is effectively restored. These expectations are indeed fulfilled in the lattice gauge theory QCD calculations [39]: there is a phase transition between the chiral symmetry broken low temperature phase to the high temperature phase where it is restored. We thus conclude that the chiral condensate Φ^{ij} is the order parameter for the so called chiral phase transition.

2.4.1 Landau-Ginzburg analysis of chiral transition: σ model

Using universality arguments of the Landau-Ginzburg analysis, one can analyze the order of chiral phase transition in the framework of linear sigma model for the order parameter field Φ^{ij}, when the quarks are considered to have no mass. The linear sigma model is an effective theory where all the terms allowed by the original chiral symmetry must appear in the effective Lagrangian [9].

$$\mathcal{L}_{\text{eff}} = \text{Tr}\,\left(\partial_0\Phi^\dagger\,\partial^0\Phi\right) - v^2\text{Tr}\,\left(\nabla\Phi^\dagger\,.\,\nabla\Phi\right) - V_{\text{eff}}(\Phi) \tag{2.46}$$

Here the ground state of the theory is determined by the effective potential written in terms of the matrix field Φ which represents effective mesonic degrees of freedom:

$$V_{\text{eff}}(\Phi) = m^2\,\text{Tr}\,\left(\Phi^\dagger\,\Phi\right) + \lambda_1\left[\text{Tr}\,\left(\Phi^\dagger\,\Phi\right)\right]^2 + \lambda_2\text{Tr}\,\left(\Phi^\dagger\,\Phi\right)^2 - c\,\left(\text{det}\Phi^\dagger + \text{det}\Phi\right) \tag{2.47}$$

The first term of Eq.(2.46) is canonically normalized. The coefficient v^2 in Eq.(2.46) may in general be different from one because Lorentz symmetry is broken explicitly at nonzero temperature in a medium. The chiral symmetry for Eq.(2.46) is $SU_L(N_f) \times SU_R(N_f)$ for $c \neq 0$ and it is $SU_L(N_f) \times SU_R(N_f) \times U_A(1)$ for $c = 0$. Thus the $U_A(1)$ anomaly is present for $c \neq 0$ and absent for $c = 0$. While these chiral symmetries are manifest in Lagrangian (2.46), the ground state of theory respects them only for $c = 0$ and $m^2 > 0$. For $c = 0$ and $m^2 < 0$ the chiral symmetry gets spontaneously broken as the order parameter assumes a nonzero vacuum expectation value. Thus we notice that the chiral transition can be studied in the framework of the linear sigma model only by ensuring $m^2 < 0$ for $c = 0$. Further there are two ways of symmetry breaking, if $\lambda_2 > 0$ the ground state is given by $\Phi^{ij}_{\text{vac.}} = \phi_0\delta^{ij}$ while for $\lambda_2 < 0$ the ground state is given by $\Phi^{ij}_{\text{vac.}} = \phi_0\delta^{i1}\,\delta^{j1}$ (the choice of 1-direction in left and right handed flavour space is arbitrary) [129]. Nature chooses the first method of symmetry breaking. No general arguments can be constructed for the $c \neq 0$ case; whether the ground state of the theory breaks chiral symmetry spontaneously depends on the particular values for the coupling constants c, λ_1, λ_2 and the number of flavours N_f.

For $N_f = 2$, and in the presence of the $U_A(1)$ anomaly, the $SU_L(N_f) \times SU_R(N_f)$ chiral symmetry, is isomorphic to $O(4)$. The effective theory for the order parameter is in universality class of the $O(4)$ Heisenberg magnet. Consequently, the transition is of second order [26]. If the $U_A(1)$ symmetry is effectively restored at the phase transition temperature, the symmetry group is larger, $SU_L(N_f) \times SU_R(N_f) \times U_A(1)$, which is isomorphic to $O(4) \times O(2)$, and the transition is of first order. Lattice QCD calculations determine the transition temperature to be $T_c \simeq 172$ MeV [39, 130]. For $N_f = 3$, the chiral transition is of first order in both the cases when the $U_A(1)$ symmetry is explicitly broken by the instantons or when it is effectively restored at the transition. In the first case, the effective theory features a cubic invariant in the order parameter field (the term $\sim \det\Phi + \det\Phi^\dagger$), which drives the chiral transition first order [26]. In the second case, the transition is of fluctuation-induced first order [26, 131]. Whether the $U_A(1)$ symmetry is explicitly broken or not, the chiral transition is of fluctuation-induced first order for all flavours $N_f \geq 4$. Lattice QCD calculations for three flavours, find the transition temperature to be $T_c \sim 155$ MeV [130]. It is to be noted that nonvanishing quark masses can also be accounted for by adding a term

$$\mathcal{L}_H \equiv \mathrm{Tr}\left[H(\Phi + \Phi^\dagger)\right] \tag{2.48}$$

to the right side of Eq.(2.46). H_{ij}'s are the explicit symmetry breaking parameters and these are proportional to quark masses.

In chapter three and chapter four of the present thesis, we have studied the thermodynamics and phase structure of quark hadron phase transition in the framework of two flavour and three flavour linear sigma model. We have constructed effective models by combining the features of spontaneous break down of both the chiral symmetry as well as the center $Z(3)$ symmetry of QCD. In these models (termed as Polyakov quark meson model (PQM)), the Polyakov loop which represents the dynamics of confinement and the chiral condensate, are simultaneously coupled to the quark degrees of freedom.

2.5 QCD phase structure and its phase diagram

The properties of strong interaction can be investigated in the approximation of zero and infinite quark mass where the finite temperature QCD has two different global symmetries namely chiral symmetry and the Z(3) symmetry. In the zero quark mass limit, chiral condensate $\langle \overline{q}q \rangle$ works as the order parameter for the chiral symmetry breaking/restoration transition and in the infinite quark mass limit, the thermal expectation value of the Polyakov loop $\langle l(x) \rangle_\beta$ serves as the order parameter for the confinement-deconfinement phase transition. Quark hadron phase transition is investigated in terms of these two transitions either separately or in a unified framework where these transitions are entangled [50]. In the real life situation, the investigation of QCD phase structure becomes a complex and challenging task because the non perturbative techniques which rely on the global symmetries of the interaction, face handicap due to explicit breaking of these symmetries because of the finite and nonzero quark masses. There is no known order parameter for the finite quark masses [117]. We consider the chiral condensate and Polyakov loop as approximate order parameters which indicate rapid changes in the thermodynamic quantities signifying a rapid crossover for finite and dynamical quark masses. Although the chiral symmetry phase transition and the deconfinement phase transition are different phenomenon and occur in the different quark mass limits, they may have the common phase boundary in the phase diagram. The lattice results confirm that the chiral symmetry restoration transition and deconfinement transition indeed has a common transition temperature, at zero chemical potential [132, 133]. For finite chemical potential, recently it was proposed that the chiral transition do not coincide with the confinement-deconfinement transition and there emerges another phase consisting of massless, but confined quarks. Thus chiral symmetry is restored while the system is still confined. Such form of quark matter has been speculated to constitute the quarkyonic phase [134, 135] and no experimental hints, for its existence have yet been found.

In this section we will be discussing the QCD phase structure and its phase diagram in the plane of temperature and chemical potential. At present relatively firm statements regarding phase structure, can be made only for limited cases - 1) at finite T with small baryon density $\mu_B << T$, 2) at asymptotically high densities $\mu_B >> \lambda_{QCD}$.

2.5.1 Inputs from lattice QCD

The quark hadron phase transition at finite temperature and zero chemical potential has been studied extensively in the first principle QCD lattice gauge theory numerical simulations. Results are dependent on the number of colours and flavours as expected from the effective theory analysis in the framework of the renormalization group together with the universality [26, 136]. For $N_c = 3$ and $N_f = 0$ a first order deconfinement transition has been established (with critical temperature $T_c \simeq 270$ MeV) from the finite size scaling analysis on the lattice [31]. Since the Z(3) symmetry is explicitly broken by the presence of dynamical quarks, the deconfinement transition for realistic case with $N_c = 3$, $N_f = 3$ of QCD has been constructed to be a rapid crossover [9,39]. Chiral phase transition can be more appropriately addressed when we have $N_f > 0$ light flavours. The recent lattice gauge theory calculations using staggered fermions and Wilson fermions for chiral quarks, indicate a crossover from the hadronic phase to the QGP phase for realistic u, d, s quark masses.

In lattice QCD simulations, the method of importance sampling is used to carry out the functional integration (for evaluating partition function) on a discretized space-time lattice with lattice spacing a and lattice volume V (large number of points for spatial dimensions (N) than for temporal direction (N_τ), decide the lattice size which is $N^3 \times N_\tau$). Physical results are obtained by the extrapolation to the thermodynamic limit ($V \to \infty$) and continuum limit ($a \to 0$). Importance sampling generates statistical errors while extrapolations generate systematic errors. Further, the reconciliation of chiral symmetry with the lattice discretization, generates different prescriptions; namely 1) Wilson fermions, 2) staggered fermions, 3) domain-wall fermions and 4) overlap fermions, for defining the light quarks on lattice [137]. Depending on different types of fermions and different lattice spacings taken for lattice simulations, the pseudo critical temperature T_{pc} values for the chiral cross over transition are estimated to fall in the range of $150 - 200$ MeV [137, 138]. It has been recently clarified that improvement of the staggered action with less taste-symmetry breaking favors smaller value of $T_{pc} \leq 170$ MeV [139, 140].

2.5.2 Effective model inputs

If the nuclear matter is compressed to high densities such that hadrons overlap with each other and start to percolate, deconfinement should set in at large chemical potentials. The MIT bag model predicts this to happen at about 0.4 GeV in the quark chemical potential. We know from the existence of nuclear matter with baryons that at zero temperature, deconfinement would start when chemical potential becomes larger than one third of the nucleon mass. First principle lattice QCD calculations, fail at finite chemical potentials because of the fermion sign problem. Investigations using effective models become the pragmatic alternative for studying the phase structure at low temperature and high chemical potentials. Most of the chiral models suggest that there is a QCD critical end point located at $\mu = \mu_E, T = T_E$ and the chiral transition becomes first order (crossover) for $\mu > \mu_E$ ($\mu < \mu_E$) for realistic u, d and s quark masses [131, 141–143]. The criticality at CEP leads to enhanced fluctuations so the search of QCD critical point has emerged as an experimental issue of great importance [144, 145].

2.5.3 Schematic phase diagram

The schematic QCD phase diagram has been shown in figure 2.1. The QCD phase transition is of strong first order on the μ axis at $T = 0$, its strength decreases with decreasing μ and one approaches the critical end point (solid dot) at smaller chemical potential and higher temperature where the transition turns second order and then the transition gets converted to a crossover at lower μ values. Two phases exist across the phase boundary. At low temperatures and chemical potentials, the matter is in hadronic phase where the quarks remain confined inside the hadrons and at higher temperatures and chemical potentials, we have the quark gluon plasma phase. At $\mu = 0$ on the temperature axis,

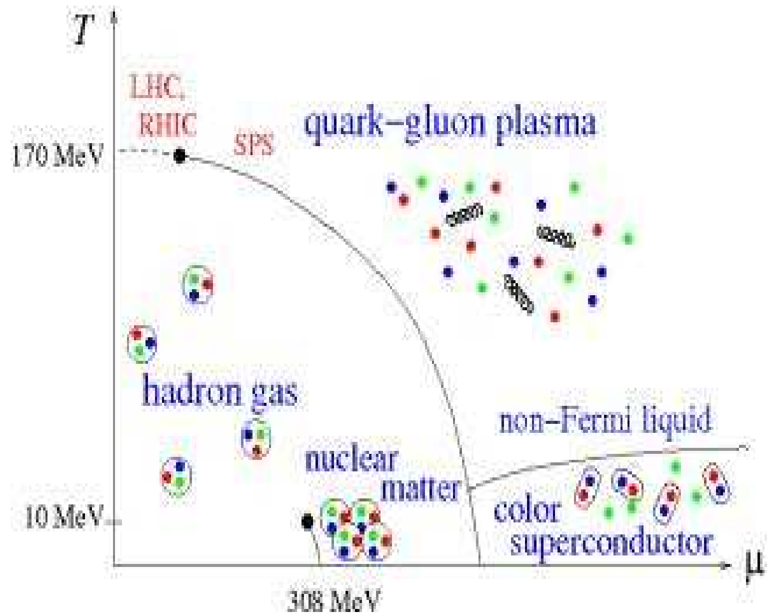

Figure 2.1: Schematic QCD phase diagram in the chemical potential and temperature plane.

we have a crossover as confirmed from the lattice QCD results. The quark hadron phase transition on the temperature axis, is similar to the transition that might have happened in the early universe. The physical situation for the quark hadron transition occurring on the chemical potential axis at $T = 0$, is found in the core of neutron stars. At very high chemical potentials, one observes the interesting phenomenon of colour superconductivity giving rise to 2SC and colour flavour locked (CFL) phases. Still at lower chemical potential $\mu \sim 308$ MeV, one observes the first order nuclear matter liquid gas phase transition where the gaseous nuclear matter makes transition to the hadronic fluid. The solid dot in the lower part of the diagram extending from $\mu = 308$ MeV represents the critical point for this liquid gas phase transition.

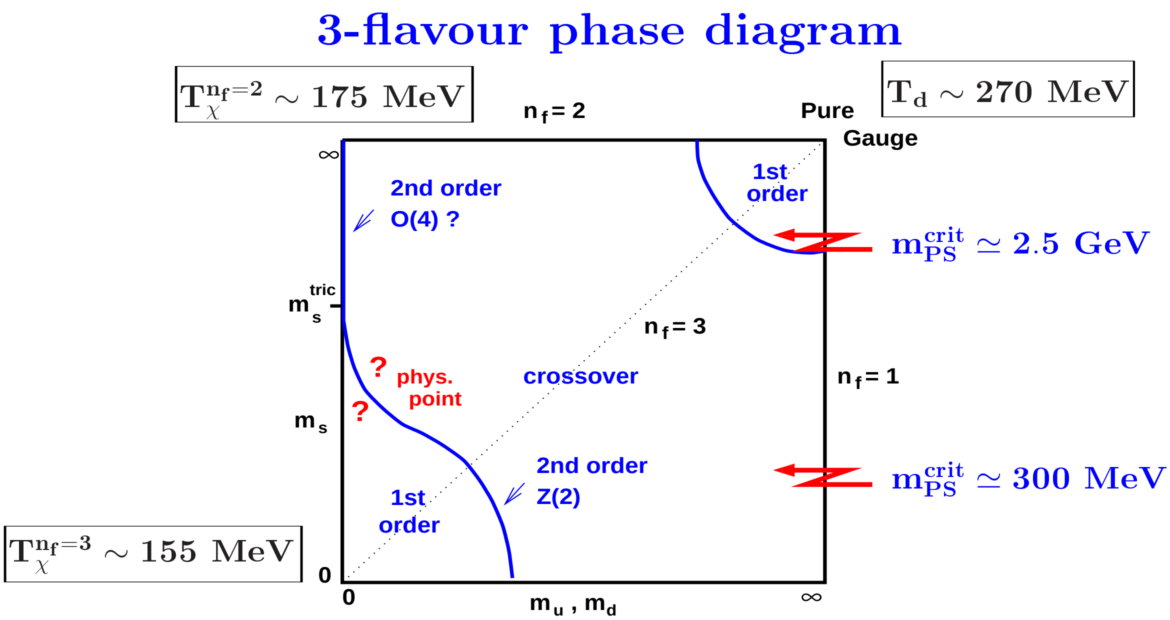

Figure 2.2: Columbia plot: phase diagram in the plane of quark masses at $\mu = 0$ and finite T, ref. [39].

2.5.4 Columbia plot and the CEP

Drawing a phase diagram by treating quark masses as external parameters at $\mu = 0$, one gets further insight on the phase structure. Fig.2.2 shows such a plot known as columbia plot where isospin degeneracy has been assumed ($m_u = m_d = m_{ud}$). The left bottom region and the right top region at finite T, represent the first order chiral transition and the first order deconfinement transition respectively. The first order and crossover regions are separated by the chiral and deconfinement critical lines. These lines belong to a universality class of the 3D, Z(2) Ising model except for special points at $m_{ud} = 0$ or $m_s = 0$ [146].

Since the chiral transition is of second order for the massless two flavour case, the Z(2) chiral critical line meets the $m_{ud} = 0$ axis at $m_s = m_s^{tri}$ (tricritical point) and changes its universality to $O(4)$ for $m_s > m_s^{tri}$ [148]. Note that the considerations of the limits ($m \to 0, \infty$) depend on the presence of $U_A(1)$ anomaly. If we introduce an extra axis

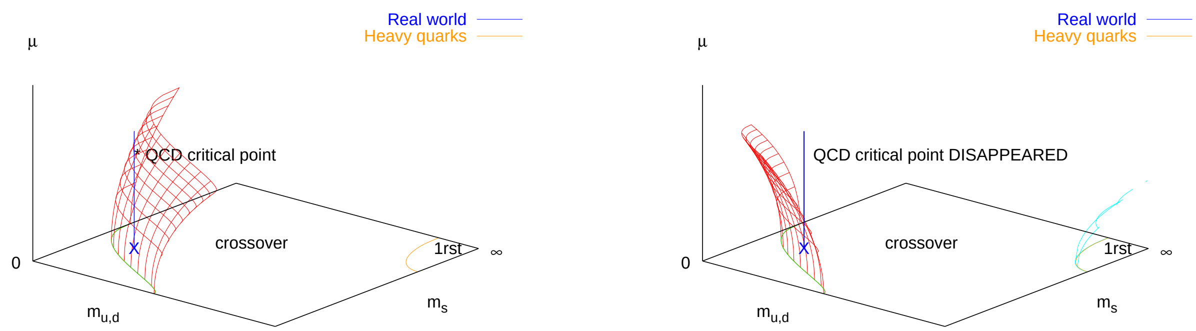

(a) Standard scenario (b) Non standard scenario

Figure 2.3: The plot of chiral critical surface in the three dimensions of light quark mass (m_u, m_d), strange quark mass (m_s) and chemical potential. Figure taken from ref. [147].

of quark chemical potential μ, to the columbia plot, the critical line extends to form a surface as shown in Fig.2.3(a) and the first order region in the lower left corner of the columbia plot, gets elongated with increasing μ. This is the so called *standard scenario* where the surface bends towards the physical points. If the physical point at $\mu = 0$ is in the crossover region, the bent surface is crossed at the critical chemical potential μ_E and there transition changes to first order from a crossover. Thus we find a critical end point (μ_E, T_E) on the QCD phase diagram in the (μ, T) plane. Fig.2.3(b) depicts the so called *exotic scenario* in which the first order region shrinks with increasing μ and the surface bends towards the lower masses and no critical chemical potential is found at the physical point. The transition always remains a crossover and no critical end point is found in the QCD phase diagram in this scenario. Hints for this scenario can be found in the lattice simulations [149, 150] and model studies [90].

The exact location of CEP, where the first order line ends and the transition becomes second order phase transition, is not clear [27]. The different approaches of studying the phase diagram, predict different locations of CEP. It is also found that the location of CEP predicted in different models, strongly depends upon the parameters used in the

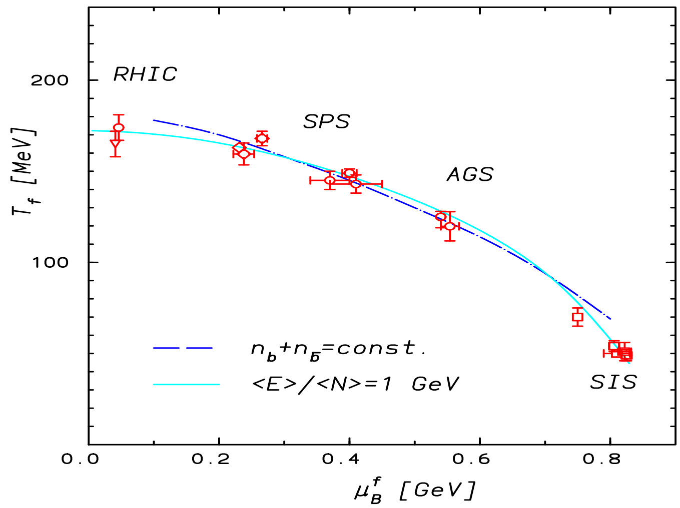

Figure 2.4: Comparison of two chemical freeze out conditions: net baryon density $n_B = 0.12 fm^3$ (dashed) and constant energy per particle equivalent to 1 GeV (solid). This figure is reproduction of Fig.(27) in ref. [151].

calculations. The possible signatures of CEP has been suggested by Stephanov et al. in the refs. [144, 145].

2.6 Experimental indications for QCD transition

The experiments looking for the signatures of the quark hadron phase transition have been performed at Alternating Gradient Synchrotron (AGS at BNL), Super Proton Synchrotron (SPS at CERN), Relativistic Heavy Ion Collider (RHIC at BNL). In the future plan, RHIC is going to perform experiments at lower energies, in order to locate the CEP [152]. Very high energetic heavy ion collisions are planned at Large Hadron Collider (LHC at CERN). Dedicated to the exploration of regions of high baryonic densities (chemical potentials) in the phase diagram, new experimental programs have been proposed for the compressed baryonic matter (CBM) experiments at the FAIR facility next to GSI in Darmstadt. However, it is very difficult to construct observables which signal the occurrence of critical behaviour uniquely and unambiguously. So far statistical models have been used to obtain a lower bound for the chiral and deconfinement transition lines [151]. A graph taken from ref. [151] in Fig.2.4. is being shown here for orientation to indicate the lower bound of the actual phase transition. The distance of the transition from these freeze out curves is a debatable issue. More information on this issue can be gathered from detailed model studies.

The angular distribution of low energy particles observed in the heavy ion collision experiments, indicates hydrodynamic flow and hence the phenomenon of thermalization which happens at much lower energies than the initial center of mass energy in the fireball. The good agreement of the measured particle ratios in the final state with thermal equilibrium statistics, also makes thermalization an accepted assumption. The so called freeze out temperature at which the particles do no longer interact, can be estimated from the particle ratios as shown in Fig.2.4. Further, abundances of particles depend, only on the number of valence quarks irrespective of mass and other quantities, hence they are showing quark number scaling [153, 154]. This means that the generation and thermalization of quarks must have happened under conditions where light and strange quarks can be treated approximately equal. This indicates that shortly after thermalization, the fireball was in a high temperature partonic phase which is a so called quark gluon plasma.

The observed high energy particles which do not equilibrate, are interpreted as remnants of partonic collisions happening at very early times. Carrying momenta in opposite directions, these so called particle jets are observed in spatially anti-correlated pairs. When the jets in heavy-ion collisions are compared with the jets in proton collisions, one concludes that one of these paired jets is attenuated in the heavy-ion case. This phenomenon is called jet suppression. The asymmetry of primary partonic collision, explains the difference in the jet energies of a pair of jets in a heavy-ion collision. In general each jet of the same pair, travels path of different lengths. The two jets suffer different attenuation depending on the differences in their way through the background of thermalizing low energy particles. Involved simulations of the fireball and its evolution are needed in order to understand the in-medium effects which lead to jet separation.

The observables whose understanding do not require detailed modeling of the fireball, are rare. In order to refine models and to benchmark lattice QCD calculations, experimental corner stones are urgently needed on the one hand while on the other hand without having sophisticated models for the fireball expansion, it becomes quite difficult to extract information from experimental data. Both ideal and viscous hydrodynamics have been used to describe the early stages of the fireball evolution [155, 156]. The assumptions needed for hydrodynamics become questionable for later stages of fireball evolution which can be studied by the application of ultrarelativistic quantum molecular dynamics (UrQMD) codes [157, 158]. Present research in this area is focused on reducing the diversity of models and identifying the most promising approaches.

High energy probes like jets or dileptons originating from a highly energetic photon and their spatial correlations are supposed to carry information about very early stages of collision. De-convoluting the process which generates these particles from the different interactions of these particles with the medium at different times, is quite difficult in the interpretation of data.

The measurements of fluctuations, are also supposed to give further information regarding heavy-ion collision. High degree of the thermalization of the fireball has been revealed by the particle abundances and ratios [159]. However, we get only a snap-shot of the sphere of last interaction which may show a dependence on the interactions involved. Since different mesons dissolve in the thermal medium at different conditions depending on the binding of the quark-antiquark pair, the concept of a sphere of last scattering is a difficult concept to begin with. In contrast, fluctuations can give some insight regarding the evolution of the final state which is observed in the detector. Fluctuations generated in the early stages may survive the interactions that they face in the medium, due to the fast evolution of the fireball. One can study fluctuations on an event-by-event basis. One can not expect fluctuations on an event-by-event basis of conserved charges, if used detectors cover the total solid angle. Since the collision products are highly relativistic, a large fraction of particles leaves the detector in forward direction without getting measured. The acceptance of detector, cuts out a window in the phase space. In principle, it is possible to extract the correlation length (the fluctuation size) from the ensemble of individual events, if the fluctuations are smaller than the acceptance window. Since the fluctuations are expected to be large near the critical point (second order phase transitions), these are of major interest in the investigation of quark-hadron phase transition. The first order phase transitions can also be detected, in principle, using event-by-event fluctuations because the fast expansion of the medium across the first order phase transition will lead to spinodial instabilities. Lots of information regarding interactions in the fluid, can be extracted from the typical size of these instabilities.

Chapter 3

PQM Model Phase Structure revisited in the presence of Vacuum Fermion Fluctuations.

In most of the QM/PQM model calculations, the fermion vacuum contributions to the free energy is frequently neglected [63, 64, 69, 70, 75–77, 160] because here, the spontaneous breaking of chiral symmetry is generated by the mesonic potential itself. While in the NJL/PNJL model investigations, fermion vacuum term leads to the dynamical breaking of the chiral symmetry, hence it gets explicitly included up to a momentum cutoff Λ. Very recently, it has been shown by Skokov et al. in ref. [103] that in a mean field approximation, where the fermion vacuum contribution to the free energy is neglected, the order of the phase transition for two flavour QM model in the massless chiral limit becomes first order at zero baryon chemical potential. They have further shown that the quark-meson model, with appropriately renormalized fermionic vacuum fluctuations in the thermodynamic potential, becomes an effective QCD-like model because now it can reproduce the second order chiral phase transition at $\mu = 0$ as expected from the universality arguments [26] for the two massless flavours of QCD. It has also been shown that in the presence of an external magnetic field, the structure of the phase diagram in the PQM model is considerably affected by the fermionic vacuum contribution [161]. The fermionic vacuum corrections (full two loop results) and its influence, has also been reported earlier in the context of finite temperature and density Yukawa theory [162–164]. In the present work, we will investigate the effect of fermionic vacuum fluctuations on the phase structure and thermodynamics of PQM/QM models in detail at non zero as well as zero chemical potential. In order to bring out the effect of fermionic vacuum term on the physical observables, we will compare the results of our calculation with the corresponding PQM model calculations without vacuum term.

The arrangement of this chapter is as follows. In Sec.3.1, we have given the formulation of PQM model for the two quark flavour. The Polyakov loop potential and the thermodynamic grand potential has been given in subsection 3.1.1. After giving a brief description of the appropriate renormalization of fermionic vacuum loop contribution, the subsection 3.1.2 describes how the new model parameters are obtained in vacuum when renormalized vacuum term is added to the effective potential. The section 3.2 investigates the effect of fermionic vacuum term on the phase structure and thermodynamics. The subsection 3.2.1 explores how, the temperature variation of order parameters and their derivatives at different chemical potentials, the structure of the phase diagram in the μ and T plane and the location of critical end point, gets affected in the presence of vacuum term. The effect on the temperature variation of thermodynamic observables namely pressure, entropy, energy density and interaction measure has been discussed in the subsection 3.2.2 while the discussion of specific heat, speed of sound and $\frac{p(T)}{\epsilon(T)}$ has been presented in subsection 3.2.3 and finally the subsection 3.2.4 describes the results for quark number density and quark number susceptibility. Summary has been presented in Sec. 3.3. The first and second partial derivatives of $\mathcal{U}_{\log}$ and $\Omega_{q\bar{q}}^{T}$ with respect to temperature and chemical potential has been evaluated in the appendix written in chapter 7.

3.1 Model Formulation

We will be working in the two flavor quark meson linear sigma model which has been combined with the Polyakov loop potential [96]. In this model, quarks coming in two flavor are coupled to the $SU_L(2) \times SU_R(2)$ symmetric four mesonic fields σ and $\vec{\pi}$ together with spatially constant temporal gauge field represented by Polyakov loop potential. Polyakov loop field $\Phi(\vec{x})$ is defined as the thermal expectation value of color trace of Wilson loop in temporal direction

$$\Phi = \frac{1}{N_c}\langle \mathrm{Tr}_c L\rangle_\beta, \qquad \Phi^* = \frac{1}{N_c}\langle \mathrm{Tr}_c L^\dagger\rangle_\beta \tag{3.1}$$

where L(x) is a matrix in the fundamental representation of the $SU_c(3)$ color gauge group.

$$L(\vec{x}) = \mathcal{P}\mathrm{exp}\left[i\int_0^\beta d\tau A_0(\vec{x},\tau)\right] \tag{3.2}$$

Here $\mathcal{P}$ is path ordering, A_0 is the temporal component of Euclidean vector field and $\beta = T^{-1}$ [29].

The model Lagrangian is written in terms of quarks, mesons, couplings and Polyakov loop potential $\mathcal{U}(\Phi, \Phi^*, T)$

$$\mathcal{L}_{PQM} = \mathcal{L}_{QM} - \mathcal{U}(\Phi, \Phi^*, T) \tag{3.3}$$

where the Lagrangian in quark meson linear sigma model

$$\mathcal{L}_{QM} = \bar{q_f}\ [i\gamma^\mu D_\mu - g(\sigma + i\gamma_5\vec{\tau}\cdot\vec{\pi})]\ q_f + \mathcal{L}_m \tag{3.4}$$

The coupling of quarks with the uniform temporal background gauge field is effected by the following replacement $D_\mu = \partial_\mu - iA_\mu$ and $A_\mu = \delta_{\mu 0}A_0$ (Polyakov gauge), where $A_\mu = g_s A^a_\mu \lambda^a/2$. g_s is the $SU_c(3)$ gauge coupling. λ_a are Gell-Mann matrices in the color space, a runs from $1\cdots 8$. $q_f = (u,d)^T$ denotes the quarks coming in two flavors and three colors. g is the flavor blind Yukawa coupling that couples the two flavor of quarks with four mesons; one scalar ($\sigma, J^P = 0^+$) and three pseudoscalars ($\vec{\pi}, J^P = 0^-$).

The quarks have no intrinsic mass but become massive after spontaneous chiral symmetry breaking because of nonvanishing vacuum expectation value of the chiral condensate. The mesonic part of the Lagrangian has the following form

$$\mathcal{L}_m = \frac{1}{2}(\partial_\mu \sigma)^2 + \frac{1}{2}(\partial_\mu \vec{\pi})^2 - U(\sigma, \vec{\pi}) \tag{3.5}$$

The pure mesonic potential is given by the expression

$$U(\sigma, \vec{\pi}) = \frac{\lambda}{4}\left(\sigma^2 + \vec{\pi}^2 - v^2\right)^2 - h\sigma, \tag{3.6}$$

Here λ is quartic coupling of the mesonic fields, v is the vacuum expectation value of scalar field when chiral symmetry is explicitly broken and $h = f_\pi m_\pi^2$.

3.1.1 Polyakov loop potential and thermodynamic grand potential

The effective potential $\mathcal{U}\left(\Phi, \Phi^*, T\right)$ is constructed such that it reproduces thermodynamics of pure glue theory on the lattice for temperatures upto about twice the deconfinement phase transition temperature. In this work, we are using two different parametrization for Polyakov loop effective potential namely the logarithmic and polynomial form [80,81]. The results produced by these potentials are known to be fitted well to the lattice results. The logarithmic Polyakov loop potential [81] is given by the following expression

$$\begin{aligned} \frac{\mathcal{U}_{\log}(\Phi, \Phi^*, T)}{T^4} &= -\frac{a\left(T\right)}{2}\Phi^*\Phi + b(T)\ln[1 - 6\Phi^*\Phi \\ &\quad +4(\Phi^{*3} + \Phi^3) - 3(\Phi^*\Phi)^2] \end{aligned} \tag{3.7}$$

where the temperature dependent coefficients are as follow

$$a(T) = a_0 + a_1\left(\frac{T_0}{T}\right) + a_2\left(\frac{T_0}{T}\right)^2; \qquad b(T) = b_3\left(\frac{T_0}{T}\right)^3 \tag{3.8}$$

The parameters of Eq.(3.7) are

$$a_0 = 3.51\ , \qquad a_1 = -2.47\ ,$$

$$a_2 = 15.2\ , \qquad b_3 = -1.75$$

The polynomial form of Polyakov loop potential [80] is written as

$$\begin{aligned}\frac{\mathcal{U}_{\text{pol}}(\Phi,\Phi^*,T)}{T^4} &= -\frac{b_2}{4}\left(|\Phi|^2+|\Phi^*|^2\right)-\frac{b_3}{6}(\Phi^3+\Phi^{*3}) \\ &\quad +\frac{b_4}{16}\left(|\Phi|^2+|\Phi^*|^2\right)^2 \end{aligned} \tag{3.9}$$

The second term that is the sum of Φ^3 and Φ^{*3} terms, causes the three degenerate vacua above the deconfinement phase transition. The potential parameters are adjusted according to the pure gauge lattice data such that the equation of state and Polyakov loop expectation values are reproduced. The temperature dependent coefficient $b_2(T)$ governs the confinement-deconfinement phase transition and is given by

$$b_2(T) = a_0 + a_1\left(\frac{T_0}{T}\right) + a_2\left(\frac{T_0}{T}\right)^2 + a_3\left(\frac{T_0}{T}\right)^3 \tag{3.10}$$

The other parameters have the following value

$$\begin{aligned} &a_0 = 6.75 \quad a_1 = -1.95 \quad a_2 = 2.625 \\ &a_3 = -7.44, \quad b_3 = 0.75 \quad b_4 = 7.5 \end{aligned} \tag{3.11}$$

The critical temperature for deconfinement phase transition $T_0 = 270$ MeV is fixed for pure gauge Yang Mills theory. In the presence of dynamical quarks T_0 is directly linked to the mass-scale Λ_{QCD}, the parameter which has a flavor and chemical potential dependence in full dynamical QCD and $T_0 \to T_0(N_f,\mu)$ [96, 104]. For our numerical calculations in this work, we have taken a fixed $T_0 = 208$ MeV for two flavours of quarks.

In the mean-field approximation, the thermodynamic grand potential for the PQM model is given as [96]

$$\Omega_{\text{MF}}(T,\mu;\sigma,\Phi,\Phi^*) = \mathcal{U}(T;\Phi,\Phi^*) + U(\sigma) + \Omega_{q\bar{q}}(T,\mu;\sigma,\Phi,\Phi^*). \tag{3.12}$$

Here, we have written the vacuum expectation values $\langle\sigma\rangle = \sigma$ and $\langle\vec{\pi}\rangle = 0$

The quark/antiquark contribution in the presence of Polyakov loop reads

$$\begin{aligned}\Omega_{q\bar{q}}(T,\mu;\sigma,\Phi,\Phi^*) &= \Omega_{q\bar{q}}^{\text{vac}} + \Omega_{q\bar{q}}^{\text{T}} \\ &= -2N_f\int\frac{d^3p}{(2\pi)^3}\left\{N_cE_q\theta(\Lambda^2-\vec{p}^{\,2}) + T\left[\ln g_q^+ + \ln g_q^-\right]\right\} \end{aligned} \tag{3.13}$$

The first term of the Eq. (3.13) denotes the fermion vacuum contribution, regularized by the ultraviolet cutoff Λ. In the second term g_q^+ and g_q^- have been defined after taking trace over color space.

$$g_q^+ = \left[1 + 3\Phi e^{-E_q^+/T} + 3\Phi^* e^{-2E_q^+/T} + e^{-3E_q^+/T}\right] \tag{3.14}$$

$$g_q^- = \left[1 + 3\Phi^* e^{-E_q^-/T} + 3\Phi e^{-2E_q^-/T} + e^{-3E_q^-/T}\right] \tag{3.15}$$

Here we use the notation $\mathrm{E}_q^{\pm} = E_q \mp \mu$ and E_q is the single particle energy of quark/antiquark.

$$E_q = \sqrt{p^2 + {m_q}^2} \tag{3.16}$$

where the constituent quark mass $m_q = g\sigma$ is a function of chiral condensate. In vacuum $\sigma(0,0) = \sigma_0 = f_\pi = 93.0$ MeV.

3.1.2 The renormalized vacuum term and model parameters

The fermion vacuum loop contribution can be obtained by appropriately renormalizing the first term of Eq. (3.13) using the dimensional regularization scheme, as done in ref. [103]. A brief description of essential steps is given below.

Fermion vacuum term is just the one-loop zero temperature effective potential at lowest order [165]

$$\begin{aligned}
\Omega_{q\bar{q}}^{\mathrm{vac}} &= -2N_f N_c \int \frac{d^3p}{(2\pi)^3} E_q \\
&= -2N_f N_c \int \frac{d^4p}{(2\pi)^4} \ln(p_0^2 + E_q^2) + \mathrm{K},
\end{aligned} \tag{3.17}$$

the infinite constant K is independent of the fermion mass, hence it is dropped.

The dimensional regularization of Eq. (3.17) near three dimensions, $d = 3 - 2\epsilon$ leads to the potential up to zeroth order in ϵ as given by

$$\Omega_{q\bar{q}}^{\mathrm{vac}} = \frac{N_c N_f}{16\pi^2} m_q^4 \left\{ \frac{1}{\epsilon} - \frac{1}{2}\left[-3 + 2\gamma_E + 4\ln\left(\frac{m_q}{2\sqrt{\pi}M}\right)\right]\right\}, \tag{3.18}$$

here M denotes the arbitrary renormalization scale.

The addition of a counter term $\delta\mathcal{L}$ in the Lagrangian of the QM or PQM model

$$\delta\mathcal{L} = \frac{N_c N_f}{16\pi^2} g^4 \sigma^4 \left\{ \frac{1}{\epsilon} - \frac{1}{2}\Big[-3 + 2\gamma_E - 4\ln\left(2\sqrt{\pi}\right) \Big] \right\}, \tag{3.19}$$

gives the renormalized fermion vacuum loop contribution as

$$\Omega_{q\bar{q}}^{\rm reg} = -\frac{N_c N_f}{8\pi^2} m_q^4 \ln\left(\frac{m_q}{M}\right). \tag{3.20}$$

Now the first term of Eq. (3.13) which is vacuum contribution will be replaced by the appropriately renormalized fermion vacuum loop contribution as given in Eq. (3.20).

The relevant part of the effective potential in Eq. (3.12) which will fix the value of the parameters λ and v in the vacuum at $T = 0$ and $\mu = 0$ is the purely σ dependent mesonic potential $U(\sigma)$ plus the renormalized vacuum term given by Eq. (3.20).

$$\Omega(\sigma) = \Omega_{q\bar{q}}^{\rm reg} + U(\sigma) = -\frac{N_c N_f}{8\pi^2} g^4 \sigma^4 \ln\left(\frac{g\sigma}{M}\right) - \frac{\lambda v^2}{2}\sigma^2 + \frac{\lambda}{4}\sigma^4 - h\sigma, \tag{3.21}$$

The first derivative of $\Omega(\sigma)$ with respect to σ at $\sigma = f_\pi$ in the vacuum is put to zero

$$\frac{\partial \Omega_{\rm MF}(0,0;\sigma,\Phi,\Phi^*)}{\partial\sigma} = \frac{\partial\Omega(\sigma)}{\partial\sigma} = 0 \tag{3.22}$$

The second derivative of $\Omega(\sigma)$ with respect to σ at $\sigma = f_\pi$ in the vacuum gives the mass of σ

$$m_\sigma^2 = \frac{\partial^2 \Omega_{\rm MF}(0,0;f_\pi,\Phi,\Phi^*)}{\partial\sigma^2} = \frac{\partial^2\Omega(\sigma)}{\partial\sigma^2} \tag{3.23}$$

Solving the equations (3.22) and (3.23), we obtain

$$\lambda = \lambda_s + \frac{N_c N_f}{8\pi^2} g^4 \left[3 + 4\ln\left(\frac{g f_\pi}{M}\right) \right] \tag{3.24}$$

and

$$\lambda v^2 = (\lambda v^2)_s + \frac{N_c N_f}{4\pi^2} g^4 \ f_\pi^2 \tag{3.25}$$

where λ_s and $(\lambda v^2)_s$ are the values of the parameters in the pure sigma model

$$\lambda_s = \frac{m_\sigma^2 - m_\pi^2}{2f_\pi^2} \tag{3.26}$$

$$(\lambda v^2)_s = \frac{m_\sigma^2 - 3m_\pi^2}{2} \tag{3.27}$$

It is evident from the equations (3.24) and (3.25) that the value of the parameters λ and v^2 have a logarithmic dependence on the arbitrary renormalization scale M. However, when we put the value of λ and λv^2 in Eq.(3.21), the M dependence cancels out neatly after the rearrangement of terms. Finally we obtain

$$\Omega(\sigma) = -\frac{N_c N_f}{8\pi^2} g^4 \sigma^4 \ln\left(\frac{\sigma}{f_\pi}\right) - \frac{\lambda_r v_r^2}{2}\sigma^2 + \frac{\lambda_r}{4}\sigma^4 - h\sigma, \tag{3.28}$$

Here, we define λ_r and $\lambda_r v_r^2$ as the values of the parameters after proper accounting of the renormalized fermion vacuum contribution.

$$\lambda_r = \lambda_s + \frac{3N_c N_f}{8\pi^2} g^4 \tag{3.29}$$

and

$$\lambda_r v_r^2 = (\lambda v^2)_s + \frac{N_c N_f}{4\pi^2} g^4 \ f_\pi^2 \tag{3.30}$$

Now the thermodynamic grand potential for the PQM model in the presence of appropriately renormalized fermionic vacuum contribution (PQMVT model) will be written as

$$\Omega_{\rm MF}(T,\mu;\sigma,\Phi,\Phi^*) = \mathcal{U}(T;\Phi,\Phi^*) + \Omega(\sigma) + \Omega_{q\bar{q}}^{\rm T}(T,\mu;\sigma,\Phi,\Phi^*). \tag{3.31}$$

Thus in the PQMVT model, One can get the chiral condensate σ, and the Polyakov loop expectation values Φ, Φ^* by searching the global minima of the grand potential in Eq.(3.31) for a given value of temperature T and chemical potential μ

$$\frac{\partial \Omega_{\rm MF}}{\partial \sigma} = \frac{\partial \Omega_{\rm MF}}{\partial \Phi} = \frac{\partial \Omega_{\rm MF}}{\partial \Phi^*} = 0 \ , \tag{3.32}$$

We will take the values $m_\pi = 138$ MeV, $m_\sigma = 500$ MeV, and $f_\pi = 93$ MeV in our numerical computation. The constituent quark mass in vacuum $m_q^0 = 335$ MeV fixes the value of Yukawa coupling $g = 3.3$.

3.2 Effect of The Vacuum Term on The Phase Structure and Thermodynamics

We are presenting the results of our calculation for studying the temperature variation of the order parameters σ, Φ, Φ^*, their temperature derivatives and various thermodynamic observables at zero and non zero quark chemical potentials in the presence of the renormalized fermionic vacuum term in the effective potential of the PQM model. These results have been termed as PQMVT model calculations and we have investigated the interplay of chiral symmetry restoration and confinement-deconfinement transition in the influence of fermionic vacuum term. The phase diagram together with the location of critical end point (CEP) has been obtained in μ, and T plane for both the cases with and without fermionic vacuum contribution in the effective potential. In order to have a comparison, we have also shown the temperature variations of order parameters and their derivatives in the PQM model calculation with the same parameter set. The impact of the sigma meson mass (m_σ) and the choice taken for the parametrization of Polyakov loop potential (polynomial versus logarithmic), on the phase structure and location of the critical end point (CEP), has also been explored. The temperature variations of thermodynamic observables namely pressure, energy density and entropy density at three different chemical potentials (zero, μ_{CEP} and $\mu > \mu_{CEP}$) have been shown in PQMVT model calculations. In order to study the effect of fermionic vacuum term at zero chemical potential, the temperature variation of the interaction measure, speed of sound, p/ϵ ratio and specific heat, has been calculated in PQMVT model and QMVT model (Quark Meson model with vacuum term) and these results have been compared with the corresponding results in the PQM and QM model calculations. Logarithmic form of Polyakov loop potential has been used in these computations. Interaction measure at $\mu = 0$ and phase diagram for $m_\sigma = 500$ MeV, has also been computed with the polynomial choice of Polyakov loop potential in PQMVT model. Finally we will be presenting the results of the temperature variation of baryon number density and quark number susceptibility at different chemical potentials in PQMVT model calculation.

We point out that in an earlier work, Skokov et al. [103] investigated, the influence of fermionic vacuum fluctuations on the thermodynamic observables near the chiral crossover transition at $\mu = 0$ by computing the second (c_2: quark number susceptibility) and the fourth (c_4) cumulants of the net quark number fluctuations for several values of pion mass and $m_\sigma = 700$ MeV. In the present work, we compute the quark number susceptibility with $m_\sigma = 500$ MeV and the physical pion mass at nonzero chemical potentials for identifying the emerging pattern of divergence in its behaviour near the CEP where the transition turns second order. Further all the quantities that we have chosen to calculate at zero chemical potential, are different from those of their calculation and even the temperature variation of order parameters at $\mu = 0$ MeV in our calculation, has been computed for different values of m_σ i.e. $m_\sigma = 500$ MeV and 600 MeV.

3.2.1 Phase structure

The solutions of the coupled gap equations, Eq.(3.32) determine the nature of chiral and deconfinement phase transition through the temperature and chemical potential dependence of chiral condensate σ, the expectation value of the Polyakov loop Φ and Φ^*. Fig.3.1 shows the temperature variation of the chiral condensate σ normalized with the vacuum value on the left while the right end of the plot shows the Polyakov loop Φ and Φ^* temperature variation for the PQMVT model calculations, the corresponding temperature variation of the chiral and Polyakov loop order parameters in PQM model calculations, has been shown in Fig.3.3(a). In Fig.3.1, the continuous dots, thin dash and thin solid

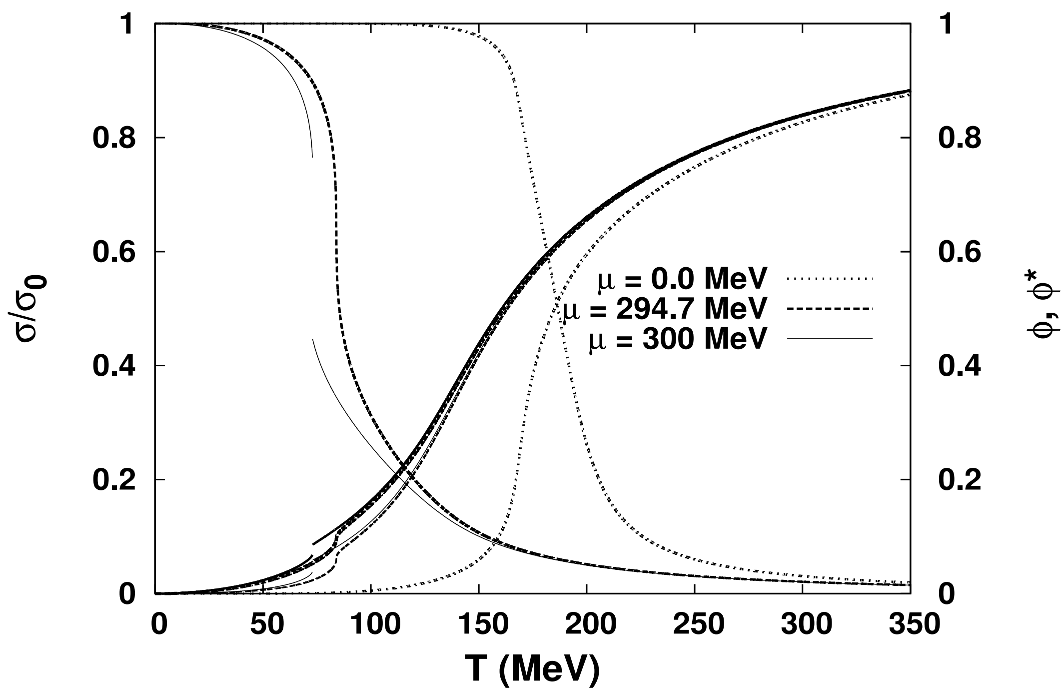

Figure 3.1: The σ, Φ, Φ^* variation with respect to temperature in PQMVT model are shown. The continuous dots, dash and solid lines represent the variation of $\frac{\sigma}{\sigma_0}$ on the left end and Φ on the right end of the plot at $\mu = 0$, 294.73 (CEP) and 300 MeV respectively. Thick dash and thick solid lines in the right end of the plot represent the Φ^* variations at $\mu = 294.7$ and 300 MeV respectively.

lines represent the variation of $\frac{\sigma}{\sigma_0}$ on the left and Φ on the right at $\mu = 0$, 294.7 (CEP) and 300 MeV respectively. Thick dash and thick solid lines in the right end of the plot represent the Φ^* variations at $\mu = 294.7$ and 300 MeV respectively. Fig.3.2(a), 3.2(b) and 3.2(c), show the temperature derivatives of σ, Φ and Φ^* fields as a function of temperature respectively at three different chemical potentials $\mu = 0$,100 and 200 MeV in PQMVT model calculations while the temperature variations of the same derivatives in the PQM model at $\mu = 0$ MeV has been shown in Fig.3.3(b). The characteristic temperatures (pseudocritical temperatures) for the chiral transition T_c^χ and the confinement-deconfinement

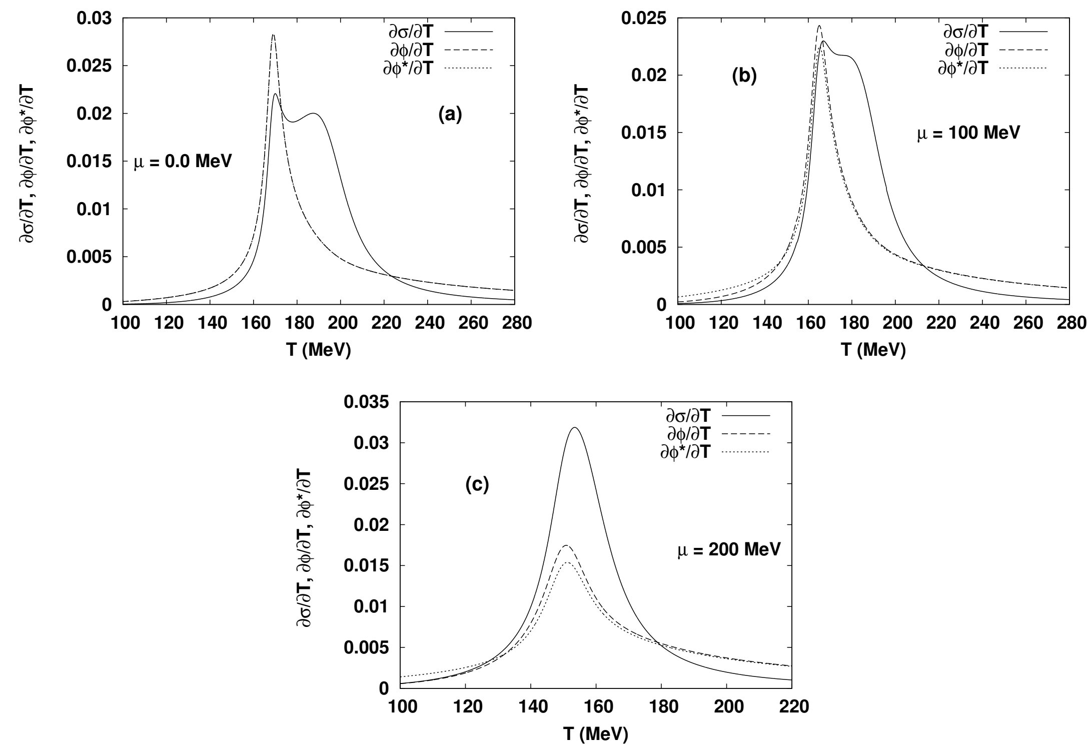

Figure 3.2: Temperature variations in the PMQVT model. (a), (b) and (c), show the temperature derivatives of σ, Φ and Φ^* fields as a function of temperature respectively at three different chemical potentials μ= 0, 100 and 200 MeV.

transition for the Φ field T_c^{Φ} and for the Φ^* field $T_c^{\Phi^*}$, are defined by the peak positions (inflection point) in the temperature derivatives of σ, Φ and Φ^* fields respectively.

The chiral crossover transition for the realistic case of explicitly broken chiral symmetry, becomes quite soft and smooth at $\mu = 0$ because the corresponding chiral phase transition for massless quarks turns second order in the chiral limit after having a proper accounting of the fermionic vacuum contribution in the PQMVT model. The smoothness of crossover at $\mu = 0$ is evident from the temperature variation of the chiral order parameter in Fig.3.1, while the Polyakov loop order parameter variation at the same chemical potential, is sharp in comparison. The chiral crossover at $\mu = 0$ becomes less smooth as we increase the chemical potential. We find quite a large range ($\mu = 0$ at $T_c^{\chi} = 186.5$ MeV to $\mu_{CEP} = 294.7$ MeV at $T_c^{\chi} = 84.0$ MeV) in the values of chemical potential that makes the temperature variation of chiral order parameter, sharp and sharper such that eventually the crossover turns into a second order transition at CEP. The narrow width of the coincident variation of Φ and Φ^* temperature derivative at zero chemical potential in Fig.3.2(a), signifies a sharp crossover for the confinement-deconfinement transition at $T_c^{\Phi} = 169.0$ MeV. Similar to the findings of NJL model calculation in ref. [88] at $\mu = 0$, the σ field temperature derivative shows a broad double peak structure. The second peak position at higher temperature $T_c^{\chi} = 186.5$ MeV, has been identified as the pseudocritical temperature for chiral crossover transition in Fig.3.2(a). The first peak in the σ derivative is driven by the sharp peak of the Polyakov loop variation. As the chemical potential is increased, the variation of Polyakov loop Φ derivative becomes smoother and broader with increasing width, while the σ derivative variation shows a decreasing width and double peak structure starts getting smeared after $\mu = 100$ MeV as shown in Fig.3.2(b). For the chiral crossover transition in the chemical potential range $\mu = 100$ to 160 MeV, the identification of pseudocritical temperature T_c^{χ} becomes ambiguous (with an ambiguity of about ± 5 MeV) due to the smearing of double peak structure. For $\mu > 160$ MeV in the PQMVT model, double peak structure disappears from the temperature variation of

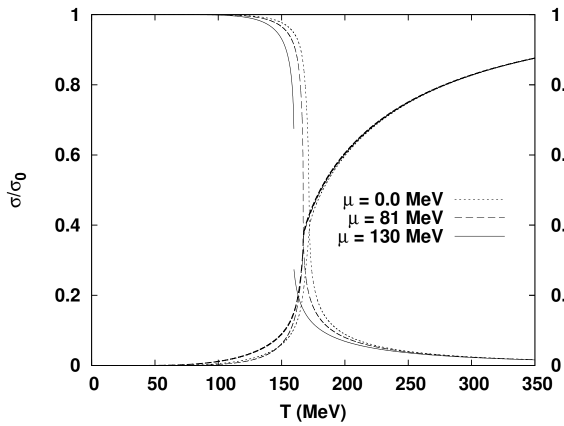

(a)

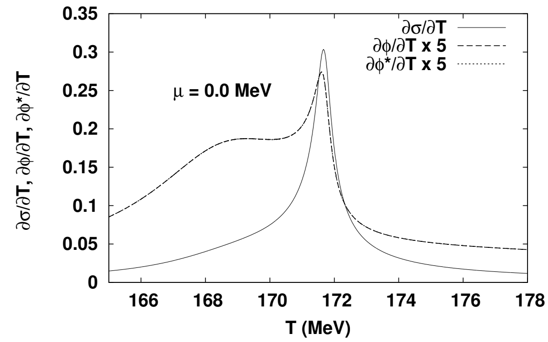

(b)

Figure 3.3: (a) The continuous dots, dash and solid lines in the left half of the figure represent the variation of $\frac{\sigma}{\sigma_0}$ in the PQM model at $\mu = 0$, $\mu = 81$ and $\mu = 130$ MeV respectively. In the right end of the plot, continuous dots represent coincident variation of Φ and Φ^* at $\mu = 0$ while thick and thin dash lines represent the Φ^* and Φ variations at $\mu = 81$ MeV respectively. (b) shows the temperature derivatives of σ, Φ and Φ^* fields as a function of temperature at $\mu = 0$ in the PQM model.

the chiral order parameter temperature derivative as shown in Fig.3.2(c) and its width decreases becoming narrow, narrower and narrowmost till the CEP at $\mu = 294.7$ MeV and $T = 84.0$ MeV is reached where the chiral transition turns second order.

For the realistic case of explicitly broken symmetry, the temperature variation of chiral order parameter at $\mu = 0$, turns out to be quite sharp and rapid in Fig.3.3(a) in comparison to the corresponding PQMVT model variation in Fig.3.1 because the chiral transition in the massless quark limit, is first order in the PQM model where vacuum term is absent. Further the chiral transition remains a crossover in quite a small range from $\mu = 0$ at $T_c^\chi = 171.5$ MeV to $\mu = 81$ MeV at $T_c^\chi = 167$ MeV in the PQM model results of Fig.3.3(a). Since the chiral crossover is sharper than the confinement-deconfinement crossover in the PQM model calculations, the single peak of the σ field temperature derivative in Fig.3.3(b)) at $\mu = 0$ is narrower and a lot higher than the peak in the variation of temperature derivatives of Φ and Φ^*. We have scaled the variation of Φ and Φ^* temperature derivatives in Fig.3.3(b) by a multiple of 5 which shows a very small double peak kind of structure. We consider the chiral and confinement-deconfinement crossovers nearly coincident at $\mu = 0$, $T_c^\chi = 171.5$ and we get exact coincidence as we move towards the CEP ($T = 167.0$ MeV and $\mu = 81.0$ MeV) of the model where on account of the transition turning second order, we get highest and narrowmost peak in $\frac{d\sigma}{dT}$ temperature variation.

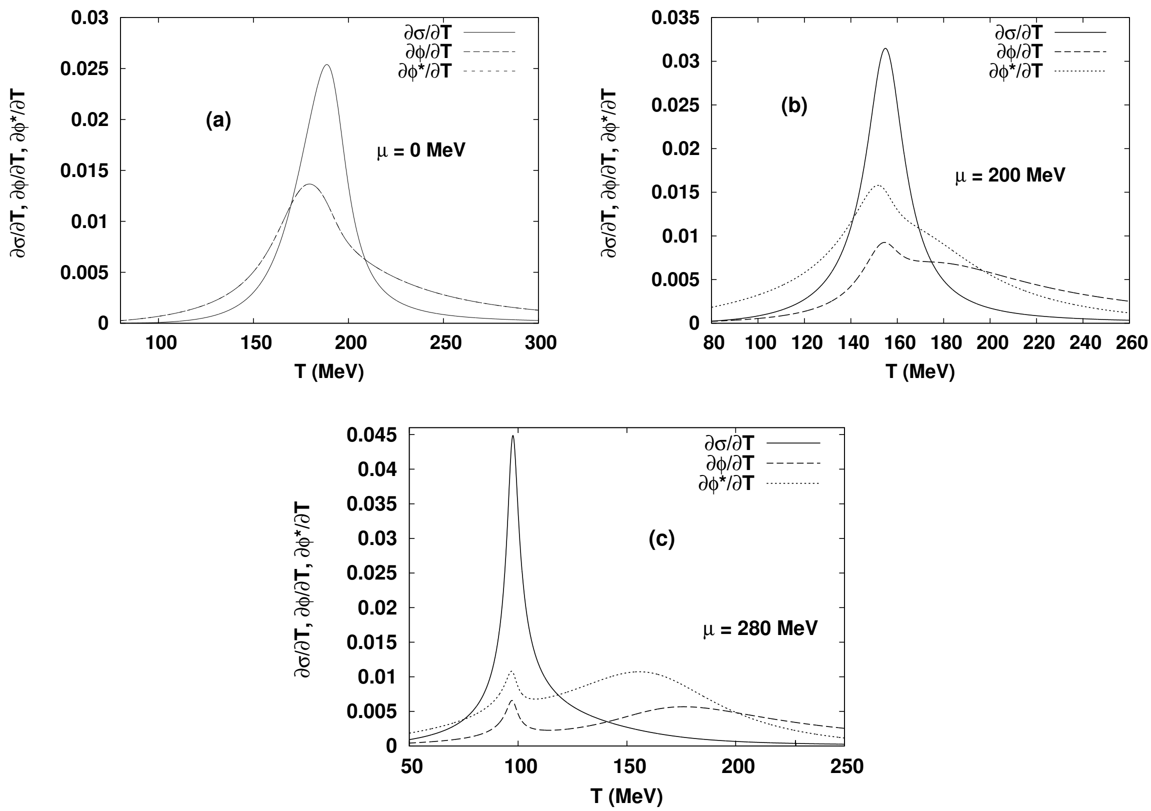

Figure 3.4: Temperature variation of order parameter derivatives with polynomial Polyakov loop potential in PQMVT model calculation.

In order to probe the issue of double peak structures emerging in Fig.3.2(a), 3.2(b), the temperature derivatives of σ, Φ and Φ^* fields, have been evaluated as function of temperature by taking the Polynomial form [80] for Polyakov loop potential instead of the logarithmic form in PQMVT model. In the resulting calculation of Fig.3.4(a), none of the field derivatives shows a double peak structure at $\mu = 0$ and the temperature variations for Φ and Φ^* temperature derivatives, show a coincident peak at crossover temperature $T_c^{\Phi} = T_c^{\Phi^*} = 180$ MeV which is lower than $T_c^{\chi} = 189$ MeV, the chiral crossover transition temperature identified from the location of peak in the σ field temperature derivative. As we increase the chemical potential beyond a small value, the peaks in Φ and Φ^* temperature derivatives, fail to coincide and are noticed to occur at a value lower than the T_c^{χ} (peak position in the $\frac{d\sigma}{dT}$ temperature variation). Thus we get $T_c^{\Phi^*} < T_c^{\Phi} < T_c^{\chi}$ for $\mu < 200$ MeV. For this calculation when $\mu > 200$ MeV, the double peak structure starts appearing separately in Φ and Φ^* derivatives as shown in Fig.3.2(b) and we find robust noncoincident second peaks respectively at $T_c^{\Phi} = 176$ MeV, $T_c^{\Phi^*} = 156$ MeV for $\mu = 280$ MeV as shown in Fig.3.2(c). The highest peak noticed in the temperature variation of $\frac{d\sigma}{dT}$, drives the formation of first peak in $\frac{d\Phi}{dT}$ and $\frac{d\Phi^*}{dT}$ temperature variations at the same location of temperature (T_c^{χ}). The second peak in $\frac{d\Phi}{dT}$ and $\frac{d\Phi^*}{dT}$ temperature variations occurs at a higher value of temperature than the chiral crossover transition temperature (T_c^{χ}), i.e. $T_c^{\Phi} > T_c^{\Phi^*} > T_c^{\chi}$. Thus the chiral symmetry restoration occurs earlier than the deconfinement transition for the range of chemical potential values $\mu >$ 210 MeV to $\mu = \mu_{CEP}$ in our PQMVT model calculation with polynomial Polyakov loop potential. Divergence of quark number susceptibility at the first and highest peak in σ field temperature derivative, gives the location of CEP at $T_{CEP} = 77.0$ MeV and $\mu_{CEP} = 293.6$ MeV. We again point out that logarithmic choice for Polyakov loop potential in PQMVT model instead of polynomial choice, leads to the formation of double peak structure in $\frac{d\sigma}{dT}$ temperature variations rather than in $\frac{d\Phi}{dT}$, $\frac{d\Phi^*}{dT}$ temperature variations. We get $T_c^{\chi} > T_c^{\Phi} = T_c^{\Phi^*}$ for logarithmic Polyakov loop PQMVT model calculations, hence chiral symmetry restoration takes place always after the deconfinement transition.

In Fig.3.5, we have obtained the phase diagram in our calculation with logarithmic

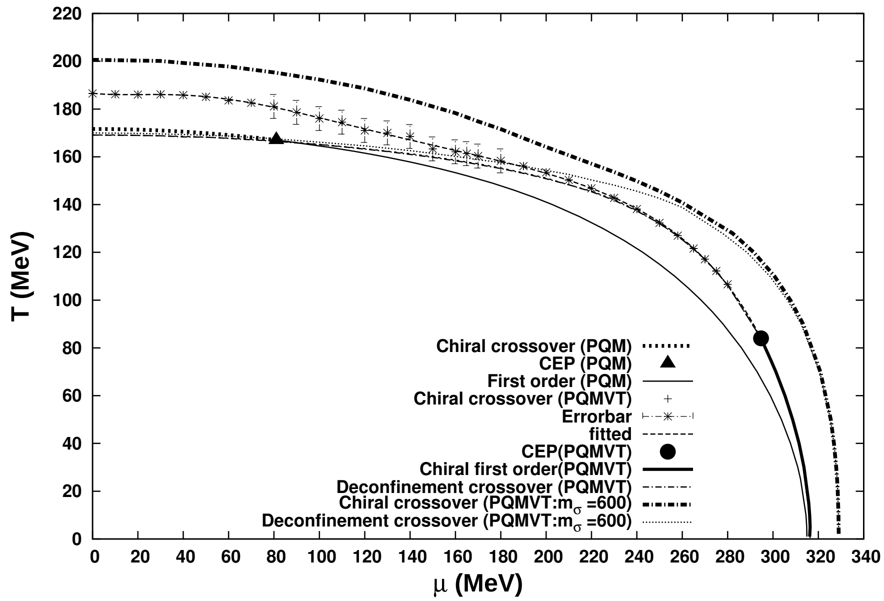

Figure 3.5: Phase diagram for logarithmic potential in PQMVT model with $m_\sigma = 500$ MeV and $m_\sigma = 600$ MeV. Thick dash dot line signifies the chiral crossover transition while thin continuous dot line denotes the deconfinement crossover transition for $m_\sigma = 600$ MeV in PQMVT model. For $m_\sigma = 500$ case, the chiral crossover transition has been depicted by the thin dash line which results due to the curve fitting of pseudocritical temperature data points (denoted by symbol +) identified with an ambiguity of ± 5 MeV (shown by error bars with x at the center) in the chemical potential range $\mu = 100$ MeV to $\mu = 160$ MeV. The thin dash dot line denotes the deconfinement crossover transition. First order transition has been shown by thick solid line which ends at CEP (filled circle) of the PQMVT model. Line with thick dots denotes the coincident chiral and deconfinement crossover transition at $m_\sigma = 500$ MeV in PQM model, while thin solid line denotes the first order transition which ends at the CEP (filled triangle) of the model.

Polyakov loop potential and located the critical end point (CEP) in the PQMVT as well as PQM model calculations for $m_\sigma = 500$ MeV. In order to obtain the phase diagram, we calculated the temperature variation of order parameter fields Φ, Φ^*, σ and their derivatives $\frac{d\Phi}{dT}$, $\frac{d\Phi^*}{dT}$, $\frac{d\sigma}{dT}$ for fixed values of different chemical potentials taken at a small interval. The pseudocritical temperatures T_c^{Φ}, $T_c^{\Phi^*}$ and T_c^{χ} signifying crossover transitions for Φ, Φ^* and σ fields respectively, got identified by the location of the peaks in the temperature variations of $\frac{d\Phi}{dT}$, $\frac{d\Phi^*}{dT}$, $\frac{d\sigma}{dT}$. We identified the critical end point (CEP) by locating a point in the chemical potential and temperature plane where the quark number susceptibility diverges. The structure of the phase diagram is very sensitive to the chosen value of the sigma meson mass. For the value $m_\sigma = 600$ MeV in the PQMVT model calculation, the transition becomes a crossover in the entire μ and T plane as shown by thick dash dot line and thin continuous dot line for the chiral restoration and deconfinement transition respectively. The coincident crossover transition for Φ and Φ^* lie below the chiral crossover transition line and later these two lines merge with each other. For $m_\sigma = 500$ MeV, we have shown the chiral crossover transition by a dash line (curve fitted) which starts from $T_c^{\chi} = 186.5$ MeV at $\mu = 0$ axis and ends at CEP; $T_{CEP} = 84$ MeV and $\mu_{CEP} = 294.7$ MeV in PQMVT model. Due to the smearing of double peak structure in the temperature derivative of chiral order parameter in the range $\mu = 100$ to 160 MeV, the chiral crossover transition temperature T_c^{χ} has been identified with an ambiguity of about ± 5 MeV. The pseudocritical temperature data points (shown by the symbol +) having this ambiguity in the range $\mu = 100$ to 160 MeV, have been curve fitted (dash line) by a polynomial of order seven using gnuplot program and error bars of ± 5 MeV have been shown in the figure. We get a unique T_c^{χ} for $\mu > 160$ MeV in the phase diagram because of a single peak structure which gets narrow and narrower for higher chemical potentials till we reach the CEP. The thin dash dot line which starts at $T_c^{\Phi} = 169$ MeV and ends at CEP of the PQMVT model, signifies the confinement-deconfinement crossover transition. The chiral and confinement-deconfinement crossover transition lines merge at $\mu = 250$ MeV and $T_c^{\chi} = T_c^{\Phi} = 132$ MeV. The thick solid line for $\mu > \mu_{CEP}$ represents the first order phase transition corresponding to the jump in all the order parameters at the same critical temperature. The chiral crossover transition line lies above the crossover line for the confinement-deconfinement transition. Thus our results of the PQMVT model calculation are in tune with the standard scenario [104] where chiral symmetry restoration occurs at a higher critical temperature $T_c^{\chi} = 186.5$ MeV than the confinement-deconfinement transition temperature $T_c^{\Phi} = 169$ MeV at $\mu = 0$ axis and we find $T_c^{\chi} > T_c^{\Phi} = T_c^{\Phi^*}$ for the whole crossover range of μ, T values. Further the crossover transition temperature at $\mu = 0$ compare well with the lattice [45, 48] results and QCD based computations [104, 166] in two flavour model. For the PQM model calculation without vacuum fermionic term at $m_\sigma = 500$ MeV, the chiral and confinement-deconfinement crossover transition lines are coincident (as shown by the thick dots) and start from $T_c^{\chi} = T_c^{\Phi} = 171.5$ MeV at $\mu = 0$ MeV to end at the CEP ($T_{CEP} = 167.0$ MeV and $\mu_{CEP} = 81.0$ MeV) of the PQM model. The first order transition for $\mu > \mu_{CEP}$ in the PQM model, has been shown by the thin solid line. The CEP of the PQM model gets located near the temperature axis at $\mu_{CEP} = 81$ MeV and $T_{CEP} = 167$ MeV because the chiral crossover at $\mu = 0$, having the background of a first order phase transition in the chiral limit, is rapid and sharp and soon it gets converted to a first order phase transition as we increase the chemical potential. While the critical end point (CEP) gets shifted close to the chemical potential axis at $\mu_{CEP} = 294.7$ MeV and $T_{CEP} = 84$ MeV in PQMVT model because the chiral crossover transition at $\mu = 0$ MeV is quite soft and smooth as it emerges from a phase transition which turns second order in the chiral limit due to the effect of renormalized fermionic vacuum contribution in the effective potential and further it remains a crossover for large range of values in the chemical potential.

The location of the critical end point and the structure of the phase diagram is also sensitive to the parametrization of the Polyakov loop potential. We explored this sensitivity by calculating the phase diagram as shown in Fig.3.6 for $m_\sigma = 500$ MeV taking polynomial ansatz for Polyakov loop potential in the PQMVT model. The dash line showing the chiral crossover transition, starts at $T_c^{\chi} = 189$ MeV at $\mu = 0$ MeV and ends at the CEP ($\mu_{CEP} = 293.6$ MeV and $T_{CEP} = 77$ MeV) of PQMVT model with polynomial

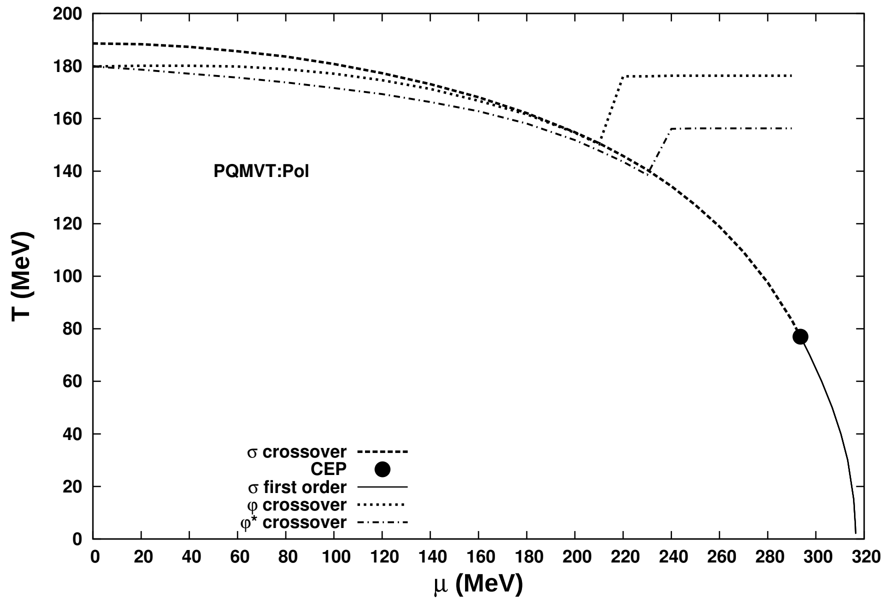

Figure 3.6: Phase diagram for polynomial potential in PQMVT model with $m_\sigma = 500$ MeV. Dash line denotes the chiral crossover transition and it ends at the CEP (filled circle), the solid line denotes the first order transition. Continuous dots denote the deconfinement crossover transition for Φ field while the dash dot line denotes the deconfinement crossover transition for Φ^* field.

Polyakov loop potential. Line with continuous dots signify the deconfining crossover transition for the Φ field while the dash dotted line show the deconfining crossover transition for the Φ^* field. We notice that the deconfinement crossover lines for Φ and Φ^* fields, lie below the chiral crossover transition line i.e. $T_c^{\Phi^*} < T_c^{\Phi} < T_c^{\chi}$ in the chemical potential range $\mu = 0$ to $\mu = 210 - 225$ MeV. When $\mu > 210$ MeV, confinement-deconfinement crossover transition lines for Φ^* and Φ fields get located above the chiral crossover phase boundary from $\mu > 210$ to $\mu = \mu_{CEP} = 293.6$ MeV and we get $T_c^{\Phi} > T_c^{\Phi^*} > T_c^{\chi}$. We point out that in this region of phase diagram, the chiral symmetry restoring crossover transition sets up earlier than the deconfining crossover transition. It has been speculated that a region of confinement with restored chiral symmetry in phase diagram [134], signals the onset of quarkyoinc phase [135]. Thus, similar to the results of ref. [75–77, 104], we are finding a quarkyonic phase like region of confinement with chiral symmetry in our PQMVT model calculations when the Polyakov loop potential has a polynomial form.

3.2.2 Thermodynamic Observables: Pressure, Entropy and Energy Density

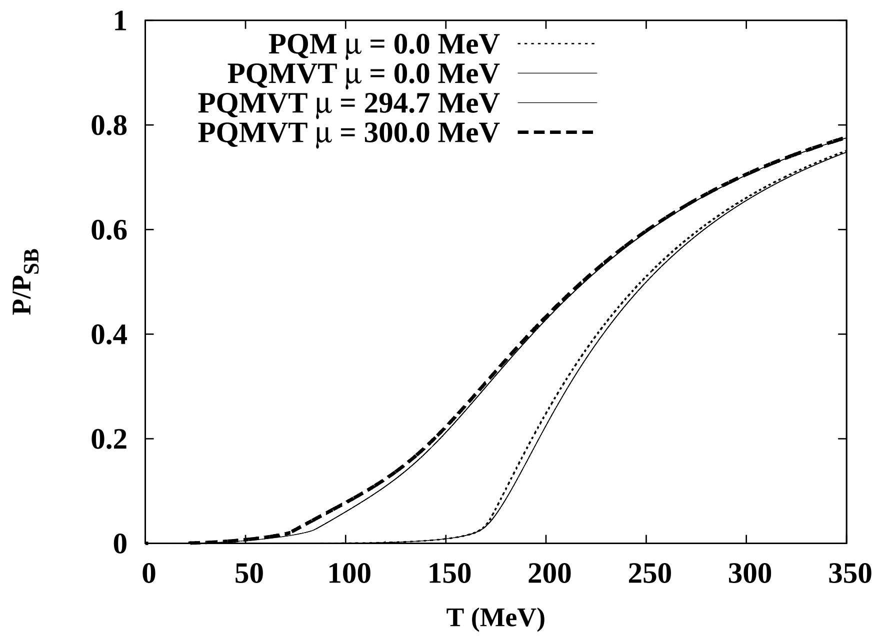

Figure 3.7: Pressure variation with respect to temperature.

The negative of grand potential gives the thermodynamic pressure

$$p(T, \mu) = -\Omega_{\mathrm{MF}}(T, \mu) \tag{3.33}$$

Thermodynamic pressure divided by the QCD Stefan-Boltzmann (SB) limit has been shown for three chemical potentials $\mu = 0, 294.7$ (CEP) and 300 MeV in Fig.3.7 for PQMVT model. It has been normalized to vanish at $T = \mu = 0$. We have shown the pressure calculated in PQM model also for comparison at $\mu = 0$. For N_f massless quarks and $N_c^2 - 1$ massless gluons in the deconfined phase, the QCD pressure in the SB limit is given by

$$\frac{p_{\mathrm{SB}}}{T^4} = (N_c^2 - 1)\frac{\pi^2}{45} + N_c N_f \left[\frac{7\pi^2}{180} + \frac{1}{6}\left(\frac{\mu}{T}\right)^2 + \frac{1}{12\pi^2}\left(\frac{\mu}{T}\right)^4\right] . \tag{3.34}$$

The fermionic vacuum contribution makes the pressure variation in PQMVT model smooth at $\mu = 0$ and this curve (thin solid line) lies slightly below the curve (line with continuous dots) obtained in PQM model. The pressure variations at $\mu_{CEP} = 294.7$ and $\mu = 300$ MeV of PQMVT model are represented by the thick solid and dash line respectively. The pressure increases near the chiral transition due to the melting of the constituent quark masses and saturates at about eighty percent of the SB limit.

The entropy density is defined as negative of the temperature derivative of the grand potential.

$$s = -\frac{\partial \Omega_{\mathrm{MF}}}{\partial T} \tag{3.35}$$

The implicit variation of σ, Φ and Φ^* fields with respect to temperature has been accounted for, in the temperature derivative of $\Omega(\sigma)$, $\mathcal{U}_{\log}$ and $\Omega_{\mathrm{q\bar{q}}}^{\mathrm{T}}$ as evaluated in the appendix. The temperature variation of entropy density normalized by its QCD, SB limit has been shown in Fig.3.8. It is continuous for crossover transition and attains about 40-45 percent of its SB value at pseudocritical transition temperature. Again due to the fermionic vacuum fluctuations, the entropy density variation (thin solid line) at $\mu = 0$ turns out to be a smoother function of temperature in PQMVT model when it is compared with corresponding curve (line with continuous dots) of PQM model calculation. At $\mu_{\mathrm{CEP}} = 294.7$ MeV, the entropy density curve (thick solid line) shows a steep rise at $T_{\mathrm{CEP}} = 84.$ MeV in PQMVT model, then it takes a bend to reach its saturation. The PQM model entropy density curve (dash dotted line) at $\mu = 294.7$ MeV shows a large

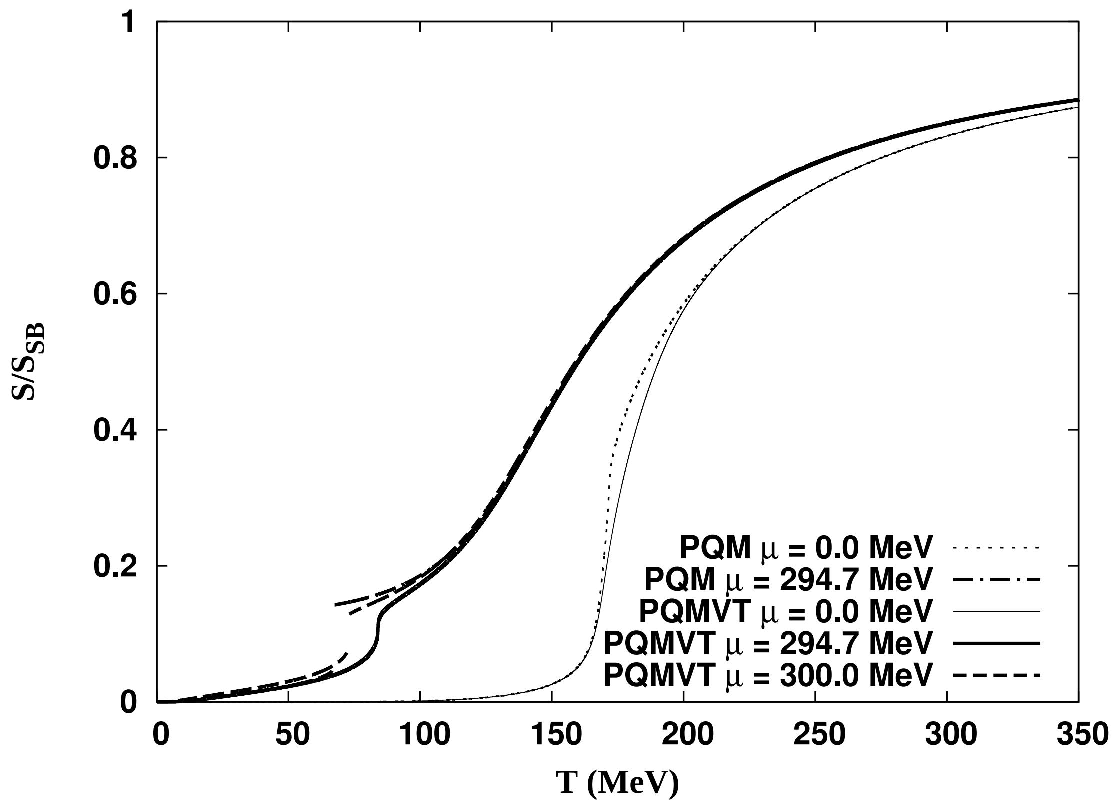

Figure 3.8: Entropy density variation with respect to temperature.

jump because chiral transition is strong first order at this chemical potential. The first order chiral transition of PQMVT model at $\mu = 300.0$ MeV, generates another jump in the entropy density curve (line with dash), though this jump is smaller than the first order jump seen in PQM model entropy curve at a lower chemical potential $\mu = 294.7$ MeV.

The energy density in the presence of chemical potential is given as

$$\epsilon = -p + Ts + \mu n \tag{3.36}$$

where n is the number density. The temperature variation of energy density normalized by its QCD, SB limit value has been shown in Fig.3.9 for $\mu = 0, 280$, 294.7 (CEP) and 300 MeV in PQMVT model. The energy density variation (thin solid line) at $\mu = 0$ similar to entropy density variation, is smoother in comparison to the corresponding

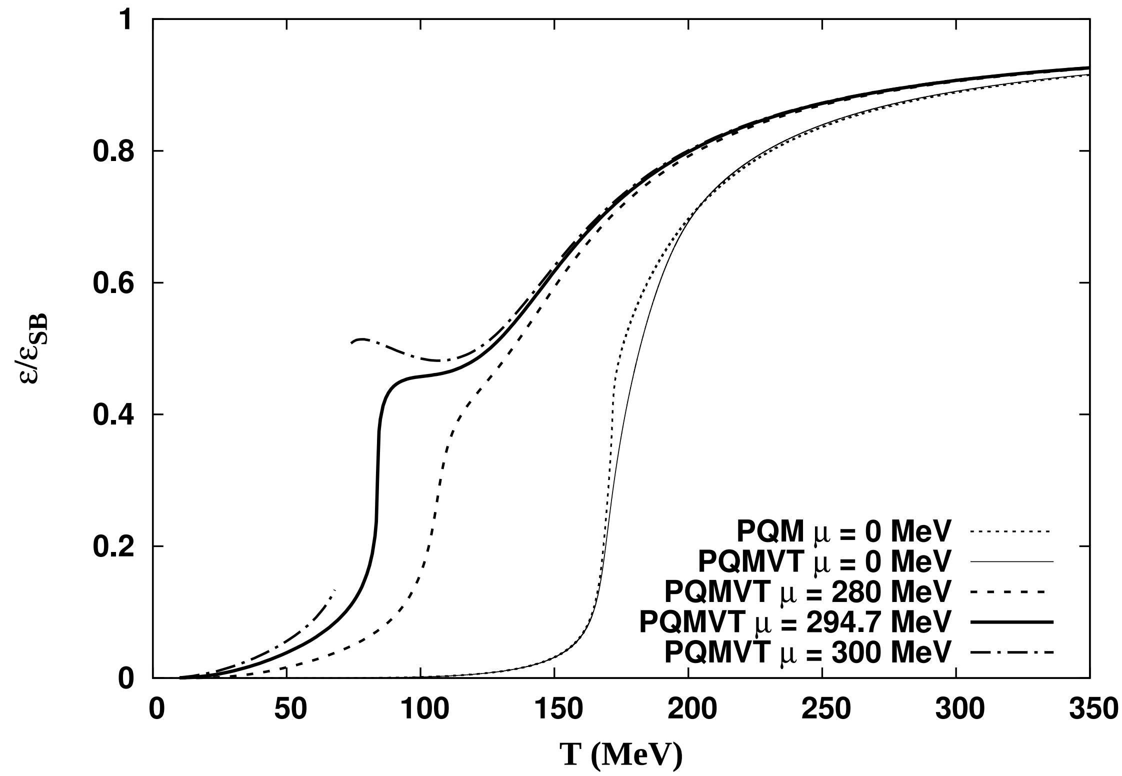

Figure 3.9: Variation of energy density with respect to temperature.

variation in PQM model calculation (line with continuous dots), this again is due to the influence of fermionic vacuum fluctuations. Similar to the entropy density variation at $\mu_{\text{CEP}} = 294.7$ MeV, the energy density (thick solid line) also shows a very steep and large rise at $T_{\text{CEP}} = 84.0$ MeV, then it curves to attain the saturation. At $\mu = 300.0$ MeV, we get a large jump in the energy density curve (dash-dotted line) which of course is a signature of the first order chiral transition. Since quark degrees of freedom get liberated and become light, the energy density registers a rapid increase near the crossover/phase transition point and reaches almost to the value of SB limit.

The trace anomaly of energy momentum tensor is also known as interaction measure. The temperature variation of the interaction measure $\triangle = (E - 3p)/T^4$ has been shown in Fig.3.10 at $\mu = 0$ MeV in QM, QMVT model calculations together with PQM and

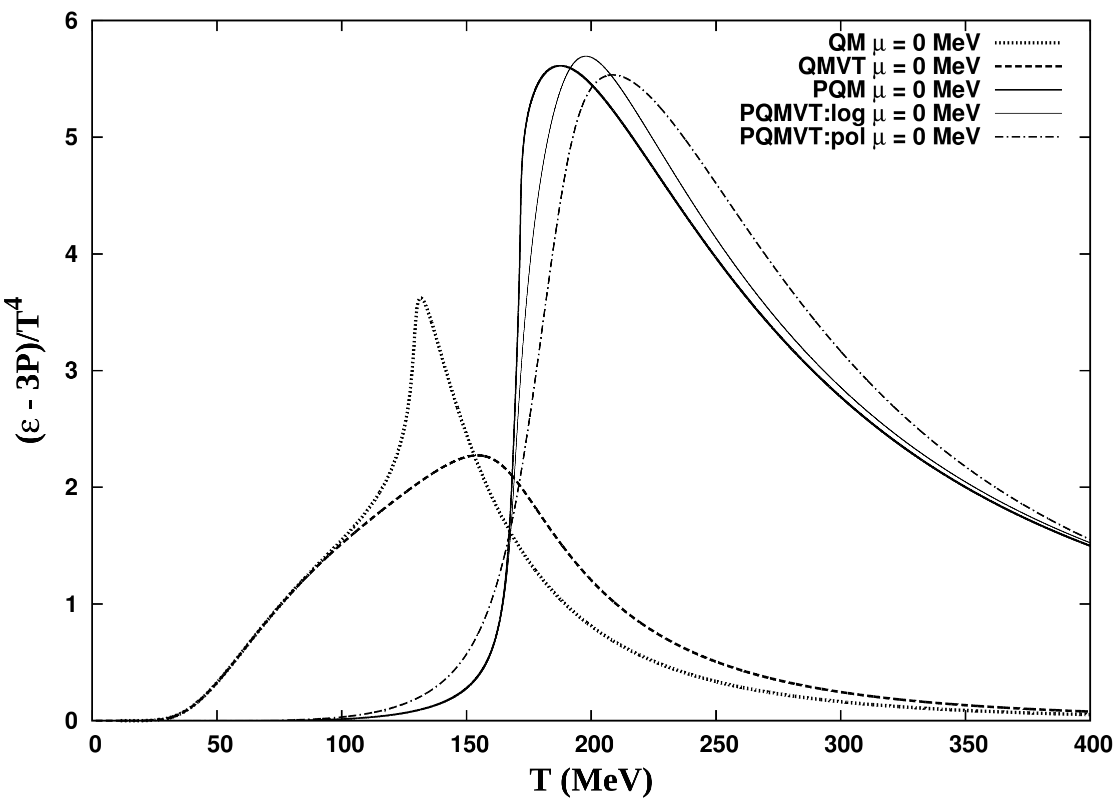

Figure 3.10: Change in interaction measure with respect to temperature.

PQMVT model calculations for logarithmic choice of Polyakov loop potential. In order to see the impact of the parametrization of Polyakov loop potential on the temperature variation of interaction measure, we have also shown the result for the polynomial choice of Polyakov loop potential in PQMVT model. The QM model variation of the interaction measure (line with continuous dots) shows a sharp and narrow peak near the pseudocritical transition temperature which becomes very broad and smooth in the corresponding variation (thick dash line) of QMVT model calculation due to the effect of inclusion of fermion vacuum term contribution in the effective potential of QM model. The peak of interaction measure temperature variation (thin solid line) in PQMVT model shifts to a slightly higher temperature value in comparison to the corresponding peak in the variation (thick solid line) of PQM model calculations done with the logarithmic choice of Polyakov loop potential. The temperature variation of interaction measure shown by dash-dot line, registers largest rightward shift if we take polynomial form of Polyakov loop potential in PQMVT model calculation.

3.2.3 Specific heat C_V and Speed of sound C_S

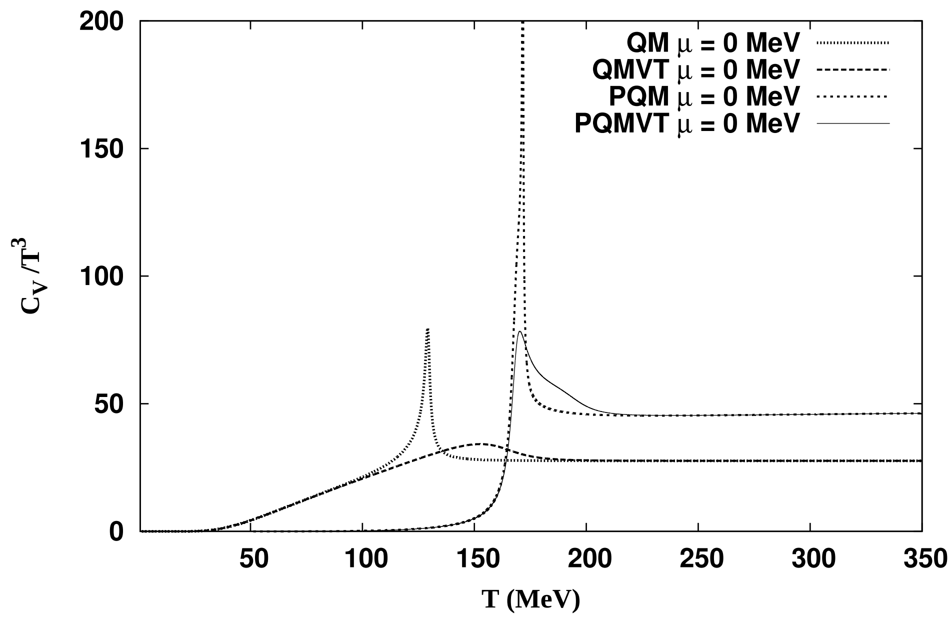

Figure 3.11: Specific heat variation with respect to temperature.

The expression of specific heat at constant volume is given by

$$C_V = \left.\frac{\partial \epsilon}{\partial T}\right|_V = -T \left.\frac{\partial^2 \Omega_{\mathrm{MF}}}{\partial T^2}\right|_V \tag{3.37}$$

The second partial temperature derivatives of σ, Φ and Φ^* fields contribute in the double derivatives of $\Omega(\sigma)$, $\mathcal{U}_{\log}$ and $\Omega_{q\bar{q}}^{\mathrm{T}}$ with respect to temperature as given in the appendix in chapter 7. Fig.3.11 shows the temperature variation of the specific heat C_V normalized by T^3 in QM, QMVT and in PQM, PQMVT model calculations at $\mu = 0$. The specific heat variation while growing with the temperature, peaks at the crossover transition temperature and then saturates at the corresponding SB limit at the higher temperature. The QM model specific heat variation shows a large and sharp peak which becomes quite smooth and broad in the corresponding variation of QMVT model calculation due to the presence of fermionic vacuum term, further the peak position gets shifted to a higher transition temperature. The qualitative difference of structures in the curves of QM and QMVT model gets reduced due to the influence of Polyakov loop potential and we notice that the PQM model specific heat variation has quite a high and sharp peak which becomes small and a little less sharp in the PQMVT model variation and the peaks occur at the same transition temperature. Further, we remark that the peak positions of the temperature variation of order parameter derivatives in Fig.3.2(a) and Fig.3.3(b) give different transition temperatures for chiral crossover in PQMVT and PQM model calculations while for confinement-deconfinement crossover, the transition temperature is almost same in both the models.

The speed of sound is an important quantity for hydrodynamical investigations of relativistic heavy-ion collisions. It is given by

$$C_s^2 = \left.\frac{\partial p}{\partial \epsilon}\right|_S = \left.\frac{\partial p}{\partial T}\right|_V \Big/ \left.\frac{\partial \epsilon}{\partial T}\right|_V = \frac{s}{C_V} \ , \tag{3.38}$$

The equation of state parameter $p(T)/\epsilon(T)$ also represents the information contained in trace anomaly. The velocity of sound C_s^2 and the equation of state parameter $p(T)/\epsilon(T)$ ratio has been shown as a function of temperature in QM, QMVT and PQM, PQMVT model calculations at $\mu = 0$ in Fig.3.12. Thick lines denote the result for the sound velocity C_s^2 and thin lines show the variation of $p(T)/\epsilon(T)$ ratio. The presence of fermion vacuum term in QMVT model leads to a very smooth temperature variation for C_s^2 (line with thick long dash) and $p(T)/\epsilon(T)$ ratio (line with thin long dash). The C_s^2 temperature variation (line with thick small dash) in the QM model calculation, shows a very sharp drop followed by a rapid rise while the EOS parameter $p(T)/\epsilon(T)$ ratio (line with thin small dash) shows a cusp at crossover transition temperature. The temperature variation

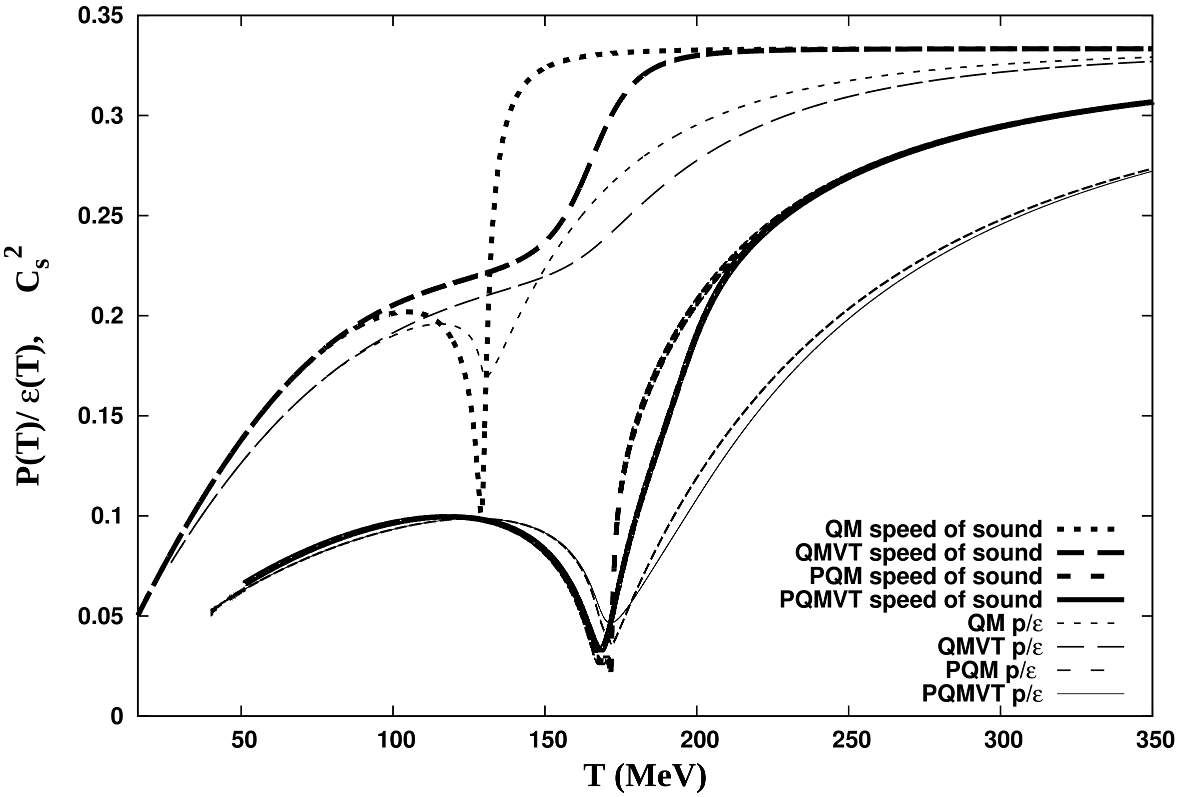

Figure 3.12: The variation of $p(T)/\epsilon(T)$ has been shown by thin lines while thick lines show the variation of C_s^2. Upper curves show QM and QMVT model results while PQM and PQMVT model results are shown in lower curves.

of C_s^2 (thick solid line) and $p(T)/\epsilon(T)$ ratio (thin solid line) in the PQMVT model turns out to be smoother than the corresponding variation of C_s^2 (line with thick, short and dark dash) and $p(T)/\epsilon(T)$ ratio (thin dash line) in the PQM model calculation. At higher temperatures C_s^2 and $p(T)/\epsilon(T)$ ratio approach the ideal gas value 1/3 in all the cases of model calculation. In PQM and PQMVT models, the value of C_s^2 almost matches with the $p(T)/\epsilon(T)$ ratio for lower temperatures and C_s^2 value is always larger than the $p(T)/\epsilon(T)$ ratio except near the transition temperature, similar as in ref. [83,99]. The minimum value of $p(T)/\epsilon(T)$ ratio is about .033 in PQMVT model which being slightly larger than the

PQM model value .026, is less than the lattice result .075 [49,167]. Similar to the findings of ref. [99], interestingly the C_s^2 value is found to be less than 0.1 around half the crossover transition temperature in our PQM and PQMVT model results. In contrast,using a model of confinement, the results of ref. [168] find values of about $C_s^2 \sim 0.2$ around half the transition temperature and $C_s^2 = 0.15$ around the transition temperature.

3.2.4 Quark number density and Susceptibility

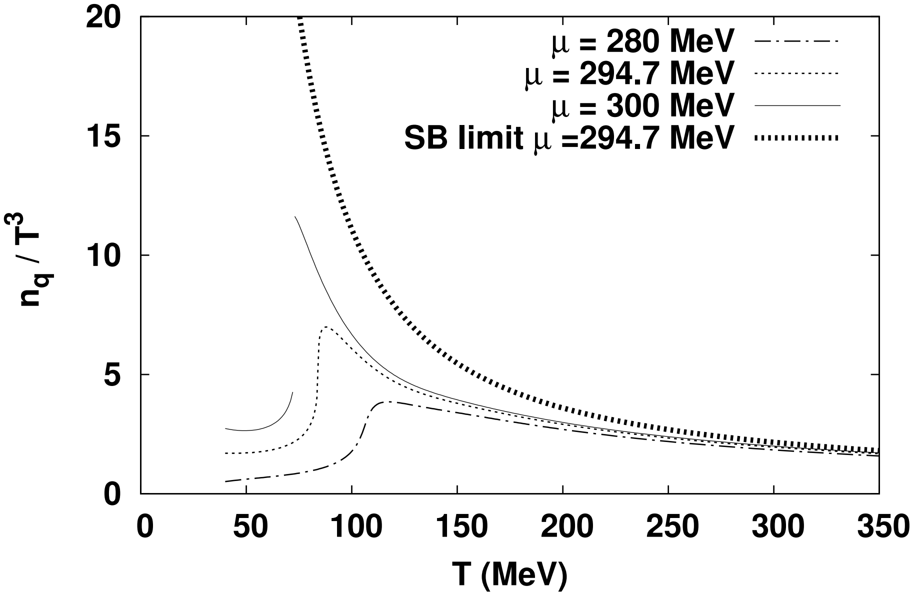

Figure 3.13: Temperature variation of quark number density divided by T^3.

The first derivative of grand potential with respect to chemical potential gives the quark number density

$$n = -\frac{\partial \Omega_{\rm MF}}{\partial \mu} \tag{3.39}$$

The implicit variation of σ, Φ and Φ^* fields with respect to chemical potential has been accounted for, in the evaluation of first derivative of $\Omega(\sigma)$, $\mathcal{U}_{\log}$ and $\Omega^{\mathrm{T}}_{\mathrm{q}\bar{\mathrm{q}}}$ with respect to chemical potential as given in the appendix. The temperature variation of the quark number density normalized by T^3 in the PQMVT model calculation has been shown in Fig.3.13 for three quark chemical potentials $\mu = 280, 294.7$ (CEP) and 300 MeV. The dash dotted line shows the number density variation for a crossover transition at $\mu = 280$ MeV, here we see a small peak structure. The dotted line number density variation shows a sharper rise with a narrow peak at $\mu_{\mathrm{CEP}} = 294.7$ MeV and it approaches the SB value of number density variation (shown by thick dots) for higher temperatures. At $\mu = 300$ MeV, the Phase transition becomes first order, hence the quark number density being a first derivative of the grand potential with respect to the chemical potential, shows a jump in the solid line temperature variation.

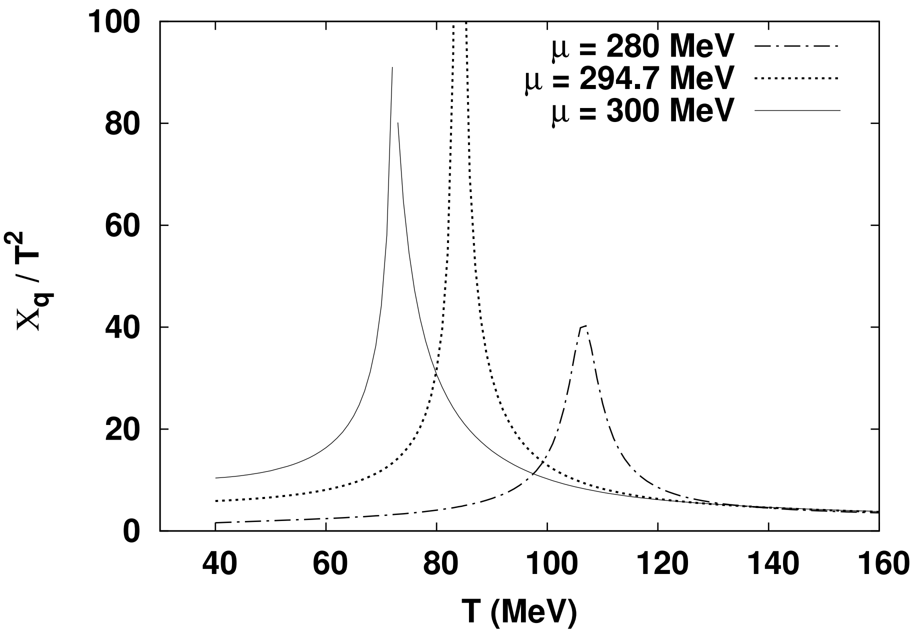

Figure 3.14: Susceptibility χ_q/T^2 variation with respect to temperature.

The expression of quark number susceptibility is obtained as

$$\chi_q = -\frac{\partial^2 \Omega_{\rm MF}}{\partial \mu^2} \tag{3.40}$$

The second partial derivatives of σ, Φ and Φ^* fields with respect to chemical potential contribute in the double derivatives of $\Omega(\sigma)$, $\mathcal{U}_{\rm log}$ and $\Omega_{\rm q\bar{q}}^{\rm T}$ with respect to chemical potential as given in the appendix. Fig.3.14 shows the variation of quark number susceptibility normalized by T^2 as a function of temperature in the PQMVT model calculation for chemical potentials $\mu = 280, 294.7$ (CEP) and 300 MeV. The dash dotted line susceptibility variation at $\mu = 280$ MeV shows a continuous peak structure at the crossover transition temperature. Since at $\mu_{\rm CEP} = 294.7$ MeV, the phase transition turns second order, the dotted line of quark number susceptibility variation shows a very large and strongly divergent peak at $T_{\rm CEP}$. The solid line shows the quark number susceptibility at $\mu = 300$ MeV for the first order transition case, we get a discontinuous variation because order parameter registers a jump in the first order transition.

3.3 Summary

We have investigated the temperature variation of the order parameters σ, Φ, Φ^*, their temperature derivatives and various thermodynamic physical observables at non zero and zero quark chemical potentials in the presence of renormalized fermionic vacuum term in the effective potential of the PQM model. The results termed as the PQMVT model calculations have been compared with the results of PQM model without vacuum term. We have used logarithmic Polyakov loop potential for large part of our calculation. We have used the polynomial form of Polyakov loop potential also in the PQMVT model calculation in order to investigate the impact of the choice of Polyakov loop potential on the phase structure and location of critical end point.

The chiral crossover transition for the realistic case of explicit chiral symmetry breaking, becomes quite soft and smooth at $\mu = 0$ in PQMVT model due to the proper accounting of the fermionic vacuum term contribution in the PQM model because the corresponding phase transition at $\mu = 0$ turns second order in the chiral limit of massless quarks. The σ derivative shows a broad double peak structure at $\mu = 0$. The second peak position at higher transition temperature $T_c^\chi = 186.5$ MeV identifies the chiral crossover because the first peak results due to a sharp peak in the Polyakov loop temperature variation which signals a rapid confinement-deconfinement crossover transition at $\mu = 0$. In a large range of μ, T values (from $\mu = 0$ and $T = 186.5$ MeV to $\mu = 294.7$ MeV and $T = 84$ MeV), the chiral transition remains a crossover and it keeps on becoming sharper with the increase in chemical potential till the point of second order transition at μ_{CEP} is reached in the PQMVT model. Instead of logarithmic form, if we take polynomial form for Polyakov loop potential in our PQMVT model calculation, the temperature derivatives of Polyakov loop field Φ and its conjugate Φ^* show distinct non coincident double peak structure in the chemical potential range $\mu > 200$ MeV to $\mu_{CEP} = 293.6$ MeV and we do not find any double peak structure near $\mu = 0$ in the temperature derivative of σ field. Hence confinement-deconfinement crossover transition lines for Φ^* and Φ fields get located above the chiral crossover phase boundary from $\mu = 210$ to $\mu = \mu_{CEP} = 293.6$ MeV. Since the chiral transition in the massless quark limit is first order at zero chemical potential, the corresponding crossover transition for the realistic case has been found to be quite sharp and rapid in the PQM model without any vacuum term. Further the chiral transition remains a crossover in quite a small range only from $\mu = 0$ and $T_c^\chi = 171.5$ MeV to $\mu = 81$ MeV and $T_c^\chi = 167$ MeV in the PQM model calculations.

The phase diagram together with the location of critical end point (CEP) has been obtained in μ, and T plane for $m_\sigma = 500$ MeV in both the models PQMVT as well as PQM with the logarithmic choive of Polyakov loop potential. The structure of the phase diagram is very sensitive to the chosen value of sigma meson mass. For the value $m_\sigma = 600$ MeV, the transition becomes a crossover in the entire μ and T plane for the PQMVT model calculation. We do not have a coincident chiral and confinement-deconfinement crossover transitions in the PQMVT model as the chiral crossover transition line lies above the crossover line for the confinement-deconfinement transition. Our results of the PQMVT model calculation with logarithmic Polyakov loop potential, are in tune with the standard scenario where chiral symmetry restoration occurs at a higher critical temperature than the confinement-deconfinement transition temperature. The critical end point (CEP) gets shifted close to the chemical potential axis ($\mu_{CEP} = 294.7$ MeV, $T_{CEP} = 84.0$ MeV) in PQMVT model because the chiral crossover transition at $\mu = 0$ emerging from a second order phase transition in the chiral limit, becomes quite soft and smooth due to the effect of fermionic vacuum contribution in the effective potential and further it remains a crossover for large values of the chemical potential. The chiral and confinement-deconfinement crossover transition lines are coincident in the PQM model and its' CEP gets located near the temperature axis at $\mu_{CEP} = 81$ MeV and $T_{CEP} = 167$ MeV because the chiral crossover at $\mu = 0$, having the background of a first order phase transition in the chiral limit, is quite rapid and sharp and soon it gets converted to a first order phase transition as we increase the chemical potential. The sensitive dependence of the phase structure and location of the critical end point, has also been explored by calculating another phase diagram for $m_\sigma = 500$ MeV taking polynomial choice of Polyakov loop potential in the PQMVT model. It is noticed that the chiral crossover transition line, lies above the deconfinement crossover lines for the Φ and Φ^* fields in the chemical potential range $\mu = 0$ to $\mu = 210 - 225$ MeV. Deconfinement crossover transition lines for fields Φ and Φ^*, cross the chiral crossover phase boundary around $\mu \approx 210$ MeV and get located above it from $\mu > 210$ MeV to $\mu = \mu_{CEP} = 293.6$ MeV. Chiral symmetry restoration occurs earlier than the deconfinement transition in this region of the phase diagram. Thus we are finding a quarkyonic phase like region of confinement with chiral symmetry in our PQMVT model calculations with polynomial choice for Polyakov loop potential.

The temperature variation of thermodynamic observables namely pressure, energy density, entropy density at three different chemical potentials (zero, μ_{CEP} and $\mu > \mu_{CEP}$) has been shown in PQMVT model. Due to the proper accounting of appropriately renormalized fermionic vacuum fluctuations, the pressure ,entropy density and energy density variations at $\mu = 0$ turn out to be a smoother function of temperature in PQMVT model when it is compared with corresponding curves in PQM model calculation. The temperature variations of the interaction measure, speed of sound, $p(T)/\epsilon(T)$ and specific heat, have been calculated in PQMVT model and QMVT (Quark Meson model with vacuum term) model and these results have been compared with the corresponding results in the PQM and QM model calculations. In PQMVT model, the calculated temperature variation of interaction measure at $\mu = 0$ for polynomial choice of Polyakov loop potential, shows a noticeable rightward shift. Again we find that the presence of fermionic vacuum contribution in effective potential leads to the smoother variation of the thermodynamic quantities. Finally we have shown the results of the temperature variations of baryon number density and quark number susceptibility at different chemical potentials in PQMVT model calculations.

Chapter 4

Meson Masses and Mixing Angles in 2+1 Flavor Polyakov Quark Meson Sigma Model and Symmetry Restoration Effects

In order to calculate the properties of mesons in hot and dense medium, several investigations have been done in the two and three flavor Nambu-Jona-Lasinio (NJL), Polyakov-Nambu-Jona-Lasinio (PNJL) models (e.g. [92, 93, 169, 170]) and also in the $SU(2)$ and $SU(3)$ versions of linear sigma model (e.g. [63,69,171]). Since chiral symmetry restoration is signaled by parity doubling, these studies look for the patterns of emerging convergence in the masses of the chiral partners in pseudoscalar (π, η, η', K) and scalar mesons (σ, a_0, f_0, κ). It is a common knowledge that the basic QCD Lagrangian has the global $SU_{R+L}(3) \times SU_{R-L}(3) \times U_A(1)$ symmetry. Different patterns of spontaneous as well as explicit breaking of $SU_V(3) \times SU_A(3)$, have been discussed by Lenaghan et al. [55] in the ambit of $SU(3)$ linear sigma model. Schaefer et al. enlarged the linear sigma model with the inclusion of quarks [64] and then they studied in the 2+1 flavor breaking scenario, the consequences of $SU(3)$ chiral symmetry restoration for scalar and pseudoscalar meson masses and mixing angles, in the presence as well as the absence of $U_A(1)$ axial symmetry, as the temperature is increased through the phase transition temperature. The $U_A(1)$ axial symmetry does not exist at the quantum level and as shown by 't Hooft [124, 125], it gets explicitly broken to $Z_A(N_f)$ by the instanton effects. The $U_A(1)$ anomaly does not let the η' meson remain massless Goldstone boson in the chiral limit by giving it a mass of about 1 GeV. This happens due to flavor mixing, a phenomenon that lifts the degeneracy between the π and η' which otherwise would have been degenerate with π in $U(3)$ even if the explicit chiral symmetry breaking is present. There is large violation in the Okubo-Zweig-Iizuka rule for both pseudoscalar and scalar mesons and ideal mixing is not achieved because of strong flavor mixing between nonstrange and strange flavor components of the mesons [93]. Hence $U_A(1)$ restoration will have important observable effects on scalar and pseudoscalar meson masses as well as the mixing angles.

In a three flavor PNJL model calculation, Costa and collaborators [93] have discussed in detail how the inclusion of Polyakov loop in the NJL model, affects the results of meson mass and mixing angle calculations. However in an earlier paper, they have pointed out that the description of the η' in the NJL model has some problem [169]. The NJL model does not confine and the meson degrees of freedom are generated in the model by some prescription. The polarization function for the meson gets an imaginary part above the $\bar{q}q$ threshold, hence η' becomes unbound completely in the model soon after the temperature is raised from zero. Thus η' in the NJL model is not a well defined quantity [172]. Schaefer et al. [64, 97, 98] have also made an elaborate study of meson masses and mixing angles with and without $U_A(1)$ axial anomaly in the 2+1 flavor quark meson linear sigma model where the mesons are included in the Lagrangian from the very outset and the $U_A(1)$ breaking 't Hooft coupling term is constant. The behavior of the scalar and pseudoscalar mixing angles in their calculation is opposite to what has been reported in the calculation by Costa et al. [93]. It is worthwhile and important to investigate the influence of Polyakov loop on meson mass and mixing angle calculations in scalar and pseudoscalar sector, in the framework of generalized 2+1 flavor quark meson linear sigma model enlarged with the inclusion of the Polyakov loop [98–100]. Since we are lacking in the experimental information on the behavior of mass and mixing angle observables in the medium, a comparative study of these quantities in different models and circumstances becomes all the more desirable. We will be investigating how the inclusion of Polyakov loop, qualitatively and quantitatively affects the convergence of the masses of chiral partners, when the parity doubling takes place as the temperature is increased through T_c and the partial restoration of chiral symmetry is achieved. We will also be studying the effect of Polyakov loop on the interplay of $SU_A(3)$ chiral symmetry and $U_A(1)$ symmetry restoration.

The arrangement of this chapter is as follows. In Sec.4.1 we have given the formulation of the model. The description of grand potential in the mean field approach has been presented in Sec. 4.2. We have derived the modification of meson masses due to the $\bar{q}q$ contribution in the presence of Polyakov loop in Sec.4.3 where the formulae for meson masses and mixing angles have been discussed. In Sec.4.4, we will be discussing the numerical results and plots for understanding and analyzing the effect of Polyakov loop on chiral symmetry restoration. Summary is presented in the last Sec.4.5.

4.1 Model Formulation

We will be working in the generalized three flavor quark meson linear sigma model which has been combined with the Polyakov loop potential [98–100]. In this model, quarks coming in three flavor are coupled to the $SU_V(3) \times SU_A(3)$ symmetric mesonic fields together with spatially constant temporal gauge field represented by Polyakov loop potential. Polyakov loop field $\Phi(\vec{x})$ is defined as the thermal expectation value of color trace of Wilson loop in temporal direction

$$\Phi = \frac{1}{N_c}\langle \mathrm{Tr}_c L\rangle_\beta, \qquad\qquad \Phi^* = \frac{1}{N_c}\langle \mathrm{Tr}_c L^\dagger\rangle_\beta \tag{4.1}$$

where L(x) is a matrix in the fundamental representation of the $SU_c(3)$ color gauge group.

$$L(\vec{x}) = \mathcal{P}\mathrm{exp}\left[i\int_0^\beta d\tau A_0(\vec{x},\tau)\right] \tag{4.2}$$

Here $\mathcal{P}$ is path ordering, A_0 is the temporal component of Euclidean vector field and $\beta = T^{-1}$ [29].

The model Lagrangian is written in terms of quarks, mesons, couplings and Polyakov loop potential $\mathcal{U}(\Phi, \Phi^*, T)$.

$$\mathcal{L}_{PQMS} = \mathcal{L}_{QMS} - \mathcal{U}(\Phi, \Phi^*, T) \tag{4.3}$$

where the Lagrangian in quark meson linear sigma model

$$\mathcal{L}_{QMS} = \bar{q_f}(i\gamma^\mu D_\mu - g\, T_a(\sigma_a + i\gamma_5\pi_a))q_f + \mathcal{L}_m \tag{4.4}$$

The coupling of quarks with the uniform temporal background gauge field is effected by the following replacement $D_\mu = \partial_\mu - iA_\mu$ and $A_\mu = \delta_{\mu 0}A_0$ (Polyakov gauge), where $A_\mu = g_s A^a_\mu \lambda^a/2$. g_s is the $SU_c(3)$ gauge coupling. λ_a are Gell-Mann matrices in the color space, a runs from $1\cdots 8$. $q_f = (u,d,s)^T$ denotes the quarks coming in three flavors and three colors. g is the flavor blind Yukawa coupling that couples the three flavor of quarks with nine mesons in the scalar ($\sigma_a, J^P = 0^+$) and pseudoscalar ($\pi_a, J^P = 0^-$) sectors.

The quarks have no intrinsic mass but become massive after spontaneous chiral symmetry breaking because of nonvanishing vacuum expectation value of the chiral condensate. The mesonic part of the Lagrangian has the following form

$$\begin{aligned}\mathcal{L}_m &= \mathrm{Tr}\left(\partial_\mu M^\dagger \partial^\mu M\right) - m^2\mathrm{Tr}(M^\dagger M) - \lambda_1\left[\mathrm{Tr}(M^\dagger M)\right]^2 \\ &\quad -\lambda_2 \mathrm{Tr}\left(M^\dagger M\right)^2 + c[det(M) + det(M^\dagger)] \\ &\quad +\mathrm{Tr}\left[H(M+M^\dagger)\right].\end{aligned} \tag{4.5}$$

The chiral field M is a 3×3 complex matrix comprising of the nine scalars σ_a and the nine pseudoscalar π_a mesons.

$$M = T_a \xi_a = T_a(\sigma_a + i\pi_a) \tag{4.6}$$

Here T_a represent 9 generators of $U(3)$ with $T_a = \frac{\lambda_a}{2}$. $a = 0, 1 \ldots\ 8$. λ_a are standard Gell-Mann matrices with $\lambda_0 = \sqrt{\frac{2}{3}}\,\mathbf{1}$. The generators follow $U(3)$ algebra $[T_a, T_b] = i f_{abc} T_c$ and $\{T_a, T_b\} = d_{abc} T_c$ where f_{abc} and d_{abc} are standard antisymmetric and symmetric structure constants respectively with $f_{ab0} = 0$ and $d_{ab0} = \sqrt{\frac{2}{3}}\,\mathbf{1}\ \delta_{\mathbf{ab}}$ and matrices are normalized as $\mathrm{Tr}(T_a T_b) = \frac{\delta_{ab}}{2}$.

The $SU_L(3) \times SU_R(3)$ chiral symmetry is explicitly broken by the explicit symmetry breaking term

$$H = T_a h_a \tag{4.7}$$

Here H is a 3×3 matrix with nine external parameters. The ξ field picks up the nonzero vacuum expectation value, $\bar{\xi}$ due to the spontaneous breakdown of the chiral symmetry. Since $\bar{\xi}$ must have the quantum numbers of the vacuum, explicit breakdown of the chiral symmetry is only possible with three nonzero parameters h_0, h_3 and h_8. We are neglecting isospin symmetry breaking hence we choose $h_0,\ h_8 \neq 0$. This leads to the $2 + 1$ flavor symmetry breaking scenario with nonzero condensates $\bar{\sigma_0}$ and $\bar{\sigma_8}$.

Apart from h_0 and h_8, the other parameters in the model are five in number. These are the squared tree-level mass of the meson fields m^2, quartic coupling constants λ_1 and λ_2, a Yukawa coupling g and a cubic coupling constant c which models the $U_A(1)$ axial anomaly of the QCD vacuum.

Since it is broken by the quantum effects, the $U_A(1)$ axial which otherwise is a symmetry of the classical Lagrangian, becomes anomalous [173] and gives large mass to η' meson ($m_{\eta'} = 940$ MeV). In the absence of $U_A(1)$ anomaly, η' meson would have been the ninth pseudoscalar Goldstone boson, resulting due to the spontaneous break down of the chiral $U_A(3)$ symmetry. The entire pseudoscalar nonet corresponding to spontaneously broken $U_A(3)$, would consist of the three π, four K, η and η' mesons, which are the massless pure Goldstone modes when $H = 0$ and they become pseudo Goldstone modes after acquiring finite mass due to nonzero H in different symmetry breaking scenarios. The particles coming from octet (a_0, f_0, κ) and singlet (σ) representations of $SU_V(3)$ group, constitute scalar nonet (σ, a_0, f_0, κ). In order to study the chiral symmetry restoration at high temperatures, we will be investigating the trend of convergence in the masses of chiral partners occurring in pseudoscalar (π, η, η', K) and scalar (σ, a_0, f_0, κ) nonets, in the $2+1$ flavor symmetry breaking scenario.

4.1.1 Choice of Potentials for the Polyakov Loop

The effective potential $\mathcal{U}\left(\Phi, \Phi^*, T\right)$ is constructed such that it reproduces thermodynamics of pure glue theory on the lattice for temperatures upto about twice the deconfinement phase transition temperature. At much higher temperatures, the transverse gluons become effective degrees of freedom, hence the construction of effective potential in terms of the Polyakov loop potential is not reliable [80, 92].

At low temperatures, the effective potential $\mathcal{U}\left(\Phi, \Phi^*, T\right)$ has only one minimum at $\Phi = 0$ in the confined phase. Above the critical temperature for deconfinement transition, $\Phi = 0$ becomes metastable local minimum and now, the effective potential has three degenerate global minima at $\Phi \neq 0$ due to the spontaneous breakdown of the $Z(3)$ center symmetry.

In this work, we use the following two choices of the effective potential. The first choice is based on the polynomial expansion in terms of Polyakov loop order parameter Φ and is given [80] as

$$\begin{aligned} \frac{\mathcal{U}_{\mathrm{pol}}\left(\Phi, \Phi^*, T\right)}{T^4} &= -\frac{b_2}{4}\left(|\Phi|^2 + |\Phi^*|^2\right) - \frac{b_3}{6}(\Phi^3 + \Phi^{*3}) \\ &\quad + \frac{b_4}{16}\left(|\Phi|^2 + |\Phi^*|^2\right)^2 \end{aligned} \tag{4.8}$$

The second term that is the sum of Φ^3 and Φ^{*3} terms, causes the three degenerate vacua above the deconfinement phase transition. The potential parameters are adjusted according to the pure gauge lattice data such that the equation of state and Polyakov loop expectation values are reproduced. The temperature dependent coefficient $b_2(T)$ governs the confinement-deconfinement phase transition and is given by

$$b_2(T) = a_0 + a_1\left(\frac{T_0}{T}\right) + a_2\left(\frac{T_0}{T}\right)^2 + a_3\left(\frac{T_0}{T}\right)^3 . \tag{4.9}$$

The other parameters have the following value

$$a_0 = 6.75\ , \quad a_1 = -1.95\ , \quad a_2 = 2.625\ ,$$
$$a_3 = -7.44, \quad b_3 = 0.75\ , \quad b_4 = 7.5\ .$$

The other choice of effective potential as given in ref. [81], has the logarithmic form. The results produced by this potential are known to be fitted well to lattice results.

$$\begin{aligned} \frac{\mathcal{U}_{\log}\left(\Phi, \Phi^*, T\right)}{T^4} &= -\frac{a\left(T\right)}{2}\Phi^*\Phi + b(T)\ln[1 - 6\Phi^*\Phi \\ &\quad +4(\Phi^{*3} + \Phi^3) - 3(\Phi^*\Phi)^2] \end{aligned} \tag{4.10}$$

where the temperature dependent coefficients are as follow

$$a(T) = a_0 + a_1\left(\frac{T_0}{T}\right) + a_2\left(\frac{T_0}{T}\right)^2 \quad b(T) = b_3\left(\frac{T_0}{T}\right)^3 . \tag{4.11}$$

The critical temperature for deconfinement phase transition $T_0 = 270$ MeV is fixed for pure gauge sector. The parameters of Eq.(4.10) are

$$a_0 = 3.51\ , \qquad a_1 = -2.47\ ,$$
$$a_2 = 15.2\ , \qquad b_3 = -1.75$$

Both effective potential fits reproduce equally well the equation of state and the Polyakov loop expectation value.

4.2 Grand Potential in the Mean-Field Approach

The thermodynamics of changing numbers of particles and antiparticles is governed by grand canonical partition function. We are considering a spatially uniform system in thermal equilibrium at finite temperature T and quark chemical potential $\mu_f (f = u, d, s)$. The partition function is written as the path integral over quark/antiquark and meson fields [64]

$$\begin{aligned} \mathcal{Z} &= \mathrm{Tr}\exp[-\beta(\hat{\mathcal{H}} - \sum_{f=u,d,s} \mu_f \hat{\mathcal{N}}_f)] \\ &= \int \prod_a \mathcal{D}\sigma_a \mathcal{D}\pi_a \int \mathcal{D}q\mathcal{D}\bar{q} \exp\Big[- \int_0^\beta d\tau \int_V d^3x \\ & \quad \Big(\mathcal{L}^{\mathcal{E}}_{\mathcal{QMS}} + \sum_{f=u,d,s} \mu_f \bar{q}_f \gamma^0 q_f\Big)\Big]. \end{aligned} \tag{4.12}$$

where V is the three dimensional volume of the system, and $\beta = \frac{1}{T}$. For three quark flavors, in general, the three quark chemical potential are different. In this work, we assume that $SU_V(2)$ symmetry is preserved and neglect the small difference in masses of u and d quarks. Thus the quark chemical potential for u and d quarks become equal $\mu_x = \mu_u = \mu_d$. The strange quark chemical potential is $\mu_y = \mu_s$. Further we consider symmetric quark matter and net baryon number to be zero.

The partition function for the $SU(3)$ version of the linear sigma model with or without quarks can be evaluated by the more advanced many-body resummation techniques such as the self consistent Hartree approximation in the Cornwall, Jackiw and Tomboulis [55, 174] formalism or the so called optimized perturbation theory [57] in its improved version [59–61]. However the predictive power of these methods depends on how they are implemented in different approximation schemes.

In the simple mean field approximation, one does not encounter various problems of the more advanced many-body resummation techniques. In our work, the partition function has been evaluated in the mean-field approximation [63,64,97]. We replace meson field by their expectation values $\langle\Phi\rangle = T_0\bar{\sigma}_0 + T_8\bar{\sigma}_8$ and neglect both thermal as well as quantum fluctuations of meson fields while quarks and antiquarks are retained as quantum field. Now following the standard procedure as given in Refs. [79,80,96,115] one can obtain the expression of grand potential as sum of pure gauge field contribution $\mathcal{U}(\Phi, \Phi^*, T)$, meson contribution and quark/antiquark contribution evaluated in the presence of the Polyakov loop,

$$\begin{aligned} \Omega(T,\mu) = -\frac{T\ln Z}{V} &= U(\sigma_0,\sigma_8) + \mathcal{U}(\Phi,\Phi^*,T) \\ &+\Omega_{\bar{q}q}(T,\mu) \end{aligned} \tag{4.13}$$

In order to study 2 + 1 flavor case, one performs following basis transformation of condensates and external fields from original singlet octet (0, 8) basis to nonstrange strange basis (x, y).

$$\sigma_x = \sqrt{\frac{2}{3}}\bar{\sigma}_0 + \frac{1}{\sqrt{3}}\bar{\sigma}_8, \tag{4.14}$$

$$\sigma_y = \frac{1}{\sqrt{3}}\bar{\sigma}_0 - \sqrt{\frac{2}{3}}\bar{\sigma}_8. \tag{4.15}$$

Similar expressions exist for writing the external fields (h_x, h_y) in terms of (h_0, h_8). Thus the nonstrange and strange quark/antiquark decouple and the quark masses become

$$m_x = g\frac{\sigma_x}{2}, \qquad m_y = g\frac{\sigma_y}{\sqrt{2}} \tag{4.16}$$

Quarks become massive in symmetry broken phase because of non zero vacuum expectation values of the condensates.

The mesonic potential in the nonstrange-strange basis reads,

$$\begin{aligned} U(\sigma_x,\sigma_y) &= \frac{m^2}{2}\left(\sigma_x^2+\sigma_y^2\right) - h_x\sigma_x - h_y\sigma_y - \frac{c}{2\sqrt{2}}\sigma_x^2\sigma_y \\ &+\frac{\lambda_1}{2}\sigma_x^2\sigma_y^2 + \frac{1}{8}\left(2\lambda_1+\lambda_2\right)\sigma_x^4 \\ &+\frac{1}{8}\left(2\lambda_1+2\lambda_2\right)\sigma_y^4 \ , \end{aligned} \tag{4.17}$$

	C[MeV]	m^2 $[MeV^2]$	λ_1	λ_2	h_x $[MeV^3]$	h_y $[MeV^3]$
W/$U_A(1)$	4807.84	$(342.52)^2$	1.40	46.48	$(120.73)^3$	$(336.41)^3$
W/o$U_A(1)$	0	$-(189.85)^2$	-17.01	82.47	$(120.73)^3$	$(336.41)^3$

Table 4.1: parameters for $m_\sigma = 600$ MeV with and without $U_A(1)$ axial anomaly term.

The chiral part of the Polyakov loop augmented quark meson linear sigma (PQMS) model has the six input parameters and therefore require six known quantities as input. In general m_π, m_K, the pion and kaon decay constant f_π, f_K, mass square of η, η' and m_σ are used to fix these parameters. The parameters are fitted such that in vacuum the model produces observed pion mass 138 MeV. In the present work we are using the set of parameters for sigma mass $m_\sigma = 600$ MeV. The parameters used in this work, taken from [64], are shown in Table 4.1.

Finally the quark/antiquark Polyakov loop contribution reads,

$$\Omega_{\bar{q}q}(T,\mu) = -2T \sum_{f=u,d,s} \int \frac{d^3p}{(2\pi)^3} \left[\ln g_f^+ + \ln g_f^-\right] \tag{4.18}$$

We define g_f^+ and g_f^- after taking trace over color space

$$g_f^+ = \left[1 + 3\Phi e^{-E_f^+/T} + 3\Phi^* e^{-2E_f^+/T} + e^{-3E_f^+/T}\right] \tag{4.19}$$

$$g_f^- = \left[1 + 3\Phi^* e^{-E_f^-/T} + 3\Phi e^{-2E_f^-/T} + e^{-3E_f^-/T}\right] \tag{4.20}$$

Here we use the notation $E_f^\pm = E_f \mp \mu$ and E_f is the flavor dependent single particle energy of quark/antiquark.

$$E_f = \sqrt{p^2 + {m_f}^2} \tag{4.21}$$

m_f is flavor dependent quark mass and is function of condensates σ_0 and σ_8.

One can very easily notice from equations (4.19) and (4.20) that the role of quarks and antiquarks as well as that of the Polyakov loop and its conjugate can be interchanged by the transformation $\mu \rightarrow -\mu$. Confinement is the very interesting feature of the QCD and the PQMS model describes this behavior qualitatively. The Polyakov loop is order parameter for confinement-deconfinement phase transition. In the confined phase $\Phi = 0$. It can also be noticed from the grand potential that one and two quark state contributions are vanishing. Only the three quark states contribute. In this way the PQMS model qualitatively mimics confinement of quark/antiquark within three quark color singlet states [84].

One can get the quark condensates σ_x, σ_y and the Polyakov loop expectation values Φ, Φ^* by searching the global minima of the grand potential for a given value of temperature T and chemical potential μ.

$$\frac{\partial \Omega}{\partial \sigma_x} = \frac{\partial \Omega}{\partial \sigma_y} = \frac{\partial \Omega}{\partial \Phi} = \frac{\partial \Omega}{\partial \Phi^*}\bigg|_{\sigma_x=\bar{\sigma}_x, \sigma_y=\bar{\sigma}_y, \Phi=\bar{\Phi}, \Phi^*=\bar{\Phi}^*} = 0 \ . \tag{4.22}$$

In this work we are always considering the $\mu = 0$ case.

4.3 Meson masses and Mixing angles

The curvature of grand potential Eq.(4.13) at the global minimum determines scalar and pseudoscalar meson masses.

$$m^2_{\alpha,ab} = \frac{\partial^2 \Omega(T,\mu)}{\partial \xi_{\alpha,a} \partial \xi_{\alpha,b}}\bigg|_{min} \tag{4.23}$$

where subscript $\alpha =$ s, p; s stands for scalar and p stands for pseudoscalar meson and a, $b = 0 \cdots 8$. We note that the Polyakov loop decouples from the mesonic sector at T=0 and the meson masses do not receive contribution from quark/antiquark in vacuum and hence meson masses are governed by mesonic potential only. The mesonic contribution to the meson masses is summarized in Table 4.2. The diagonalization of (0 - 8) component of mass matrix gives masses of σ and f_0 mesons in scalar sector and masses of η' and η in pseudoscalar sector. The scalar mixing angle θ_s and pseudoscalar mixing angle θ_p are

	Scalar Meson Sector
$m^2_{a_0}$	$m^2 + \lambda_1(x^2+y^2) + \frac{3\lambda_2}{2}x^2 + \frac{\sqrt{2}c}{2}y$
m^2_{κ}	$m^2 + \lambda_1(x^2+y^2) + \frac{\lambda_2}{2}(x^2+\sqrt{2}xy+2y^2) + \frac{c}{2}x$
$m^2_{s,00}$	$m^2 + \frac{\lambda_1}{3}(7x^2+4\sqrt{2}xy+5y^2) + \lambda_2(x^2+y^2) - \frac{\sqrt{2}c}{3}(\sqrt{2}x+y)$
$m^2_{s,88}$	$m^2 + \frac{\lambda_1}{3}(5x^2-4\sqrt{2}xy+7y^2) + \lambda_2(\frac{x^2}{2}+2y^2) + \frac{\sqrt{2}c}{3}(\sqrt{2}x-\frac{y}{2})$
$m^2_{s,08}$	$\frac{2\lambda_1}{3}(\sqrt{2}x^2-xy-\sqrt{2}y^2) + \sqrt{2}\lambda_2(\frac{x^2}{2}-y^2) + \frac{c}{3\sqrt{2}}(x-\sqrt{2}y)$
m^2_{σ}	$m^2_{s,00}\cos^2\theta_s + m^2_{s,88}\sin^2\theta_s + 2m^2_{s,08}\sin\theta_s\cos\theta_s$
$m^2_{f_0}$	$m^2_{s,00}\sin^2\theta_s + m^2_{s,88}\cos^2\theta_s - 2m^2_{s,08}\sin\theta_s\cos\theta_s$
$m^2_{\sigma_{NS}}$	$\frac{1}{3}(2m^2_{s,00} + m^2_{s,88} + 2\sqrt{2}m^2_{s,08})$
$m^2_{\sigma_S}$	$\frac{1}{3}(m^2_{s,00} + 2m^2_{s,88} - 2\sqrt{2}m^2_{s,08})$
	Pseudoscalar Meson Sector
m^2_{π}	$m^2 + \lambda_1(x^2+y^2) + \frac{\lambda_2}{2}x^2 - \frac{\sqrt{2}c}{2}y$
m^2_{K}	$m^2 + \lambda_1(x^2+y^2) + \frac{\lambda_2}{2}(x^2-\sqrt{2}xy+2y^2) - \frac{c}{2}x$
$m^2_{p,00}$	$m^2 + \lambda_1(x^2+y^2) + \frac{\lambda_2}{3}(x^2+y^2) + \frac{c}{3}(2x+\sqrt{2}y)$
$m^2_{p,88}$	$m^2 + \lambda_1(x^2+y^2) + \frac{\lambda_2}{6}(x^2+4y^2) - \frac{c}{6}(4x-\sqrt{2}y)$
$m^2_{p,08}$	$\frac{\sqrt{2}\lambda_2}{6}(x^2-2y^2) - \frac{c}{6}(\sqrt{2}x-2y)$
$m^2_{\eta'}$	$m^2_{p,00}\cos^2\theta_p + m^2_{p,88}\sin^2\theta_p + 2m^2_{p,08}\sin\theta_p\cos\theta_p$
m^2_{η}	$m^2_{p,00}\sin^2\theta_p + m^2_{p,88}\cos^2\theta_p - 2m^2_{p,08}\sin\theta_p\cos\theta_p$
$m^2_{\eta_{NS}}$	$\frac{1}{3}(2m^2_{p,00} + m^2_{p,88} + 2\sqrt{2}m^2_{p,08})$
$m^2_{\eta_S}$	$\frac{1}{3}(m^2_{p,00} + 2m^2_{p,88} - 2\sqrt{2}m^2_{p,08})$

Table 4.2: The mesonic contribution of squared masses of scalar and pseudoscalar mesons appear in nonstrange-strange basis. In this table x denotes σ_x and y denotes σ_y. The masses of nonstrange σ_{NS}, strange σ_S, nonstrange η_{NS} and strange η_S mesons are given in the last two rows of the respective cases.

given by,

$$\tan 2\theta_\alpha = \Big(\frac{2m^2_{\alpha,08}}{m^2_{\alpha,00} - m^2_{\alpha,88}}\Big) \tag{4.24}$$

Here α stands for scalar and pseudoscalar field. The detail expressions for masses and mixing angles are given in ref. [55,64]. The meson masses are further modified in medium at finite temperature by the quark contributions in the grand potential. In order to calculate the second derivative Eq.(4.23) for evaluating the quark contribution in the presence of the Polyakov loop potential, the complete dependence of all scalar and pseudoscalar meson fields Eq.(4.6) has to be taken into account. We have to diagonalize the resulting quark mass matrix. The expression for the meson mass modification due to quark contribution at finite temperature in QMS model, has been evaluated by Schaefer et al. [64] and is given as

$$\begin{aligned} \delta m^2_{\alpha,ab} &= \frac{\partial^2 \Omega_{\bar{q}q}(T,\mu)}{\partial \xi_{\alpha,a} \partial \xi_{\alpha,b}}\Big|_{min} = \nu_c \sum_{f=x,y} \int \frac{d^3p}{(2\pi)^3} \frac{1}{2E_f} \\ & \Big[(a_f^+ + a_f^-)\Big(m^2_{f,ab} - \frac{m^2_{f,a} m^2_{f,b}}{2E_f^2}\Big) \\ & -(b_f^+ + b_f^-)\Big(\frac{m^2_{f,a} m^2_{f,b}}{2E_f T}\Big)\Big] \end{aligned} \tag{4.25}$$

$m^2_{f,a} \equiv \partial m^2_f / \partial \xi_{\alpha,a}$ is the first derivative and $m^2_{f,ab} \equiv \partial m^2_{f,a} / \partial \xi_{\alpha,b}$ is the second derivative of squared quark mass with respect to meson fields $\xi_{\alpha,b}$. The number of internal quark degrees of freedom, $\nu_c = 2N_c = 6$. Here $a_f^{\pm}$ are quark/antiquark occupation numbers; given as

$$a_f^{\pm} = \frac{1}{1 + e^{E^{\pm}/T}} \tag{4.26}$$

and the notations $b_f^{\pm} = a_f^{\pm} - (a_f^{\pm})^2$ stand for particle (+) and antiparticle (−) in quark meson linear sigma model without inclusion of the Polyakov loop.

The expression of mass modification due to quark contribution at finite temperature, will change in the presence of the Polyakov loop. We are obtaining the following formula for the mass modification that results on account of quark contribution in the PQMS model

$$\delta m^2_{\alpha,ab} = \frac{\partial^2 \Omega_{\bar{q}q}(T,\mu)}{\partial \xi_{\alpha,a} \partial \xi_{\alpha,b}}\Big|_{min} = 3 \sum_{f=x,y} \int \frac{d^3p}{(2\pi)^3} \frac{1}{E_f}$$
$$\Big[(A_f^+ + A_f^-)\Big(m^2_{f,ab} - \frac{m^2_{f,a} m^2_{f,b}}{2E_f^2}\Big)$$
$$+(B_f^+ + B_f^-)\Big(\frac{m^2_{f,a} m^2_{f,b}}{2E_f T}\Big)\Big] \tag{4.27}$$

The notations $A_f^{\pm}$ and $B_f^{\pm}$ have the following definitions

$$A_f^+ = \frac{\Phi e^{-E_f^+/T} + 2\Phi^* e^{-2E_f^+/T} + e^{-3E_f^+/T}}{g_f^+} \tag{4.28}$$

$$A_f^- = \frac{\Phi^* e^{-E_f^-/T} + 2\Phi e^{-2E_f^-/T} + e^{-3E_f^-/T}}{g_f^-} \tag{4.29}$$

and $B_f^{\pm} = 3(A_f^{\pm})^2 - C_f^{\pm}$, where we again define

$$C_f^+ = \frac{\Phi e^{-E_f^+/T} + 4\Phi^* e^{-2E_f^+/T} + 3e^{-3E_f^+/T}}{g_f^+} \tag{4.30}$$

$$C_f^- = \frac{\Phi^* e^{-E_f^-/T} + 4\Phi e^{-2E_f^-/T} + 3e^{-3E_f^-/T}}{g_f^-} \tag{4.31}$$

The squared quark mass derivatives evaluated at minimum which were originally derived in ref. [64], are collected in Table 4.3. The inclusion of Polyakov loop in QMS model does not make any change in these equations.

4.4 Effect of The Polyakov Loop on The Restoration of Chiral Symmetry

We are presenting the result of our calculation for estimating the effect of the Polyakov loop potential on the restoration of chiral symmetry when it is included in the 2+1 flavor quark meson linear sigma model at finite temperature and zero chemical potential with and without axial $U_A(1)$ breaking. We have considered the two different ansatzs for the Polyakov loop potential namely the polynomial potential and logarithmic potential and compared the results with the existing calculations in the quark meson linear sigma model [64]. The interplay of the effect of $U_A(1)$ axial restoration and chiral symmetry restoration in the presence of the Polyakov loop potential has been shown through the temperature variation of strange, nonstrange chiral condensates, meson masses and mixing angles. The $U_A(1)$ axial breaking term has been kept constant throughout the investigation. The value of Yukawa coupling g has been fixed from the nonstrange constituent quark mass $m_q = 300$ MeV and is equal to 6.5. This predicts the strange quark mass $m_s \backsimeq 433$ MeV.

		$m^2_{x,a}m^2_{x,b}/g^4$	$m^2_{x,ab}/g^2$	$m^2_{y,a}m^2_{y,b}/g^4$	$m^2_{y,ab}/g^2$
σ_0	σ_0	$\frac{1}{3}\sigma_x^2$	$\frac{2}{3}$	$\frac{1}{3}\sigma_y^2$	$\frac{1}{3}$
σ_1	σ_1	$\frac{1}{2}\sigma_x^2$	1	0	0
σ_4	σ_4	0	$\sigma_x\frac{\sigma_x+\sqrt{2}\sigma_y}{\sigma_x^2-2\sigma_y^2}$	0	$\sigma_y\frac{\sqrt{2}\sigma_x+2\sigma_y}{2\sigma_y^2-\sigma_x^2}$
σ_8	σ_8	$\frac{1}{6}\sigma_x^2$	$\frac{1}{3}$	$\frac{2}{3}\sigma_y^2$	$\frac{2}{3}$
σ_0	σ_8	$\frac{\sqrt{2}}{6}\sigma_x^2$	$\frac{\sqrt{2}}{3}$	$-\frac{\sqrt{2}}{3}\sigma_y^2$	$-\frac{\sqrt{2}}{3}$
π_0	π_0	0	$\frac{2}{3}$	0	$\frac{1}{3}$
π_1	π_1	0	1	0	0
π_4	π_4	0	$\sigma_x\frac{\sigma_x-\sqrt{2}\sigma_y}{\sigma_x^2-2\sigma_y^2}$	0	$\sigma_y\frac{\sqrt{2}\sigma_x-2\sigma_y}{\sigma_x^2-2\sigma_y^2}$
π_8	π_8	0	$\frac{1}{3}$	0	$\frac{2}{3}$
π_0	π_8	0	$\frac{\sqrt{2}}{3}$	0	$-\frac{\sqrt{2}}{3}$

Table 4.3: First and second derivative of squared quark mass in nonstrange-strange basis with respect to meson fields are evaluated at minimum. Sum over two light flavors, denoted by symbol x, are in third and fourth columns. The last two columns have only strange quark mass flavor denoted by the symbol y.

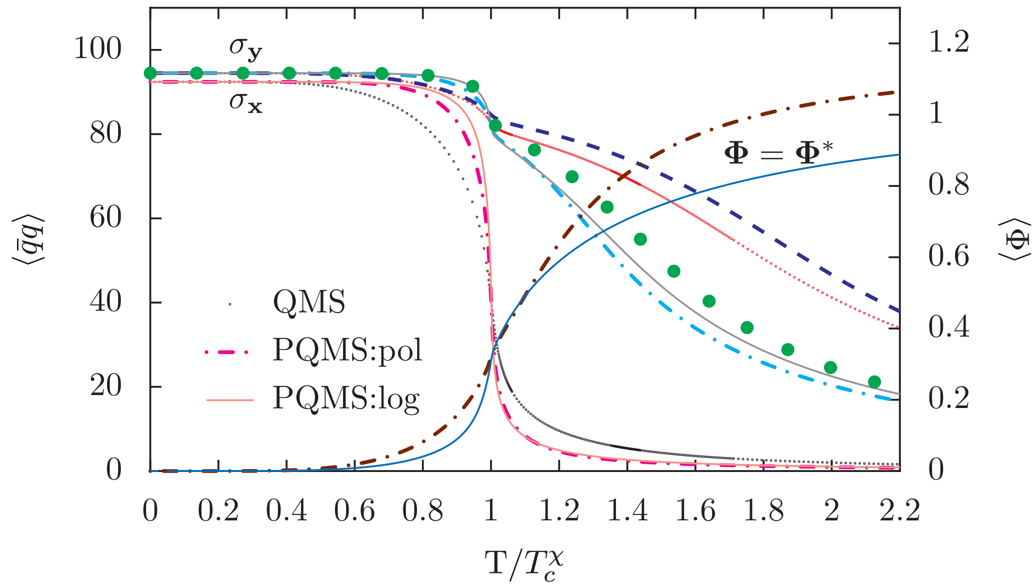

Figure 4.1: The variation of nonstrange σ_x, strange σ_y condensates with respect to the relative temperature scale (T/T_c^χ) at zero chemical potential ($\mu = 0$) in the QMS model and PQMS models with polynomial and logarithmic potentials for the Polyakov loop is shown. The lines with continuous dots represent the variation in the QMS model, while the dashed-dotted lines show the variation in PQMS:pol model and the solid lines are the variations in the PQMS:log model. The line with the big solid dots shows the σ_y variation in the PQMS:log model, while the dark dashed line shows the pure QMS model results when anomaly is absent, i.e. $c = 0$. The expectation value of the Polyakov loop $\langle\Phi\rangle$, in PQMS:pol and PQMS:log model is shown in the right plots.

4.4.1 Condensates and the Polyakov Loop

The solutions of the coupled gap equations, Eq.(4.22) determine the nature of chiral and deconfinement phase transition through the temperature and chemical potential dependence of nonstrange and strange condensates (σ_x and σ_y) and the expectation value of the Polyakov loop ($\langle\Phi\rangle$ and $\langle\Phi^*\rangle$). The temperature variation of σ_x, σ_y and $\langle\Phi\rangle$ in mean-field approximation, at zero chemical potential in the PQMS models with the polynomial

	QMS	PQMS:pol	PQMS:log
T_c^χ (MeV)	146	204	206
T_s^χ (MeV)	248	262	274
T_c^Φ (MeV)	–	204	206

Table 4.4: The characteristic temperature (pseudocritical temperature) for the chiral transition in the nonstrange sector T_c^χ, strange sector T_s^χ and confinement-deconfinement transition T_c^Φ, in the QMS, PQMS:log and PQMS:pol models.

Polyakov loop potential Eq.(4.8) (PQMS:pol) and the logarithmic Polyakov loop potential Eq.(4.10) (PQMS:log) is shown in Fig4.1. We have also plotted the strange and non-strange condensate in QMS model to compare and investigate the effect of the Polyakov loop potential inclusion on chiral symmetry restoration trend reflected through masses and mixing angles of mesonic excitations. The characteristic temperatures (pseudocritical temperature) for the confinement - deconfinement transition T_c^Φ, the chiral transition in the nonstrange sector T_c^χ and strange sector T_s^χ are defined through the inflection point of $\langle\Phi\rangle$, σ_x, and σ_y. We note that the $\langle\Phi\rangle = \langle\Phi^*\rangle$ at zero chemical potential. The numerical value of the pseudocritical temperature for various transitions in the QMS model and the PQMS model with the polynomial and the logarithmic potentials for the Polyakov loop has been given in Table 4.4. It is evident from the table that the chiral transition gets shifted to the higher temperatures as a result of the inclusion of the Polyakov loop potential in the QMS model.

We have chosen to compare the results of our calculation in the PQMS model with the corresponding results in the QMS model on a relative temperature scale T/T_c^χ. Such a choice is justified on account of the Ginzburg-Landau effective theory, where absolute comparison of the characteristic temperatures between two models of the same universality class can not be made [93]. The condensates start with fixed values $\sigma_x = 92.4$ MeV and $\sigma_y = 94.5$ MeV at $T = 0$ as shown in Fig4.1. It is known from the lattice simulations that transition from hadronic matter to quark gluon plasma is a analytic and rapid crossover ([39,45]). The Polyakov loop potential inclusion in the QMS models makes the crossover in $SU_L(2)\times SU_R(2)$ sector quite sharp as the nonstrange condensate σ_x changes rapidly in the transition region. The $U_A(1)$ anomaly does not cause any difference in the behavior of nonstrange condensate and σ_x remain unchanged in the presence as well as in the absence of $U_A(1)$ anomaly term. The variation of the strange condensate is lot more smooth on account of the large constituent mass of the strange quark $m_s = 433$ MeV. The Polyakov loop potential inclusion has a strong effect on the strange condensate variation also and generates a significant melting of σ_y in our calculation. The interesting physical consequences of the earlier and significant melting of the strange condensate will be an early emergence of mass degeneration trend in the masses of the chiral partners (K, κ) and (η, f_0) and an early setting up of a $U_A(1)$ restoration trend on reduced temperature scale. In the presence of the $U_A(1)$ anomaly, σ_y temperature variation shows a little more decrease in the respective cases.

Curves starting from the right end of the plot represent the variation of the Polyakov loop expectation value $\langle\Phi\rangle$ on the relative temperature scale at zero chemical potential. Though the thermodynamics of quark gluon plasma reproduced with the Polyakov loop polynomial potential is found to be in agreement with that of lattice simulations, upto twice of the critical temperature ([80,96,99]) at higher temperatures $\langle\Phi\rangle$ increases above unity and this is unphysical. In the improved ansatz, logarithmic potential replaces the higher order terms of Φ and Φ^* in the polynomial potential by the logarithm of Jacobi determinant which results from integrating out six nondiagonal Lie algebra directions while keeping the two diagonal ones [79,81] and thus the logarithmic divergence avoids an expectation value higher than one. This means that the logarithmic potential describes the dynamics of gluons more correctly and effectively. Keeping this in mind, we will be mainly focusing on the discussion of the results in our calculation with the inclusion of the logarithmic Polyakov loop potential, though the curves of the calculation with the

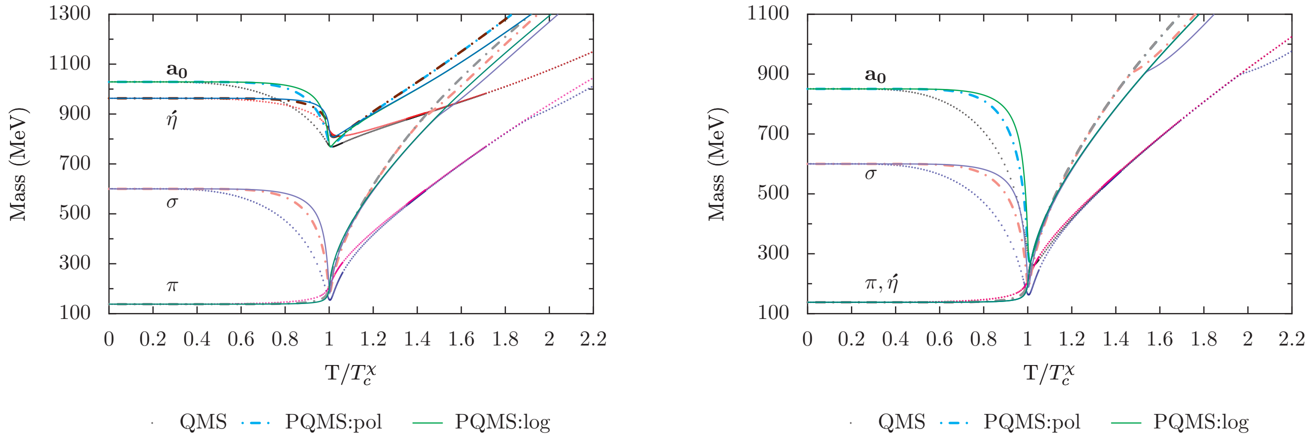

(a) With $U_A(1)$ anomaly term

(b) Without $U_A(1)$ anomaly term

Figure 4.2: The mass variations of the chiral partners as functions of reduced temperature (T/T_c^χ) at zero chemical potential ($\mu = 0$), in the presence of axial $U_A(1)$ breaking term, are plotted for (σ, π) and (a_0, η') in Fig.4.2(a) and the corresponding mass variations, in the absence of the $U_A(1)$ axial breaking term, are plotted in Fig.4.2(b). The dotted line plots are the mass variations in the pure QMS model, dashed- dotted line plots represent the PQMS:pol model results, and the solid line plots are the mass variations in the PQMS:log model.

polynomial Polyakov loop potential will also be shown. The real physical effect of the Polyakov loop potential inclusion in the QMS model on mesonic excitations, will become apparent when the results of our calculation in the PQMS models are compared with the corresponding results in the QMS model.

4.4.2 Meson Mass Variations

We are calculating the masses of the scalar and pseudoscalar mesons at finite temperature in the presence of the Polyakov loop potential in the QMS model. We have collected the vacuum value of all the scalar and pseudoscalar meson masses in Table 4.2. The mass modifications calculated at finite temperature (Eq.4.27) will be added to the vacuum masses of Table 4.2. The mass variations of the chiral partners as functions of reduced temperature, in the presence of axial $U_A(1)$ breaking term, are plotted for (σ, π) and (a_0, η') in Fig.4.2(a) and for (η, f_0) and (K, κ) in Fig.4.3(a), while the corresponding mass variations, in the absence of the $U_A(1)$ axial breaking term, are plotted in Fig.4.2(b) and Fig.4.3(b). Further, since the focus of our investigation is the influence of the Polyakov loop on the effective restoration of symmetries, we will be comparing the mesonic observables below and above T_c^χ.

In Fig.4.2(a), the chiral partners (σ, π) and (a_0, η') become mass degenerate in the close vicinity of reduced temperature $T/T_c^\chi = 1$. The masses of these particles are dominated by the contribution from the nonstrange quarks and a rapid crossover in the nonstrange sector (Fig.4.1) appears as sharper and faster mass degeneration in our calculation in the PQMS model. Thus, the Polyakov loop inclusion in the QMS model makes a sharper mass degeneration as well as faster occurrence of chiral $SU_L(2) \times SU_R(2)$ symmetry restoration transition in the nonstrange sector.

In Fig.4.3(a), the presence of the Polyakov loop potential in the QMS model generates, the similar trend of sharper and faster mass degeneration in the masses of the chiral partners (η,f_0) and (K, κ). Though the mass degeneration of chiral partners (K, κ) with η does not occur at $T/T_c^\chi = 1$, it sets up early in the PQMS models at $T/T_c^\chi = 1.3$, while it occurs at $T/T_c^\chi = 1.5$ in the QMS model. In the PQMS models, the intersection point of the f_0 and η masses, occurs early when $T/T_c^\chi = 1.4$, while in the QMS model it is found at $T/T_c^\chi = 1.7$. This trend of mass degeneration reflects the effect of the Polyakov loop potential on chiral symmetry restoration in the strange sector and it results due to sharper and stronger melting of the strange condensate (Fig.4.1) in the influence of the Polyakov loop potential in the PQMS models.

The $U_A(1)$ breaking generates the mass gap between the two sets of the chiral partners, (σ, π) and (a_0, η'), i.e. $m_\pi = m_\sigma < m_{a_0} = m_{\eta'}$ for $T/T_C^\chi > 1$. This mass gap results due to the opposite sign of the anomaly term ($\sqrt{2}c\sigma_y$) in the scalar and

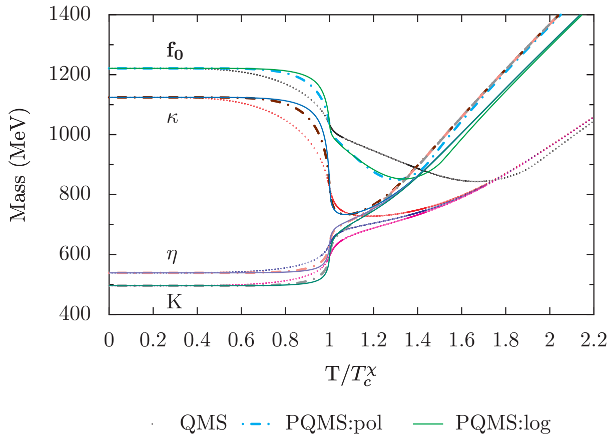

(a) With $U_A(1)$ anomaly term

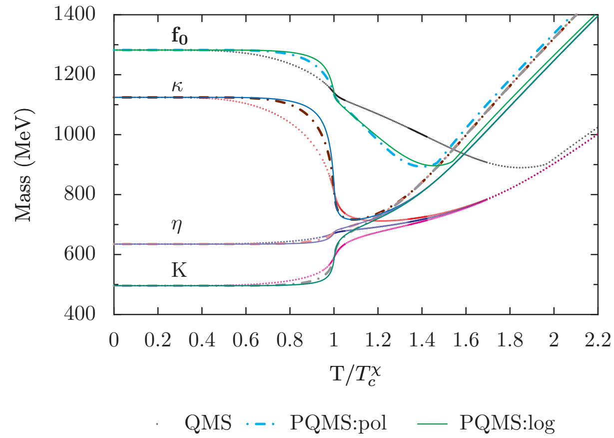

(b) Without $U_A(1)$ anomaly term

Figure 4.3: The mass variations of the chiral partners as functions of reduced temperature (T/T_c^χ) at zero chemical potential ($\mu = 0$), in the presence of axial $U_A(1)$ breaking term, are shown for (η, f_0) and (K, κ) in Fig.4.3(a), and the corresponding mass variations, in the absence of the $U_A(1)$ axial breaking term, are shown in Fig.4.3(b). The dotted line plots are the mass variations in the pure QMS model, dashed-dotted line plots represent the PQMS:pol model results, and the solid line plots are the mass variations in the PQMS:log model.

pseudoscalar meson masses. Hence, it will be reduced due to the melting of the strange order parameter σ_y for the higher values of the reduced temperature $T/T_c^\chi > 1$. Since the melting of the strange condensate is stronger and sharper (Fig.4.1) in the PQMS model, the convergence in the masses of the two sets of chiral partners gets enhanced in these calculations. Thus the inclusion of the Polyakov loop potential in the QMS model also effects an early set up of $U_A(1)$ restoration trend on the reduced temperature scale.

Now we discuss the variations in the masses of chiral partners when the explicit $U_A(1)$ symmetry breaking term has been taken as zero (c=0). We notice in Fig.4.2(b) and Fig.4.3(b), again, the same sharper and faster trend of mass degeneration that we identify as the effect generated by the inclusion of the Polyakov loop potential. The η' meson degenerates with the pion in vacuum and stays the same for all temperatures in Fig.4.2(b) due to the absence of the anomaly term. Further the mass gap between the chiral partners (σ, π) and (a_0, η') becomes zero and all four of the mesons become degenerate at $T/T_c^\chi = 1.0$. The T/T_c^χ numerical value, where the K, κ, and η masses degenerate in different models, is not influenced by the $U_A(1)$ anomaly as expected since the nonstrange condensate does not have any anomaly dependence. Further, in Fig.4.3(b), the intersection point of the f_0 and η masses in the PQMS models, is obtained when T/T_c^χ is around 1.6 while in the QMS model, this intersection point is found around $T/T_c^\chi = 2.0$. We are also obtaining the mild anomaly dependence of the intersection point of the f_0 and η in all the models. Here, we note that the mass of f_0 in vacuum increases by about 60 MeV in the absence of anomaly.

The temperature variations of meson masses, in general, result due to the interplay of the bosonic thermal contributions (decreasing the meson masses) and fermionic quark contributions (increasing the meson masses). Quark contributions which are negligible at small temperatures, dominate the mesonic contributions for high temperatures, and this generates a rising trend in meson masses, which ultimately leads to the mass degeneration of the chiral partners [64]. In the PQMS models, the one quark and two quark fermionic contributions are suppressed due to the presence of the Polyakov loop potential. Since the chiral phase transition is driven by the fermionic contributions, chiral restoration gets delayed due to the delay in the deconfinement transition and because of this we get higher value of the pseudocritical temperature T_c^{χ} in the Polyakov loop augmented quark meson linear sigma model. The higher value of the T_c^{χ} makes the ratio T/T_c^{χ} small. Hence, in comparison to the QMS model, the mass degeneration trend among the chiral partners, in general, sets up early in the PQMS models on the reduced temperature scale.

The variation of meson masses with the polynomial Polyakov loop potential are similar though a little less sharp than the mass calculations with the logarithmic potential. The difference appears mainly because of difference in the Polyakov loop expectation value $\langle\Phi\rangle$ with these two potentials. The calculations with the polynomial Polyakov loop potential make sense only for $T < 2T_c^{\chi}$.

The mass variation of scalar σ and f_0 show kink around $T/T_c^{\chi} = 1.8$ in the QMS model while it is seen around $T/T_c^{\chi} = 1.4$ in the PQMS models. The kink generation results because the meson masses seem to interchange their identities for higher values of the reduced temperature [64]. In order to have a proper perspective of the kink behavior in the curves, one has to study and analyze the scalar and pseudoscalar meson mixing angles.

4.4.3 Meson Mixing Angle Variations

The analysis of axial $U_A(1)$ restoration pattern identification will become complete, only after studying the variation of scalar θ_S and pseudoscalar θ_P mixing angles on the relative temperature scale in Fig.4.4 considering the cases in the presence as well as the absence of the axial $U_A(1)$ explicit symmetry breaking term. The anomaly term has a strong effect in the pseudoscalar sector in the broken phase for $T/T_c^{\chi} < 1$ while no effect of anomaly is found in the scalar sector. The nonstrange and strange quark mixing is strong, at T=0 one gets $\theta_P = -5^{\circ}$, which remains almost constant in the chiral broken phase.

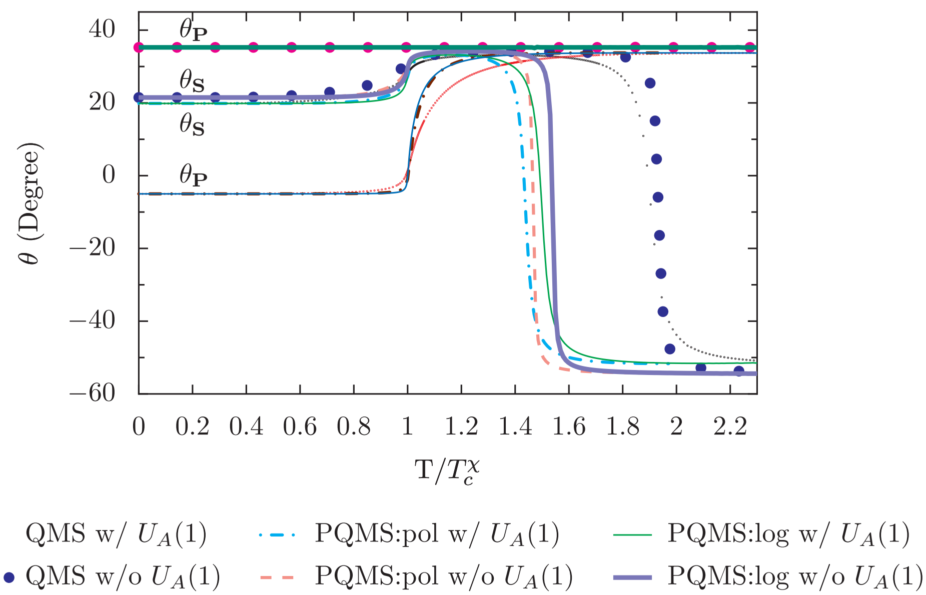

Figure 4.4: The scalar θ_S and pseudoscalar θ_P mixing angle variations with respect to the reduced temperature (T/T_c^χ) at zero chemical potential ($\mu = 0$) are plotted. We have given the plots for the QMS, PQMS:log, and PQMS:pol models considering the cases in the presence as well as absence of the axial $U_A(1)$ explicit symmetry breaking term. The dotted lines show the result with anomaly in the QMS model while the solid big dot lines show the result without anomaly. In the PQMS:log model, the thick solid lines represent the variations without anomaly while thin solid lines show the result with anomaly. The dashed-dotted lines are the variations with anomaly in the PQMS:pol model, while the dashed lines are the corresponding results in the absence of anomaly.

In the vicinity of $T/T_c^\chi = 1$, the θ_P variations start approaching the ideal mixing angle $\theta_P \longrightarrow \arctan\frac{1}{\sqrt{2}} \sim 35^\circ$, the corresponding $\Phi_P = 90^\circ$. Here, Φ_P is the pseudoscalar mixing angle in the strange nonstrange basis (see ref. [64] for details). The smooth approach towards the ideal mixing in the QMS model, becomes sharper and faster in the PQMS model calculations due to the influence of the Polyakov loop potential. Further, the ideal mixing is achieved earlier on the reduced temperature scale in the PQMS models. In the absence of axial $U_A(1)$ anomaly, the pseudoscalar mixing angle remains ideal $\theta_P = 35^\circ$

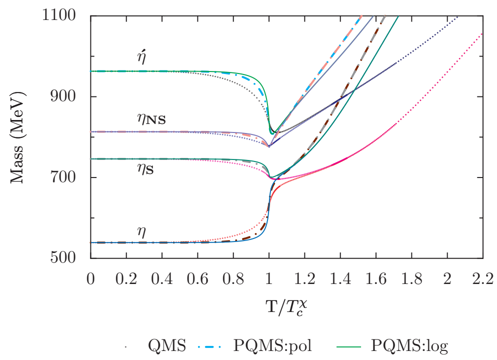

(a) With $U_A(1)$ anomaly term

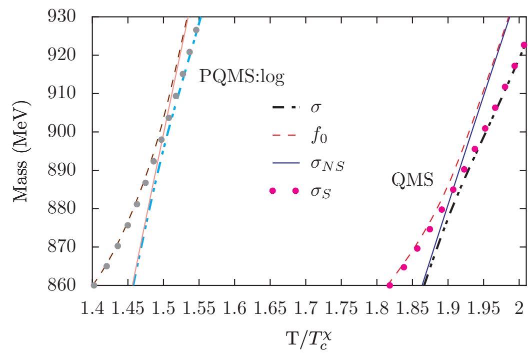

(b) With $U_A(1)$ anomaly term.

Figure 4.5: Figure4.5(a) shows the mass variations for the physical η, η' and the nonstrange-strange η_{NS}, η_S complex, on the reduced temperature scale (T/T_c^χ) at zero chemical potential ($\mu = 0$). The masses of the physical σ and f_0 anticross and the nonstrange-strange $\sigma_{NS} - \sigma_S$ system masses cross in Figure4.5(b).

everywhere on the reduced temperature scale.

The η and η' mesons become a purely strange η_S and nonstrange η_{NS} quark system as a consequence of the ideal pseudoscalar mixing, which gets fully achieved at higher values of the reduced temperature. In order to show this, we have plotted in Fig.4.5(a) the mass variations for the physical η, η' and the nonstrange-strange η_{NS}, η_S complex. Mass formulae $m_{\eta_{NS}}$ and m_{η_S} are given in Table 4.2. Again, the smooth mass convergence trend, of the pure QMS model in $m_{\eta'} \to m_{\eta_{NS}}$ and $m_\eta \to m_{\eta_S}$ approach, becomes sharper and faster around $T/T_c^\chi = 1$ in the influence of the Polyakov loop potential in the QMS model. The exact $m_{\eta'} \to m_{\eta_{NS}}$ and $m_\eta \to m_{\eta_S}$ mass convergence in the PQMS models, occurs closer to the value $T/T_c^\chi = 1$.

In Fig.4.4 for $m_\sigma = 600$ MeV at T = 0 scalar mixing angle $\theta_S \sim 19.9°$ in the presence of anomaly, while $\theta_S \sim 21.5°$ in the absence of anomaly. The θ_S around $T/T_c^\chi = 1$ grows to its ideal value but for higher temperatures on the reduced temperature scale, in the chiral symmetric phase, the scalar mixing angle drops down to $\theta_S \sim -51°$ and $\theta_S \sim -54°$ in the respective cases considered with and without anomaly. In the presence of the

$U_A(1)$ symmetry breaking term, this drop happens in the QMS model around $T/T_c^\chi \sim 1.9$ and due to the effect of the Polyakov loop potential the similar drop occurs earlier for $T/T_c^\chi \sim 1.5$ in the PQMS model. In the close vicinity of these reduced temperatures, the masses of the physical σ and f_0 anticross and the nonstrange - strange ($\sigma_{NS} - \sigma_S$) system masses cross as shown in Fig4.5(b). It means that after anticrossing the physical σ becomes identical with the pure strange quark system σ_S, while the physical f_0 becomes degenerate with the pure nonstrange quark system σ_{NS}. A similar drop for the calculations without anomaly happens at a little higher value on the reduced temperature scale in respective models.

4.5 Summary

We have calculated the meson masses and mixing angles for the scalar and pseudoscalar sector in the framework of the generalized 2+1 flavor PQMS model. We have used two different forms of the effective Polyakov loop potential for the calculation, namely, the polynomial potential and logarithmic potential. In order to investigate the influence of Polyakov loop potential on chiral symmetry restoration, these calculations have been compared with the corresponding results in the QMS model.

The temperature dependence of nonstrange, strange condensates and the Polyakov loop field Φ at zero chemical potential has been calculated from the gap equation in the QMS and PQMS models. Comparison of pseudocritical temperatures calculated from the inflection points of these order parameters indicates, that the chiral transition gets shifted to the higher temperatures as a result of the inclusion of the Polyakov loop in the QMS model. We further observe that the variation of the nonstrange condensate in the T/T_c^χ = 0.8 to 1.2 range becomes quite sharp due to the effect of the Polyakov loop potential in our calculation in PQMS models. We infer from the curves in the PQMS models that the inclusion of the Polyakov loop potential in the QMS model together with the presence of axial anomaly, triggers an early and significant melting of the strange condensate. The interesting physical consequences of the earlier melting of the strange condensate are an early emergence of mass degeneration trend in the masses of the chiral partners (K, κ) and (η, f_0) and an early setting up of a $U_A(1)$ restoration trend.

The mass degeneration of chiral partners (σ, π) and (a_0, η') in the close vicinity of $T/T_c^\chi = 1.0$ becomes sharper and faster in our calculations in the PQMS model. This sharpening of the mass variations in the small neighborhood of $T/T_c^\chi = 1$ results due to the stronger and sharper melting of the nonstrange condensate triggered by the presence of the Polyakov loop potential in the QMS model. Thus, we can corroborate also from the behavior of the chiral partners that the net effect of the Polyakov loop inclusion in the QMS model, is to make a sharper occurrence of the chiral $SU(2)_L \times SU(2)_R$ symmetry restoration transition in the nonstrange sector. Further, the mass degeneration of chiral partners (K, κ) with η does not occur when the value of the reduced temperature is equal to one, it sets up early in the PQMS models at $T/T_c^\chi = 1.3$, while it occurs at $T/T_c^\chi = 1.5$ in the QMS model. In the PQMS models, the intersection point of the f_0 and η masses, occurs early when the reduced temperature $T/T_c^\chi = 1.3$, while in the pure QMS model this intersection point is found at $T/T_c^\chi = 1.7$. This trend of mass degeneration emerges, again as a result of the sharper and stronger melting of the strange condensate in the influence of the Polyakov loop potential in the PQMS models.

The $U_A(1)$ breaking anomaly effect that leads to the mass gap between the two sets of the chiral partners,(σ, π) and (a_0, η') i.e. $m_\pi = m_\sigma < m_{a_0} = m_{\eta'}$ for $T/T_C^\chi > 1$, is proportional to the strange condensate σ_y. Since the melting of the strange condensate is stronger and sharper in the PQMS models, the convergence in the masses of the two sets of chiral partners will be enhanced in these calculations. Thus, the inclusion of the Polyakov loop potential in the PQMS models also effects an early set up of the $U_A(1)$ restoration trend on the reduced temperature scale.

The smooth approach of the pseudoscalar mixing angle θ_P towards the ideal mixing in the QMS model, becomes sharper and faster in the PQMS models due to the influence of the Polyakov loop potential. Further, in comparison to QMS model results, the ideal mixing on the reduced temperature scale is achieved earlier in the PQMS models. The θ_S around $T/T_c^\chi = 1$ grows to its ideal value but for higher temperatures on the reduced temperature scale, in the chirally symmetric phase, the scalar mixing angle drops down to $\theta_S \sim -51°$. In the presence of $U_A(1)$ symmetry breaking term, this drop happens in the QMS model for $T/T_c^\chi \sim 1.85$ and in the PQMS:log model, the similar drop occurs for $T/T_c^\chi \sim 1.5$. In the close vicinity of these reduced temperatures, the masses of the physical σ and f_0 anticross and the nonstrange-strange $\sigma_{NS} - \sigma_S$ system masses cross.

Chapter 5

Effects of quarks on the dynamics of Z(3) domain walls and strings in an effective model near the QCD deconfining transition

The possibility of existence of topologically non-trivial structures such as Z(3) interfaces and associated QGP strings in the quark-gluon plasma phase [107] is very exciting. In the context of relativistic heavy-ion collision experiments (RHICE), it provides the only system where domain walls and strings arise in a relativistic quantum field theory which can be investigated under laboratory control. In earlier works [38,106,107], various aspects of existence of these objects in cosmology as well as in RHICE, have been discussed. These topological objects arise in the high temperature deconfined phase of QCD due to spontaneous breaking of the Z(3) global symmetry of finite temperature QCD, where Z(3) is the center of the $SU(3)$ color gauge group of QCD. Spontaneous breaking of Z(3) symmetry arises from the non-zero expectation value of the Polyakov loop, $l(x)$, which is an order parameter for the confinement-deconfinement phase transition for pure gauge theory [12, 32]. The interpolation of $l(x)$ between three different degenerate $Z(3)$ vacua leads to the existence of domain walls (interfaces) together with topological strings when the three interfaces make a junction. We call these strings as QGP strings [107].

The properties and physical consequences of these $Z(3)$ interfaces have been discussed in the literature [175, 176]. It has also been suggested that these interfaces should not be taken as physical objects in the Minkowski space [177]. Existence of these Z(3) vacua becomes especially a non-trivial issue when considering the presence of dynamical quarks. The effect of quarks on $Z(3)$ symmetry and $Z(3)$ interfaces etc. has been discussed in detail in the literature [178, 179]. It has been argued that the $Z(3)$ symmetry becomes meaningless in the presence of quarks [178]. Other view-point as advocated in many research papers, asserts that one can take the effect of quarks in terms of explicit breaking of $Z(3)$ symmetry [37, 110–112, 179, 180], and we will follow this approach. In this context we mention the recent work of Deka et al. [181] which has provided a support for the existence of these metastable vacua from Lattice. Although the temperatures are high (close to 1 GeV) at which the indications of metastable vacuum are seen in ref. [181], the important point is that these metastable Z(3) vacua seem to exist at some temperature. Since the presence of quarks lifts the degeneracy of different $Z(3)$ vacua [37,110–112,179,180], the $Z(3)$ interfaces become unstable and move away from the region with the unique true vacuum. Thus, with quark effects taken in terms of explicit symmetry breaking, the interfaces survive as non-trivial topological structures, though they do not remain solutions of time independent equations of motion. In the context of early universe as well as in RHICE, the earlier investigations of the dynamics of these Z(3) walls and QGP strings, have neglected the effects of such an explicit symmetry breaking due to the presence of quarks [38,106,107]. In the present work, we will incorporate effects of explicit symmetry breaking from quarks in the study of these objects.

Our numerical simulations in this work aim to investigate how the formation of $Z(3)$ walls and string network during the initial confinement-deconfinement (C-D) transition in RHICE, and their subsequent evolution, gets affected by such explicit breaking of Z(3) symmetry. As in our earlier work [107], we model the pre-equilibrium stage of phase transition in our simulation as a quasi-equilibrium stage with an effective temperature which first rises (with rapid particle production) to a maximum temperature $T_0 > T_c$, where T_c is the critical transition temperature, and then decreases due to continued expansion of plasma.

In order to study the confinement-deconfinement (C-D) phase transition in earlier works for the pure gauge case, we have been using the mean field effective potential of a polynomial form written in terms of the Polyakov loop expectation value $l(x)$ as proposed by Pisarski [37,110–112,180]. A linear term in $l(x)$ added to this effective potential in the mean field framework [182–185] accounts for the explicit breaking of $Z(3)$ symmetry by the dynamical quarks whose presence act like a background magnetic field [186,187]. In our analysis in ref. [107] we had discussed the effects of the explicit symmetry breaking term in view of the estimates of such a term from ref. [188,189]. We had found that the two degenerate vacua ($l = e^{i2\pi/3}$, and $l = e^{i4\pi/3}$), which get lifted with respect to the true vacuum (with $l = 1$) on account of explicit breaking of $Z(3)$ symmetry in the QGP phase, have higher free energy than even the hadronic phase (with $l = 0$) at temperatures of order 200 MeV. This does not seem reasonable because one would expect that any of the $Z(3)$ vacua which become meta-stable due to explicit symmetry breaking should still have lower free energy than the hadronic phase for values of temperature $T > T_c$ enforcing that the system lies in the deconfining regime for such temperatures. In any case, the estimates of [188,189] refer to high temperature regime and may not be applicable to temperatures near T_c. We thus use following considerations to constrain the magnitude of the strength of the explicit symmetry breaking term. One approach can be to limit it such that the metastable vacuum remains lower than the confining vacuum for temperatures above T_c. We, however, limit explicit symmetry breaking to further lower values by requiring that the first order nature of the transition remains the same at least in some range of temperatures above T_c.

We are using this first order transition model in the present work to discuss the dynamical details of quark-hadron transition, even though the lattice results show that quark-hadron transition is most likely a cross-over at zero chemical potential. The quark-hadron phase transition in the context of relativistic heavy-ion collision experiments is expected to be of first order for not too small values of the chemical potential which may be relevant for our study. Further, we are primarily interested in determining the time dependence of $Z(3)$ interfaces and string network structures, which result due to explicit breaking of $Z(3)$ symmetry during the phase transition. The formation of these objects is independent of the nature of phase transition as it results entirely due to finite correlation length in a fast evolving system, as shown by Kibble [109, 190]. The Kibble mechanism was first proposed for the formation of topological defects in the context of the early universe [109, 190], but is now utilized extensively for discussing topological defects production in a wide variety of systems from condensed matter physics to cosmology [191]. Essential ingredient of the Kibble mechanism is the existence of uncorrelated domains of the order parameter which result after every phase transition occurring in finite time due to finite correlation length. A first order transition allows easy implementation of the resulting domain structure especially when the transition proceeds via bubble nucleation. Keeping this view in mind, we use the potential for Polyakov loop augmented with the addition of a linear term as in [110–112, 180, 182–184] to model the phase transition. Further we will be confining ourselves to the temperature/time ranges and such values of the coefficient of linear term in the effective potential that the first order quark-hadron transition proceeds via bubble nucleation.

The $Z(3)$ interfaces and strings will develop dynamics in the presence of explicit symmetry breaking and the interfaces will start moving away from the direction where true vacuum exists. The strings will also not have three interfaces forming symmetrically around it, and hence will start moving in some direction. Such motions may cause important differences on the long time behavior. Due to the quark effects, we will get different nucleation probabilities/rates for the bubbles of meta-stable $Z(3)$ vacua and the true vacuum bubbles of the QGP phase. Meta-stable bubbles, being larger in size, may cover a larger fraction of the physical space and hence may lead to non-trivial consequences. The effects of quarks will be significant if a closed spherical wall (with true vacuum inside) starts expanding instead of collapsing. This effect may play an important role in the early universe case because an expanding closed domain wall has to be large enough such that the surface energy contribution does not dominate over the volume energy. In the case of RHICE, the asymmetrical $Z(3)$ walls and associated strings will eventually melt away when the temperature drops below the deconfinement-confinement phase transition temperature T_c. However they will be leaving their signatures in the form of extended regions of energy density fluctuations (as well as P_T enhancement of heavy-flavor hadrons [192] We will be estimating these energy density fluctuations which will lead to multiplicity fluctuations. Our main focus will be in looking for the signals of extended regions of large energy densities in space-time reconstruction of hadron density. We mention here that a simulation of spinodal decomposition in Polyakov loop model has been carried out in ref. [193], where fluctuations in the Polyakov loop are investigated in detail. Our work, here and in ref. [107] is focused on the formation of extended structures like Z(3) walls, strings, and extended regions of energy density etc. The present work estimates the effects of quarks on these structures.

This chapter is organized in the following manner. In section 5.1, we briefly recall the Polyakov loop model of confinement-deconfinement phase transition and describe the effective potential proposed by Pisarski [37, 180]. Here we discuss the effects of quarks in terms of a linear term in the Polyakov loop in the effective potential, which leads to explicit breaking of the Z(3) symmetry. We discuss different estimates for the strength of this linear term in the context of situations such that the transition is of first order. In section 5.2, we discuss the effect of this term on the structure of Z(3) walls and strings, and on the structure of bubbles through which the phase transition is completed. Here we describe our approach to extend the conventional technique of false vacuum decay to this case where different Z(3) bubbles have different profiles. What is of crucial importance to our discussion of the formation of these objects is the nucleation rates of the bubbles of different Z(3) vacua. Since these vacua are no more degenerate, the corresponding bubbles will in general have different nucleation rates. Section 5.3 discusses nucleation rates for these different bubbles. One may expect that the metastable Z(3) vacua should be suppressed as the corresponding bubbles have larger actions. We discuss the very interesting possibility that despite having larger action the metastable vacua may have similar (or even larger) nucleation rates as compared to the true vacuum. This can happen when the pre-exponential factor dominates over the exponential suppression term in the nucleation rate. This possibility is intriguing as the metastable vacua, being larger in size, may cover a larger fraction of the physical space and hence may dominate the dynamics of phase transition.

Section 5.4 presents the numerical technique of simulating the phase transition via random nucleation of bubbles, which now have different sizes depending on the corresponding Z(3) vacuum inside the bubble. Resulting domain walls may show non-trivial behavior compared to the case without the quark effects as a closed domain wall, enclosing the true vacuum, may expand instead of contracting. Rough estimates, with our parameter choices, show that this is expected when domain wall size exceeds about 50 fm. The discussion of such a large physical region is more relevant in the context of the early universe and we plan to study this in a future work. Here we will consider the case relevant to RHICE with lattice sizes of about (15 fm)^2 and study the effects of domain wall and string formation with temperature evolution as expected in a longitudinally expanding plasma. These results are presented in section 5.5. We also calculate the energy density fluctuations associated with $Z(3)$ wall network and strings, as in our earlier work [107], and discuss important differences for the present case with quark effects. In section 5.6

we discuss possible experimental signatures resulting from the presence of $Z(3)$ wall network and associated strings especially including the effects of explicit symmetry breaking. Summary is presented in section 5.7.

5.1 The Polyakov loop model with quark effects

We first briefly recall the Polyakov loop model for the confinement - deconfinement phase transition. For the case of pure $SU(N)$ gauge theory, the expectation value of Polyakov loop $l(x)$ is the order parameter for confinement - deconfinement phase transition.

$$l(\vec{x}) = \frac{1}{N} Tr(\mathcal{P} exp(ig \int_0^\beta A_0(\vec{x}, \tau) d\tau)) \tag{5.1}$$

Where $A_0(\vec{x}, \tau)$ is the time component of the vector potential $A_\mu(\vec{x}, \tau) = A_\mu^a(\vec{x}, \tau) T^a$, T^a are the generators of $SU(N)$ in the fundamental representation, $\mathcal{P}$ denotes path ordering in the Euclidean time τ, g is the gauge coupling, and $\beta = 1/T$ with T being the temperature. N (= 3 for QCD) is the number of colors. The complex scalar field $l(\vec{x})$ transform under the global $Z(N)$ (center) symmetry transformation as

$$l(\vec{x}) \rightarrow exp(2\pi i n/N) l(\vec{x}),\ n = 0, 1, ...(N-1) \tag{5.2}$$

The expectation value of $l(x)$ is related to $e^{-\beta F}$ where F is the free energy of an infinitely heavy test quark. For temperatures below T_c, in the confined phase, the expectation value of Polyakov loop is zero corresponding to the infinite free energy of an isolated test quark. (Hereafter, we will use the same notation $l(x)$ to denote the expectation value of the Polyakov loop.) Hence the Z(N) symmetry is restored below T_c. Z(N) symmetry is broken spontaneously above T_c where $l(x)$ is non-zero corresponding to the finite free energy of the test quark. Effective theory of the Polyakov loop has been proposed by several authors with various parameters fitted to reproduce lattice results for pure QCD [37, 79, 81, 110–112, 180, 194]. We use the Polyakov loop effective theory proposed by Pisarski [37, 110–112, 180]. The effective Lagrangian density can be written as

$$L = \frac{N}{g^2}|\partial_\mu l|^2 T^2 - V(l) \tag{5.3}$$

Where the effective potential $V(l)$ for the Polyakov loop, in case of pure gauge theory is given as

$$V(l) = (\frac{-b_2}{2}|l|^2 - \frac{b_3}{6}(l^3 + (l^*)^3) + \frac{1}{4}(|l|^2)^2)b_4 T^4 \tag{5.4}$$

At low temperature where $l = 0$, the potential has only one minimum. As temperature becomes higher than T_c the Polyakov loop develops a non vanishing vacuum expectation value l_0, and the cos3θ term, coming from the $l^3 + l^{*3}$ term above leads to $Z(3)$ generate vacua. Now in the deconfined phase, for a small range of temperature above T_c, the $l = 0$ extremum becomes the local minimum (false vacuum) and a potential barrier exist between the local minimum and global minimum (true vacuum) of the potential.

To include the effects of dynamical quarks, we will follow the approach where the explicit breaking of the $Z(3)$ symmetry is represented in the effective potential by inclusion of a linear term in l [37, 110–112, 179, 180, 182]. The potential of Eq.(5.4) with the linear term becomes,

$$V(l) = \Big(-\frac{b_1}{2}(l + l^*) - \frac{b_2}{2}|l|^2 - \frac{b_3}{6}(l^3 + l^{*3}) + \frac{1}{4}(|l|^2)^2\Big)b_4 T^4 \tag{5.5}$$

Here coefficient b_1 measures the strength of explicit symmetry breaking. The coefficients b_1, b_2, b_3 and b_4 are dimensionless quantities. With $b_1 = 0$, other parameters b_2, b_3 and b_4 are fitted in ref. [37, 110–112, 180, 195] such that that the effective potential reproduces the thermodynamics of pure $SU(3)$ gauge theory on lattice [182,195–197]. The coefficient b_2 is temperature dependent and given by

$$b_2(r) = (1 - \frac{1.11}{r})(1 + \frac{0.265}{r})^2 (1 + \frac{0.3}{r})^3 - 0.487; \quad r = \frac{T}{T_c}; \quad T_c = 182\,\text{MeV} \tag{5.6}$$

We use the value of temperature independent coefficients $b_3 = 2.0$ and $b_4 = 0.6061 \times \frac{47.5}{16}$. We choose the same value of b_2 for real QCD (with three massless quarks flavors). b_4 is rescaled by factor $\frac{47.5}{16}$ to incorporate extra degrees of freedom of QCD relative to pure $SU(3)$ gauge theory [195]. As temperature $T \to \infty$ the Polyakov loop expectation value approaches the value $x \sim b_3/2 + \frac{1}{2}\sqrt{b_3^2 + 4b_2(T = \infty)}$. To have the normalization $\langle l(x) \rangle \to 1$ at $T \to \infty$, the coefficients and field in the effective potential $V(l)$ in Eq.(5.5) are rescaled as $b_1(T) \to b_1(T)/x^3$, $b_2(T) \to b_2(T)/x^2$, $b_3 \to b_3/x$ and $b_4 \to b_4 x^4$, $l \to l/x$.

At temperatures above the critical temperature T_c the potential $V(l)$ has three degenerate vacua in pure gauge theory (with $b_1 = 0$). The barrier heights between the local minimum ($l(x) = 0$) and the three global minima ($l = 1, \mathrm{z}, \mathrm{z}^2$, corresponding to $\theta = 0, 2\pi/3, 4\pi/3$) are all same. As the value of b_1 becomes non zero, the degeneracy of $Z(3)$ vacua gets lifted. Vacua corresponding to $\theta = 2\pi/3$ ($l = \mathrm{z}$) and $\theta = 4\pi/3$ ($l = \mathrm{z}^2$) remain degenerate, with energy which is higher than the $l = 1$ ($\theta = 0$) vacuum. Thus, $l = z$ and $l = z^2$ vacua become metastable and the $l = 1$ remains the only true vacuum (global minimum). Note that $l = z$ and $l = z^2$ are the two metastable vacua in the QGP phase. Along with these, there is a metastable vacuum at $l = 0$ (for a small range of temperature above T_c) which corresponds to the confining phase.

Estimates of explicit $Z(3)$ symmetry breaking arising from quark effects have been discussed in the literature. In the high temperature limit, the estimate of the difference in the potential energies of the $l = z$ vacuum, and the $l = 1$ vacuum, ΔV, is given in ref. [188, 189] as,

$$\Delta V \sim \frac{2}{3}\pi^2 T^4 \frac{N_l}{N^3}(N^2 - 2) \tag{5.7}$$

where N_l is the number of massless quarks. If we take $N_l = 2$ then $\Delta V \simeq 3T^4$. At $T = 200$ MeV, the difference between the confining vacuum and the true vacuum from the effective potential in Eq.(5.5) is about 150 MeV/fm^3 while ΔV from Eq.(5.7) at $T = 200$ MeV is about four times larger, equal to 600 MeV/fm^3. As T approaches T_c, this difference will become larger as the metastable vacuum and the stable vacuum become degenerate at T_c, while ΔV remains non-zero. It does not seem reasonable that at temperatures of order 200 MeV (with $T_c = 182$ MeV for Eq.(5.5)) a QGP phase (with quarks) has higher free energy than the hadronic phase. In any case, the estimates of Eq.(5.7) were made in high temperature limit and the extrapolation of these to T near T_c may be invalid. We, thus, use different physical considerations to estimate the strength of the explicit symmetry breaking term, i.e. the value of parameter b_1 in Eq.(5.5), as follows.

Note that as b_1 is increased from zero, the potential tilts such that the barrier between the metastable confining phase and the true vacuum in the $\theta = 0$ direction decreases, resulting in the weakening of the first order phase transition. Finally, this barrier disappears for $b_1 \geq 0.11$ (at $T = T_c = 182$ MeV). For $b_1 \geq 0.11$ there is no range of temperature where the phase transition is first order. As we mentioned, our approach is to study the phase transition dynamics via bubble nucleation. We thus choose a small value of $b_1 = 0.005$ such that the confinement - deconfinement phase transition is (weakly) first order phase transition for a reasonable range of temperature. The plot of the potential in $\theta = 0$ direction for $b_1 = 0.005$ is shown in Fig.5.1 for $T = 200$ MeV. Note that with $b_1 > 0$ the confining vacuum at $l = 0$ shifts towards positive real value of l. With this value of b_1, the barrier between the confining metastable vacuum and the true vacuum exists upto temperature $\simeq 225$ MeV which allows for a reasonable range of temperatures to discuss the bubble profiles and their nucleation probabilities. If we choose larger values of b_1, the range of temperature allowing first order transition becomes very narrow and formation and nucleation of bubbles require fine tuning of time scale.

This, apparently ad hoc, procedure of fixing value of b_1 can be given a physical basis in the following way. Changing the value of coefficient b_1 changes the nature of phase transition from strong first order to a very weak one. One can attempt to interpret it in the context of QCD phase diagram, drawn in the plane of chemical potential (μ) and temperature (T). The QCD phase transition is of strong first order for large μ, it becomes

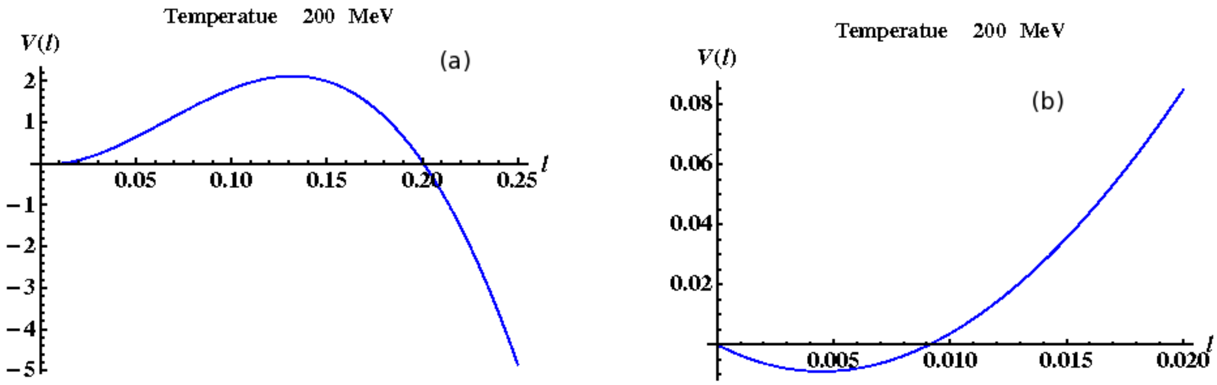

Figure 5.1: (a) Plot of $V(l)$ (in MeV/fm^3) in $\theta = 0$ direction for $T = 200$ MeV with $b_1 = 0.005$. (b) shows the plot near the origin, showing that the confining vacuum has shifted slightly from $l = 0$ towards $\theta = 0$ direction.

a weak first order transition with decreasing μ, reaches to critical end point where the transition is of second order and then becomes crossover at lower μ values. If we assume that the effective potential in Eq.(5.5) (at least in form) can describe these situations of varying chemical potential, then it looks natural to assume that changing the value of μ is interpreted in terms of changing the value of b_1 parameter in Eq.(5.5). Thus increasing μ corresponds to lowering the value of b_1 making the phase transition of stronger first order.

Note that the potential barrier between the confining vacuum and the true vacuum is maximum when b_1 is zero and the first order phase transition is strongest. This should correspond to the situation of largest μ according to the above argument, presumably corresponding to the transition at very low temperatures in the QCD phase diagram. However, with $b_1 = 0$ there is no explicit symmetry breaking. This will not be consistent with the expectation of explicit symmetry breaking arising from quark effects. Though one cannot exclude the possibility that the effects of dynamical quarks and that of net baryon number density may have opposite effects on the value of b_1, so that a strong first order transition at large μ can be consistently interpreted in terms of $b_1 = 0$. However, it is simpler to assume that even for the largest value of μ (where the first order curve intersects the μ axis in the QCD phase diagram), b_1 never becomes zero so that explicit symmetry breaking remains present as expected.

Of course, it is clear that the parameter values used in Eq.(5.5), which were fitted using lattice results for $\mu = 0$ case, are no longer applicable, if non-zero values of b_1 are interpreted in terms of non-zero μ. We will then need to assume that the required changes in the parameters of Eq.(5.5) for non-zero μ are not large. At the very least we can say that, even if b_1 values we use here cannot be justified, they help us capture some qualitative aspects of changes in the formation and evolution of Z(3) walls and QGP strings when quark effects are incorporated.

5.2 Domain walls, strings and bubbles with explicit symmetry breaking

The explicit symmetry breaking arising from quark effects will have important effects on the structure of topological objects; Z(3) walls and the QGP strings. It will obviously also affect the nucleation of bubbles of different Z(3) phases. First we qualitatively discuss its effects on Z(3) walls and the QGP strings. For non-degenerate vacua, even planar $Z(3)$ interfaces do not remain static, and move away from the region with the unique true vacuum. Thus, while for the degenerate vacua case every closed domain wall collapses, for the non-degenerate case this is not true any more. A closed wall enclosing the true vacuum may expand if it is large enough so that the surface energy contribution does not dominate. Similarly it is no more possible to have time independent solution for the QGP string. Without explicit symmetry breaking a QGP string forming at the intersection of three symmetrically placed Z(3) walls will be stationary. However, with $b_1 \neq 0$ this is not possible for any configuration of domain walls. In fact this type of situation has been discussed in the context of early universe for certain types of axionic string models

[198, 199].

Apart from the structure of these objects, one also expects important changes in the basic mechanism of formation of these objects during phase transition. Without explicit symmetry breaking, these objects will form via the Kibble mechanism, as discussed in detail in [107]. In the presence of explicit symmetry breaking new effects may arise as discussed in [200, 201] where many string-antistring pairs with small separations (which means small loops of strings or small closed domain walls in the present context) can form at the coalescence region of two bubbles. This mode of production of topological objects arises from the fluctuations of the order parameter and is entirely different from the basic physics of the Kibble mechanism. As we are using very small value of explicit symmetry breaking, we do not expect this new mechanism to play an important role here. However, for larger values of b_1, this production mechanism may play an important role in determining the Z(3) wall and string network resulting from a first order QCD phase transition.

General picture of the formation of these objects during first order QCD transition via bubble nucleation was described in detail in ref. [107] for the case without explicit symmetry breaking and we briefly summarize it below. Subsequently we will discuss the effects of explicit symmetry breaking on the bubble profiles, their nucleation rates, and on general dynamics of the phase transition.

We calculate the bubble profile of QGP phase using Coleman's technique of bounce solution [113, 202] for true vacuum ($l = 1$) and for metastable vacua ($l = z, z^2$). We seed these bubbles in the false (hadronic) background randomly with their nucleation rates calculated at an appropriate value of temperature $T > T_c$ (such that the nucleation rate is appreciable). The value of the phase of the complex order parameter l is constant inside a given bubble (to minimize the free energy), while it changes from one bubble to another randomly (corresponding to the choices of three vacua). The variation of the orientation of the order parameter from one bubble to another provides the essential ingredient of the

Kibble mechanism leading to a domain structure and formation of topological objects at the intersection of domains. We evolve this initial field configuration with the equations of motion using leap frog algorithm. Bubbles grow with time and coalesce with each other. The bubbles with same vacuum merge together to form a bigger region of same vacuum while the bubbles with different vacua remain separated by a wall/interface of high energy density after coalescence. These are the Z(3) domain walls. These domain walls are solutions of field equations of motion, interpolating between different Z(3) vacua, and survive till very long time as QGP evolves. Eventually, either walls collapse/merge away, or they melt as the temperature of expanding QGP falls below T_c and Z(3) symmetry is restored.

Spontaneous breaking of Z(3) symmetry in the QGP phase leads to three different topological domain walls separating the three different $Z(3)$ vacua. The intersection point of the three domains walls leads to a topological string (the QGP string) which was discussed in detail in ref. [106]. This string arises as the order parameter l completes a closed loop around $l = 0$ in the complex l space when one encircles the intersection point of the three domain walls in the physical space [106]. Thus, these are topological strings which exist in the QGP phase and have confining core (with $l = 0$). As bubbles of different Z(3) vacua coalesce with each other, a network of Z(3) walls forms and at the intersection of Z(3) walls, QGP strings form. A detailed investigation of this for the case without explicit symmetry breaking (i.e. $b_1 = 0$), using 2+1 dimensional simulation representing the central rapidity region, was carried out in ref. [107].

The above picture of the dynamics of bubble nucleation, coalescence, and formation and evolution of Z(3) walls and QGP strings will be affected by the presence of explicit symmetry breaking in important ways. With $b_1 \neq 0$, the three $Z(3)$ vacua are no longer degenerate. The two vacua ($l = z, z^2$) corresponding to $\theta = 2\pi/3, 4\pi/3$ get lifted and become metastable. Only the third one with real expectation value of l remains stable. The energy difference between the confining vacuum (near $l = 0$, note that due to $b_1 \neq 0$, the confining vacuum shifts slightly) and the two metastable Z(3) vacua (with $l = z, z^2$) is smaller than the energy difference between the confining vacuum and the true vacuum. This leads to larger bubble size for metastable vacuum than the bubble of true vacuum, with larger value of associated action (free energy). The energy difference between the confining vacuum and true or metastable vacuum increases with increase in temperature so the bubble sizes decreases with increase in temperature.

In the non-degenerate case with non vanishing explicit symmetry breaking the false vacuum of potential gets shifted towards real axis by an small amount ϵ. This shift is minimum for temperature closer to T_c and increases as we increase the temperature. Further, the local maximum of the potential barrier and the metastable vacua are not in same direction but there is a small angular shift between them. These aspects make it difficult to apply the Coleman's technique of bounce solution of a scalar field for the present case as we will discuss below. First we review the basic features of the first order transition via bubble nucleation.

A first order phase transition proceeds by the nucleation of a true vacuum bubble in the background of false vacuum. A true vacuum bubble produced, will grow or collapse depending on the free energy change of the system. The change in the free energy of the system because of the creation of a true vacuum bubble of radius R is

$$F(R) = F_s + F_v = 4\pi R^2 \sigma - \frac{4\pi}{3} R^3 \eta \tag{5.8}$$

Here F_v is the volume energy and F_s is the surface energy of the bubble. For a strong first order phase transition, one can analytically determine the potential energy difference η between the confining vacuum and relevant Z(3) vacuum and the surface tension σ from bounce solution (at least for a scalar field). Minimization of this free energy determines the critical radius $R_c = \frac{2\sigma}{\eta}$. The volume energy of the bubbles with radius $R > R_c$ dominates over its surface energy and the bubbles expand to transform the false vacuum to true vacuum. The smaller bubbles ($R < R_c$) for which surface energy dominates over the volume energy, shrink and disappear. For strong first order transition, calculation of

η and σ separately can be done as one is dealing with the thin wall bubbles where the bubble size is much larger than the thickness of the bubble wall, so that there is clear separation between the bubble core and the bubble wall. For the parameter values, and the temperature range of our interest, we will be dealing with thick wall bubbles where bubble size if of the same order as the bubble wall. For this purpose, the expression in Eq.(5.8) is not of use, and one has to calculate the bubble profile numerically using Coleman's technique of bounce solution and determine its action to calculate nucleation probabilities.

The theory of semiclassical decay of false vacuum at zero temperature is given in ref. [113,202] and its extension to finite temperature was given in ref. [203]. The Coleman's technique is applicable for real scalar field. To calculate bubble profile for complex scalar field l (with $b_1 = 0$), in ref. [107], the phase angle θ was taken to be constant by fixing it in the direction of the relevant Z(3) vacuum, i.e. $\theta = 0, 2\pi/3, \text{or}, 4\pi/3$. This reduced the problem again to a real scalar field calculation and Coleman's technique could be directly applied. (However, there are important issues for the case of complex scalar field regarding the calculation of nucleation rates which require calculation of determinant of fluctuations around the bounce solution. A brief discussion of these issues is provided in ref. [107].

We calculate the bubble profile in 3+1 dimension. However, we evolve it only by the $2 + 1$ dimensional field equations. This is because of rapid longitudinal expression which simply stretches the bubbles in the longitudinal direction, while its transverse evolution proceeds according to field equations. We neglect the transverse expansion of system which is certainly a good approximation during early stages of bubble nucleation (during initial transition from confining phase to the QGP phase with time scales of order 1 fm). At finite temperature, the 3+1 - dimensional theory will reduce to an effectively 3 Euclidean dimensional theory if the temperature is sufficiently high, which we will take to be the case [107]. For this 3 dimensional Euclidean theory, the bubble profile is the solution of the following equation

$$\frac{d^2l}{dr^2} + \frac{2}{r}\frac{dl}{dr} = \frac{g^2}{2NT^2}\frac{\partial V}{\partial l} \tag{5.9}$$

where $r = r_E = \sqrt{\vec{x}^2 + {t_E}^2}$, subscript E denotes coordinates in the 3 dimensional Euclidean space. We use fourth order Runge-Kutta method to solve Eq.(5.9). For $b_1 = 0$, the relevant boundary conditions on l to calculate the bubble profile are $l = 0$ as $r \to \infty$ and $\frac{dl}{dr} = 0$ at $r = 0$. However, with $b_1 > 0$ this is no longer applicable. This is because with $b_1 \neq 0$ the confining vacuum is shifted from $l = 0$ along $\theta = 0$ direction by an amount ϵ. We calculate the bubble profile at $T = 200$ MeV and at this temperature $\epsilon = 0.0045$ (see, Fig.5.1(b)). We thus re-write the effective potential in Eq.(5.5) in terms of a shifted field $l' = l - \epsilon$. In terms of l' the confining vacuum again occurs at $l' = 0$ and the standard boundary conditions as discussed above can be applied for solving Eq.(5.9) for the bounce solution. Hereafter all discussion will be in terms of this shifted field l' which, for simplicity we will denote as l only.

Another complication occurs in calculating the bubble profile for the metastable Z(3) vacua. The earlier technique for $b_1 = 0$ case of simply fixing $\theta = 2\pi/3$ or $\theta = 4\pi/3$ for the two respective vacua, thereby reducing the problem to a real scalar field case, cannot be applied here directly. This is because with $b_1 \neq 0$, the maximum of the respective potential barrier and direction of the corresponding metastable vacuum are not in the same direction (due to the tilt of the potential resulting from $b_1 \neq 0$). However, the difference between the two directions, i.e. between the $l = z$ vacuum and the direction of the top of the corresponding barrier, is very small, of order $\theta = 0.9°$. Same is true for $l = z^2$ vacuum. We then fix θ along $l = z$ and $l = z^2$ vacua respectively to get the approximately valid bubble profile using Eq.(5.9). (Both these directions differ slightly from $\theta = 2\pi/3$ and $\theta = 4\pi/3$ now. Note again all this is using the shifted field which we are again denoting as l.) Recall, that we are calculating 3+1 dimensional critical bubble and evolving it by 2+1 dimensional equations with the bubble becoming supercritical for 2+1 dim. equations [107]. Further we are studying the situation of rapidly changing temperature. Thus exact profile of the critical bubble at the nucleation time is not of much relevance.

As we had mentioned above, we choose the value of b_1 such that the barrier between the confining vacuum and various Z(3) vacua remains non-zero up to some range of temperature so that bubble formation can be carried out. We choose $b_1 = 0.005$ with which the barrier between the confining vacuum and true vacuum exist upto temperature $\simeq 225$ MeV. The first order phase transition via bubble nucleation is possible only upto this temperature.

5.3 Nucleation rates for different bubbles

For the finite temperature case, the tunneling probability per unit volume per unit time in the high temperature approximation is given by [203] (in natural units)

$$\Gamma = A \; e^{-S_3(l)/T} \tag{5.10}$$

where $S_3(l)$ is the 3-dimensional Euclidean action for the Polyakov loop field configuration that satisfies the classical Euclidean equations of motion. The dominant contribution to the exponential term in Γ comes from the bounce solution which is the least action $O(3)$ symmetric solution of Eq.(5.9). For a theory with one real scalar field in three Euclidean dimensions the pre-exponential factor arising in the nucleation rate of critical bubbles has been estimated, see ref. [203]. The pre-exponential factor obtained from [203] for our case becomes

$$A = T^4 \left(\frac{S_3(l)}{2\pi T} \right)^{3/2} \tag{5.11}$$

As emphasized in [107], the results of [203] were for a single real scalar field and one of the crucial ingredients used in [203] for calculating the pre-exponential factor was the fact that for a bounce solution the only light modes contributing to the determinant of fluctuations were the deformations of the bubble perimeter. Even though we are discussing the case of a complex scalar field $l(x)$, this assumption may still hold as we are calculating the tunneling from the false vacuum to one of the Z(3) vacua. This assumption may need to be revised when light modes e.g. Goldstone bosons are present which then also have to be accounted for in the calculation of the determinant.

A somewhat different approach for the pre-exponential factor in Eq.(5.10) is obtained from the nucleation rate of bubbles per unit volume for a liquid-gas phase transition as given in ref. [204–208]. In ref. [107] we had considered these estimates for the nucleation rate as well as those obtained from Eq.(5.11). It was found that for the parameter values in Eq.(5.5) and for the temperature/time scales relevant for RHICE, the nucleation rates obtained using the liquid-gas transition approach of ref. [204–208] were completely negligible such that even nucleation of one bubble of QGP phase was not likely at RHICE. As one needs several bubbles to discuss the formation of Z(3) walls and strings, these estimates clearly cannot be used here. As in ref. [107] we will follow the approach based on Eq.(5.11) for our case which gave reasonable nucleation rates leading to the possibility of formation of several bubbles for the case of RHICE. We may mention here that for nucleation of bubbles of the Polyakov loop l it may anyway be better to use a field theory approach as in ref. [203] rather than the approach of ref. [204–208] which is more suitable for the description of phase transition in terms of plasma degrees of freedom. Though, the parameters of Eq.(5.5) have been fitted with lattice QCD, it is still not very clear whether the bubbles should be viewed in terms of an order parameter field representing some background condensate (as the Polyakov loop l), or just different phases of an interacting plasma.

We thus proceed with the calculation of nucleation rates of the bubbles using Eqs.(5.10),(5.11). Fig.5.2 shows the profiles of the bubbles for $l = 1$ and $l = z$ vacua at $T = 200$ MeV ($l = z^2$ bubbles has the same profile as the $l = z$ bubble). We note that $l = z$ bubble is somewhat larger as expected. Using such bubble profiles we calculate the respective values of the action S_3 and estimate the nucleation rates for metastable

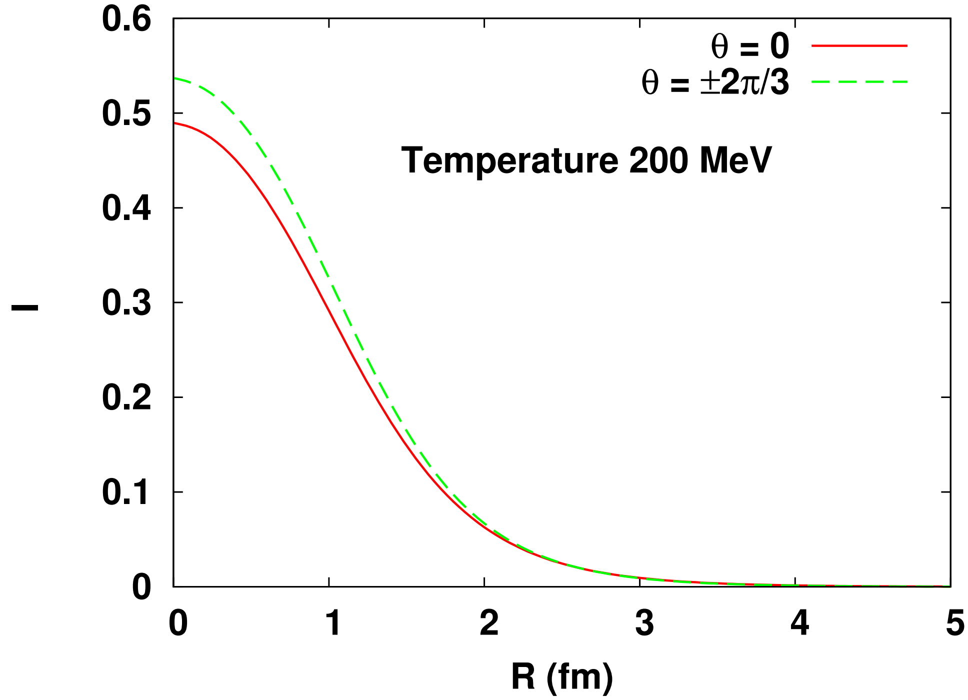

Figure 5.2: Critical bubble profiles for the different Z(3) vacua for $b_1 = 0.005$.

and true vacuum at different temperatures. To calculate number of bubbles for a typical nucleus nucleus collision, we consider a circle of 8 fm radius in transverse plane with 1 fm thickness in the longitudinal direction. The bubble nucleation for 1 fm time obtained from the nucleation rate given in Eqs.(5.10), (5.11) leads to about 3 - 5 bubbles in this region. (The approach followed in ref. [207, 208] gives the nucleation rate of about 10^{-4} fm^{-4} in the relevant temperature range, leading to negligible nucleation of bubbles).

One may expect that nucleation rate of the two metastable Z(3) vacua will be smaller than that of the true Z(3) vacuum due to larger action S_3 of the metastable vacuum leading to exponential suppression. However, here we see an interesting interplay between the exponential factor $e^{-S_3(T)/T}$ (Eq.(5.10)) and the prefactor A as given in Eq.(5.11). If $S_3(T)$ is much larger than T then the nucleation rate is dominated by the exponential factor confirming the above expectation. Thus, the nucleation rate of metastable vacuum bubble is much smaller than the true vacuum bubble when temperature is closer to T_c. The nucleation rate of true vacuum bubble and metastable vacuum bubble at temperature near T_c (at $T = 185$ MeV) is of the order of $\sim 1.3 \times 10^{-5}$ fm^{-4} and $\sim 3.4 \times 10^{-7}$ fm^{-4} respectively. As we increase the temperature from $T_c = 182$ MeV, the nucleation rate of metastable vacuum bubble increases and becomes almost equal to that of true vacuum bubble at $T \simeq 200$ MeV (both rates being about $\sim 2.4 \times 10^{-2}$ fm^{-4}). This happens because at these temperatures $S_3 \simeq T$ so that the decrease of the exponential term for a larger S_3 (corresponding to the metastable vacuum) is not very significant. However, the pre-exponential factor A in Eq.(5.11) increases with S_3 and this increase of the prefactor term starts dominating the exponential factor in the nucleation rate equation for $T \geq 200$ MeV. For larger temperatures, the nucleation rate for metastable vacuum bubbles become larger than the true vacuum bubbles. The nucleation rates of metastable and true vacuum bubble at temperature 215 MeV are of the order of $\sim 1.5 \times 10^{-2}$ fm$^{-}4$ and 7.7×10^{-3} fm^{-4} respectively. At higher temperatures, though the nucleation rate for both bubbles decrease but the metastable bubble nucleation rate remains larger. This result is very interesting as it shows that at suitable temperatures the metastable Z(3) vacua will have larger nucleation rate than the true Z(3) vacuum. Further, these metastable vacuum bubbles are also of larger size than the bubble of true vacuum. Thus one may expect a larger fraction of the QGP region to end up in the metastable Z(3) vacuum regions after the phase transition which may have interesting implications. For example, we will see below that the metastable vacuum bubble walls have much higher concentration of energy density than the true vacuum bubble walls. We will use $T = 200$ MeV for the bubble nucleation as the nucleation rate are same for both the true vacuum and metastable vacuum bubbles.

5.4 Numerical techniques

In this work, we carry out a $2+1$ dimensional field theoretic simulation of the formation and evolution of QGP phase bubbles representing the central rapidity region of QGP in RHICE. Bubbles are nucleated randomly in the confining background. We calculate the bubble profiles in $3+1$ dimension and use these profiles for the evolution in 2+1 dimensions. As explained above, this represents transverse evolution of these bubbles by field equations and their longitudinal evolution is simply given by the Bjorken longitudinal expansion [209]. We nucleate bubbles at the temperature 200 MeV at which the metastable and true vacuum bubbles have the nucleation rates of the same order $\simeq 0.024$ fm^{-4} so that the number of metastable and true vacuum bubbles seeded remains almost equal. Initially the the field $l(\vec{x})$ is zero every where and bubbles of QGP phase are nucleated over the whole lattice with random choice of their location. (Again, recall that we are using the shifted field here with $b_1 \neq 0$). Bubbles are nucleated with the condition that one bubble should not overlap with the other. We implement this condition by checking that whether the region where bubble is going to be nucleated, lies in the false vacuum or not. If in the region a bubble has seeded already, the next bubbles will be seeded at some other random position with same conditions. (These techniques for the formation and evolution of bubbles in a first order transition are the same as used in ref. [210–212].)

We take the initial temperature of the system to be zero (representing initial confining system) and it is taken to increases linearly with time up to T =400 MeV, at (proper) time $\tau = \tau_0 = 1$ fm. The bubble nucleation is possible only in the range of temperature where the transition is of first order. The barrier in between false vacuum and true vacuum as well as false vacuum and metastable vacua of Eq.(5.5) exist only for the temperature $T = 182$ MeV to $T \simeq 225$ MeV for our chosen value of $b_1 = 0.005$. The nucleation of bubbles is possible only during the time when temperature linearly increases from $T = T_c = 182$ MeV to $T \simeq 225$ MeV. In order to have a reasonable range of temperatures for bubble nucleation and evolution we nucleate bubbles at $T = 200$ MeV. Note that bubbles should also be nucleated at higher temperatures, say near $T = 225$ MeV. These will be smaller in size. Along with such bubbles there will also be subcritical bubble which shrink fast and disappear due to the surface energy domination. Such bubbles should be incorporated to account for fluctuations [210–212], but we will ignore these here.

In Relativistic Heavy Ion Collision Experiments the QGP bubbles are nucleated in the hadronic phase during the time span when temperature changes from the transition temperature to the maximum temperature $T_0 = 400$ MeV in the pre-equilibrium stage, hence this should lead to the presence of metastable and true vacuum bubbles of different sizes at a given time. These bubbles expand in hadronic background with time and ultimately the whole system gets converted to the QGP phase. We choose to seed the bubbles at a fix nucleation temperature because the QGP bubbles being nucleated in hadronic background have zero velocity initially and remain almost static during the remaining pre-equilibrium time $\simeq 0.5$ fm when temperature increases from $T = T_c = 182$ MeV to $T = T_0 = 400$ MeV. The growth of bubbles nucleated at different time and the increase in their velocity until the temperature reaches to 400 MeV from the nucleation temperature, are negligible in this short time span. Therefore our choice, for simplicity to seed bubbles at fixed temperature is a reasonable approximation. We choose $T = 200$ MeV as at this temperature the true vacuum and the metastable vacuum bubbles have almost equal nucleation rate and both kind of bubbles are possible with equal probability. This provides us a better opportunity to study the dynamics of metastable vacuum bubbles together with that of true vacuum bubbles and its effect on true vacuum bubbles evolution.

After nucleation, bubbles are evolved by time dependent equation of motion in the Minkowski space [213]

$$\frac{\partial^2 l_j}{\partial \tau^2} + \frac{1}{\tau}\frac{\partial l_j}{\partial \tau} - \frac{\partial^2 l_j}{\partial x^2} - \frac{\partial^2 l_j}{\partial y^2} = -\frac{g^2}{2NT^2}\frac{\partial V(l)}{\partial l_j}; \quad j = 1, 2 \tag{5.12}$$

with $\frac{\partial l_j}{\partial \tau} = 0$ at $\tau = 0$ and $l = l_1 + i l_2$.

We take a 2000×2000 lattice with physical size 16 fm x 16 fm. (as appropriate for, say Au-Au collision at RHICE). We take this lattice as the transverse plane of the QGP formed in a central collision and consider the longitudinal extension of 1 fm in the mid rapidity region. The evolution of metastable and true vacuum bubbles with different $Z(3)$ vacuum inside gives rise to the domain wall and string networks. The domain walls form when the two bubbles of different $Z(3)$ vacua coalesce with each other. The intersection of three domain walls forms a string. In our simulation these objects are formed in the transverse plane. Hence, the domain walls appear as curves while the cross section of three dimensional strings appear as vortices.

In the relativistic heavy ion collision, the thermalization time for a Au - Au collision at 200 MeV is expected to be $\tau \leq 1$ fm time. As mentioned above, we model the system in our simulation such that there is a linear increase in temperature in the pre-equilibrium stage. It starts from $T = 0$ and reaches to a maximum value of $T = 400$ within time $\tau = 0$ to $\tau = \tau_0 = 1$ fm. After that it decreases according to Bjorken's scaling due to the continued expansion in longitudinal direction [209]

$$T(\tau) = T(\tau_0)\left(\frac{\tau_0}{\tau}\right)^{1/3} \tag{5.13}$$

In our numerical simulation, we evolve the field using the periodic, fixed, and free boundary conditions for the square lattice. We present our results for the free boundary condition case where the field (waves) crossing the boundary during evolution go out permanently. This condition minimizes effects due to boundary points in the evolution of field (field reflection from boundary points in fixed boundary condition and mirror reflection as in periodic boundary condition). We use additional dissipation in a thin strip of ten points near the boundary to reduce the (minor) boundary effects in the use of free boundary conditions. For representing the situation of heavy ion collision experiments we nucleate bubbles within a circular region of 8 fm radius on the lattice of physical size 16 fm x 16 fm. With $\Delta x = 0.008$ fm, we use $\Delta t = \Delta x/\sqrt{2}$ and $\Delta t = 0.9\Delta x/\sqrt{2}$ to satisfy the Courant stability criteria. The stability and accuracy of the simulation is checked using the conservation of energy during simulation. The total energy fluctuations remains few percent without any net increase or decrease of total energy in the absence of dissipative $\dot{l}$ term in Eq.(5.12) as well as any other dissipation for periodic and fixed boundary condition.

5.5 Results of the simulation

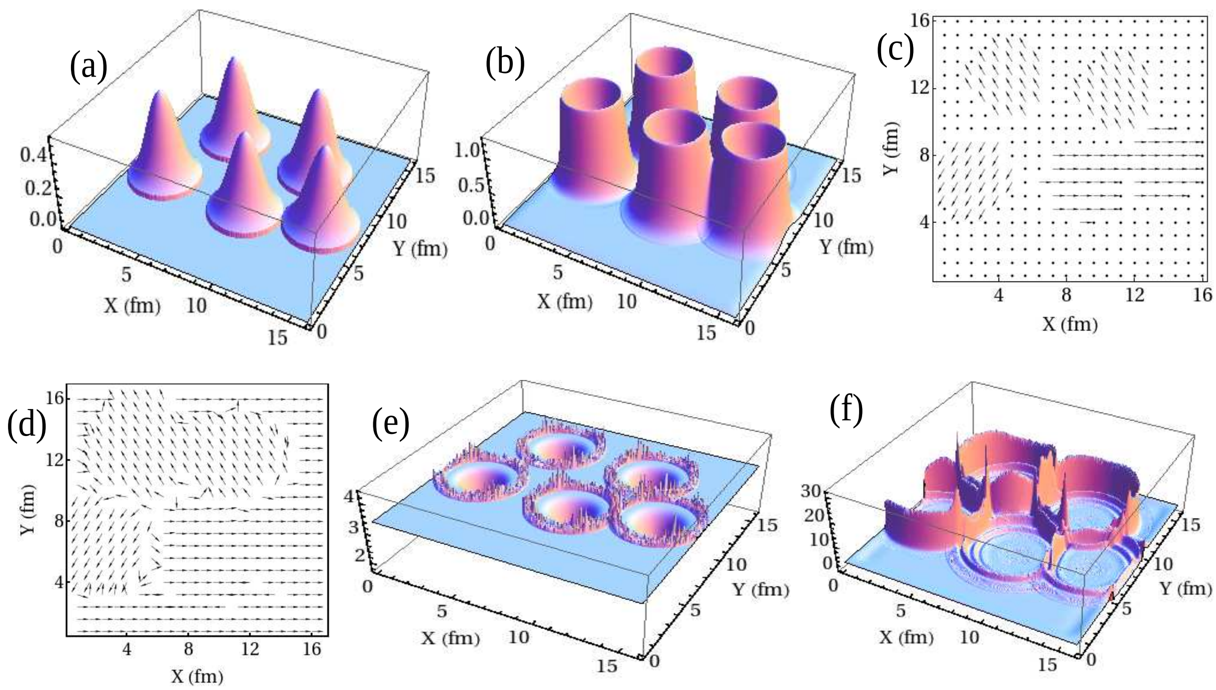

Figure 5.3: (a) and (b) show plots of profiles of l at $\tau = 0.5$ fm and 1.5 fm respectively showing expansion of bubbles. (c),(d) show the plots of the phase of l at $\tau = 0.5$ and 3.2 fm. (e) and (f) show the surface plots of energy density (in GeV/fm^3) at $\tau = 0.75$ and 2.6 fm showing very different energetics of the walls of the true vacuum bubbles and the metastable vacuum bubbles.

General picture of the phase transition remains similar to the case of $b_1 = 0$ discussed in [107], but there are important differences. We show in Fig.5.3 the various stages of the formation and evolution of different Z(3) bubbles and subsequent formation and evolution of Z(3) walls and strings. In order that one can compare with the case discussed in ref. [107] for $b_1 = 0$ case, we present in Fig.5.3 the case of 5 bubbles in a 16 fm $\times$ 16 fm region, similar to the case discussed in ref. [107]. Fig.5.3(a) shows the initial plot of $l(x)$ showing nucleation of 5 bubbles at $\tau = 0.5$ fm. Fig.5.3(b) shows the plot of $l(x)$ at $\tau = 1.5$ fm showing the expansion of bubbles. Fig.5.3(c) shows the plot of the phase of $l(x)$ at the initial stage and Fig.5.3(d) shows the phase plot at $\tau = 3.2$ fm showing clearly the formation of domain walls and a QGP string near (x=8 fm,y=9 fm). The important difference in the dynamics of true vacuum bubbles and the metastable vacuum bubbles can be seen in the surface plots of energy density (in GeV/fm^3) at $\tau = 0.75$ fm (Fig.5.3(e)) and at $\tau = 2.6$ fm (Fig.5.3(f)). Note that in all the figures we plot energy density in GeV/fm^3 as we are considering the central rapidity region with thickness of about 1 fm. With similar energy densities to begin with, by the time $\tau = 2.6$ fm, the energy density at the walls of bubbles of true vacuum is much smaller than the energy density of walls for the false vacuum bubbles.

5.5.1 Variance of energy density

General evolution of bubble coalescence and formation of walls and strings are similar to those shown in ref. [107] for the $b_1 = 0$ case and we do not show those here. As we are discussing the case of relatively small value of b_1 here we do not expect dramatic effects arising from explicit symmetry breaking (e.g. from the different mechanism of production of topological objects as demonstrated in ref. [200, 201]). However, it is still important to see if there are any qualitative differences between the $b_1 = 0$ case and $b_1 \neq 0$ case. We find an interesting difference in the plot of the variance of energy density between the two cases. We calculated the variance of energy density $\Delta\varepsilon$ at each time stage to study how energy fluctuations change during the evolution. In Fig.5.4 we show the plot of $\Delta\varepsilon/\varepsilon$ as a function of proper time. Here ε is the average value of energy density at that time stage. The energy density ε decreases due to longitudinal expansion, hence we

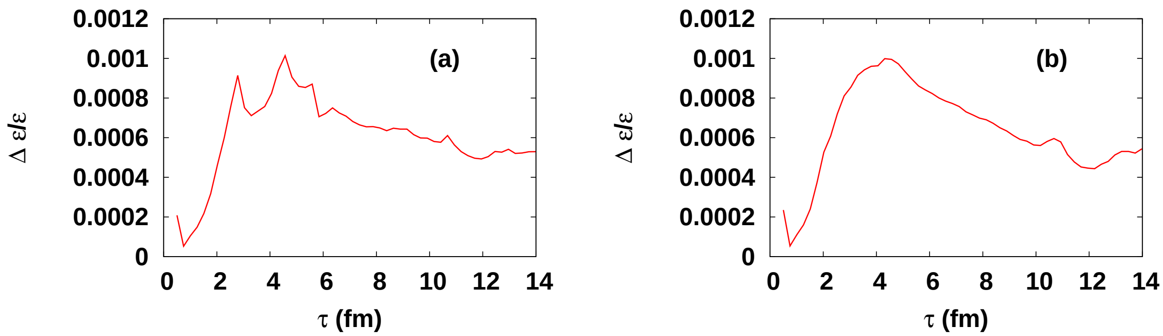

Figure 5.4: (a) and (b) show plots of the ratio of variance of energy density $\Delta\varepsilon$ and the average energy density ε as a function of proper time for $b_1 = 0.005$ case and $b_1 = 0$ case respectively.

plot this ratio to get an idea of relative importance of energy density fluctuations. For comparison we reproduce such a plot from ref. [107] for $b_1 = 0$ case in Fig.5.4(b). We note that fluctuations have an overall tendency to decrease in Fig.5.4(b) while there seems no such decrease in Fig.5.4(a) for the case with quark effects. Note also the presence of a peak for small times near $\tau \simeq 3$ fm in $b_1 > 0$ case. There is no such sharp peak for $b_1 = 0$ case. Remaining features of the plot can be interpreted as follows. The initial rapid drop in $\Delta\varepsilon/\varepsilon$ is due to large increase in ε during the heating stage upto $\tau = 1$ fm, followed by a rise due to increased energy density fluctuations during the stage when bubbles coalesce and bubble walls decay, as expected. The peak in the plot near $\tau = 10$ fm when T drops below T_c should correspond to the decay of domain walls and may provide a signal for the formation and subsequent decay of such objects in RHICE.

The small peak at short times for $b_1 > 0$ case seems to arise from the difference between the collisions of metastable vacuum bubbles and true vacuum bubbles and hence seems of qualitative importance. We have checked for various situations, different number of bubbles etc. and this peak is always present. Fig.5.5 shows different cases, for number of bubbles ranging from 4 to 10 and we see the presence of this peak in all these cases.

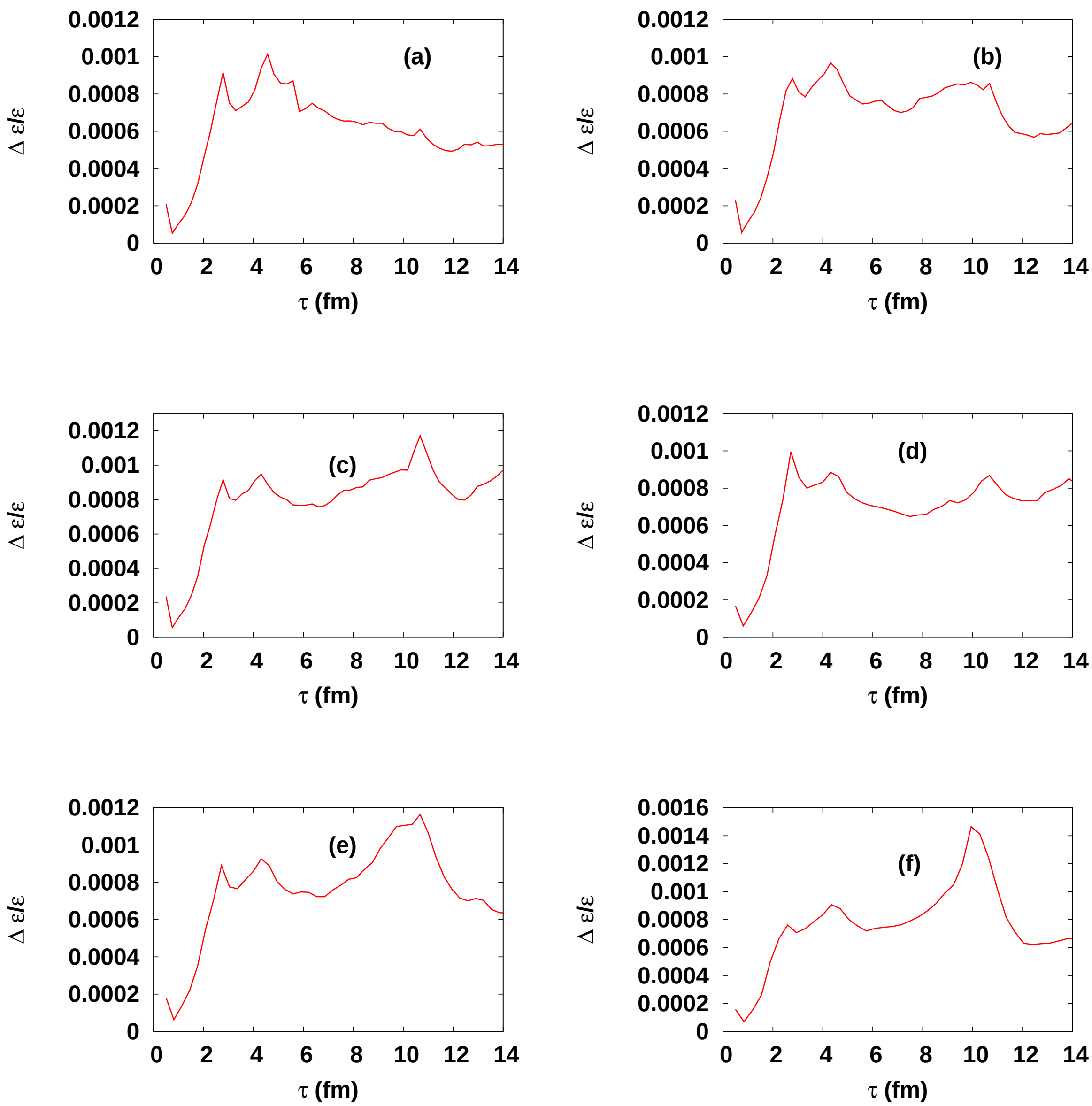

Figure 5.5: Plots of the ratio $\Delta\varepsilon/\varepsilon$ as a function of proper time for $b_1 = 0.005$ case for different number of bubbles. (a) - (f) show curves for number of bubbles = 4,5,5(different realization),7,8, and 10, respectively. Note the presence of small peak for short times in all these cases. Also note that there is no overall decrease for large times as was seen in Fig.5.4(b) for $b_1 = 0$ case.

5.5.2 Wall velocity

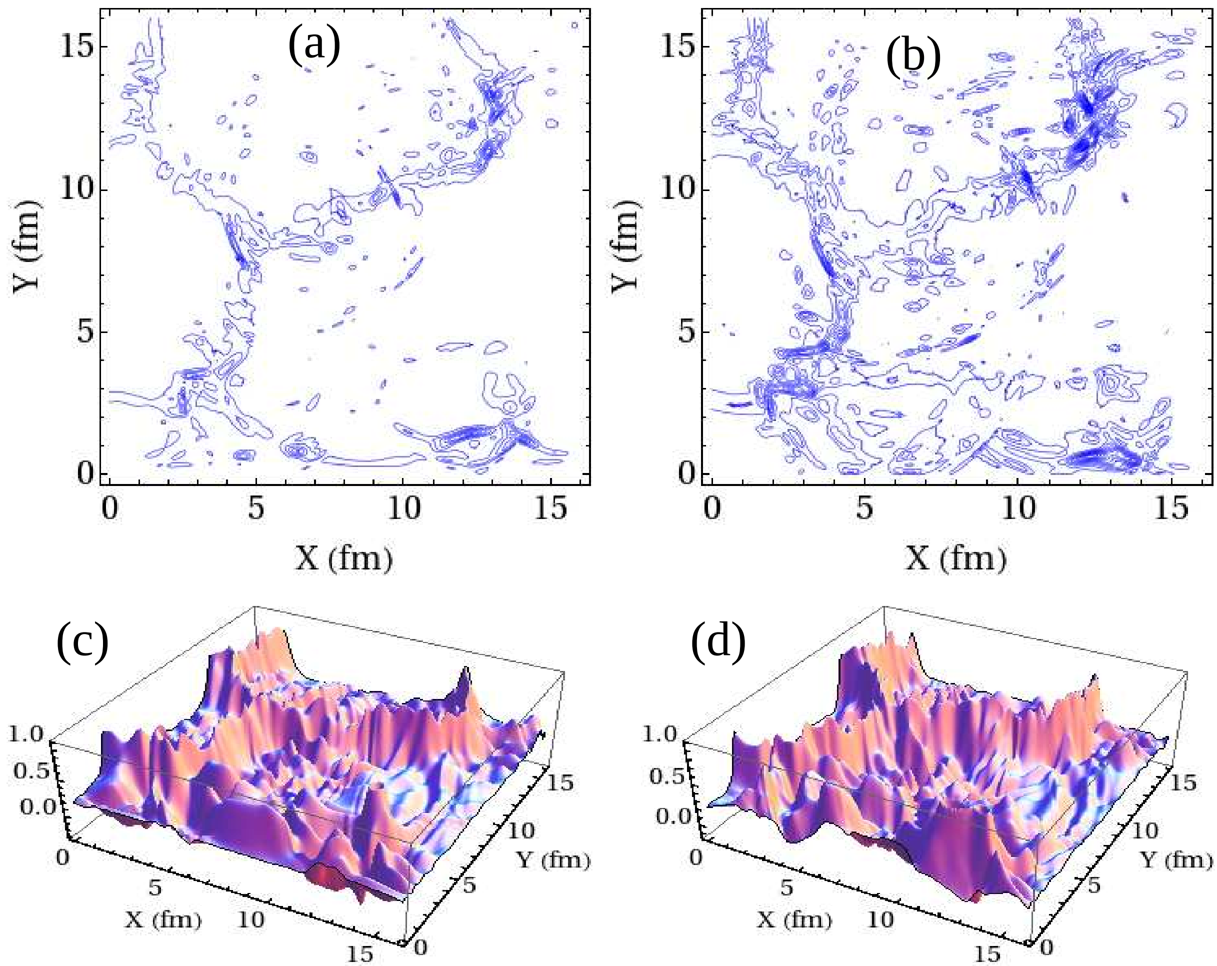

Figure 5.6: Contour plot of energy density at (a) $\tau = 7.2$ fm and (b) at $\tau = 7.8$ fm. Wall portion near x=14 fm, y=12 fm in (a) is seen to move towards left in (b) with large velocity. (c) and (d) show the profile plots of $l_0 - l$ at these stages confirming the motion of the domain wall.

An important difference we note is in the wall velocity. We have estimated wall velocities for the domain walls separating the two degenerate metastable Z(3) vacua, and the metastable and the true vacuum. We find that the typical velocity of the domain walls

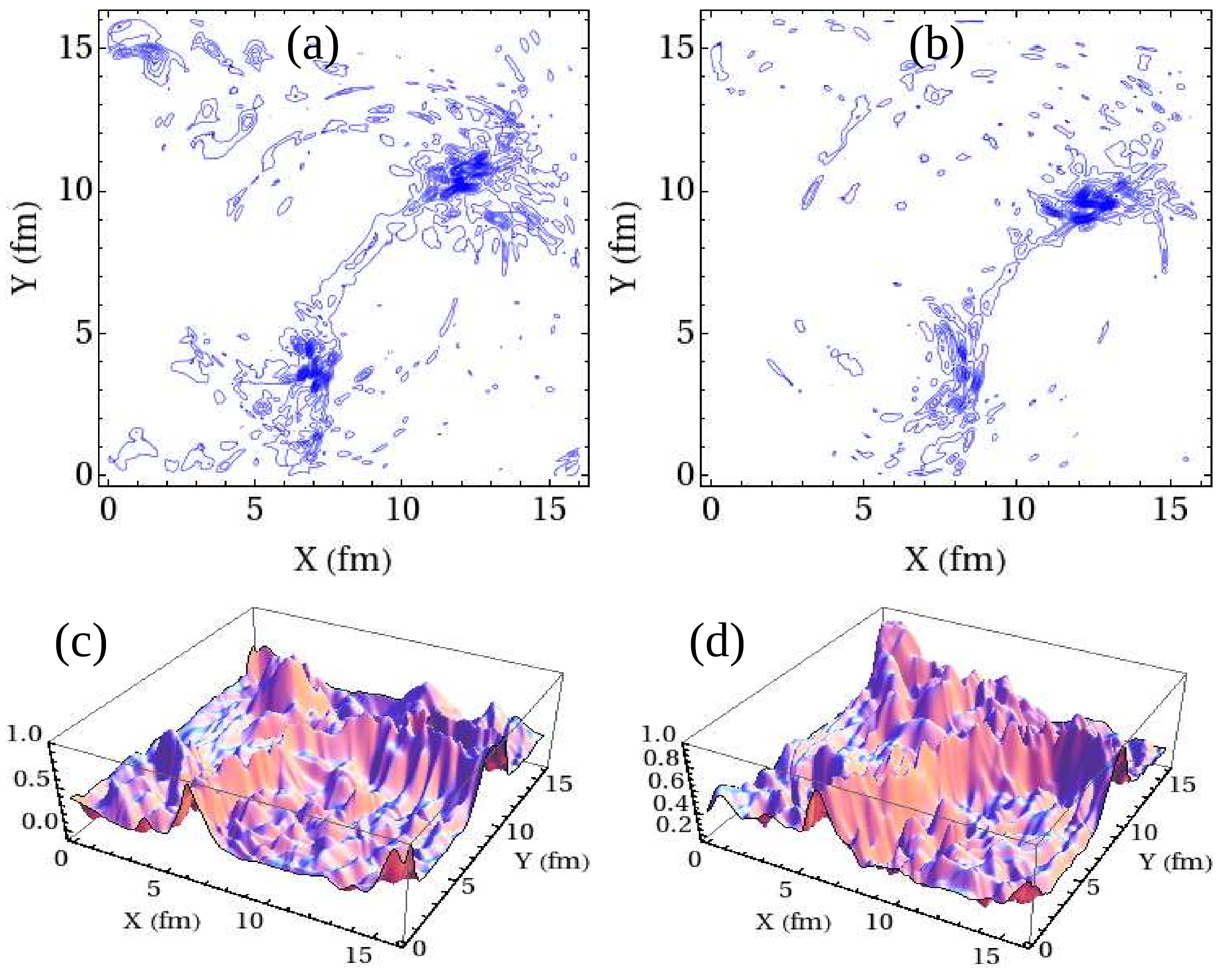

Figure 5.7: A different realization of 5 bubble nucleation. Contour plot of energy density at (a) τ = 9.6 fm and (b) at τ = 10.9 fm. Wall portion near x=9 fm, y=8 fm in (a) is seen to move towards lower right in (b) with large velocity. (c) and (d) show the profile plots of $l_0 - l$ at these stages confirming the motion of the domain wall.

separating the two (degenerate) metastable vacua is 0.7 - 0.8, similar to that obtained in ref. [107] for $b_1 = 0$ case. This is certainly expected. However, the velocity of domain wall separating the true vacuum and the metastable vacuum is found to be much larger in many cases, close to 1. Very accurate wall velocity estimates are not possible due to uncertainties in identifying wall location (with dynamically evolving wall profile). We show in Fig.5.6 and Fig.5.7 two different cases of 5 bubble nucleations (with different locations and phases inside the bubbles). Contour plots of energy density are shown in Fig.5.6(a) and Fig.5.6(b) at $\tau = 7.2$ and 7.8 fm (temperature at these stages is 208 and 201 MeV respectively). The portion of the domain wall near x = 14 fm, y = 12 fm in Fig.5.6(a) is seen to move towards left in Fig.5.6(b) with $v \simeq 1$. This is confirmed by the profile plot of $l_0 - l$ in Figs.5.6(c) and 5.6(d) at same stages, $\tau = 7.2$ and 7.8 fm respectively.

Fig.5.7 shows a different case of 5 bubble nucleation. (a) and (b) show the contour plots of energy density at $\tau = 9.6$ and 10.9 fm. Temperature at these stages is $T =$ 188 and 180 MeV (note, this is slightly below T_c). The location of wall in (a) is near x=9 fm,y=8 fm and this is seen to move towards lower right corner. This wall motion is confirmed by the profile plots of $l_0 - l$ in Figs.5.7(c), 5.7(d).

5.5.3 Rapid Collapse and Re-expansion

Perhaps the most dramatic difference between the present case with $b_1 \neq 0$ and the previous case [107] of $b_1 = 0$ is seen in Fig.5.8 and Fig.5.9. This shows the case of nucleation of 10 bubbles in a region of 22 fm $\times$ 22 fm. Though both of these numbers are somewhat large for RHICE, at least the size may not be too unrealistic for later stages of plasma evolution. Fig.5.8 shows a time sequence of the contour plot of energy density at $\tau = 6.44$, 8.20, 9.94, 11.34, 12.74, and 14.5 fm. The temperature at these stage is $T =$ 215.0, 198.4, 186.0, 178.0, 171.2, and 164.1 MeV respectively. Note that T is below T_c in (d) and after that. A closed domain wall is seen in the lower left region in (a) with x = 1-6 fm and y = 5-11 fm. This wall collapses rapidly by $\tau = 9.94$ fm. The collapse velocity again is seen to be close to $v \simeq 1$. Interesting dynamics is seen for later plots when an expanding front is seen from the point of collapse. It rapidly expands, again with $v \simeq 1$ all the way until last stages in (f). Presence of such an energetic expanding front is confirmed by the surface plots of energy density at the same stages as shown in

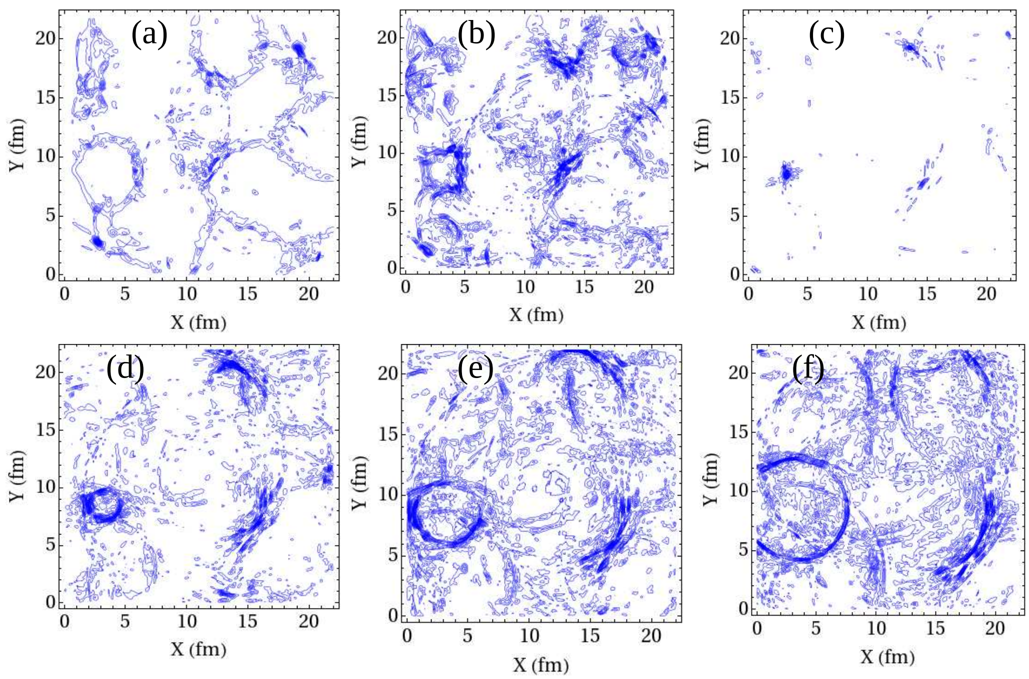

Figure 5.8: A case of 10 bubbles in 22 fm $\times$ 22 fm region. This figure shows a time sequence of contour plot of energy density showing rapid collapse of a domain wall (towards lower left) and subsequent rapid expansion of a circular front.

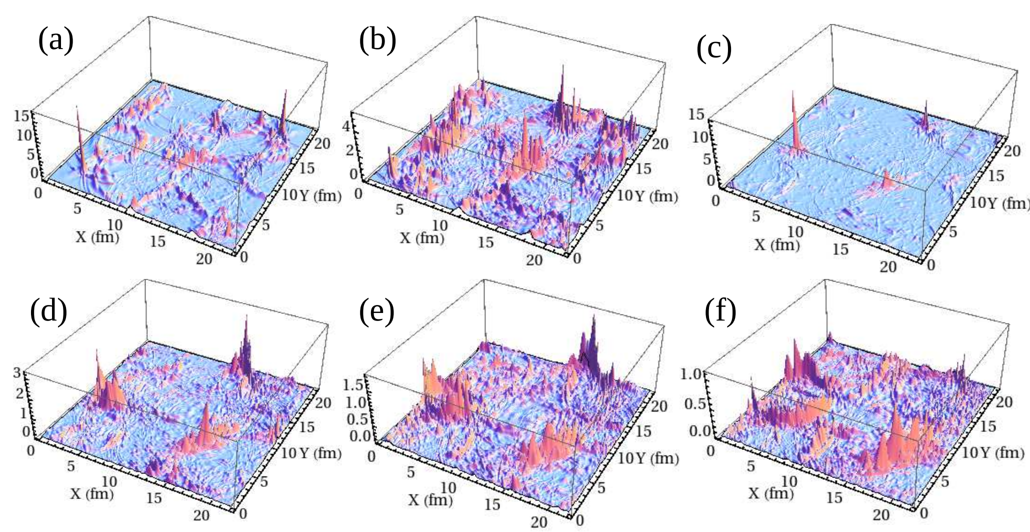

Figure 5.9: Surface plots of energy density for various stages shown in Fig.5.8

Fig.5.9. Due to very large velocity and sharp profile of the expanding front it may well represent a shock front in the plasma.

5.6 Possible experimental signatures of Z(3) walls and strings with explicit symmetry breaking

The $Z(3)$ wall network and associated strings exist only during the QGP phase, melting away when the temperature drops below T_c. However, they may leave their signatures in the distribution of final particles due to large concentration of energy density in extended regions as well as due to non-trivial scatterings of quarks and antiquarks with these objects. The extended regions of high energy density resulting from the domain walls and strings are clearly seen in our simulations and some extended structures/hot spots also survive after the temperature drops below the transition temperature T_c. This is just as was seen in the case of $b_1 = 0$ case in ref. [107]. We again mention that even the hot spot resulting from the collapse of closed domain walls in our simulations will be stretched in the longitudinal direction into an extended linear structure (resulting from the collapse of a cylindrical wall). These may be observable in the analysis of particle multiplicities. This is important especially in respect to the ridge phenomenon seen at RHIC [214–216]. In view of lasting extended energy density fluctuations from Z(3) walls, it is of interest to check if these structures can account for the ridge phenomenon.

Our results show interesting pattern of the evolution of the fluctuations in the energy density which show that these fluctuations do not decrease with time which was the case for $b_1 = 0$ case studied in ref. [107]. Especially important may be the presence of small additional peak of short times for $b_1 > 0$ case. Fluctuations near the transition stage may leave direct imprints on particle distributions. However, dileptons or direct photons should be sensitive to these fluctuations, and these may give a time history of evolution of such energy density fluctuations during the early stages. In such a case the existence of small peak for $b_1 > 0$ case may be observable.

A dramatic difference between the case of $b_1 = 0$ and $b_1 \neq 0$ is seen in Figs.5.8, 5.9. Collapse of a closed wall is expected and was seen for $b_1 = 0$ case also, though the wall speed here is much higher, close to 1. In general we have seen here that walls separating true vacuum from metastable vacuum have speeds much higher than seen for the case of $b_1 = 0$. What is qualitatively new in the present case is rapidly expanding circular front after the collapse of the wall. This front continues its speed and shape even when temperature drops below T_c. Possibility of such expanding circular (cylindrical, with longitudinal expansion) energetic fronts should have important implications on particle momenta, especially on various flow coefficients.

Another important difference due to $b_1 > 0$ is expected in investigating the interactions of quarks and antiquarks with domain walls. Earlier we had argued [107] that collapsing Z(3) walls will lead to concentration of quarks (due to small non-zero chemical potential in RHICE) in small regions [38]. This will lead to enhancement of baryons, especially at high P_T [192] due to P_T enhancement of quarks/antiquarks as they undergo repeated reflections from a collapsing wall. (There is also a possibility of spontaneous CP violation in the scattering of quarks and antiquarks from Z(3) walls, see ref. [217].) However, with $b_1 > 0$, there may also be a possibility that some Z(3) wall may actually expand (the one enclosing the true vacuum and with sufficiently large size). In that case it will have opposite effect and baryon number will be more diffused. Even the enhancement of P_T may happen for some domain walls (those which enclose metastable vacuum) while the expanding closed walls (enclosing the true vacuum) should lead to the redshift of the momenta for the enclosed quarks. All these issue need to be explored with more elaborate simulations. In this context the difference in the wall velocity between different types of Z(3) walls is of importance. While studying the effects of quark reflections from these walls and associated modification of P_T spectrum, wall velocity is of crucial importance and the presence of different types of collapsing Z(3) walls may lead to bunches of hadrons with different patterns of modified P_T spectra.

5.7 Summary

We have studied the effects of explicit symmetry breaking arising from quark effects on the formation and evolution of $Z(3)$ interfaces and associated strings. Explicit symmetry breaking makes Z(3) vacua non-degenerate with two vacua $l = z, z^2$ remaining degenerate with each other but having higher energy than the true $l = 1$ vacuum. Thus $l = z, z^2$ vacua become metastable. We have used an effective potential for the Polyakov loop expectation value $l(x)$ from ref. [37,110–112,180,182] with incorporation of explicit symmetry breaking in terms of a linear term in l and have studied the dynamics of the (C-D) phase transition in the temperature/time range when the first order transition of this model proceeds via bubble nucleation. This allows for only relatively small explicit symmetry breaking (characterized by the strength b_1 of the linear term in l). We again emphasize that, though our study is in the context of a first order transition, its results are expected to be valid even when the transition is a cross-over. This is because our focus is only on the formation of topological objects whose formation (via Kibble mechanism) only depends on the formation of a domain structure and not crucially on the dynamics of the phase transition. Though, our statements about the energetics of bubble walls etc. clearly apply only for a first order transition.

An important result we have discussed in this work relates to expected relative importance of the metastable Z(3) vacua. Due to higher energy of these vacua one would expect that bubbles with these vacua should form with relatively lower probability (even with small values of b_1 we have used). However, we find interesting results due to nontrivial interplay of the pre-exponential factor and the exponential term in the nucleation rate for the bubbles. While the exponential term leads to a decrease in the rate for metastable vacua due to larger action, the pre-exponential factor leads to an increase in the rate for larger action. For a suitable range of temperatures, which for our choice of parameter values lies between $T = 200$ MeV to $T = 225$ MeV, the metastable vacuum bubbles have the same or larger nucleation rate compared to the true vacuum bubbles. As the metastable vacuum bubbles also have larger sizes it means that a larger fraction of QGP phase may get converted to the metastable Z(3) vacua than to the true Z(3) vacuum. The dynamics of these domains being so different its effects on the evolution of plasma and various signals may be important.

Chapter 6

Conclusions

The presentation of this thesis started with the introduction of the quarks, hadrons and the quark-hadron transition in chapter one. The strong interaction properties were briefly outlined and a brief description of the strong interaction theory called Quantum Chromodynamics (QCD), has been given. The chiral symmetry and center Z(3) symmetry of strong interaction were briefly introduced. Situations of phase transitions and constructions of phase boundaries were briefly explained. The concept of order parameter was introduced. Current experimental and theoretical initiatives for the investigation of quark hadron transition, were briefly outlined.

In the next chapter, we presented the mathematical description of the QCD Lagrangian, its symmetries and the finite temperature formulation of statistical QCD in a medium. Mathematical structures of chiral symmetry and centre Z(3) symmetry were discussed. Explicit as well as spontaneous breakdown of these symmetries were also discussed. Chiral condensate as an order parameter for the chiral transition and Polyakov loop as an order parameter for confinement-deconfinement transition, were discussed. We briefly described the Landau-Ginzburg analysis of the chiral transition in the framework of linear sigma model. We gave a discussion of the phase structure of QCD. We discussed the inputs from lattice QCD simulations and effective model studies. The experimental signatures for QCD phase transition also got discussed.

The presentation of about two third of the total volume of research work in this thesis, is centered around effective model building where the features of spontaneous breakdown of both the chiral symmetry as well as the center Z(3) symmetry of QCD has been incorporated in one single model. We have combined, the chiral condensate and the Polyakov loop simultaneously to the quark degrees of freedom in the $SU_L(2) \times SU_R(2)$ and $SU_L(3) \times SU_R(3)$ linear sigma models. We thus constructed Polyakov quark meson models for two flavours and three flavours of quark. These models have incorporated the symmetries and symmetry breaking scenarios of QCD in a realistic way. These are QCD like theories which can give a realistic description of quark hadron phase transition. We have investigated in detail the phase structure, phase diagram and the interplay of chiral symmetry restoration and confinement - deconfinement phase transition.

We improved the effective potential of Polyakov loop extended Quark Meson Model (PQM) for the two quark flavour by considering the contribution of fermionic vacuum loop and explored the phase structure and thermodynamics of the resulting PQMVT model (Polyakov Quark Meson Model with Vacuum Term) in detail at nonzero as well as zero chemical potentials. We investigated the interplay of chiral symmetry restoration and connement-deconnement transition with the proper accounting of renormalized fermionic vacuum term in chapter three. We obtained, the QCD phase diagram together with the location of critical end point (CEP) in μ, and T plane in both the models PQMVT and PQM. The PQMVT model analysis was compared with the calculations in PQM model in order to bring out the effect of fermionic vacuum term on the thermodynamics of the physical observables [105]. We explored the sensitivity of the phase structure/phase diagram on the choice of Polyakov loop potential parameterization also. This sensitivity has also been explored for the different chosen values of the sigma meson mass. We used logarithmic Polyakov loop potential as well as polynomial Polyakov loop potential in our calculations.

We conclude, in our PQMVT model calculation with logarithmic Polyakov loop potential, that the chiral crossover transition for the realistic case of explicit chiral symmetry breaking, becomes quite soft and smooth at $\mu = 0$ in PQMVT model due to the proper accounting of the fermionic vacuum term contribution in the PQM model because the corresponding phase transition at $\mu = 0$ turns second order in the chiral limit of massless quarks. The chiral order parameter σ derivative has a broad double peak structure in its temperature variation at $\mu = 0$, and this structure is absent in the temperature variation of Polyakov loop derivative. Thus we conclude that the Polyakov loop (C-D) crossover transition at $\mu = 0$ is quite rapid and sharp than the chiral crossover transition which is very smooth. In a large range of μ, T values (from $\mu = 0$ and $T = 186.5$ MeV to $\mu = 294.7$ MeV and $T = 84$ MeV), the chiral transition remains a crossover and it keeps on becoming sharper with the increase in chemical potential till the point of second order transition at μ_{CEP} is reached in the PQMVT model. Since the chiral transition in the massless quark limit is first order at zero chemical potential, the corresponding crossover transition for the realistic case has been found to be quite sharp and rapid in the PQM model without any vacuum term. Further the chiral transition remains a crossover in quite a small range only from $\mu = 0$ and $T_c^\chi = 171.5$ MeV to $\mu = 81$ MeV and $T_c^\chi = 167$ MeV in the PQM model calculations. Here T_c^χ is pseudocritical temperature for chiral transition.

Instead of logarithmic form, if we take polynomial form for Polyakov loop potential in our PQMVT model calculation, the temperature derivatives of Polyakov loop field Φ and its conjugate Φ^* has distinct non coincident double peak structure in the chemical potential range $\mu > 200$ MeV to $\mu_{CEP} = 293.6$ MeV and we do not find any double peak structure near $\mu = 0$ in the temperature derivative of σ field.

The phase diagram together with the location of critical end point (CEP) has been obtained in μ, and T plane for $m_\sigma = 500$ MeV in both the models PQMVT and PQM with logarithmic Polyakov loop potential. The structure of the phase diagram is found to be very sensitive to the chosen value of sigma meson mass. For the value $m_\sigma = 600$ MeV, the transition becomes a crossover in the entire μ and T plane for the PQMVT model calculation. We do not find a coincident chiral and confinement-deconfinement crossover transitions in the PQMVT model as the chiral crossover transition line lies above the crossover line for the confinement-deconfinement transition. Our results of the PQMVT model calculation with logarithmic Polyakov loop potential, are in tune with the standard scenario where chiral symmetry restoration occurs at a higher pseudocritical temperature than the confinement-deconfinement transition temperature. The critical end point (CEP) gets shifted close to the chemical potential axis ($\mu_{CEP} = 294.7$ MeV, $T_{CEP} = 84.0$ MeV) in PQMVT model because the chiral crossover transition at $\mu = 0$ emerging from a second order phase transition in the chiral limit, becomes quite soft and smooth due to the effect of fermionic vacuum contribution in the effective potential and further it remains a crossover for large values of the chemical potential. The chiral and confinement-deconfinement crossover transition lines are coincident in the PQM model and its' CEP gets located near the temperature axis at $\mu_{CEP} = 81$ MeV and $T_{CEP} = 167$ MeV because the chiral crossover at $\mu = 0$, having the background of a first order phase transition in the chiral limit, is quite rapid and sharp and soon it gets converted to a first order phase transition as we increase the chemical potential.

The sensitive dependence of the phase structure and location of the critical end point, has also been explored by calculating another phase diagram for $m_\sigma = 500$ MeV taking polynomial choice of Polyakov loop potential in the PQMVT model. We conclude that the chiral crossover transition line, lies above the deconfinement crossover lines for the Φ and Φ^* fields in the chemical potential range $\mu = 0$ to $\mu = 210 - 225$ MeV. Deconfinement crossover transition lines for fields Φ and Φ^*, cross the chiral crossover phase boundary around $\mu \approx 210$ MeV and get located above it from $\mu > 210$ MeV to $\mu = \mu_{CEP} = 293.6$ MeV. Chiral symmetry restoration occurs earlier than the deconfinement transition in this region of the phase diagram. Thus we are finding a quarkyonic phase like region of confinement with chiral symmetry in our PQMVT model calculations with polynomial choice for Polyakov loop potential.

In the next work presented in chapter four, we investigated the influence of Polyakov loop on meson mass and mixing angle calculations in scalar and pseudoscalar sector of mesons, in the framework of generalized $2 + 1$ flavour quark meson linear sigma model enlarged with the inclusion of the Polyakov loop [101]. We derived the modification of meson masses due to the $\bar{q}q$ contribution in the presence of Polyakov loop. We studied how the inclusion of Polyakov loop, qualitatively and quantitatively affects the convergence of the masses of chiral partners, when the parity doubling takes place as the temperature is increased through T_c and the partial restoration of chiral symmetry is achieved. Further, we investigated the effect of Polyakov loop on the interplay of $SU_A(3)$ chiral symmetry and $U_A(1)$ symmetry restoration. We used two different forms of the effective Polyakov loop potential for the calculation, namely, the polynomial potential and logarithmic potential. In order to investigate the influence of Polyakov loop potential on chiral symmetry restoration, these calculations were compared with the corresponding results in the quark meson sigma (QMS) model.

Comparison of pseudocritical temperatures, calculated from the inflection points of the temperature variation of order parameters σ, Φ and Φ^* indicates, that the chiral transition got shifted to the higher temperatures as a result of the inclusion of the Polyakov loop in the QMS model. We further observed that the variation of the nonstrange condensate in the $T/T_c^{\chi} = 0.8$ to 1.2 range becomes quite sharp due to the effect of the Polyakov loop potential in our calculation in PQMS models. We infer from the curves in the PQMS models that the inclusion of the Polyakov loop potential in the QMS model together with the presence of axial anomaly, triggers an early and significant melting of the strange condensate. The interesting physical consequences of the earlier melting of the strange condensate are an early emergence of mass degeneration trend in the masses of the chiral partners (K, κ) and (η, f_0) and an early setting up of a $U_A(1)$ restoration trend.

The mass degeneration of chiral partners (σ, π) and (a_0, η') in the close vicinity of $T/T_c^\chi = 1.0$ on the reduced temperature scale, becomes sharper and faster in our calculations in the PQMS model. This sharpening of the mass variations in the small neighborhood of $T/T_c^\chi = 1$ results due to the stronger and sharper melting of the non-strange condensate triggered by the presence of the Polyakov loop potential in the QMS model. Thus, we conclude also from the behavior of the chiral partners that the net effect of the Polyakov loop inclusion in the QMS model, is to make a sharper occurrence of the chiral $SU(2)_L \times SU(2)_R$ symmetry restoration transition in the nonstrange sector. Further, the mass degeneration of chiral partners (K, κ) with η does not occur when the value of the reduced temperature is equal to one, it sets up early in the PQMS models at $T/T_c^\chi = 1.3$, while it occurs at $T/T_c^\chi = 1.5$ in the QMS model. In the PQMS models, the intersection point of the f_0 and η masses, occurs early when the reduced temperature $T/T_c^\chi = 1.3$, while in the pure QMS model this intersection point is found at $T/T_c^\chi = 1.7$. This trend of mass degeneration emerges, again as a result of the sharper and stronger melting of the strange condensate in the influence of the Polyakov loop potential in the PQMS models.

The inclusion of the Polyakov loop potential in the PQMS models also effects an early set up of the $U_A(1)$ restoration trend on the reduced temperature scale.

The smooth approach of the pseudoscalar mixing angle θ_P towards the ideal mixing in the QMS model, becomes sharper and faster in the PQMS models due to the influence of the Polyakov loop potential. Further, in comparison to QMS model results, the ideal mixing on the reduced temperature scale is achieved earlier in the PQMS models.

We have developed a new and different approach for investigating the dynamics of quark hadron phase transition. This work completes the last chapter (chapter five) of the thesis. In this approach, we exploited the non trivial topology of spontaneously broken, center Z(3) symmetric vacuum of pure gauge QCD. This non trivial topology, leads to the exciting possibility of topologically non-trivial structures such as Z(3) domain walls and associated QGP strings in the quark-gluon plasma phase [107]. Relativistic heavy-ion collision experiments (RHICE), give us an opportunity where domain walls and strings arising in a relativistic quantum field theory, can be investigated under laboratory control. In earlier works [38, 106, 107], various aspects of existence of these objects in cosmology as well as in RHICE, have been discussed. These topological objects arise in the high temperature deconfined phase of QCD due to spontaneous breaking of the Z(3) global symmetry of finite temperature QCD, where Z(3) is the center of the $SU(3)$ color gauge group of QCD. Spontaneous breaking of Z(3) symmetry arises from the non-zero expectation value of the Polyakov loop, $l(x)$, which is an order parameter for the confinement-deconfinement phase transition for pure gauge theory [12, 32]. The interpolation of $l(x)$ between three different degenerate $Z(3)$ vacua leads to the existence of domain walls (interfaces) together with topological strings when the three interfaces make a junction. We call these strings as QGP strings [107].

In the present work, we studied the effects of explicit symmetry breaking arising from quark effects on the formation and evolution of $Z(3)$ interfaces and associated strings. Explicit symmetry breaking makes Z(3) vacua non-degenerate with two vacua $l = z, z^2$ remaining degenerate with each other but having higher energy than the true $l = 1$ vacuum. Thus $l = z, z^2$ vacua become metastable. We have used an effective potential for the Polyakov loop expectation value $l(x)$ from ref. [37,110–112,180,182] with incorporation of explicit symmetry breaking in terms of a linear term in l and have studied the dynamics of the (C-D) phase transition in the temperature/time range when the first order transition of this model proceeds via bubble nucleation. This allows for only relatively small explicit symmetry breaking (characterized by the strength b_1 of the linear term in l).

The $Z(3)$ wall network and associated strings exist only during the QGP phase, melting away when the temperature drops below T_c. However, they may leave their signatures in the distribution of final particles due to large concentration of energy density in extended regions as well as due to non-trivial scatterings of quarks and antiquarks with these objects. The extended regions of high energy density resulting from the domain walls and strings are clearly seen in our simulations and some extended structures/hot spots also survive after the temperature drops below the transition temperature T_c. This is just as was seen in the case of $b_1 = 0$ case in ref. [107]. We again mention that even the hot spot resulting from the collapse of closed domain walls in our simulations will be stretched in the longitudinal direction into an extended linear structure (resulting from the collapse of a cylindrical wall). These may be observable in the analysis of particle multiplicities. This is important especially in respect to the ridge phenomenon seen at RHIC [214–216]. In view of lasting extended energy density fluctuations from Z(3) walls, it is of interest to check if these structures can account for the ridge phenomenon.

Our results show interesting pattern of the evolution of the fluctuations in the energy density which show that these fluctuations do not decrease with time which was the case for $b_1 = 0$ case studied in ref. [107]. Especially important may be the presence of small additional peak of short times for $b_1 > 0$ case. Fluctuations near the transition stage may leave direct imprints on particle distributions. However, dileptons or direct photons should be sensitive to these fluctuations, and these may give a time history of evolution of such energy density fluctuations during the early stages. In such a case the existence of small peak for $b_1 > 0$ case may be observable.

A dramatic difference between the case of $b_1 = 0$ and $b_1 \neq 0$ is seen in Fig.5.8 and Fig.5.9. Collapse of a closed wall is expected and was seen for $b_1 = 0$ case also, though the wall speed here is much higher, close to 1. In general we have seen here that walls separating true vacuum from metastable vacuum have speeds much higher than seen for the case of $b_1 = 0$. What is qualitatively new in the present case is rapidly expanding circular front after the collapse of the wall. This front continues its speed and shape even when temperature drops below T_c. Possibility of such expanding circular (cylindrical, with longitudinal expansion) energetic fronts should have important implications on particle momenta, especially on various flow coefficients.

Another important difference due to $b_1 > 0$ is expected in investigating the interactions of quarks and antiquarks with domain walls. Earlier it had been argued [107] that collapsing Z(3) walls will lead to concentration of quarks (due to small non-zero chemical potential in RHICE) in small regions [38]. This will lead to enhancement of baryons, especially at high P_T [192] due to P_T enhancement of quarks/antiquarks as they undergo repeated reflections from a collapsing wall. (There is also a possibility of spontaneous CP violation in the scattering of quarks and antiquarks from Z(3) walls, see ref. [217].) However, with $b_1 > 0$, there may also be a possibility that some Z(3) wall may actually expand (the one enclosing the true vacuum and with sufficiently large size). In that case it will have opposite effect and baryon number will be more diffused. Even the enhancement of P_T may happen for some domain walls (those which enclose metastable vacuum) while the expanding closed walls (enclosing the true vacuum) should lead to the redshift of the momenta for the enclosed quarks. All these issue need to be explored with more elaborate simulations. In this context the difference in the wall velocity between different types of Z(3) walls is of importance. While studying the effects of quark reflections from these walls and associated modification of P_T spectrum, wall velocity is of crucial importance and the presence of different types of collapsing Z(3) walls may lead to bunches of hadrons with different patterns of modified P_T spectra.

Chapter 7

appendix

7.1 First and second partial derivatives of grand potential

First partial derivative of logarithmic Polyakov loop potential with respect to chemical potential and temperature

$$\frac{\partial\mathcal{U}_{\log}}{\partial\mu} = \mathrm{T}^4\Big[-\frac{\mathrm{a(T)}}{2}\Big\{\frac{\partial\Phi}{\partial\mu}\Phi^* + \Phi\frac{\partial\Phi^*}{\partial\mu}\Big\} - 6\mathrm{b(T)}\ \mathrm{X}_\mu\Big] \tag{7.1}$$

$$\begin{aligned}\frac{\partial\mathcal{U}_{\log}}{\partial\mathrm{T}} = {} & 4\mathrm{T}^3\Big[-\frac{\mathrm{a(T)}}{2}\Phi^*\Phi + \mathrm{b(T)}\ln[W]\Big] + \mathrm{T}^4\Big[-\frac{1}{2}\Big\{\frac{\mathrm{da(T)}}{\mathrm{dT}}\Phi\Phi^* + \mathrm{a(T)}\frac{\partial\Phi}{\partial\mathrm{T}}\Phi^* + \mathrm{a(T)}\Phi\frac{\partial\Phi^*}{\partial\mathrm{T}}\Big\} \\ & + \frac{\mathrm{db(T)}}{\mathrm{dT}}\ln[\mathrm{W}] - 6\mathrm{b(T)}\ \mathrm{X_T}\Big]\end{aligned} \tag{7.2}$$

where

$$X_y = \frac{(1+\Phi\Phi^*)\left(\Phi\frac{\partial\Phi^*}{\partial\mathrm{y}} + \Phi^*\frac{\partial\Phi}{\partial\mathrm{y}}\right) - 2\left(\Phi^2\frac{\partial\Phi}{\partial\mathrm{y}} + \Phi^{*2}\frac{\partial\Phi^*}{\partial\mathrm{y}}\right)}{\mathrm{W}} \tag{7.3}$$

$$W = 1 - 6\Phi^*\Phi + 4(\Phi^{*3} + \Phi^3) - 3(\Phi^*\Phi)^2 \tag{7.4}$$

Second partial derivative of logarithmic Polyakov loop potential with respect to chemical potential and temperatures

$$
\begin{aligned}
\frac{\partial^2 \mathcal{U}_{\log}}{\partial \mu^2} &= \mathrm{T}^4\Big[-\frac{\mathrm{a(T)}}{2}\Big(\frac{\partial^2\Phi}{\partial\mu^2}\Phi^* + 2\frac{\partial\Phi}{\partial\mu}\frac{\partial\Phi^*}{\partial\mu} + \Phi\frac{\partial^2\Phi^*}{\partial\mu^2}\Big) - 36\mathrm{b(T)}{\mathrm{X}_\mu}^2 \\
&\quad -\frac{6\mathrm{b(T)}}{W}\Big\{\left(\Phi\frac{\partial\Phi^*}{\partial\mu} + \Phi^*\frac{\partial\Phi}{\partial\mu}\right)^2 + (1+\Phi\Phi^*)\left(\Phi\frac{\partial^2\Phi^*}{\partial\mu^2} + 2\frac{\partial\Phi}{\partial\mu}\frac{\partial\Phi^*}{\partial\mu} + \Phi^*\frac{\partial^2\Phi}{\partial\mu^2}\right) \\
&\quad -2\left(\Phi^2\frac{\partial^2\Phi}{\partial\mu^2} + 2\Phi\left(\frac{\partial\Phi}{\partial\mu}\right)^2 + \Phi^{*2}\left(\frac{\partial^2\Phi^*}{\partial\mu^2}\right) + 2\Phi^*\left(\frac{\partial\Phi^*}{\partial\mu}\right)^2\right)\Big\}\Big]
\end{aligned} \tag{7.5}
$$

$$
\begin{aligned}
\frac{\partial^2 \mathcal{U}_{\log}}{\partial T^2} &= 12\mathrm{T}^2\Big[-\frac{\mathrm{a(T)}}{2}\Phi^*\Phi + \mathrm{b(T)}\ln[\mathrm{W}]\Big] \\
&\quad +8\mathrm{T}^3\Big[-\frac{1}{2}\Big(\frac{\mathrm{da(T)}}{\mathrm{dT}}\Phi\Phi^* + \mathrm{a(T)}\frac{\partial\Phi}{\partial\mathrm{T}}\Phi^* + \mathrm{a(T)}\Phi\frac{\partial\Phi^*}{\partial\mathrm{T}}\Big) + \frac{\mathrm{db(T)}}{\mathrm{dT}}\ln[\mathrm{W}] - 6\mathrm{b(T)}X_T\Big] \\
&\quad +\mathrm{T}^4\Big[-\frac{1}{2}\Big(\frac{\mathrm{d^2a(T)}}{\mathrm{dT^2}}\Phi\Phi^* + \mathrm{a(T)}\frac{\partial^2\Phi}{\partial\mathrm{T}^2}\Phi^* + \mathrm{a(T)}\Phi\frac{\partial^2\Phi^*}{\partial\mathrm{T}^2}\Big) \\
&\qquad -\Big(\frac{\mathrm{da(T)}}{\partial\mathrm{T}}\frac{\partial\Phi}{\partial\mathrm{T}}\Phi^* + \frac{\mathrm{da(T)}}{\mathrm{dT}}\Phi\frac{\partial\Phi^*}{\partial\mathrm{T}} + \mathrm{a(T)}\frac{\partial\Phi}{\partial\mathrm{T}}\frac{\partial\Phi^*}{\partial\mathrm{T}}\Big) + \frac{\mathrm{d^2b(T)}}{\mathrm{dT^2}}\ln[\mathrm{W}]\Big] \\
&\quad -12\frac{\mathrm{db(T)}}{\mathrm{dT}}\mathrm{X_T} - 36\mathrm{b(T)}\,{\mathrm{X_T}}^2 \\
&\quad -6\mathrm{b(T)}\Big[\Big\{\left(\Phi\frac{\partial\Phi^*}{\partial\mathrm{T}} + \Phi^*\frac{\partial\Phi}{\partial\mathrm{T}}\right)^2 + (1+\Phi\Phi^*)\left(\Phi\frac{\partial^2\Phi^*}{\partial\mathrm{T}^2} + 2\frac{\partial\Phi}{\partial\mathrm{T}}\frac{\partial\Phi^*}{\partial\mathrm{T}} + \Phi^*\frac{\partial^2\Phi}{\partial\mathrm{T}^2}\right) \\
&\qquad -2\left(\Phi^2\frac{\partial^2\Phi}{\partial\mathrm{T}^2} + 2\Phi\left(\frac{\partial\Phi}{\partial\mathrm{T}}\right)^2 + \Phi^{*2}\left(\frac{\partial^2\Phi^*}{\partial\mathrm{T}^2}\right) + 2\Phi^*\left(\frac{\partial\Phi^*}{\partial\mathrm{T}}\right)^2\right)\Big\}\frac{1}{W}\Big]\Big]
\end{aligned} \tag{7.6}
$$

First partial derivative of $\Omega^{\mathrm{T}}_{q\bar{q}}$ with respect to chemical potential and temperature

$$
\frac{\partial\Omega^{\mathrm{T}}_{\mathrm{q\bar{q}}}}{\partial\mu} = -12\int\frac{\mathrm{d^3p}}{(2\pi)^3}\Big[\mathrm{T}\left(B^+_{q,\mu} + B^-_{q,\mu}\right)\Big] \tag{7.7}
$$

$$
\frac{\partial\Omega^{\mathrm{T}}_{\mathrm{q\bar{q}}}}{\partial\mathrm{T}} = -4\int\frac{\mathrm{d^3p}}{(2\pi)^3}\Big[\ln g^+_q + \ln g^-_q + 3\mathrm{T}\left(B^+_{q,T} + B^-_{q,T}\right)\Big] \tag{7.8}
$$

where

$$A_q^+ = \Phi \mathrm{e}^{-\beta \mathrm{E_q}^+} + 2\Phi^* \mathrm{e}^{-2\beta \mathrm{E_q}^+} + \mathrm{e}^{-3\beta \mathrm{E_q}^+} \tag{7.9}$$

$$A_q^- = \Phi^* \mathrm{e}^{-\beta \mathrm{E_q}^-} + 2\Phi \mathrm{e}^{-2\beta \mathrm{E_q}^-} + \mathrm{e}^{-3\beta \mathrm{E_q}^-} \tag{7.10}$$

$$B_{q,\mathrm{x}}^+ = \frac{1}{g_q^+}\Big\{A_q^+ \frac{\partial}{\partial \mathrm{x}}(-\beta \mathrm{E_q}^+) + \frac{\partial \Phi}{\partial \mathrm{x}} \mathrm{e}^{-\beta \mathrm{E_q}^+} + \frac{\partial \Phi^*}{\partial \mathrm{x}} \mathrm{e}^{-2\beta \mathrm{E_q}^+}\Big\} \tag{7.11}$$

$$B_{q,\mathrm{x}}^- = \frac{1}{g_q^-}\Big\{A_q^- \frac{\partial}{\partial \mathrm{x}}(-\beta \mathrm{E_q}^-) + \frac{\partial \Phi^*}{\partial \mathrm{x}} \mathrm{e}^{-\beta \mathrm{E_q}^-} + \frac{\partial \Phi}{\partial \mathrm{x}} \mathrm{e}^{-2\beta \mathrm{E_q}^-}\Big\} \tag{7.12}$$

Second partial derivative of $\Omega_{q\bar{q}}^{\mathrm{T}}$ with respect to chemical potential and temperature

$$\frac{\partial^2 \Omega_{\mathrm{q\bar{q}}}^{\mathrm{T}}}{\partial \mu^2} = -12\mathrm{T} \int \frac{\mathrm{d^3p}}{(2\pi)^3} \mathrm{D_{q,\mu}} \tag{7.13}$$

$$\frac{\partial^2 \Omega_{\mathrm{q\bar{q}}}^{\mathrm{T}}}{\partial \mathrm{T}^2} = -12 \int \frac{\mathrm{d^3p}}{(2\pi)^3} \Big[2\left(B_q^+ + B_q^-\right) + \mathrm{T}\ \mathrm{D_{q,T}}\Big] \tag{7.14}$$

where

$$\begin{aligned}
\mathrm{D_{q,x}} = \ & \Big[-3\left({B_q^+}^2 + {B_q^-}^2\right) \\
& + \frac{1}{g_q^+}\Big\{C_q^+\Big[\frac{\partial}{\partial \mathrm{x}}(-\beta \mathrm{E_q}^+)\Big]^2 + \left(2\frac{\partial \Phi}{\partial \mathrm{x}} \mathrm{e}^{-\beta \mathrm{E_q}^+} + 4\frac{\partial \Phi^*}{\partial \mathrm{x}} \mathrm{e}^{-2\beta \mathrm{E_q}^+}\right)\frac{\partial}{\partial \mathrm{x}}(-\beta \mathrm{E_q}^+) + A_q^+ \frac{\partial^2}{\partial^2 \mathrm{x}}(-\beta \mathrm{E_q}^+) \\
& + \left(\frac{\partial^2 \Phi}{\partial \mathrm{x}^2} + \frac{\partial^2 \Phi^*}{\partial \mathrm{x}^2}\right) \mathrm{e}^{-\beta \mathrm{E_q}^+}\Big\} \\
& + \frac{1}{g_q^-}\Big\{C_q^-\Big[\frac{\partial}{\partial \mathrm{x}}(-\beta \mathrm{E_q}^-)\Big]^2 + \left(\frac{\partial \Phi^*}{\partial \mathrm{x}} \mathrm{e}^{-\beta \mathrm{E_q}^-} + 4\frac{\partial \Phi}{\partial \mathrm{x}} \mathrm{e}^{-2\beta \mathrm{E_q}^-}\right)\frac{\partial}{\partial \mathrm{x}}(-\beta \mathrm{E_q}^-) + A_q^- \frac{\partial^2}{\partial^2 \mathrm{x}}(-\beta \mathrm{E_q}^-) \\
& + \left(\frac{\partial^2 \Phi^*}{\partial \mathrm{x}^2} + \frac{\partial^2 \Phi}{\partial \mathrm{x}^2})\right) \mathrm{e}^{-\beta \mathrm{E_q}^-}\Big\}\Big]
\end{aligned} \tag{7.15}$$

$$C_q^+ = \Phi \mathrm{e}^{-\beta \mathrm{E_q}^+} + 4\Phi^* \mathrm{e}^{-2\beta \mathrm{E_q}^+} + 3\mathrm{e}^{-3\beta \mathrm{E_q}^+} \tag{7.16}$$

$$C_q^- = \Phi^* \mathrm{e}^{-\beta \mathrm{E_q}^-} + 4\Phi \mathrm{e}^{-2\beta \mathrm{E_q}^-} + 3\mathrm{e}^{-3\beta \mathrm{E_q}^-} \tag{7.17}$$

List of Publications

1. *** Effects of quarks on the formation and evolution of Z(3) walls and strings in relativistic heavy-ion collisions.**.

   Uma Shankar Gupta (Allahabad U.), Ranjita K. Mohapatra (Inst. of Phys.), Vivek K. Tiwari (Allahabad U.), Ajit M. Srivastava (Inst. of Phys.).

   Publication recommended in **Phys. Rev. D.** e-Print: **arXiv:1111.5402 [hep-ph]**

2. *** Revisiting the Phase Structure of the Polyakov-quark-meson Model in the presence of Vacuum Fermion Fluctuations**.

   Uma Shankar Gupta, Vivek K. Tiwari. (Allahabad U.)

   Phys. Rev. D85 (2012) Issue 1, to be published online on 9 January 2012.
   e-Print: **arXiv:1107.1312 [hep-ph]**

3. **Simulation of first order confinement transition in relativistic heavy-ion collisions**.

   Uma Shankar Gupta (Allahabad U.), Ranjita K. Mohapatra (Inst. of Phys.), Vivek K. Tiwari (Allahabad U.), Ajit M. Srivastava (Inst. of Phys.).

   Indian J. Phys. 85 (2011) 115-121. e-Print: **arXiv:1111.5402 [hep-ph]**

4. **Simulation of Z(3) walls and string producrion via bubble nucleation in a quark-hadron transition**.

   Uma Shankar Gupta (Allahabad U.), Ranjita K. Mohapatra (Inst. of Phys.), Vivek K. Tiwari (Allahabad U.), Ajit M. Srivastava (Inst. of Phys.).

   Phys. Rev. D82 (2010) 074020. e-Print: **arXiv:1007.5001 [hep-ph]**

5. *** Meson Masses and Mixing Angles in 2+1 Flavor Polyakov Quark Meson Sigma Model and Symmetry Restoration Effects**.
   Uma Shankar Gupta, Vivek K. Tiwari (Allahabad U.).
   Phys. Rev. D81 (2010) 054019. e-Print: **arXiv:0911.2464 [hep-ph]**

(*) This thesis is based on these papers.

Study of Hadron Production in The Context of Quark-Hadron Phase Transition

A Thesis submitted to the

University of Allahabad

for the degree of

Doctor of Philosophy
in Science

by

Uma Shankar Gupta

under the supervision of

Dr. Vivek Kumar Tiwari

Department of Physics

University of Allahabad

Allahabad – 211002, India

Year 2011

Thesis Summary

The presentation of this thesis started with the introduction of the quarks, hadrons and the quark-hadron transition in chapter one. The strong interaction properties were briefly outlined and a brief description of the strong interaction theory called Quantum Chromodynamics (QCD), has been given. The chiral symmetry and center Z(3) symmetry of strong interaction were briefly introduced. Situations of phase transitions and constructions of phase boundaries were briefly explained. The concept of order parameter was introduced. Current experimental and theoretical initiatives for the investigation of quark hadron transition, were briefly outlined.

In the next chapter, we presented the mathematical description of the QCD Lagrangian, its symmetries and the finite temperature formulation of statistical QCD in a medium. Mathematical structures of chiral symmetry and centre Z(3) symmetry were discussed. Explicit as well as spontaneous breakdown of these symmetries were also discussed. Chiral condensate as an order parameter for the chiral transition and Polyakov loop as an order parameter for confinement-deconfinement transition, were discussed. We briefly described the Landau-Ginzburg analysis of the chiral transition in the framework of linear sigma model. We gave a discussion of the phase structure of QCD. We discussed the inputs from lattice QCD simulations and effective model studies. The experimental signatures for QCD phase transition also got discussed.

The presentation of about two third of the total volume of research work in this thesis, is centered around effective model building where the features of spontaneous breakdown of both the chiral symmetry as well as the center Z(3) symmetry of QCD has been incorporated in one single model. We have combined, the chiral condensate and the Polyakov loop simultaneously to the quark degrees of freedom in the $SU_L(2) \times SU_R(2)$ and $SU_L(3) \times SU_R(3)$ linear sigma models. We thus constructed Polyakov quark meson models for two flavours and three flavours of quark. These models have incorporated the symmetries and symmetry breaking scenarios of QCD in a realistic way. These are QCD like theories which can give a realistic description of quark hadron phase transition. We have investigated in detail the phase structure, phase diagram and the interplay of chiral symmetry restoration and confinement - deconfinement phase transition.

We improved the effective potential of Polyakov loop extended Quark Meson Model (PQM) for the two quark flavour by considering the contribution of fermionic vacuum loop and explored the phase structure and thermodynamics of the resulting PQMVT model (Polyakov Quark Meson Model with Vacuum Term) in detail at nonzero as well as zero chemical potentials. We investigated the interplay of chiral symmetry restoration and connement-deconnement transition with the proper accounting of renormalized fermionic vacuum term in chapter three. We obtained, the QCD phase diagram together with the location of critical end point (CEP) in μ, and T plane in both the models PQMVT and PQM. The PQMVT model analysis was compared with the calculations in PQM model in order to bring out the effect of fermionic vacuum term on the thermodynamics of the physical observables [1]. We explored the sensitivity of the phase structure/phase diagram on the choice of Polyakov loop potential parameterization also. This sensitivity has also been explored for the different chosen values of the sigma meson mass. We used logarithmic Polyakov loop potential as well as polynomial Polyakov loop potential in our calculations.

We conclude, in our PQMVT model calculation with logarithmic Polyakov loop potential, that the chiral crossover transition for the realistic case of explicit chiral symmetry breaking, becomes quite soft and smooth at $\mu = 0$ in PQMVT model due to the proper accounting of the fermionic vacuum term contribution in the PQM model because the corresponding phase transition at $\mu = 0$ turns second order in the chiral limit of massless quarks. The chiral order parameter σ derivative has a broad double peak structure in its temperature variation at $\mu = 0$, and this structure is absent in the temperature variation of Polyakov loop derivative. Thus we conclude that the Polyakov loop (C-D) crossover transition at $\mu = 0$ is quite rapid and sharp than the chiral crossover transition which is very smooth. In a large range of μ, T values (from $\mu = 0$ and $T = 186.5$ MeV to

$\mu = 294.7$ MeV and $T = 84$ MeV), the chiral transition remains a crossover and it keeps on becoming sharper with the increase in chemical potential till the point of second order transition at μ_{CEP} is reached in the PQMVT model. Since the chiral transition in the massless quark limit is first order at zero chemical potential, the corresponding crossover transition for the realistic case has been found to be quite sharp and rapid in the PQM model without any vacuum term. Further the chiral transition remains a crossover in quite a small range only from $\mu = 0$ and $T_c^\chi = 171.5$ MeV to $\mu = 81$ MeV and $T_c^\chi = 167$ MeV in the PQM model calculations. Here T_c^χ is pseudocritical temperature for chiral transition.

Instead of logarithmic form, if we take polynomial form for Polyakov loop potential in our PQMVT model calculation, the temperature derivatives of Polyakov loop field Φ and its conjugate Φ^* has distinct non coincident double peak structure in the chemical potential range $\mu > 200$ MeV to $\mu_{CEP} = 293.6$ MeV and we do not find any double peak structure near $\mu = 0$ in the temperature derivative of σ field.

The phase diagram together with the location of critical end point (CEP) has been obtained in μ, and T plane for $m_\sigma = 500$ MeV in both the models PQMVT and PQM with logarithmic Polyakov loop potential. The structure of the phase diagram is found to be very sensitive to the chosen value of sigma meson mass. For the value $m_\sigma = 600$ MeV, the transition becomes a crossover in the entire μ and T plane for the PQMVT model calculation. We do not find a coincident chiral and confinement-deconfinement crossover transitions in the PQMVT model as the chiral crossover transition line lies above the crossover line for the confinement-deconfinement transition. Our results of the PQMVT model calculation with logarithmic Polyakov loop potential, are in tune with the standard scenario where chiral symmetry restoration occurs at a higher pseudocritical temperature than the confinement-deconfinement transition temperature. The critical end point (CEP) gets shifted close to the chemical potential axis ($\mu_{CEP} = 294.7$ MeV, $T_{CEP} = 84.0$ MeV) in PQMVT model because the chiral crossover transition at $\mu = 0$

emerging from a second order phase transition in the chiral limit, becomes quite soft and smooth due to the effect of fermionic vacuum contribution in the effective potential and further it remains a crossover for large values of the chemical potential. The chiral and confinement-deconfinement crossover transition lines are coincident in the PQM model and its' CEP gets located near the temperature axis at $\mu_{CEP} = 81$ MeV and $T_{CEP} = 167$ MeV because the chiral crossover at $\mu = 0$, having the background of a first order phase transition in the chiral limit, is quite rapid and sharp and soon it gets converted to a first order phase transition as we increase the chemical potential.

The sensitive dependence of the phase structure and location of the critical end point, has also been explored by calculating another phase diagram for $m_\sigma = 500$ MeV taking polynomial choice of Polyakov loop potential in the PQMVT model. We conclude that the chiral crossover transition line, lies above the deconfinement crossover lines for the Φ and Φ^* fields in the chemical potential range $\mu = 0$ to $\mu = 210 - 225$ MeV. Deconfinement crossover transition lines for fields Φ and Φ^*, cross the chiral crossover phase boundary around $\mu \approx 210$ MeV and get located above it from $\mu > 210$ MeV to $\mu = \mu_{CEP} = 293.6$ MeV. Chiral symmetry restoration occurs earlier than the deconfinement transition in this region of the phase diagram. Thus we are finding a quarkyonic phase like region of confinement with chiral symmetry in our PQMVT model calculations with polynomial choice for Polyakov loop potential.

In the next work presented in chapter four, we investigated the influence of Polyakov loop on meson mass and mixing angle calculations in scalar and pseudoscalar sector of mesons, in the framework of generalized $2+1$ flavour quark meson linear sigma model enlarged with the inclusion of the Polyakov loop [2]. We derived the modification of meson masses due to the $\bar{q}q$ contribution in the presence of Polyakov loop. We studied how the inclusion of Polyakov loop, qualitatively and quantitatively affects the convergence of the masses of chiral partners, when the parity doubling takes place as the temperature is increased through T_c and the partial restoration of chiral symmetry is achieved. Further, we investigated the effect of Polyakov loop on the interplay of $SU_A(3)$ chiral symmetry and $U_A(1)$ symmetry restoration. We used two different forms of the effective Polyakov loop potential for the calculation, namely, the polynomial potential and logarithmic potential. In order to investigate the influence of Polyakov loop potential on chiral symmetry restoration, these calculations were compared with the corresponding results in the quark meson sigma (QMS) model.

Comparison of pseudocritical temperatures, calculated from the inflection points of the temperature variation of order parameters σ, Φ and Φ^* indicates, that the chiral transition got shifted to the higher temperatures as a result of the inclusion of the Polyakov loop in the QMS model. We further observed that the variation of the nonstrange condensate in the $T/T_c^\chi = 0.8$ to 1.2 range becomes quite sharp due to the effect of the Polyakov loop potential in our calculation in PQMS models. We infer from the curves in the PQMS models that the inclusion of the Polyakov loop potential in the QMS model together with the presence of axial anomaly, triggers an early and significant melting of the strange condensate. The interesting physical consequences of the earlier melting of the strange condensate are an early emergence of mass degeneration trend in the masses of the chiral partners (K, κ) and (η, f_0) and an early setting up of a $U_A(1)$ restoration trend.

The mass degeneration of chiral partners (σ, π) and (a_0, η') in the close vicinity of $T/T_c^\chi = 1.0$ on the reduced temperature scale, becomes sharper and faster in our calculations in the PQMS model. This sharpening of the mass variations in the small neighborhood of $T/T_c^\chi = 1$ results due to the stronger and sharper melting of the nonstrange condensate triggered by the presence of the Polyakov loop potential in the QMS model. Thus, we conclude also from the behavior of the chiral partners that the net effect of the Polyakov loop inclusion in the QMS model, is to make a sharper occurrence of the chiral $SU(2)_L \times SU(2)_R$ symmetry restoration transition in the nonstrange sector. Further, the mass degeneration of chiral partners (K, κ) with η does not occur when the value of the reduced temperature is equal to one, it sets up early in the PQMS models at $T/T_c^\chi = 1.3$, while it occurs at $T/T_c^\chi = 1.5$ in the QMS model. In the PQMS models, the intersection point of the f_0 and η masses, occurs early when the reduced temperature $T/T_c^\chi = 1.3$, while in the pure QMS model this intersection point is found at $T/T_c^\chi = 1.7$. This trend of mass degeneration emerges, again as a result of the sharper and stronger melting of the strange condensate in the influence of the Polyakov loop potential in the PQMS models.

The inclusion of the Polyakov loop potential in the PQMS models also effects an early set up of the $U_A(1)$ restoration trend on the reduced temperature scale.

The smooth approach of the pseudoscalar mixing angle θ_P towards the ideal mixing in the QMS model, becomes sharper and faster in the PQMS models due to the influence of the Polyakov loop potential. Further, in comparison to QMS model results, the ideal mixing on the reduced temperature scale is achieved earlier in the PQMS models.

We have developed a new and different approach for investigating the dynamics of quark hadron phase transition. This work completes the last chapter (chapter five) of the thesis. In this approach, we exploited the non trivial topology of spontaneously broken, center Z(3) symmetric vacuum of pure gauge QCD. This non trivial topology, leads to the exciting possibility of topologically non-trivial structures such as Z(3) domain walls and associated QGP strings in the quark-gluon plasma phase [3]. Relativistic heavy-ion collision experiments (RHICE), give us an opportunity where domain walls and strings arising in a relativistic quantum field theory, can be investigated under laboratory control. In earlier works [3–5], various aspects of existence of these objects in cosmology as well as in RHICE, have been discussed. These topological objects arise in the high temperature deconfined phase of QCD due to spontaneous breaking of the Z(3) global symmetry of finite temperature QCD, where Z(3) is the center of the $SU(3)$ color gauge group of QCD. Spontaneous breaking of Z(3) symmetry arises from the non-zero expectation value of the Polyakov loop, $l(x)$, which is an order parameter for the confinement-deconfinement phase transition for pure gauge theory [6, 7]. The interpolation of $l(x)$ between three different degenerate $Z(3)$ vacua leads to the existence of domain walls (interfaces) together with topological strings when the three interfaces make a junction. We call these strings as QGP strings [3].

In the present work, we studied the effects of explicit symmetry breaking arising from quark effects on the formation and evolution of $Z(3)$ interfaces and associated strings. Explicit symmetry breaking makes Z(3) vacua non-degenerate with two vacua $l = z, z^2$ remaining degenerate with each other but having higher energy than the true $l = 1$ vacuum. Thus $l = z, z^2$ vacua become metastable. We have used an effective potential for the Polyakov loop expectation value $l(x)$ from ref. [8–13] with incorporation of explicit symmetry breaking in terms of a linear term in l and have studied the dynamics of the (C-D) phase transition in the temperature/time range when the first order transition of this model proceeds via bubble nucleation. This allows for only relatively small explicit symmetry breaking (characterized by the strength b_1 of the linear term in l).

The $Z(3)$ wall network and associated strings exist only during the QGP phase, melting away when the temperature drops below T_c. However, they may leave their signatures in the distribution of final particles due to large concentration of energy density in extended regions as well as due to non-trivial scatterings of quarks and antiquarks with these objects. The extended regions of high energy density resulting from the domain walls and strings are clearly seen in our simulations and some extended structures/hot spots also survive after the temperature drops below the transition temperature T_c. This is just as was seen in the case of $b_1 = 0$ case in ref. [3]. We again mention that even the hot spot resulting from the collapse of closed domain walls in our simulations will be stretched in the longitudinal direction into an extended linear structure (resulting from the collapse of a cylindrical wall). These may be observable in the analysis of particle multiplicities. This is important especially in respect to the ridge phenomenon seen at RHIC [14–16]. In view of lasting extended energy density fluctuations from Z(3) walls, it is of interest to check if these structures can account for the ridge phenomenon.

Our results show interesting pattern of the evolution of the fluctuations in the energy density which show that these fluctuations do not decrease with time which was the case for $b_1 = 0$ case studied in ref. [3]. Especially important may be the presence of small additional peak of short times for $b_1 > 0$ case. Fluctuations near the transition stage may leave direct imprints on particle distributions. However, dileptons or direct photons should be sensitive to these fluctuations, and these may give a time history of evolution of such energy density fluctuations during the early stages. In such a case the existence of small peak for $b_1 > 0$ case may be observable.

A dramatic difference between the case of $b_1 = 0$ and $b_1 \neq 0$ is seen in Fig.5.8 and Fig.5.9 of chapter 5 of the thesis. Collapse of a closed wall is expected and was seen for $b_1 = 0$ case also, though the wall speed here is much higher, close to 1. In general we have seen here that walls separating true vacuum from metastable vacuum have speeds much higher than seen for the case of $b_1 = 0$. What is qualitatively new in the present case is rapidly expanding circular front after the collapse of the wall. This front continues its speed and shape even when temperature drops below T_c. Possibility of such expanding circular (cylindrical, with longitudinal expansion) energetic fronts should have important implications on particle momenta, especially on various flow coefficients.

Another important difference due to $b_1 > 0$ is expected in investigating the interactions of quarks and antiquarks with domain walls. Earlier it had been argued [3] that collapsing Z(3) walls will lead to concentration of quarks (due to small non-zero chemical potential in RHICE) in small regions [4]. This will lead to enhancement of baryons, especially at high P_T [17] due to P_T enhancement of quarks/antiquarks as they undergo repeated reflections from a collapsing wall. (There is also a possibility of spontaneous CP violation in the scattering of quarks and antiquarks from Z(3) walls, see ref. [18].) However, with $b_1 > 0$, there may also be a possibility that some Z(3) wall may actually expand (the one enclosing the true vacuum and with sufficiently large size). In that case it will have opposite effect and baryon number will be more diffused. Even the enhancement of P_T may happen for some domain walls (those which enclose metastable vacuum) while the expanding closed walls (enclosing the true vacuum) should lead to the redshift of the momenta for the enclosed quarks. All these issue need to be explored with more elaborate simulations. In this context the difference in the wall velocity between different types of Z(3) walls is of importance. While studying the effects of quark reflections from these walls and associated modification of P_T spectrum, wall velocity is of crucial importance and the presence of different types of collapsing Z(3) walls may lead to bunches of hadrons with different patterns of modified P_T spectra.

Bibliography

[1] U. S. Gupta and V. K. Tiwari, *Revisiting the Phase Structure of the Polyakov-quark-meson Model in the presence of Vacuum Fermion Fluctuation*, `arXiv:1107.1312`. * Temporary entry *.

[2] U. S. Gupta and V. K. Tiwari, *Meson Masses and Mixing Angles in 2+1 Flavor Polyakov Quark Meson Sigma Model and Symmetry Restoration Effects*, *Phys.Rev.* **D81** (2010) 054019, [`arXiv:0911.2464`].

[3] U. S. Gupta, R. K. Mohapatra, A. M. Srivastava, and V. K. Tiwari, *Simulation of Z(3) walls and string production via bubble nucleation in a quark-hadron transition*, *Phys.Rev.* **D82** (2010) 074020, [`arXiv:1007.5001`].

[4] B. Layek, A. P. Mishra, A. M. Srivastava, and V. K. Tiwari, *Baryon inhomogeneity generation in the quark-gluon plasma phase*, *Phys.Rev.* **D73** (2006) 103514, [`hep-ph/0512367`].

[5] B. Layek, A. P. Mishra, and A. M. Srivastava, *Strings with a confining core in a quark-gluon plasma*, *Phys.Rev.* **D71** (2005) 074015, [`hep-ph/0502250`].

[6] L. D. McLerran and B. Svetitsky, *Quark Liberation at High Temperature: A Monte Carlo Study of SU(2) Gauge Theory*, *Phys.Rev.* **D24** (1981) 450.

[7] B. Svetitsky, *Symmetry Aspects of Finite Temperature Confinement Transitions*, *Phys.Rept.* **132** (1986) 1–53.

[8] R. D. Pisarski, *Quark gluon plasma as a condensate of SU(3) Wilson lines*, *Phys.Rev.* **D62** (2000) 111501, [hep-ph/0006205].

[9] A. Dumitru and R. D. Pisarski, *Event-by-event fluctuations from decay of a Polyakov loop condensate*, *Phys.Lett.* **B504** (2001) 282–290, [hep-ph/0010083].

[10] A. Dumitru and R. D. Pisarski, *Two point functions for SU(3) Polyakov loops near T(c)*, *Phys.Rev.* **D66** (2002) 096003, [hep-ph/0204223].

[11] A. Dumitru and R. D. Pisarski, *Explosive collisions at RHIC?*, *Nucl.Phys.* **A698** (2002) 444–447, [hep-ph/0102020].

[12] R. D. Pisarski, *Why the quark gluon plasma isn't a plasma*, hep-ph/0101168.

[13] A. Dumitru, D. Roder, and J. Ruppert, *The Quark mass dependence of T(c) in QCD: Working up from m = 0 or down from m = infinity?*, *Phys.Rev.* **D70** (2004) 074001, [hep-ph/0311119].

[14] **STAR** Collaboration, J. Adams *et. al.*, *Transverse-momentum p(t) correlations on (eta,Phi) from mean-p(t) fluctuations in Au - Au collisions at s(NN)**(1/2) = 200-GeV*, *J. Phys.* **G32** (2006) L37–L48, [nucl-ex/0509030].

[15] S. A. Voloshin, *Transverse radial expansion in nuclear collisions and two particle correlations*, *Phys.Lett.* **B632** (2006) 490–494, [nucl-th/0312065].

[16] A. Dumitru, F. Gelis, L. McLerran, and R. Venugopalan, *Glasma flux tubes and the near side ridge phenomenon at RHIC*, *Nucl.Phys.* **A810** (2008) 91–108, [arXiv:0804.3858].

[17] A. P. Mishra, A. M. Srivastava, and V. K. Tiwari, *Enhancement of high P(T) hadrons due to collapsing Z(3) walls in heavy-ion collisions*, *Indian J. Phys.* **85** (2011) 1161–1167.

[18] A. Atreya, A. Sarkar, and A. M. Srivastava, *Spontaneous CP violation in quark scattering from QCD Z(3) interfaces*, `arXiv:1111.3027`. * Temporary entry *.

Bibliography

[1] S. Glashow, *Partial Symmetries of Weak Interactions*, *Nucl.Phys.* **22** (1961) 579–588.

[2] P. W. Higgs, *Broken symmetries, massless particles and gauge fields*, *Phys.Lett.* **12** (1964) 132–133.

[3] P. W. Higgs, *Spontaneous Symmetry Breakdown without Massless Bosons*, *Phys.Rev.* **145** (1966) 1156–1163.

[4] D. Gross and F. Wilczek, *Ultraviolet Behavior of Nonabelian Gauge Theories*, *Phys.Rev.Lett.* **30** (1973) 1343–1346.

[5] H. Politzer, *Reliable Perturbative Results for Strong Interactions?*, *Phys.Rev.Lett.* **30** (1973) 1346–1349.

[6] S. Bethke, α_s *at Zinnowitz 2004*, *Nucl.Phys.Proc.Suppl.* **135** (2004) 345–352, [hep-ex/0407021].

[7] R. Hagedorn, *Statistical thermodynamics of strong interactions at high-energies*, *Nuovo Cim.Suppl.* **3** (1965) 147–186.

[8] R. Stock, *Relativistic Nuclear Collisions*, arXiv:0907.5071.

[9] D. H. Rischke, *The Quark gluon plasma in equilibrium*, *Prog.Part.Nucl.Phys.* **52** (2004) 197–296, [nucl-th/0305030].

[10] H. Meyer-Ortmanns, *Phase transitions in quantum chromodynamics*, *Rev.Mod.Phys.* **68** (1996) 473–598, [hep-lat/9608098].

[11] B. Muller, *Physics and signatures of the quark - gluon plasma*, *Rept.Prog.Phys.* **58** (1995) 611–636, [nucl-th/9410005].

[12] L. D. McLerran and B. Svetitsky, *Quark Liberation at High Temperature: A Monte Carlo Study of SU(2) Gauge Theory*, *Phys.Rev.* **D24** (1981) 450.

[13] F. Gelis, *The early stages of a high energy heavy ion collision*, arXiv:1110.1544. * Temporary entry *.

[14] E. V. Shuryak and I. Zahed, *Rethinking the properties of the quark gluon plasma at T approximately T(c)*, *Phys.Rev.* **C70** (2004) 021901, [hep-ph/0307267].

[15] E. Shuryak, *Why does the quark gluon plasma at RHIC behave as a nearly ideal fluid?*, *Prog.Part.Nucl.Phys.* **53** (2004) 273–303, [hep-ph/0312227].

[16] E. V. Shuryak and I. Zahed, *Towards a theory of binary bound states in the quark gluon plasma*, *Phys.Rev.* **D70** (2004) 054507, [hep-ph/0403127].

[17] E. V. Shuryak, *What RHIC experiments and theory tell us about properties of quark-gluon plasma?*, *Nucl.Phys.* **A750** (2005) 64–83, [hep-ph/0405066].

[18] M. Gyulassy and L. McLerran, *New forms of QCD matter discovered at RHIC*, *Nucl.Phys.* **A750** (2005) 30–63, [nucl-th/0405013]. RIKEN BNL Research Center Scientific Articles, Vol.9.

[19] P. Jacobs and X.-N. Wang, *Matter in extremis: Ultrarelativistic nuclear collisions at RHIC*, *Prog.Part.Nucl.Phys.* **54** (2005) 443–534, [hep-ph/0405125].

[20] U. W. Heinz, *Concepts of heavy ion physics*, hep-ph/0407360.

[21] P. Braun-Munzinger and J. Wambach, *Colloquium: Phase diagram of strongly interacting matter*, *Rev.Mod.Phys.* **81** (2009) 1031–1050.

[22] K. Fukushima, *QCD matter in extreme environments*, `arXiv:1108.2939`.

[23] K. Fukushima and T. Hatsuda, *The phase diagram of dense QCD*, *Rept.Prog.Phys.* **74** (2011) 014001, [`arXiv:1005.4814`].

[24] T. Schafer and E. V. Shuryak, *Instantons in QCD*, *Rev. Mod. Phys.* **70** (1998) 323–426, [`hep-ph/9610451`].

[25] D. W. Griffin, A. Snoke and S. Stringari, *Bose-Einstein Condensation*, *Cambridge University Press, Cambridge* (2006).

[26] R. D. Pisarski and F. Wilczek, *Remarks on the Chiral Phase Transition in Chromodynamics*, *Phys.Rev.* **D29** (1984) 338–341.

[27] M. Stephanov, *QCD phase diagram: An Overview*, *PoS* **LAT2006** (2006) 024, [`hep-lat/0701002`].

[28] L. D. McLerran and B. Svetitsky, *A Monte Carlo Study of SU(2) Yang-Mills Theory at Finite Temperature*, *Phys.Lett.* **B98** (1981) 195.

[29] A. M. Polyakov, *Thermal Properties of Gauge Fields and Quark Liberation*, *Phys.Lett.* **B72** (1978) 477–480.

[30] M. Okawa, *Universality of deconfining phase transition in (3+1)-dimensional SU(2) lattice gauge theory*, *Phys.Rev.Lett.* **60** (1988) 1805.

[31] M. Fukugita, M. Okawa, and A. Ukawa, *Finite size scaling study of the deconning phase transition in pure SU(3) lattice gauge theory*, *Nucl.Phys.* **B337** (1990) 181.

[32] B. Svetitsky, *Symmetry Aspects of Finite Temperature Confinement Transitions*, *Phys.Rept.* **132** (1986) 1–53.

[33] F. Karsch and S. Stickan, *The Three-dimensional, three state Potts model in an external field*, *Phys.Lett.* **B488** (2000) 319–325, [hep-lat/0007019].

[34] B. Lucini, M. Teper, and U. Wenger, *The High temperature phase transition in SU(N) gauge theories*, *JHEP* **0401** (2004) 061, [hep-lat/0307017]. Dedicated to the memory of Ian Kogan.

[35] S. Datta and S. Gupta, *Scaling and the continuum limit of the finite temperature deconfinement transition in $SU(N_c)$ pure gauge theory*, *Phys.Rev.* **D80** (2009) 114504, [arXiv:0909.5591].

[36] F. Wu, *The Potts model*, *Rev.Mod.Phys.* **54** (1982) 235–268.

[37] R. D. Pisarski, *Quark gluon plasma as a condensate of SU(3) Wilson lines*, *Phys.Rev.* **D62** (2000) 111501, [hep-ph/0006205].

[38] B. Layek, A. P. Mishra, A. M. Srivastava, and V. K. Tiwari, *Baryon inhomogeneity generation in the quark-gluon plasma phase*, *Phys.Rev.* **D73** (2006) 103514, [hep-ph/0512367].

[39] F. Karsch, *Lattice QCD at high temperature and density*, *Lect. Notes Phys.* **583** (2002) 209–249, [hep-lat/0106019].

[40] Z. Fodor, S. Katz, and K. Szabo, *The QCD equation of state at nonzero densities: Lattice result*, *Phys.Lett.* **B568** (2003) 73–77, [hep-lat/0208078].

[41] **CP-PACS collaboration** Collaboration, A. Ali Khan *et. al.*, *Equation of state in finite temperature QCD with two flavors of improved Wilson quarks*, *Phys.Rev.* **D64** (2001) 074510, [hep-lat/0103028].

[42] C. Allton, M. Doring, S. Ejiri, S. Hands, O. Kaczmarek, *et. al.*, *Thermodynamics of two flavor QCD to sixth order in quark chemical potential*, *Phys.Rev.* **D71** (2005) 054508, [hep-lat/0501030].

[43] **MILC Collaboration** Collaboration, C. Bernard *et. al.*, *QCD thermodynamics with three flavors of improved staggered quarks*, *Phys.Rev.* **D71** (2005) 034504, [`hep-lat/0405029`].

[44] Y. Maezawa, S. Aoki, S. Ejiri, T. Hatsuda, N. Ishii, *et. al.*, *Thermodynamics of two-flavor lattice QCD with an improved Wilson quark action at non-zero temperature and density*, *J.Phys.G* **G34** (2007) S651–654, [`hep-lat/0702005`].

[45] Y. Aoki, Z. Fodor, S. Katz, and K. Szabo, *The QCD transition temperature: Results with physical masses in the continuum limit*, *Phys.Lett.* **B643** (2006) 46–54, [`hep-lat/0609068`].

[46] F. Karsch, *Thermodynamic properties of strongly interacting matter at non-zero baryon number density*, *J. Phys.* **G31** (2005) S633–S640, [`hep-lat/0412038`].

[47] F. Karsch, *Transition temperature in QCD with physical light and strange quark masses*, `hep-ph/0701210`.

[48] M. Cheng, N. Christ, S. Datta, J. van der Heide, C. Jung, *et. al.*, *The Transition temperature in QCD*, *Phys.Rev.* **D74** (2006) 054507, [`hep-lat/0608013`].

[49] M. Cheng, N. Christ, S. Datta, J. van der Heide, C. Jung, *et. al.*, *The QCD equation of state with almost physical quark masses*, *Phys.Rev.* **D77** (2008) 014511, [`arXiv:0710.0354`].

[50] S. Digal, E. Laermann, and H. Satz, *Deconfinement through chiral symmetry restoration in two flavor QCD*, *Eur.Phys.J.* **C18** (2001) 583–586, [`hep-ph/0007175`].

[51] Y. Aoki, S. Borsanyi, S. Durr, Z. Fodor, S. D. Katz, *et. al.*, *The QCD transition temperature: results with physical masses in the continuum limit II.*, *JHEP* **0906** (2009) 088, [`arXiv:0903.4155`].

[52] A. Bazavov, T. Bhattacharya, M. Cheng, N. Christ, C. DeTar, *et. al.*, *Equation of state and QCD transition at finite temperature*, *Phys.Rev.* **D80** (2009) 014504, [arXiv:0903.4379].

[53] V. Bornyakov, R. Horsley, S. Morozov, Y. Nakamura, M. Polikarpov, *et. al.*, *Probing the finite temperature phase transition with N(f) = 2 nonperturbatively improved Wilson fermions*, *Phys.Rev.* **D82** (2010) 014504, [arXiv:0910.2392].

[54] M. Cheng, N. H. Christ, M. Li, R. D. Mawhinney, D. Renfrew, *et. al.*, *The finite temperature QCD using 2 + 1 flavors of domain wall fermions at N (t) = 8*, *Phys.Rev.* **D81** (2010) 054510, [arXiv:0911.3450].

[55] J. T. Lenaghan, D. H. Rischke, and J. Schaffner-Bielich, *Chiral symmetry restoration at nonzero temperature in the SU(3)(r) x SU(3)(l) linear sigma model*, *Phys.Rev.* **D62** (2000) 085008, [nucl-th/0004006].

[56] J. T. Lenaghan and D. H. Rischke, *The O(N) model at finite temperature: Renormalization of the gap equations in Hartree and large-N approximation*, *J. Phys.* **G26** (2000) 431–450, [nucl-th/9901049].

[57] S. Chiku and T. Hatsuda, *Optimized perturbation theory at finite temperature*, *Phys.Rev.* **D58** (1998) 076001, [hep-ph/9803226].

[58] S. Chiku, *Optimized perturbation theory at finite temperature: Two loop analysis*, *Prog.Theor.Phys.* **104** (2000) 1129–1150, [hep-ph/0012322].

[59] T. Herpay, A. Patkos, Z. Szep, and P. Szepfalusy, *Mapping the boundary of the first order finite temperature restoration of chiral symmetry in the (m(pi) - m(K))-plane with a linear sigma model*, *Phys.Rev.* **D71** (2005) 125017, [hep-ph/0504167].

[60] T. Herpay and Z. Szep, *Resummed one-loop determination of the phase boundary of the SU(3)(R) x SU(3)(L) linear sigma model in the (m(pi) - m(K))-plane*, *Phys.Rev.* **D74** (2006) 025008, [hep-ph/0604086].

[61] P. Kovacs and Z. Szep, *The critical surface of the $SU(3)_L \times SU(3)_R$ chiral quark model at non-zero baryon density*, *Phys.Rev.* **D75** (2007) 025015, [hep-ph/0611208].

[62] G. Fejos and A. Patkos, *A Renormalized large-n solution of the $U(n) \times U(n)$ linear sigma model in the broken symmetry phase*, *Phys.Rev.* **D82** (2010) 045011, [arXiv:1005.1382].

[63] O. Scavenius, A. Mocsy, I. Mishustin, and D. Rischke, *Chiral phase transition within effective models with constituent quarks*, *Phys.Rev.* **C64** (2001) 045202, [nucl-th/0007030].

[64] B.-J. Schaefer and M. Wagner, *The Three-flavor chiral phase structure in hot and dense QCD matter*, *Phys.Rev.* **D79** (2009) 014018, [arXiv:0808.1491].

[65] R. Khan and L. T. Kyllingstad, *The chiral phase transition and the role of vacuum fluctuations*, *AIP Conf. Proc.* **1343** (2011) 504–506, [arXiv:1011.6507].

[66] A. Jakovac, A. Patkos, Z. Szep, and P. Szepfalusy, *T - mu phase diagram of the chiral quark model from a large flavor number expansion*, *Phys.Lett.* **B582** (2004) 179–186, [hep-ph/0312088].

[67] A. Mocsy, I. Mishustin, and P. Ellis, *Role of fluctuations in the linear sigma model with quarks*, *Phys.Rev.* **C70** (2004) 015204, [nucl-th/0402070].

[68] B.-J. Schaefer and J. Wambach, *The Phase diagram of the quark meson model*, *Nucl.Phys.* **A757** (2005) 479–492, [nucl-th/0403039].

[69] B.-J. Schaefer and J. Wambach, *Susceptibilities near the QCD (tri)critical point*, *Phys.Rev.* **D75** (2007) 085015, [hep-ph/0603256].

[70] E. Bowman and J. I. Kapusta, *Critical Points in the Linear Sigma Model with Quarks*, *Phys.Rev.* **C79** (2009) 015202, [arXiv:0810.0042].

[71] A. Jakovac and Z. Szep, *Strange mass dependence of the tricritical point in the $U(3)_L \times U(3)_R$ chiral sigma model*, *Phys.Rev.* **D82** (2010) 125038, [arXiv:1007.2877].

[72] L. Ferroni, V. Koch, and M. B. Pinto, *Multiple Critical Points in Effective Quark Models*, *Phys.Rev.* **C82** (2010) 055205, [arXiv:1007.4721].

[73] P. Costa, M. Ruivo, and C. de Sousa, *Thermodynamics and critical behavior in the Nambu-Jona-Lasinio model of QCD*, *Phys.Rev.* **D77** (2008) 096001, [arXiv:0801.3417].

[74] J.-L. Kneur, M. B. Pinto, and R. O. Ramos, *Thermodynamics and Phase Structure of the Two-Flavor Nambu–Jona-Lasinio Model Beyond Large-N_c*, *Phys.Rev.* **C81** (2010) 065205, [arXiv:1004.3815].

[75] T. Kahara and K. Tuominen, *Degrees of freedom and the phase transitions of two flavor QCD*, *Phys.Rev.* **D78** (2008) 034015, [arXiv:0803.2598].

[76] T. Kahara and K. Tuominen, *Effective models of two-flavor QCD: From small towards large m(q)*, *Phys.Rev.* **D80** (2009) 114022, [arXiv:0906.0890].

[77] T. Kahara and K. Tuominen, *Effective models of two-flavor QCD: Finite μ and m_q-dependence*, *Phys.Rev.* **D82** (2010) 114026, [arXiv:1006.3931].

[78] D. Nickel, *Inhomogeneous phases in the Nambu-Jona-Lasino and quark-meson model*, *Phys.Rev.* **D80** (2009) 074025, [arXiv:0906.5295].

[79] K. Fukushima, *Chiral effective model with the Polyakov loop*, *Phys.Lett.* **B591** (2004) 277–284, [hep-ph/0310121].

[80] C. Ratti, M. A. Thaler, and W. Weise, *Phases of QCD: Lattice thermodynamics and a field theoretical model*, *Phys.Rev.* **D73** (2006) 014019, [hep-ph/0506234].

[81] S. Roessner, C. Ratti, and W. Weise, *Polyakov loop, diquarks and the two-flavour phase diagram*, *Phys.Rev.* **D75** (2007) 034007, [hep-ph/0609281].

[82] S. Roessner, T. Hell, C. Ratti, and W. Weise, *The chiral and deconfinement crossover transitions: PNJL model beyond mean field*, *Nucl.Phys.* **A814** (2008) 118–143, [arXiv:0712.3152].

[83] S. K. Ghosh, T. K. Mukherjee, M. G. Mustafa, and R. Ray, *Susceptibilities and speed of sound from PNJL model*, *Phys.Rev.* **D73** (2006) 114007, [hep-ph/0603050].

[84] C. Sasaki, B. Friman, and K. Redlich, *Susceptibilities and the Phase Structure of a Chiral Model with Polyakov Loops*, *Phys.Rev.* **D75** (2007) 074013, [hep-ph/0611147].

[85] T. Hell, S. Roessner, M. Cristoforetti, and W. Weise, *Dynamics and thermodynamics of a non-local PNJL model with running coupling*, *Phys.Rev.* **D79** (2009) 014022, [arXiv:0810.1099].

[86] H. Abuki, R. Anglani, R. Gatto, G. Nardulli, and M. Ruggieri, *Chiral crossover, deconfinement and quarkyonic matter within a Nambu-Jona Lasinio model with the Polyakov loop*, *Phys.Rev.* **D78** (2008) 034034, [arXiv:0805.1509].

[87] M. Ciminale, R. Gatto, N. Ippolito, G. Nardulli, and M. Ruggieri, *Three flavor Nambu-Jona Lasinio model with Polyakov loop and competition with nuclear matter*, *Phys.Rev.* **D77** (2008) 054023, [arXiv:0711.3397].

[88] W.-j. Fu, Z. Zhang, and Y.-x. Liu, *2+1 flavor Polyakov-Nambu-Jona-Lasinio model at finite temperature and nonzero chemical potential*, *Phys.Rev.* **D77** (2008) 014006, [arXiv:0711.0154].

[89] K. Fukushima, *Phase diagrams in the three-flavor Nambu-Jona-Lasinio model with the Polyakov loop*, *Phys.Rev.* **D77** (2008) 114028, [arXiv:0803.3318].

[90] K. Fukushima, *Critical surface in hot and dense QCD with the vector interaction*, *Phys.Rev.* **D78** (2008) 114019, [arXiv:0809.3080].

[91] K. Fukushima, *Isentropic thermodynamics in the PNJL model*, *Phys.Rev.* **D79** (2009) 074015, [arXiv:0901.0783].

[92] H. Hansen, W. Alberico, A. Beraudo, A. Molinari, M. Nardi, *et. al.*, *Mesonic correlation functions at finite temperature and density in the Nambu-Jona-Lasinio model with a Polyakov loop*, *Phys.Rev.* **D75** (2007) 065004, [hep-ph/0609116].

[93] P. Costa, M. Ruivo, C. de Sousa, H. Hansen, and W. Alberico, *Scalar-pseudoscalar meson behavior and restoration of symmetries in SU(3) PNJL model*, *Phys.Rev.* **D79** (2009) 116003, [arXiv:0807.2134].

[94] K. Kashiwa, H. Kouno, M. Matsuzaki, and M. Yahiro, *Critical endpoint in the Polyakov-loop extended NJL model*, *Phys.Lett.* **B662** (2008) 26–32, [arXiv:0710.2180].

[95] A. Radzhabov, D. Blaschke, M. Buballa, and M. Volkov, *Nonlocal PNJL model beyond mean field and the QCD phase transition*, *Phys.Rev.* **D83** (2011) 116004, [arXiv:1012.0664].

[96] B.-J. Schaefer, J. M. Pawlowski, and J. Wambach, *The Phase Structure of the Polyakov–Quark-Meson Model*, *Phys.Rev.* **D76** (2007) 074023, [arXiv:0704.3234].

[97] B.-J. Schaefer and M. Wagner, *On the QCD phase structure from effective models*, arXiv:0812.2855.

[98] B.-J. Schaefer, M. Wagner, and J. Wambach, *QCD thermodynamics with effective models*, *PoS* **CPOD2009** (2009) 017, [arXiv:0909.0289].

[99] B.-J. Schaefer, M. Wagner, and J. Wambach, *Thermodynamics of (2+1)-flavor QCD: Confronting Models with Lattice Studies*, *Phys.Rev.* **D81** (2010) 074013, [arXiv:0910.5628].

[100] H. Mao, J. Jin, and M. Huang, *Phase diagram and thermodynamics of the Polyakov linear sigma model with three quark flavors*, *J. Phys.* **G37** (2010) 035001, [arXiv:0906.1324].

[101] U. S. Gupta and V. K. Tiwari, *Meson Masses and Mixing Angles in 2+1 Flavor Polyakov Quark Meson Sigma Model and Symmetry Restoration Effects*, *Phys.Rev.* **D81** (2010) 054019, [arXiv:0911.2464].

[102] G. Marko and Z. Szep, *Influence of the Polyakov loop on the chiral phase transition in the two flavor chiral quark model*, *Phys.Rev.* **D82** (2010) 065021, [arXiv:1006.0212].

[103] V. Skokov, B. Friman, E. Nakano, K. Redlich, and B.-J. Schaefer, *Vacuum fluctuations and the thermodynamics of chiral models*, *Phys.Rev.* **D82** (2010) 034029, [arXiv:1005.3166].

[104] T. K. Herbst, J. M. Pawlowski, and B.-J. Schaefer, *The phase structure of the Polyakov–quark-meson model beyond mean field*, *Phys.Lett.* **B696** (2011) 58–67, [arXiv:1008.0081].

[105] U. S. Gupta and V. K. Tiwari, *Revisiting the Phase Structure of the Polyakov-quark-meson Model in the presence of Vacuum Fermion Fluctuation*, `arXiv:1107.1312`. * Temporary entry *.

[106] B. Layek, A. P. Mishra, and A. M. Srivastava, *Strings with a confining core in a quark-gluon plasma*, *Phys.Rev.* **D71** (2005) 074015, [`hep-ph/0502250`].

[107] U. S. Gupta, R. K. Mohapatra, A. M. Srivastava, and V. K. Tiwari, *Simulation of Z(3) walls and string production via bubble nucleation in a quark-hadron transition*, *Phys.Rev.* **D82** (2010) 074020, [`arXiv:1007.5001`].

[108] U. Gupta, R. Mohapatra, A. Srivastava, and V. Tiwari, *Simulation of first order confinement transition in relativistic heavy ion collision*, *Indian J.Phys.* **85** (2011) 115–121.

[109] T. Kibble, *Some Implications of a Cosmological Phase Transition*, *Phys.Rept.* **67** (1980) 183.

[110] A. Dumitru and R. D. Pisarski, *Event-by-event fluctuations from decay of a Polyakov loop condensate*, *Phys.Lett.* **B504** (2001) 282–290, [`hep-ph/0010083`].

[111] A. Dumitru and R. D. Pisarski, *Two point functions for SU(3) Polyakov loops near T(c)*, *Phys.Rev.* **D66** (2002) 096003, [`hep-ph/0204223`].

[112] A. Dumitru and R. D. Pisarski, *Explosive collisions at RHIC?*, *Nucl.Phys.* **A698** (2002) 444–447, [`hep-ph/0102020`].

[113] S. R. Coleman, *The Fate of the False Vacuum. 1. Semiclassical Theory*, *Phys.Rev.* **D15** (1977) 2929–2936.

[114] U. S. Gupta, R. K. Mohapatra, A. M. Srivastava, and V. K. Tiwari, *Effects of quarks on the formation and evolution of Z(3) walls and strings in relativistic heavy-ion collisions*, `arXiv:1111.5402`. * Temporary entry *.

[115] J. I. Kapusta and C. Gales, *Finite Temperature Field Theory Principles and Applications*, *Cambridge University Press* (2006).

[116] K. Holland and U.-J. Wiese, *The Center symmetry and its spontaneous breakdown at high temperatures*, `hep-ph/0011193`. To be published in the Festschrift in honor of B.L. Ioffe, 'At the Frontier of Particle Physics / Handbook of QCD', edited by M. Shifman.

[117] N. Weiss, *Introduction to Z(N) symmetry in SU(N) gauge theories at finite temperatures*, `hep-ph/9311233`.

[118] K. G. Wilson, *Confinement of Quarks*, *Phys.Rev.* **D10** (1974) 2445–2459.

[119] N. Weiss, *The Effective Potential for the Order Parameter of Gauge Theories at Finite Temperature*, *Phys.Rev.* **D24** (1981) 475.

[120] N. Weiss, *The Wilson Line in Finite Temperature Gauge Theories*, *Phys.Rev.* **D25** (1982) 2667.

[121] P. B. Arnold and L. G. Yaffe, *The NonAbelian Debye screening length beyond leading order*, *Phys.Rev.* **D52** (1995) 7208–7219, [`hep-ph/9508280`].

[122] A. Hart, M. Laine, and O. Philipsen, *Static correlation lengths in QCD at high temperatures and finite densities*, *Nucl.Phys.* **B586** (2000) 443–474, [`hep-ph/0004060`].

[123] **WHOT-QCD Collaboration** Collaboration, Y. Maezawa *et. al.*, *Electric and Magnetic Screening Masses at Finite Temperature from Generalized Polyakov-Line Correlations in Two-flavor Lattice QCD*, *Phys.Rev.* **D81** (2010) 091501, [`arXiv:1003.1361`].

[124] G. 't Hooft, *Symmetry breaking through Bell-Jackiw anomalies*, *Phys. Rev. Lett.* **37** (1976) 8–11.

[125] G. 't Hooft, *Computation of the quantum effects due to a four- dimensional pseudoparticle*, *Phys. Rev.* **D14** (1976) 3432–3450.

[126] V. Bernard and U.-G. Meissner, *Chiral perturbation theory*, *Ann.Rev.Nucl.Part.Sci.* **57** (2007) 33–60, [hep-ph/0611231]. Commissioned article for Ann.Rev.Nucl.Part.Sci.

[127] B. Moussallam, *Chiral perturbation theory: A Basic introduction*, hep-ph/0407246.

[128] S. Scherer and M. R. Schindler, *A Chiral perturbation theory primer*, hep-ph/0505265.

[129] A. Paterson, *COLEMAN-WEINBERG SYMMETRY BREAKING IN THE CHIRAL SU(n) x SU(n) LINEAR sigma MODEL*, *Nucl.Phys.* **B190** (1981) 188.

[130] E. Laermann and O. Philipsen, *The Status of lattice QCD at finite temperature*, *Ann.Rev.Nucl.Part.Sci.* **53** (2003) 163–198, [hep-ph/0303042].

[131] F. Wilczek, *Application of the renormalization group to a second order QCD phase transition*, *Int.J.Mod.Phys.* **A7** (1992) 3911–3925.

[132] F. Karsch and E. Laermann, *Susceptibilities, the specific heat and a cumulant in two flavor QCD*, *Phys.Rev.* **D50** (1994) 6954–6962, [hep-lat/9406008].

[133] F. Karsch, *Lattice results on QCD thermodynamics*, *Nucl.Phys.* **A698** (2002) 199–208, [hep-ph/0103314].

[134] L. McLerran, *Quarkyonic Matter and the Revised Phase Diagram of QCD*, *Nucl.Phys.* **A830** (2009) 709C–712C, [arXiv:0907.4489].

[135] L. McLerran and R. D. Pisarski, *Phases of cold, dense quarks at large N(c)*, *Nucl.Phys.* **A796** (2007) 83–100, [arXiv:0706.2191].

[136] B. Svetitsky and L. G. Yaffe, *Critical Behavior at Finite Temperature Confinement Transitions*, *Nucl.Phys.* **B210** (1982) 423.

[137] C. DeTar and U. Heller, *QCD Thermodynamics from the Lattice*, *Eur.Phys.J.* **A41** (2009) 405–437, [arXiv:0905.2949].

[138] Y. Aoki, G. Endrodi, Z. Fodor, S. Katz, and K. Szabo, *The Order of the quantum chromodynamics transition predicted by the standard model of particle physics*, *Nature* **443** (2006) 675–678, [hep-lat/0611014].

[139] **Wuppertal-Budapest Collaboration** Collaboration, S. Borsanyi *et. al.*, *Is there still any T_c mystery in lattice QCD? Results with physical masses in the continuum limit III*, *JHEP* **1009** (2010) 073, [arXiv:1005.3508].

[140] **HotQCD collaboration** Collaboration, A. Bazavov and P. Petreczky, *Deconfinement and chiral transition with the highly improved staggered quark (HISQ) action*, *J.Phys.Conf.Ser.* **230** (2010) 012014, [arXiv:1005.1131].

[141] M. Asakawa and K. Yazaki, *CHIRAL RESTORATION AT FINITE DENSITY AND TEMPERATURE*, *Nucl.Phys.* **A504** (1989) 668–684.

[142] A. Barducci, R. Casalbuoni, S. De Curtis, R. Gatto, and G. Pettini, *CHIRAL SYMMETRY BREAKING IN QCD AT FINITE TEMPERATURE AND DENSITY*, *Phys.Lett.* **B231** (1989) 463.

[143] J. Berges and K. Rajagopal, *Color superconductivity and chiral symmetry restoration at nonzero baryon density and temperature*, *Nucl.Phys.* **B538** (1999) 215–232, [hep-ph/9804233].

[144] M. A. Stephanov, K. Rajagopal, and E. V. Shuryak, *Signatures of the tricritical point in QCD*, *Phys.Rev.Lett.* **81** (1998) 4816–4819, [hep-ph/9806219].

[145] M. A. Stephanov, K. Rajagopal, and E. V. Shuryak, *Event-by-event fluctuations in heavy ion collisions and the QCD critical point*, *Phys.Rev.* **D60** (1999) 114028, [hep-ph/9903292].

[146] S. Gavin, A. Gocksch, and R. D. Pisarski, *QCD and the chiral critical point*, *Phys.Rev.* **D49** (1994) 3079–3082, [hep-ph/9311350].

[147] O. Philipsen, *Lattice QCD at finite temperature and density*, *Eur.Phys.J.ST* **152** (2007) 29–60, [arXiv:0708.1293].

[148] Y. Hatta and T. Ikeda, *Universality, the QCD critical / tricritical point and the quark number susceptibility*, *Phys.Rev.* **D67** (2003) 014028, [hep-ph/0210284].

[149] P. de Forcrand and O. Philipsen, *The Chiral critical line of N(f) = 2+1 QCD at zero and non-zero baryon density*, *JHEP* **0701** (2007) 077, [hep-lat/0607017].

[150] P. de Forcrand and O. Philipsen, *The Chiral critical point of N(f) = 3 QCD at finite density to the order (mu/T)**4*, *JHEP* **0811** (2008) 012, [arXiv:0808.1096].

[151] P. Braun-Munzinger, K. Redlich, and J. Stachel, *Particle production in heavy ion collisions*, nucl-th/0304013. To appear in Quark Gluon Plasma 3, eds. R.C. Hwa and Xin-Nian Wang, World Scientific Publishing.

[152] M. Huang, *QCD Phase Diagram at High Temperature and Density*, arXiv:1001.3216.

[153] **the STAR Collaboration** Collaboration, B. Abelev *et. al.*, *Mass, quark-number, and sqrt s(NN) dependence of the second and fourth flow harmonics in ultra-relativistic nucleus-nucleus collisions*, *Phys.Rev.* **C75** (2007) 054906, [nucl-ex/0701010].

[154] **PHENIX Collaboration** Collaboration, A. Adare *et. al.*, *Scaling properties of azimuthal anisotropy in Au+Au and Cu+Cu collisions at s(NN) = 200-GeV*, *Phys.Rev.Lett.* **98** (2007) 162301, [nucl-ex/0608033].

[155] H. Song and U. W. Heinz, *Multiplicity scaling in ideal and viscous hydrodynamics*, *Phys.Rev.* **C78** (2008) 024902, [arXiv:0805.1756].

[156] P. Romatschke and U. Romatschke, *Viscosity Information from Relativistic Nuclear Collisions: How Perfect is the Fluid Observed at RHIC?*, *Phys.Rev.Lett.* **99** (2007) 172301, [arXiv:0706.1522].

[157] S. Bass, M. Belkacem, M. Bleicher, M. Brandstetter, L. Bravina, *et. al.*, *Microscopic models for ultrarelativistic heavy ion collisions*, *Prog.Part.Nucl.Phys.* **41** (1998) 255–369, [nucl-th/9803035].

[158] M. Bleicher *et. al.*, *Relativistic hadron hadron collisions in the ultra- relativistic quantum molecular dynamics model*, *J. Phys.* **G25** (1999) 1859–1896, [hep-ph/9909407].

[159] A. Andronic, P. Braun-Munzinger, and J. Stachel, *Hadron production in central nucleus-nucleus collisions at chemical freeze-out*, *Nucl.Phys.* **A772** (2006) 167–199, [nucl-th/0511071].

[160] J. Kapusta and E. Bowman, *Critical Points in the QCD Phase Diagram with Two Flavors of Quarks*, *Nucl.Phys.* **A830** (2009) 721C–724C, [arXiv:0907.4660].

[161] A. J. Mizher, M. Chernodub, and E. S. Fraga, *Phase diagram of hot QCD in an external magnetic field: possible splitting of deconfinement and chiral transitions*, *Phys.Rev.* **D82** (2010) 105016, [arXiv:1004.2712].

[162] L. F. Palhares and E. S. Fraga, *Perturbative Yukawa theory at finite density: The Role of masses and renormalization group flow at two loops*, *Phys.Rev.* **D78** (2008) 025013, [arXiv:0803.0262].

[163] E. S. Fraga, L. F. Palhares, and M. B. Pinto, *Nonperturbative Yukawa theory at finite density and temperature*, *Phys.Rev.* **D79** (2009) 065026, [arXiv:0902.1498].

[164] L. F. Palhares and E. S. Fraga, *Droplets in the cold and dense linear sigma model with quarks*, *Phys.Rev.* **D82** (2010) 125018, [arXiv:1006.2357].

[165] M. Quiros, *Finite temperature field theory and phase transitions*, hep-ph/9901312.

[166] J. Braun, L. M. Haas, F. Marhauser, and J. M. Pawlowski, *Phase Structure of Two-Flavor QCD at Finite Chemical Potential*, *Phys.Rev.Lett.* **106** (2011) 022002, [arXiv:0908.0008].

[167] S. Ejiri, F. Karsch, E. Laermann, and C. Schmidt, *The Isentropic equation of state of 2-flavor QCD*, *Phys.Rev.* **D73** (2006) 054506, [hep-lat/0512040].

[168] B. Mohanty and J.-e. Alam, *Velocity of sound in relativistic heavy ion collisions*, *Phys.Rev.* **C68** (2003) 064903, [nucl-th/0301086].

[169] P. Costa, M. Ruivo, C. de Sousa, and Y. Kalinovsky, *Analysis of the U(A)(1) symmetry-breaking and restoration effects on scalar-pseudoscalar spectrum*, *Phys.Rev.* **D71** (2005) 116002, [hep-ph/0503258].

[170] P. Costa, M. Ruivo, C. de Sousa, and Y. Kalinovsky, *Effective restoration of the U(A)(1) symmetry with temperature and density*, *Phys.Rev.* **D70** (2004) 116013, [hep-ph/0408177].

[171] J. Schaffner-Bielich, *Effective restoration of the U(A)(1) symmetry in the SU(3) linear sigma model*, *Phys.Rev.Lett.* **84** (2000) 3261, [hep-ph/9906361].

[172] K. Fukushima, K. Ohnishi, and K. Ohta, *Topological susceptibility at zero and finite temperature in the Nambu-Jona-Lasinio model*, *Phys.Rev.* **C63** (2001) 045203, [nucl-th/0101062].

[173] S. Weinberg, *The U(1) Problem*, *Phys. Rev.* **D11** (1975) 3583–3593.

[174] J. M. Cornwall, R. Jackiw, and E. Tomboulis, *Effective Action for Composite Operators*, *Phys.Rev.* **D10** (1974) 2428–2445.

[175] T. Bhattacharya, A. Gocksch, C. Korthals Altes, and R. D. Pisarski, *Z(N) interface tension in a hot SU(N) gauge theory*, *Nucl.Phys.* **B383** (1992) 497–524, [hep-ph/9205231].

[176] J. Boorstein and D. Kutasov, *Wilson loops, winding modes and domain walls in finite temperature QCD*, *Phys.Rev.* **D51** (1995) 7111–7123, [hep-th/9409128].

[177] A. V. Smilga, *Are Z(N) bubbles really there?*, *Annals Phys.* **234** (1994) 1–59.

[178] V. Belyaev, I. I. Kogan, G. Semenoff, and N. Weiss, *Z(N) domains in gauge theories with fermions at high temperature*, *Phys.Lett.* **B277** (1992) 331–336.

[179] C. Korthals Altes, *Z(N) bubbles and their descendants in hot QCD: Alive and bubbling*, hep-th/9402028.

[180] R. D. Pisarski, *Why the quark gluon plasma isn't a plasma*, hep-ph/0101168.

[181] M. Deka, S. Digal, and A. P. Mishra, *Meta-stable States in Quark-Gluon Plasma*, arXiv:1009.0739.

[182] A. Dumitru, D. Roder, and J. Ruppert, *The Quark mass dependence of T(c) in QCD: Working up from m = 0 or down from m = infinity?*, *Phys.Rev.* **D70** (2004) 074001, [hep-ph/0311119].

[183] T. Banks and A. Ukawa, *Deconfining and Chiral Phase Transitions in Quantum Chromodynamics at Finite Temperature*, *Nucl.Phys.* **B225** (1983) 145.

[184] F. Green and F. Karsch, *Mean Field Analysis of SU(N) Deconfining Transitions in the Presence of Dynamical Quarks*, *Nucl.Phys.* **B238** (1984) 297.

[185] P. N. Meisinger and M. C. Ogilvie, *An Effective action for finite temperature lattice gauge theories with dynamical fermions*, *Phys.Rev.* **D52** (1995) 3024–3029, [hep-lat/9502003].

[186] S. Digal, E. Laermann, and H. Satz, *Interplay between chiral transition and deconfinement*, *Nucl.Phys.* **A702** (2002) 159–163.

[187] F. Karsch, E. Laermann, A. Peikert, C. Schmidt, and S. Stickan, *Flavor and quark mass dependence of QCD thermodynamics*, *Nucl.Phys.Proc.Suppl.* **94** (2001) 411–414, [hep-lat/0010040].

[188] J. Ignatius, K. Kajantie, and K. Rummukainen, *Cosmological QCD Z(3) phase transition in the 10-TeV temperature range?*, *Phys.Rev.Lett.* **68** (1992) 737–740.

[189] V. Dixit and M. C. Ogilvie, *Metastability in SU(N) gauge theories at high temperatures*, *Phys.Lett.* **B269** (1991) 353–356.

[190] T. W. B. Kibble, *Topology of Cosmic Domains and Strings*, *J. Phys.* **A9** (1976) 1387–1398.

[191] W. H. Zurek, *Cosmological Experiments in Condensed Matter Systems*, *Phys. Rept.* **276** (1996) 177–221, [cond-mat/9607135].

[192] A. P. Mishra, A. M. Srivastava, and V. K. Tiwari, *Enhancement of high P(T) hadrons due to collapsing Z(3) walls in heavy-ion collisions*, *Indian J. Phys.* **85** (2011) 1161–1167.

[193] A. Bazavov, B. A. Berg, and A. Dumitru, *Thermalization in SU(3) gauge theory after a deconfining quench*, *Phys. Rev.* **D78** (2008) 034024, [arXiv:0805.0784].

[194] D. Diakonov and M. Oswald, *Gauge invariant effective action for the Polyakov line in the SU(N) Yang-Mills theory at high temperatures*, *Phys.Rev.* **D70** (2004) 105016, [hep-ph/0403108].

[195] O. Scavenius, A. Dumitru, and J. Lenaghan, *The K / pi ratio from condensed Polyakov loops*, *Phys.Rev.* **C66** (2002) 034903, [hep-ph/0201079].

[196] G. Boyd, J. Engels, F. Karsch, E. Laermann, C. Legeland, *et. al.*, *Thermodynamics of SU(3) lattice gauge theory*, *Nucl.Phys.* **B469** (1996) 419–444, [hep-lat/9602007].

[197] **CP-PACS Collaboration** Collaboration, M. Okamoto *et. al.*, *Equation of state for pure SU(3) gauge theory with renormalization group improved action*, *Phys.Rev.* **D60** (1999) 094510, [hep-lat/9905005].

[198] S. Chang, C. Hagmann, and P. Sikivie, *Studies of the motion and decay of axion walls bounded by strings*, *Phys.Rev.* **D59** (1999) 023505, [hep-ph/9807374].

[199] M. Huang and P. Sikivie, *THE STRUCTURE OF AXIONIC DOMAIN WALLS*, *Phys.Rev.* **D32** (1985) 1560.

[200] S. Digal and A. M. Srivastava, *Formation of topological defects with explicit symmetry breaking*, *Phys.Rev.Lett.* **76** (1996) 583–586, [hep-ph/9509263].

[201] S. Digal, S. Sengupta, and A. M. Srivastava, *Defect - antidefect pair production via field oscillations*, *Phys.Rev.* **D55** (1997) 3824–3829, [hep-ph/9608286].

[202] I. Kobzarev, L. Okun, and M. Voloshin, *Bubbles in Metastable Vacuum*, *Sov.J.Nucl.Phys.* **20** (1975) 644–646.

[203] A. D. Linde, *Decay of the False Vacuum at Finite Temperature*, *Nucl.Phys.* **B216** (1983) 421.

[204] J. Langer, *Statistical theory of the decay of metastable states*, *Annals Phys.* **54** (1969) 258–275.

[205] J. S. Langer and L. A. Turski, *Hydrodynamic model of the condensation of a vapor near its critical point*, *Phys. Rev.* **A8** (1973) 3230–3243.

[206] L. A. Turski and J. S. Langer, *Dynamics of a diffuse liquid-vapor interface*, *Phys. Rev.* **A22** (1980) 2189–2195.

[207] L. P. Csernai and J. I. Kapusta, *Nucleation of relativistic first order phase transitions*, *Phys.Rev.* **D46** (1992) 1379–1390.

[208] J. I. Kapusta, A. P. Vischer, and R. Venugopalan, *Nucleation of quark - gluon plasma from hadronic matter*, *Phys.Rev.* **C51** (1995) 901–910, [nucl-th/9408029].

[209] J. Bjorken, *Highly Relativistic Nucleus-Nucleus Collisions: The Central Rapidity Region*, *Phys.Rev.* **D27** (1983) 140–151.

[210] A. M. Srivastava, *Numerical simulation of bubble collision and formation of vortices*, *Phys.Rev.* **D45** (1992) 3304–3307.

[211] A. M. Srivastava, *Numerical simulation of dynamical production of vortices by critical and subcritical bubbles*, *Phys.Rev.* **D46** (1992) 1353–1367.

[212] S. Chakravarty and A. M. Srivastava, *Vortex production in a first order phase transition at finite temperature*, *Nucl.Phys.* **B406** (1993) 795–807, [hep-ph/9209246].

[213] T. C. Petersen and J. Randrup, *Dynamical simulation of DCC formation in Bjorken rods*, *Phys.Rev.* **C61** (2000) 024906, [nucl-th/9907051].

[214] **STAR** Collaboration, J. Adams *et. al.*, *Transverse-momentum p(t) correlations on (eta,Phi) from mean-p(t) fluctuations in Au - Au collisions at s(NN)**(1/2) = 200-GeV*, *J. Phys.* **G32** (2006) L37–L48, [nucl-ex/0509030].

[215] S. A. Voloshin, *Transverse radial expansion in nuclear collisions and two particle correlations*, *Phys.Lett.* **B632** (2006) 490–494, [nucl-th/0312065].

[216] A. Dumitru, F. Gelis, L. McLerran, and R. Venugopalan, *Glasma flux tubes and the near side ridge phenomenon at RHIC*, *Nucl.Phys.* **A810** (2008) 91–108, [arXiv:0804.3858].

[217] A. Atreya, A. Sarkar, and A. M. Srivastava, *Spontaneous CP violation in quark scattering from QCD Z(3) interfaces*, arXiv:1111.3027. * Temporary entry *.